Determining the Reaction Zone Length in Shock Initiated PETN

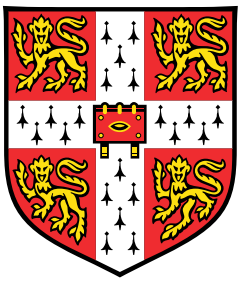

James Edgeley

Department of Physics
University of Cambridge

This dissertation is submitted for the degree of
Doctor of Philosophy

Trinity College

September 2022

Declaration

This dissertation is the result of my own work and includes nothing which is the outcome of work done in collaboration except where indicated in the text. No part of this dissertation has been submitted for any other degree at any institution. The length of this dissertation does not exceed the sixty thousand words permitted by the Physics and Chemistry Degree Committee.

James Edgeley
September 2022

Abstract

Pentaerythritol tetranitrate (PETN) is a secondary explosive used in electrical detonators in the form of a pressed powder. The reaction zone length of PETN is smaller than that of most other explosives, therefore there is a lack of data due to insufficient resolution of existing methods. Furthermore, most prior work has been on steady state behaviour, so the transition regime before steady state is particularly poorly understood.

The research described in this thesis was undertaken in order to characterise the reaction zone length and wave curvature during the evolution from initiation to steady state. The investigation was focused on a detonator setting, so confined cylindrical pellets of a similar scale were used here. To separate the effect of the chemical reaction from the mechanical response to shock, plate impact experiments were performed on an inert simulant: a fine icing sugar with comparable particle size. The shock velocity and rise time were found to exhibit dependence on the thickness of the bed, suggesting that these effects may also play a role in PETN prior to development of detonation.

A fibre launched laser flyer detonator system was constructed to allow repeatable shock initiation of the target samples with a high throughput. This apparatus could produce a highly tuneable shock without much of the electrical noise present with electrical detonators.

High-rate capacitive sensing was applied as a technique for measuring detonation properties in small columns of PETN. Development of the diagnostic incorporated design of the sensor itself, event synchronisation handling and noise reduction. A custom-made data processing algorithm was used to extract useful information from the sensor signal. This technology was found to have the temporal and spatial resolution required, as well as being cheaper and easier to implement than competing methods. Experiments using this diagnostic were performed to measure the reaction zone length and curvature for a range of densities and sample sizes. The data could also be used to calculate detonation velocity and 'lost time'. An important part of these experiments was the creation of consistent target samples.

A hydrocode incorporating the CREST reactive model was written to numerically model the detonation and provide a predictive capability. The results of the experiments were used to set the values of the parameters in the simulation.

Acknowledgements

This work was supervised by Chris Braithwaite, and I could not have asked for a better mentor. Chris's guidance got me through many difficult problems that arose during the course of this PhD, and contributed significantly to my professional and personal development.

I would also like to thank all my fellow Fracture group members who provided support and technical assistance during my time with them. I am also grateful to the Cavendish's research support staff, especially Kevin Mott for helping me to machine parts in the student workshop, and Huw Prytherch of the electronics workshop for repeatedly re-soldering my blast-damaged circuitry.

I am grateful for the financial support of AWE, and to Liz Lee and Rod Drake for their technical guidance and experience which helped focus the direction of this work and helped me to better understand the existing literature.

I wish to thank Trinity College, and my tutor Hugh Hunt for arranging additional funding. I would also like to thank all my friends at First and Third for making my university experience so enjoyable.

Finally to my family I am grateful for their unconditional support and encouragement. This work is dedicated to them.

Table of contents

List of figures

List of tables

Nomenclature

Acronyms / Abbreviations

ALE Arbitrary Lagrangian Eulerian

AMR Adaptive Mesh Refinement

AWG Arbitrary Waveform Generator

BET Brunauer-Emmet-Teller, a method for determining specific surface area

CCD Charge Coupled Device

CDU Capacitor Discharge Unit

CFL Courant-Friedrichs-Lewy

CFR Compact Folded Resonator

CGS Centimetre-Gram-Second

CJ Chapman-Jouguet, referring to either the overall theory of detonation, or the point at the rear of a detonation

CMOS Complementary Metal Oxide Semiconductor

CREST Computational Reaction Evolution dependent on Entropy (S) and Time

CWT Continuous Wavelet Transform

DAC Digital-to-Analogue Converter

DDT Deflagration to Detonation Transition, a pathway to detonation from burning

Di-PEHN Dipentaerythritol Hexanitrate

DSC Differential Scanning Calorimeter

DTI Direct Thermal Initiation

EBW Exploding Bridgewire, a type of detonator

EFI Exploding Foil Initiator, also called a slapper detonator

EOS Equation of State

FPC Flexible Printed Circuit

FSSS Fisher Sub Sieve Sizer, a method for determining specific surface area

FVM Finite Volume Method

FWHM Full Width Half Maximum

HERMES High Explosive Response to MEchanical Stimulus

HMX High Melting Explosive, also called octogen. IUPAC name: 1,3,5,7-Tetranitro-1,3,5,7-tetrazoctane

HNS Hexanitrostilbene. IUPAC name: 1,3,5-Trinitro-2-[2-(2,4,6-trinitrophenyl)ethenyl] benzene

ICE Integrated Cooler and Electronics

InGaAs Indium Gallium Arsenide, a semiconductor used in photodiode detectors

IP Initial Pressing

ISE Isentropic Solid Equation

IUPAC International Union of Pure and Applied Chemistry

JWL Jones-Wilkins-Lee

MC Monotonised Central

MUSCL Monotone Upwind Schemes for Conservation Laws

NA Numerical Aperture

Nd:YAG Neodymium doped Yttrium Aluminium Garnet, a crystal used as a lasing medium

ND Neutral Density

ORVIS Optically Recording Velocity Interferometer System

PBX Polymer-bonded explosive

PCI Phase Contrast Imaging, a diagnostic technique which measures the phase shift of a transmitted beam of radiation

PDV Photonic Doppler Velocimetry, a heterodyne laser interferometry velocity diagnostic. Also called HetV (heterodyne velocimetry).

PETN Pentaerythritol Tetranitrate. IUPAC name: 2,2-Bis[(nitrooxy)methyl]propane-1,3-diyl dinitrate

PMMA Polymethyl methacrylate

PTH Plated Through Holes

RDX Research Department Explosive. IUPAC name: 1,3,5-Trinitro-1,3,5-triazinane

SAXS Small Angle X-ray Scattering

SDT Shock to Detonation Transition, a pathway to detonation from a shock wave

SEM Scanning Electron Microscopy

SMA Sub Miniature version A, a connector used for optical fibres and radio frequency coaxial cable.

SNR Signal-to-Noise Ratio

SSA Specific Surface Area

TATB Triaminotrinitrobenzene. IUPAC name: 1,3,5-triamino-2,4,6-trinitrobenzene

TLS Total Least Squares

TMD Theoretical Maximum Density

TNT Trinitrotoluene. IUPAC name: 2-Methyl-1,3,5-trinitrobenzene

TOA Time-of-Arrival

Tri-PEON Tripentaerythritol Octonitrate

TTL Transistor-Transistor Logic

TVD Total Variation Diminishing

VISAR Velocity Interferometer System for Any Reflector, a homodyne laser interferometry velocity diagnostic

VPF Velocity Per Fringe, in VISAR analysis

WK Wood-Kirkwood, a theory of detonation involving a curved reaction zone

XDT X to Detonation Transition, a pathway to detonation with an unknown mechanism

ZND Zeldovich-Von Neumann-Döring, a theory of detonation involving a finite reaction zone

Chapter 1

Introduction

In most applications of explosives, there is a sequence of components used to produce the output. All applications must have an initiator, which must be followed by an explosive sensitive enough to be initiated. To avoid using potentially dangerous 'primary' explosives, a less sensitive and more powerful 'secondary' explosive is used. If the secondary explosive is too insensitive, an intermediate 'booster' charge can be used. Collectively this sequence of charges is known as an explosive train.

Modern detonators typically employ an electrical method to directly initiate a powder pressing of the relatively sensitive secondary explosive pentaerythritol tetranitrate (PETN) [1]. The higher initiation energy required is provided by passing a current pulse through an exploding bridgewire (EBW), or across a metal foil in an exploding foil initiator (EFI). EBWs use low density pressed PETN ($\sim$1.0 g cm^{-3}), whereas EFIs use a higher density pressing ($\sim$1.6 g cm^{-3}) of PETN or HNS.

Like other high explosives, under the right conditions PETN can support a detonation wave. This phenomenon is a shock wave which both induces and is reinforced by a series of exothermic chemical reactions in the medium it travels through. A steady-state detonation wave travels at a constant speed, and can be described analytically in the one-dimensional case. Recent developments in computational modelling along with validatory experimental data have led to a greater understanding of transient and multi-dimensional detonation waves.

Experimental investigations into detonator function have revealed that there is a difference between the total function time, and the time predicted by assuming the detonation begins instantaneously and immediately proceeds at the steady state detonation velocity [2] [3]. This difference is dubbed the 'lost time' or 'excess time', and must either be due to a delay in the onset of detonation, a retarded detonation velocity, or a combination of the two.

The delay to the onset of detonation depends on the mechanism by which the explosive is initiated – several different explanations have been proposed [4]. However, this study is

concerned with factors that reduce the detonation velocity once the explosive has been initiated, specifically looking at the effect of a finite reaction zone and wave curvature on detonation velocity. EBWs and EFIs initiate detonation over a small area, leading to a diverging detonation wave with high initial curvature which decreases as the wave travels.

An important quantity is the reaction zone length – the distance between the shock front and the sonic point. This quantity is notoriously difficult to measure in PETN due to its small size and short duration in detonators [5] [6] [7].

The finite reaction zone and curvature are strongly linked [8], and together they induce a velocity deficit, especially in the early stages of detonation. The goal of this research is to measure the reaction zone in PETN and determine its dependence on the material properties and experimental configuration. As well as measuring the reaction zone, it is necessary to measure curvature and lost time to ascertain how these quantities are related.

There is a lack of existing diagnostics that can measure these quantities simultaneously and with sufficient resolution, while also being inexpensive and unintrusive. A large part of this work was focused on the development of a novel diagnostic that fits these criteria.

The strategy adopted was:

- Conduct a thorough review of literature and data to identify the likely parameters of the problem and to guide the experimental work.
- Characterise an inert simulant to use while developing experiments and investigate its behaviour when shocked.
- Develop systems to reliably initiate detonations so that they can be studied.
- Use newly developed and existing diagnostics to measure the reaction zone and curvature of detonating PETN for a range of material properties.
- Use the data gathered to develop a numerical model describing the effects of the tested parameters on the reaction zone, wave curvature and lost time.

The literature review is found in Chapter 2. Chapter 3 describes an investigation into an inert simulant. The detonator systems are described in Chapter 4 and the new diagnostic in Chapter 5. The experimental results are presented and discussed in Chapter 6, while Chapter 7 gives the details of the numerical modelling.

Chapter 2

Literature Review

A review of the relevant literature is presented in this chapter. An overview is given of the subject explosive PETN, including a review of methods used to characterise its relevant properties. The phenomenon of detonation is introduced, with a focus on the reaction zone and the parameters affecting it such as particle size and powder density. Two types of detonator typically use PETN; their mechanism is discussed. Finally there are many diagnostic tools which have been used to measure detonations; literature involving some of these experiments is examined.

2.1 Pentaerythritol Tetranitrate

PETN is a secondary explosive, albeit one of the most sensitive. It can withstand thermal or mechanical insults which would initiate a primary explosive, but is also sensitive enough to be used in certain types of detonator without a primary explosive. As well as its application within detonators, PETN is also used as a component of plastic explosives such as Semtex [9], polymer-bonded explosives (PBX) such as LX-16 [10], and rubberised explosives such as Detasheet [11].

This section describes the chemical and physical properties of PETN. Consideration is also given to what properties are relevant to this work and how they might affect experiments.

2.1.1 Chemistry

The chemistry of PETN is dominated by the molecule's four nitrate ester functional groups – their arrangement on the molecule is shown in Figure 2.1. The main products of its explosive reaction are H_2O, CO_2, CO and N_2, which are stable and gaseous at the relevant temperatures

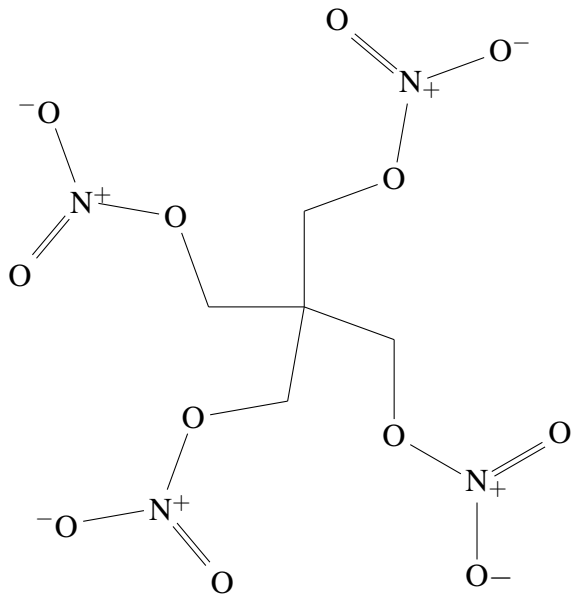

Figure 2.1 The structure of PETN is an aliphatic neopentane skeleton with four nitrate ester functional groups. The full IUPAC name is 2,2-bis[(nitrooxy)methyl]propane-1,3-diyl dinitrate.

and pressures. The release of these gases and the highly exothermic nature of the reaction makes PETN a powerful explosive.

Synthesis

The synthesis of PETN proceeds via nitration of pentaerythritol [12]. Pentaerythritol and HNO_3 in a $1:5.5$ ratio are mixed while the temperature is kept below 30 °C. The PETN precipitates out almost immediately, and can be isolated by filtering (optionally diluting to 55 % by weight acid first) and washing the PETN with water and a dilute sodium carbonate solution. It can be recrystallised by dissolving in a hot acetone solution and then reprecipitating with water. The full reaction process including synthesis of the pentaerythritol precursor from acetaldehyde and formaldehyde is shown in Figure 2.2

Impurities in PETN include the partially nitrated molecules pentaerythritol trinitrate, pentaerythritol dinitrate, pentaerythritol mononitrate; the precursor pentaerythritol itself; and the polymeric molecules dipentaerythritol hexanitrate (di-PEHN) and tripentaerythritol octonitrate (tri-PEON) [9].

Thermal Decomposition

The initial step in decomposition of primary and secondary aliphatic nitrate esters such as PETN is the reversible, rate-determining scission of the $O-NO_2$ bond to produce nitrogen dioxide

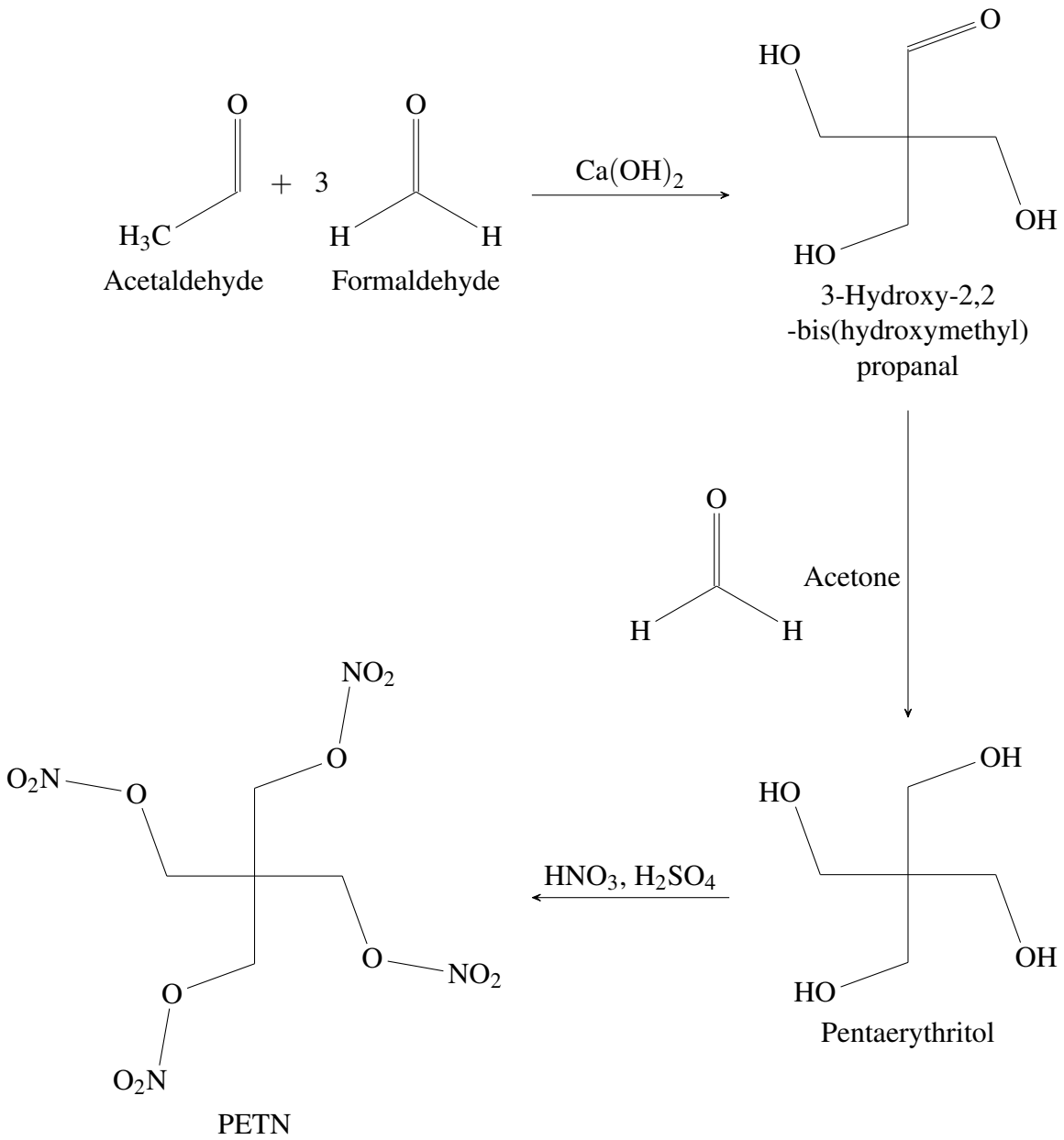

Figure 2.2 The pentaerythritol precursor can be produced with a base-catalysed addition reaction between acetaldehyde and formaldehyde, followed by adding more formaldehyde in a Cannizzaro reaction. The pentaerythritol is then nitrated to give the PETN

and an alkoxy radical [13]. This step is the most energetically favourable for decomposition of gaseous PETN.

$$C(CH_2ONO_2)_4 \rightleftharpoons C(CH_2ONO_2)_3CH_2O\cdot + NO_2 \quad (2.1)$$

Zhang et al. [14] listed seven other intermediate compounds that are produced from thermal decomposition of condensed phase PETN:

$$C(CH_2ONO_2)_4 \longrightarrow C(CH_2ONO_2)_2(CH_2O)_2 + 2NO_2 \quad (2.2)$$
$$C(CH_2ONO_2)_4 \longrightarrow C(CH_2ONO_2)_3 + NO_2 + CH_2O \quad (2.3)$$
$$C(CH_2ONO_2)_4 \longrightarrow C(CH_2ONO_2)(CH_2O)_3 + 3NO_2 \quad (2.4)$$
$$C(CH_2ONO_2)_4 \longrightarrow C(CH_2ONO_2)_3CH_2 + NO_3 \quad (2.5)$$
$$C(CH_2ONO_2)_4 \longrightarrow C(CHO)(CH_2ONO_2)_3 + HONO \quad (2.6)$$
$$C(CH_2ONO_2)_4 \longrightarrow C(CH)(CH_2ONO_2)_3 + NO_2 + OH \quad (2.7)$$
$$C(CH_2ONO_2)_4 \longrightarrow C(CHO)_2(CH_2ONO_2)_2 + 2HONO \quad (2.8)$$

If no other chemicals present, the next step can be a second order autocatalytic reaction between any these intermediate molecules, or between an intermediate molecule and a PETN molecule. Other pathways that are speculated to occur due to the NO_2 attacking the alkoxy radical result in peroxide, nitrate, or aldehyde molecules [9]. Reaction between the alkoxy radical and PETN may be the source of di-PEHN and tri-PEON polymer-like impurities commonly found in PETN. Kimura [15] found evidence for recombination of peroxy radicals (formed by oxidation of the alkoxy radicals) in the form of chemiluminescence. In the presence of water, the nitrate ester group is readily hydrolysed to an alcohol group. Unsurprisingly, the higher the temperature, the greater the degree of outgassing and variety of decomposition byproducts, although due to the strength of the C——C bonds, elemental carbon is rarely formed.

Kinetics and Thermodynamics

In order to build complete reactive models of PETN it is necessary to understand its thermodynamic stability and reaction rate. These models are used to simulate detonators, and also for predicting how they react to thermal insults. The stability and reaction rate of PETN affect the likelihood and violence of thermal ignition and therefore are important considerations for safely storing and transporting detonators. Hobbs et al. [16] collated experimental data on PETN to develop an ignition model where the rate of reaction accelerates as the extent of reaction

increases. Lee et al. [17] used a differential scanning calorimeter (DSC) to determine the kinetic parameters for PETN decomposition, finding an activation energy of $175.0(33)\,\mathrm{kJ\,mol^{-1}}$. They also tested a PETN/silicone mix which had an activation energy of $153.0(33)\,\mathrm{kJ\,mol^{-1}}$.

2.1.2 Morphology

A crystalline material may have different crystal structures depending on the arrangement of molecules – a phenomenon called polymorphism. Different polymorphs may have different thermal and structural properties, including the crystal habit, which is the external shape of the crystal. PETN has two common polymorphs: PETN-I, which is stable below 130 °C and forms a tetragonal lattice; and PETN-II, which is stable between 130 °C and its melting point of 143 °C, and forms an orthorhombic lattice. PETN-II transforms to PETN-I below 130 °C but this transition can be inhibited by impurities [18].

The crystal habit of PETN depends on the way in which it is precipitated following synthesis. An acetone solution of PETN added quickly to water will produce superfine crystals with an irregular plate shape. Adding water to the acetone solution will produce larger needle-shaped crystals, often with reentrant cavities [19]. Tetragonal crystals can be produced by evaporation of the acetone solution. The superfine crystals are the most appropriate for detonators, with irregular rod-shaped particles between 0.5 µm and 16 µm in size. Scanning electron microscopy (SEM) can be used to image PETN crystals as shown in Figure 2.3

The crystal morphology has an effect on the specific surface area (SSA) of powdered PETN, defined as the surface area per unit mass or volume. Two methods used for evaluating the SSA both use the flow of a fluid through the material [23]. The Brunauer-Emmet-Teller (BET) method measures the volume of liquid nitrogen that can be trapped by a sample, and the assumption that it adsorbs as a monolayer onto all available surfaces. The nitrogen adsorbs onto all external surfaces, but cannot penetrate to internal cavities. The Fisher sub sieve sizer (FSSS) method employs gas flow permeametry – the pressure difference across a sample can be used to calculate the average particle size and an estimate of the surface area. It does not however, account for cavities either on the surface or inside particles. The two methods therefore give different results for the SSA, but often have a simple linear relationship [20]. Over time, the specific surface area of PETN may decrease due to coarsening mechanisms [24]. Two such examples are sintering, where adjacent particles join together, and Ostwald ripening, where larger crystals grow at the expense of smaller ones due to sublimation and recrystallisation.

The specific surface area of heterogeneous powdered explosives may affect their sensitivity to certain stimuli since it determines the number of points of contact between crystals which act as centres of initiation. The presence of defects on the surface of the grains also increases the friction between them, which is known to contribute to hot spot formation [25].

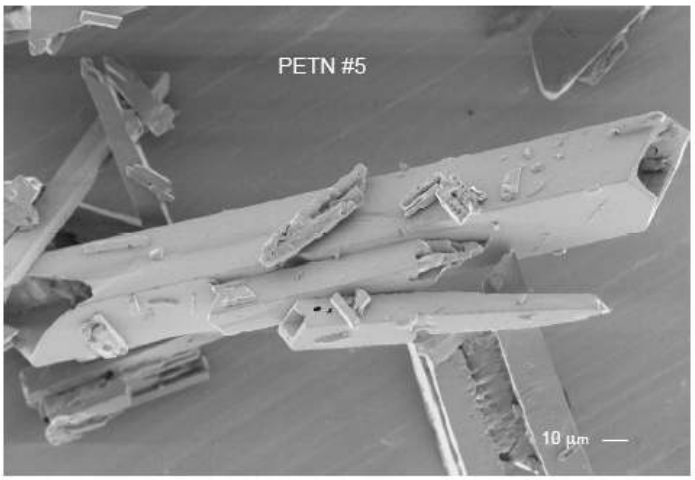

(a)

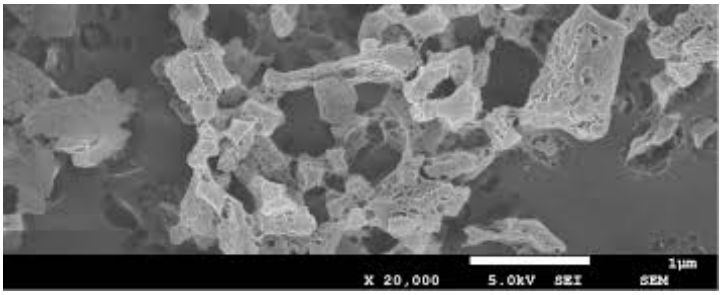

(b)

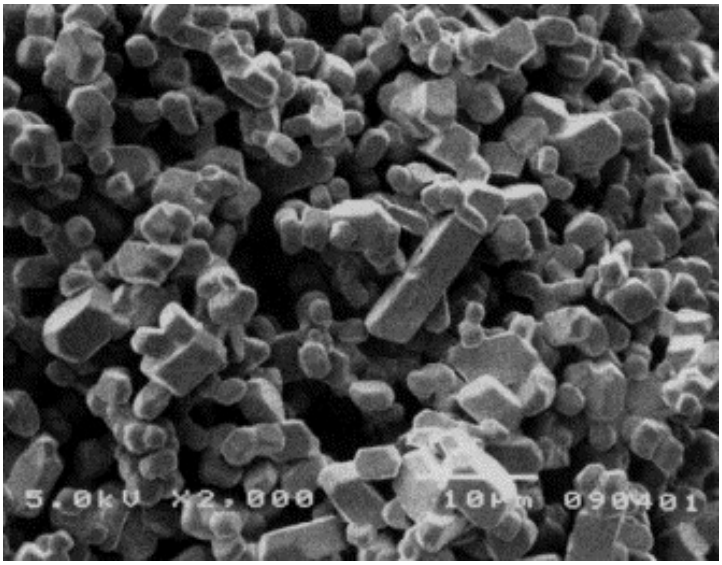

(c)

Figure 2.3 Scanning electron microscopy images of crystal habits of PETN: (a) needles with reentrant cavities [20], (b) nanocrystalline PETN [21] and (c) detonator-grade PETN [22]

2.1.3 Mechanical Properties

Along with the thermodynamic, kinetic and morphological properties of PETN, its mechanical properties have an important effect on its behaviour. In particular, it is useful to know how mechanical energy is converted to thermal energy that can initiate reactions. For this reason experiments are often performed on single crystals to study these mechanisms, including work on friction [26], fracture toughness Hagan and Chaudhri [27], indentation [28] and shear [29] [30].

The mechanical properties of PETN in powder form have significant consequences on both the preparation and performance of detonators.

Preparation

The mesoscale behaviour of PETN powder is relevant to the study of detonators since it affects the manufacturing process and sample preparation for experiments. Since detonation is highly dependent on density and specific surface area [31], it is desirable to have a tight control over these parameters. Lannutti [32] noted the importance of particle-particle and particle-wall friction in preparing powder compacts. They found that single action uniaxial compaction led to significant density gradients – in particular a high density region near the press and a low density region near the base. Density gradients can be reduced by minimising wall friction and by allowing time for the powder to settle before releasing the press.

Vannet and Ball [33] explained that due to the fine needle shape of PETN crystals and electrostatic forces between them, it pours very poorly in powdered form. They described a technique to encapsulate PETN crystals in a polymer coating, which then formed spherical agglomerates, or ‘prills’. This process improved pourability without significantly affecting initiation sensitivity, although the complexity of the process means it has not been adopted in the manufacture of detonators. Burt and Fewtrell [34] developed a centrifugal compaction method which was used by Edmonds et al. [22] to prepare detonator charges of PETN for in-situ surface area measurements.

Under quasi-static compaction, for example in the pressing of a charge or pellet, the material properties change. While the density clearly increases, the particle size and SSA may also change. Skidmore et al. [35] found evidence of microfractures of HMX crystals in a pressed PBX pellet, and of prill consolidation. They found the consolidation occurred first, then the fracturing as interparticle contact increased. At the highest densities crystal indentation occurred and there was a higher incidence of cracking. The microfractures increase the porosity, while consolidation decreases it, so the final porosity is a function of the density. There is little data available on the behaviour of PETN during pressing.

2.1.4 Summary

PETN is a high explosive used in electrical detonators for its relative sensitivity compared to other secondary explosives. The sensitivity depends on the morphology and specific surface area. The density, particle size and porosity are all key parameters affecting the rate of reaction. These parameters in turn depend upon sample preparation, which is affected by mechanical properties such as friction and fracture toughness.

2.2 Detonation

A detonation is a supersonic shock wave driven by an exothermic chemical reaction. The high pressure of the shock pulse induces reaction in the unreacted material it passes through, and the energy released by the reaction sustains the shock pulse. This section contains a review of the initiation mechanisms believed to occur in heterogeneous explosives, followed by introducing some theoretical models developed to describe detonations. Finally the reaction zone is discussed in more detail.

2.2.1 Initiation

There are two main mechanisms which can lead to detonation in heterogeneous explosives: DDT (Deflagration to Detonation Transition) and SDT (Shock to Detonation Transition). Where the mechanism is unknown it is sometimes referred to as XDT.

The sensitivity of an explosive is its readiness to detonate when subjected to a specific insult. There are many different tests and figures of merit for sensitivity, which have different utility depending on the circumstance. For an SDT mechanism, the run-to-detonation distance is the distance a shock travels before transitioning to a detonation. It depends on sample density, applied pressure and confinement. The run-to-detonation distance is often presented plotted on a logarithmic scale against input pressure on a 'Pop-plot', as shown in Figure 2.4. Pop-plots are good indicators of the sensitivity of a given material.

Deflagration to Detonation Transition

A deflagration is a rapid burning which propagates through a material, but at subsonic speeds unlike a detonation. In energetic materials, if the energy released by the exothermic reaction exceeds the heat loss, then the reaction will spread. There are two types of DDT: Type I, which occurs in densities greater than 50 % TMD, and Type II, which occurs at lower densities. In heterogeneous solid explosives, the stages of a Type I DDT are [4]:

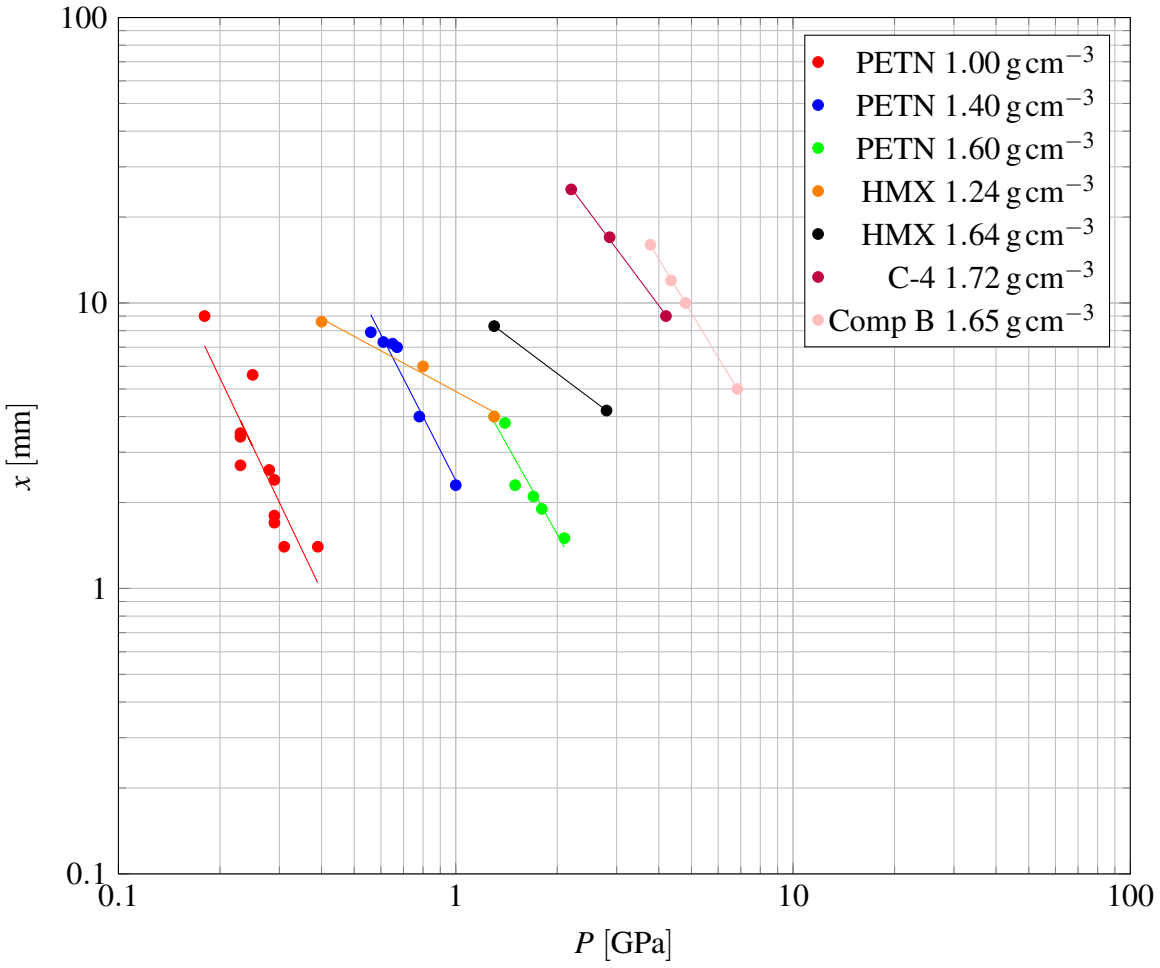

Figure 2.4 This Pop-Plot shows the run-to-detonation distance for several high explosives at different densities: PETN at 1.00 g cm^{-3} [36], 1.40 g cm^{-3} [37] and 1.60 g cm^{-3} [38]; HMX at 1.24 g cm^{-3} and 1.64 g cm^{-3} [39]; and C-4 and Comp B [40]. The more sensitive materials are further to the left of the plot.

- A thermal input initiates the reaction on the surface of a particle .
- The reaction spreads, at first conductively within individual particles and to adjacent particles. Then, as the reaction products reach a sufficient temperature, convective flow propagates the reaction to distant particles.
- Unreacted material ahead of the reaction is compacted into a dense plug, which prevents gas permeation and acts as a compressive piston.
- Thermal runaway occurs. More heat is added to each volume of explosive by reaction than is lost by thermal transport.
- As the reaction propagation becomes faster it develops a supersonic shock front and transitions to detonation.

A type II DDT does not include the formation of the dense plug and is less well understood. Gifford et al. [41] found no significant pressure build-up in very low density PETN (30 % TMD), which detonated at $5\,\mathrm{km\,s^{-1}}$ to $5.5\,\mathrm{km\,s^{-1}}$ following type II DDT, faster than the $3.7\,\mathrm{km\,s^{-1}}$ expected following direct initiation. The suggested mechanism was that the pre-transition burn created channels through which a shock could travel faster than the detonation velocity, and initiate material as it passed through.

Shock to Detonation Transition

In contrast to DDT, SDT involves a pre-existing shock, so the unreacted material has already been compressed before the detonation starts. The detonation wave travels through this material faster than it would through uncompressed material, and therefore catches the original shock before settling to the steady-state detonation velocity.

Hot Spots

The bulk temperature rise created by adiabatic compression due to strong shocks is generally insufficient to initiate reactions [42]. It is therefore believed that detonation develops via growth of ‘hot spots’ – localised regions where the mechanical energy of the shock is concentrated into thermal energy. If the activation energy is exceeded then chemical reaction will occur, releasing more thermal energy. If the reaction at the hot spot produces more heat than it loses, then it is said to be critical, and will grow larger. There are several proposed mechanisms for this effect, including friction, cavity collapse and adiabatic shear [43]. Where multiple mechanisms can contribute, they have additive effects [44].

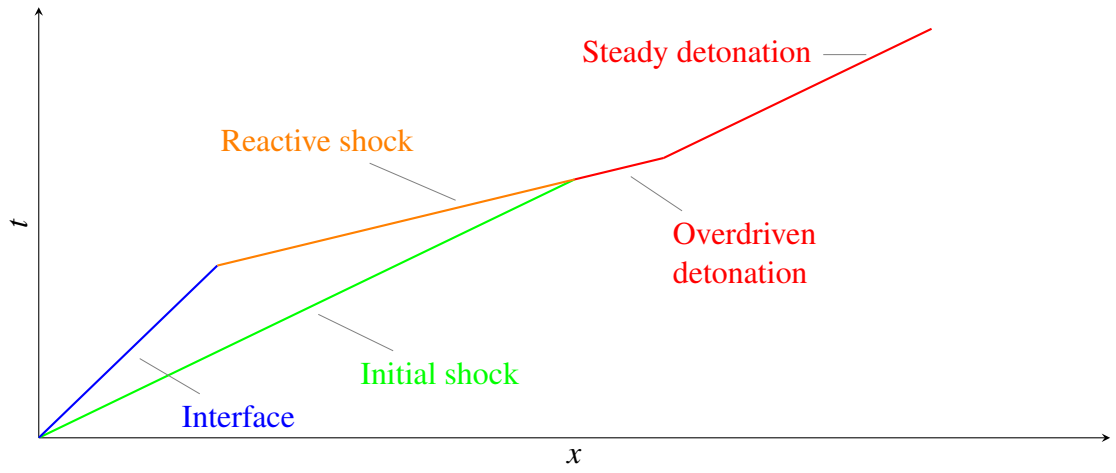

Figure 2.5 Illustration of a shock to detonation transition (SDT). The $(P-v)$ state corresponds to the strong point of an overdriven detonation

The mechanism by which friction sensitises explosives was explored by Bowden and Gurton [45] by adding grit – grits with higher melting points than the explosive led to greater sensitivity, but no such effect was seen for grits with lower melting points. This observation led to the proposed mechanism for frictional heating: that the temperature of a frictional hot spot between two solids increases to the lower of the two melting points and equilibrates there. Unlike most secondary explosives, PETN ignites at a lower temperature than its melting point, indicating that friction may contribute to initiation [16]. Amuzu et al. [26] examined the frictional properties of PETN, using single crystals sandwiched between glass substrates. Their work gave information about localised energy dissipation, and is therefore relevant to both the frictional and adiabatic shear mechanisms of hot spot growth. Their results suggested that the coefficient of friction was not temperature dependent, but that shear strength did decrease with temperature.

A shock can also induce pore collapse, which can contribute to hot spot formation in a number of ways. The mechanical action of the shock can compress the interstitial gases, increasing their temperature sufficiently to initiate reaction at hot spot sites. Evidence for this mechanism was found by Maienschein et al. [46] and V.K Mohan et al. [47] who used hollow glass microspheres to increase the void fraction in PETN and TATB based explosives respectively. Both found a profound increase in sensitivity, positing that compressional heating was at least partly responsible. On the other hand, Chick [48] found that increasing the pressure of the interstitial gases prior to initiation can inhibit shock initiation by quenching reactions and hindering gas convection.

As a cavity collapses under pressure, a jet of hot material can penetrate and cross the cavity, initiating reaction on the downstream wall [42]. The jet velocity is often faster than the shock

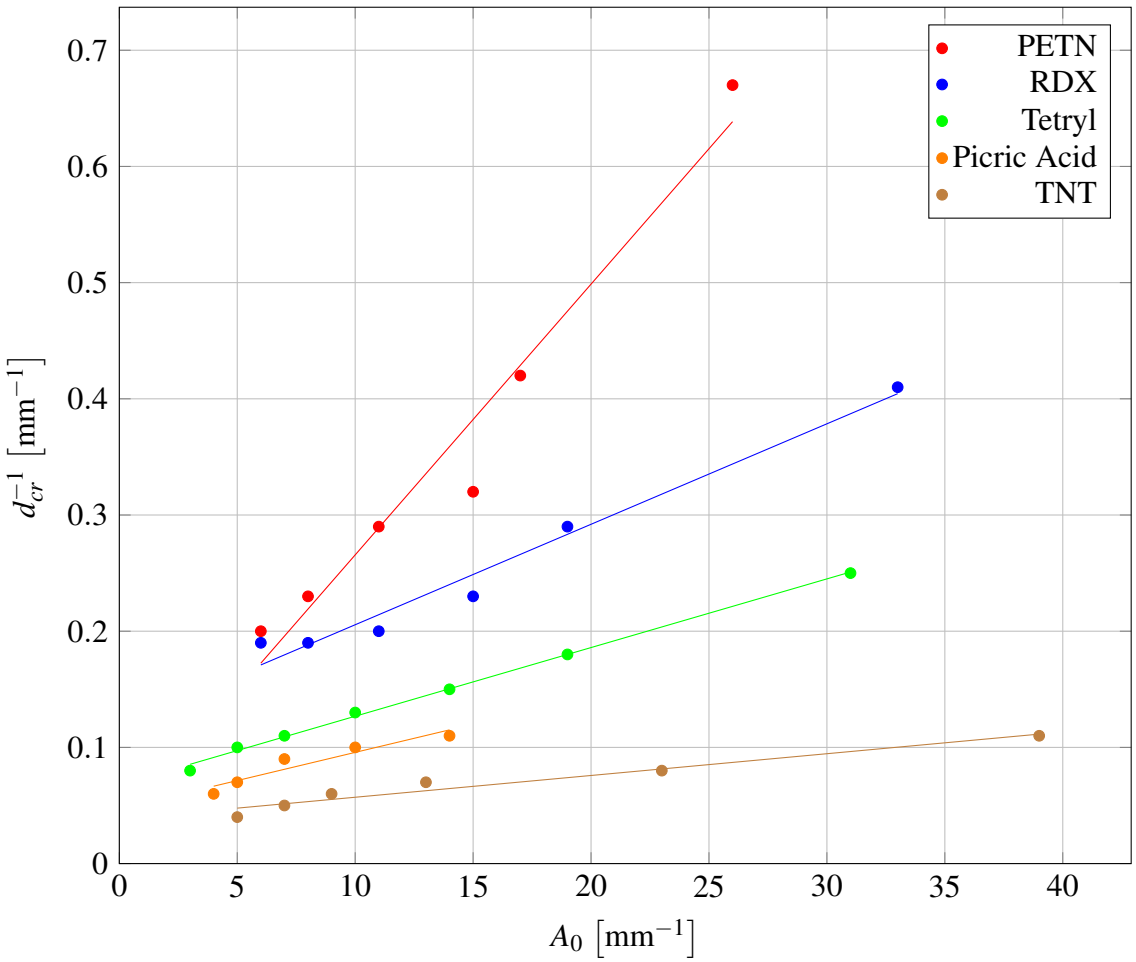

Figure 2.6 Data from Apin and Stesik [49] showing the dependence of critical diameter of a cylindrical charge for a range of explosives with different particle sizes d_p. The specific surface area is calculated as $A_0 = 6\frac{\rho}{\rho_{TMD} d_p}$

velocity, which suggests it is possible for the reaction to travel ahead of the input shock for a period of time.

Effect of Particle Size on Sensitivity

One proposed reaction process is the surface burning mechanism, where the rate of reaction is dependent on the available surface area. According to this theory an explosive with smaller particle size would have increased sensitivity. The data of Apin and Stesik [49] supported this hypothesis, as shown in Figure 2.6.

On the other hand, Dinegar et al. [31] investigated PETN pressings and instead found the opposite effect: an increase in specific surface area (as measured by permeametry) led to a slight decrease in sensitivity (as measured by the thickness of an attenuator placed in the

gap between the charge and the input) across a wide range. Chick [48] observed a similar reverse sensitivity effect, speculating that the increased convective flow of hot reaction products through coarser samples sustained the reaction after an initial surface burning reaction.

Khasainov et al. [50] resolved to explain this behaviour by considering the two separate processes of hot spot formation and growth – a model first developed by Taylor and Ervin [51] and Howe et al. [52], and applied to experimental data by Lee and Tarver [53].

Hot spot formation is governed by the relative pressure π:

$$\pi = \frac{P}{P_{ign}(a)} \tag{2.9}$$

where P_{ign} is the critical ignition pressure as a function of mean heterogeneity size a. Hot spot growth depends on the relative critical hot spot size σ:

$$\sigma = \frac{a^*(P)}{a} \tag{2.10}$$

where $a^*(P)$ is the minimum hot spot size to spontaneously grow at pressure P.

In cases when the input pressure is high, such as electrical detonators, hot spot formation is fast and a^* is small, so all heterogeneities grow spontaneously. The limiting step is then the hot spot growth, which increases with available surface area.

At low pressures, such as those present in the gap tests of Dinegar et al. [31], the fraction of initial heterogeneities that will go on to form reaction centres is small. The reaction is limited by hot spot formation, so surface burning only occurs on a small fraction of the available surface. The sensitivity then depends on P_{ign} and its relation with a.

Convective flow of reaction products through the material increases with porosity, therefore the critical pressure increases as grain size decreases. Finer grained explosives therefore have a decreased hot spot formation rate and the reverse sensitivity effect is observed.

Korotkov et al. [54] found evidence of both effects in the run-to-detonation distance of porous PETN. They found that at high porosities and low porosities the PETN was less sensitive, but that there was a maximum sensitivity at an intermediate porosity. As porosity increases the available combustion surface increases, however, above a certain porosity there is no longer a great enough pressure build-up for hot spot formation. Finer PETN had a greater critical porosity – pores are smaller so pressure build-up is easier. In a detonator the pressures are much higher than with a hot wire, so the reverse sensitivity effect is unlikely to be important (i.e. hot spot growth, rather than hot spot formation, is the limiting step).

2.2.2 Theory

Theoretical analyses of detonation encompass a range of complexities and dimensionality. Most studies on detonation involve a cylindrical rate stick or detonator, so multidimensional theories usually focus on a cylindrical geometry [55].

Chapman-Jouguet Theory

By applying conservation relations to a hypothetical one-dimensional infinitesimal detonation front, Chapman [56] and Jouguet [57] independently derived relations constraining the behaviour of a detonation wave. Conservation of mass and momentum across the front gives:

$$\frac{P_1 - P_0}{v_0 - v_1} = \frac{D^2}{v_0^2} \tag{2.11}$$

where P is pressure, v is specific volume, D is the detonation velocity, and the subscripts 0 and 1 distinguish properties ahead of and behind the detonation front respectively. This relation defines a straight line in the $P - v$ plane – the Rayleigh line.

Conservation of internal energy, denoted by E gives another relation in the $P - v$ plane – the Hugoniot curve:

$$E_1 - E_0 = \frac{1}{2}(P_0 + P_1)(v_1 - v_0) \tag{2.12}$$

The Hugoniot curve is the locus of possible states that the material can occupy at thermodynamic equilibrium. Under isentropic processes, such as weak shocks, the Hugoniot approximates the path taken between two states.

In non-reactive shocks the Rayleigh line and Hugoniot curve intersect at two points corresponding to the shocked and unshocked conditions. The slope of the Rayleigh line determines the shock velocity according to Equation (2.11).

In reactive shocks i.e. detonations, the Rayleigh line also intersects with the Hugoniot for the unreacted material at two points, again representing the shocked and unshocked conditions. However, in order to conserve mass, momentum and energy, the Rayleigh line must also intersect the Hugoniot for the reacted material. The simplest case is where the two curves are tangent to each other – at the so called Chapman-Jouguet (CJ) point. It can be shown that at the CJ point in the reference frame of the detonation, material retreats from the detonation at the speed of sound [44].

As shown in Figure 2.7, a second possibility exists which satisfies the conservation relations: the Rayleigh line crosses the reacted Hugoniot at two points. This scenario is an overdriven detonation since the pressure exceeds that necessary for a sustained detonation. The two points of intersection are called the strong and weak points. At the weak point the particle velocity

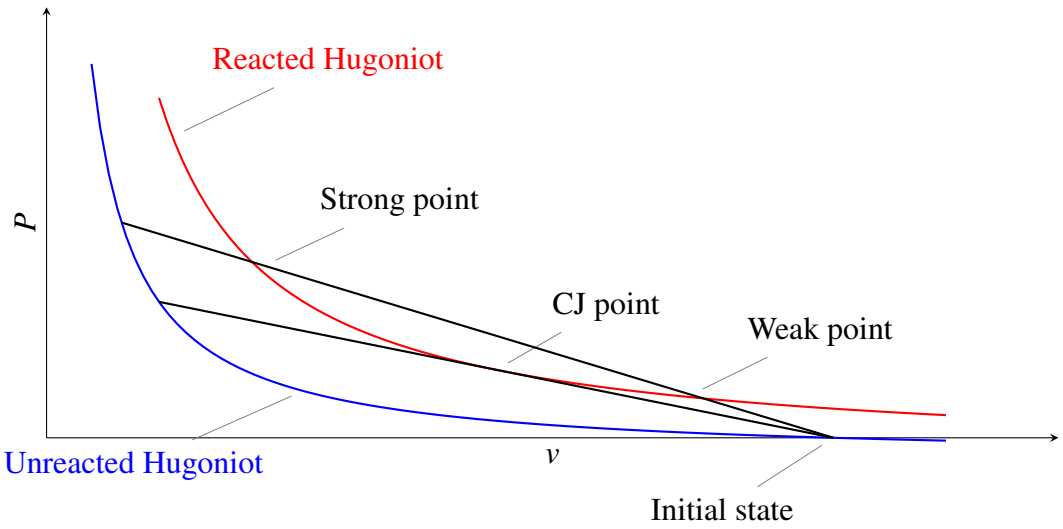

Figure 2.7 The Rayleigh line represents the available states across the shock. In a stable detonation wave it must be tangent to the Hugoniot curve of the reaction products. Any shallower and there is no solution producing the reaction products. Any steeper and there are two possible solutions: the weak point where the shock travels faster than the reaction, and the strong point, where the shock is attenuated by the release wave.

of the products exceeds the sound speed (in the detonation frame), and at the strong point the particle velocity is less than the sound speed. An overdriven detonation therefore assumes the state corresponding to the strong point. Typically the reduced particle velocity means that rarefaction waves can catch up to the detonation front and reduce its velocity down to the CJ velocity. Overdriven detonations are therefore unstable, and will revert to the CJ velocity [58]. Bdzil and Kapila [59] showed analytically that it is possible for a detonation on the weak branch to transition to a CJ detonation when there is a decelerating trigger wave.

Zeldovich-Von Neumann-Döring Theory

The Zeldovich-Von Neumann-Döring Theory [60–62] expands on the Chapman-Jouguet theory by relaxing the assumption that the reaction occurs over an infinitesimally thin region. In this way it introduces the reaction zone as the region between the shock front and the Chapman-Jouguet point. The Rayleigh line now crosses a family of Hugoniot curves corresponding to various stages of reaction completion, as shown in Figure 2.8. It can be shown that these curves do not intersect each other, and cover the entire space between the unreacted and fully reacted Hugoniot curves. Since the unreacted material (typically solid or liquid) is less compressible than the gaseous products, there is a pressure spike at the front of the reaction zone, known as the Von Neumann spike.

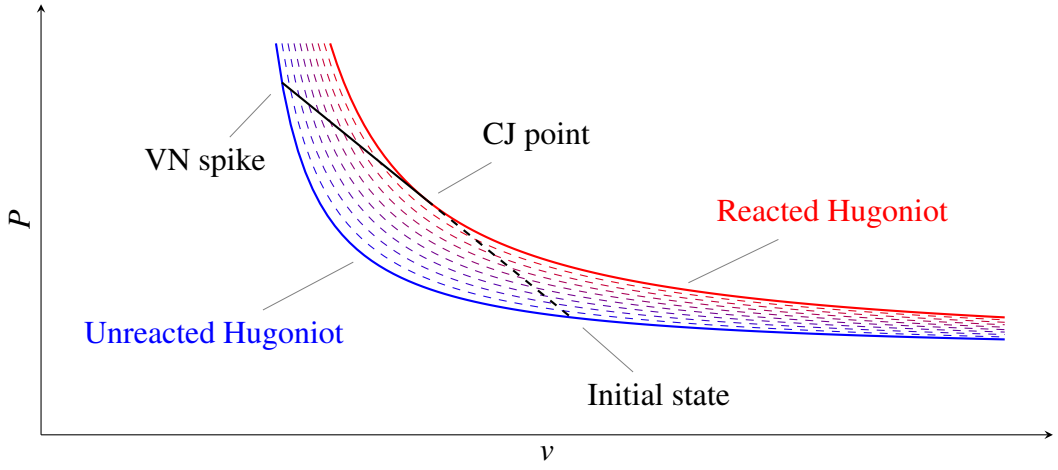

Figure 2.8 Partially reacted Hugoniot curves. The detonation profile follows the solid portion of the Rayleigh line from the Von Neumann spike on the unreacted Hugoniot to the Chapman-Jouguet point on the fully reacted Hugoniot.

Each Hugoniot has a characteristic sonic point where it is tangent to the Rayleigh line from the initial state. Just as in the CJ analysis, each partial reaction Hugoniot is divided by the sonic point into weak supersonic and strong subsonic branches. In order for the reaction to continually drive the shock front, the detonation locus cannot be on the supersonic branches of the Hugoniots. The detonation profile is therefore the locus of points of intersection between the Rayleigh line and the subsonic branches of the partially reacted Hugoniots [63].

Higher Dimensional Theories

In the case of a cylindrical tube of explosive, radial transfer of energy and momentum due to wall interactions leads to a diminished detonation velocity and a non-planar detonation front. Jones [64] derived the 'nozzle theory' to explain the first of these phenomena. Assuming a planar front and rear to the reaction zone, the hydrodynamic equations can be solved to relate the amount of radial expansion to the detonation velocity. The amount of expansion is dependent on the confinement

Eyring et al. [65] presented a detailed comparison of the nozzle theory and their own 'curved front theory'. The nozzle theory has the reaction zone beginning and ending at flat planes with unreacted material entering from the front and reacted material leaving the rear. The analysis solves the hydrodynamic equations for the detonation velocity in terms of the relative cylindrical expansion r of the nozzle:

$$\frac{D^2}{D_\infty^2} = 1 + \frac{9}{4}\left(r^4 - 1\right) \tag{2.13}$$

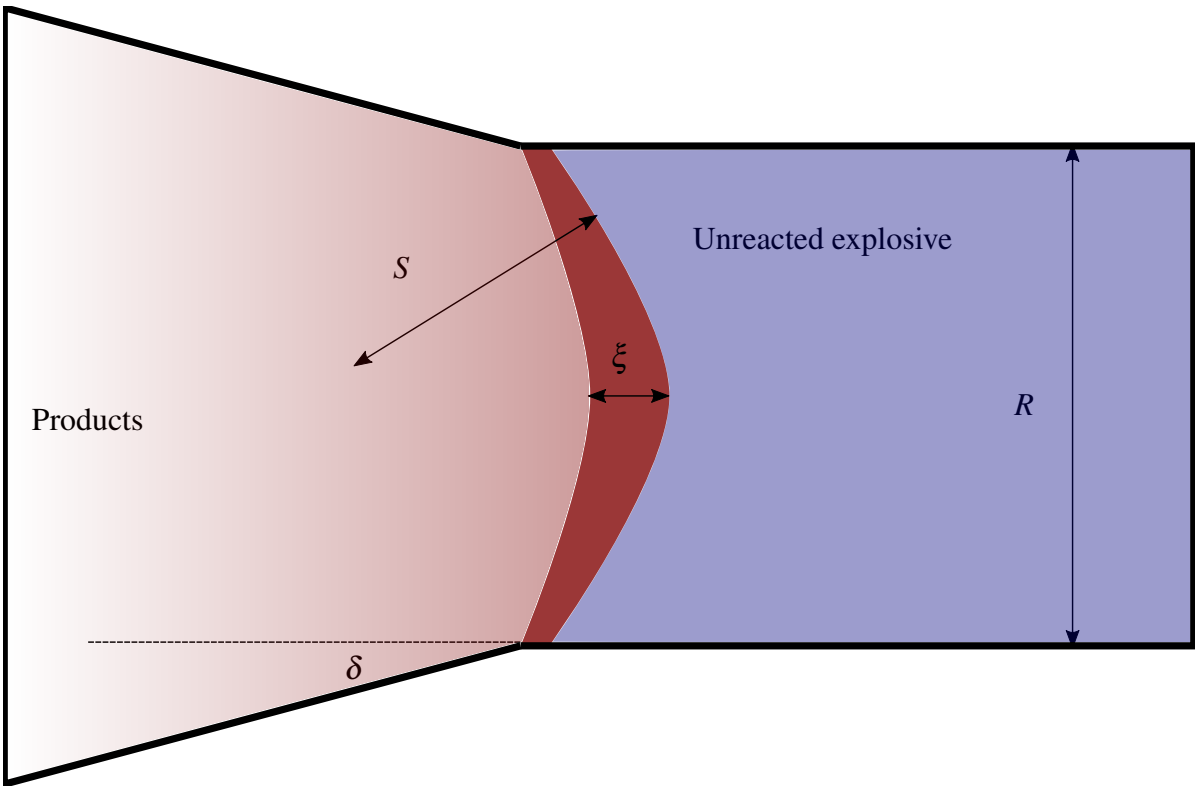

Figure 2.9 In the steady state the streamline deflection angle δ is determined by the confinement. The flow equations give a precise evaluation of the shock locus.

The curved front theory is based on the assumption that rarefaction waves at the edge of a charge will slow the detonation wave at the edges until it makes an angle at which the rarefaction waves are no longer reflected, as illustrated in Figure 2.9.

The curvature of the front then diminishes the detonation velocity. A graphical construction of the front curvature led to the velocity reduction of Equation (2.14) where ξ is the reaction zone length and R the charge diameter.

$$\frac{D}{D_\infty} = 1 - 0.5\frac{\xi}{R} \tag{2.14}$$

Wood-Kirkwood theory [8] is a further generalisation to detonation theory which deals with a cylindrically symmetric three-dimensional geometry. Their rigorous analysis found a similar deficit in velocity, this time in terms of the radius of curvature S and a constant β equal to about 3.5:

$$\frac{D}{D_\infty} = 1 - \beta\frac{\xi}{S} \tag{2.15}$$

This model has been shown to be in agreement with experiments on the curvature of the front generated by a bridgewire detonator [66].

Bdzil [55] presented a generalised Wood-Kirkwood theory along with mathematical expressions for off-axis behaviour which describe the shock locus and failure diameter. The theory was in good agreement with the experimental results of Campbell et al. [67], Davis et al. [68], and Campbell and Engelke [69] on PBX-9404, nitromethane and TNT.

Non-ideal Detonation

The analytical descriptions of detonation described above treat the explosive and its products as perfect homogeneous fluids. While this approach is reasonably justified for gaseous and liquid explosives, solid granular explosives can deviate significantly from this ideal behaviour. It is known that an unstable detonation front will pulsate [70] even in homogeneous explosives, and in some circumstances can be analysed using chaos theory [71]. The increasing intractability of theory in the face of these complexities has led many researchers to turn to computational models rather than analytical ones. These models are usually a combination of reactive models with hydrodynamic ones and may even incorporate microscale simulations of burn sites [72]. The CREST (Computational Reaction Evolution dependent on Entropy and Time) model [73] is an example of a reactive burn model that has been incorporated into performance hydrocodes and safety models such as HERMES (High Explosive Response to MEchanical Stimulus) [74]. These models rely on experimental data across a wide range of regimes for validation and refinement.

2.2.3 Reaction Zone

The concept of the reaction zone as introduced in the ZND model of detonation encompasses a complex chemical reaction pathway and energy transfer as the unreacted explosive molecules are converted into the reaction products. Tarver [75] developed the Non-equilibrium Zeldovich-Von Neumann-Döring (NEZND) model to describe the non-equilibrium processes that occur within the reaction zone that lead to the CJ state. The steps identified were:

- Multiphonon up-pumping – The shock front leads to extremely high energy translational modes for about a picosecond. These modes do not induce reaction.
- Energy is redistributed from translational modes to vibrational modes over a timescale of several tens or hundreds of picoseconds. Lower frequency modes are excited first.
- Chemical bonds are broken using energy from the excited vibrational modes. The resulting fragments give rise to electrical conductivity.

- Exothermic reactions occur between excited molecule fragments forming excited reaction product gases.
- The excited reaction products deexcite, releasing energy. The reaction steps typically take tens of nanoseconds.
- Carbon coagulation occurs. In under-oxidised explosives this step can significantly slow down the time until equilibrium by hundreds of nanoseconds.

Since the first steps are very brief, the conducting molecule fragments are present across most of the reaction zone's length giving rise to bulk conductivity – this principle is often used to measure the reaction zone [76] [77].

TATB is often used as the subject in reaction zone measurements as its reaction zone is long compared to other explosives. IJsselstein [78] used the shock imparted into a Plexiglass disc by a detonating TATB charge to make direct and indirect measurements of the reaction zone. Shock induced polarisation creates a voltage proportional to the strength of the shock. This property can be used to measure the pressure peak due to the reaction zone. Indirect measurements of the reaction time were also made by calculating the transit times of the shock across the Plexiglass and performing impedance calculations. Frank et al. [79] examined the effect of explosive thickness on reaction zone length using a Fabry-Pérot interferometer and a LiF window with ultrafine TATB. They found a gradually increasing reaction zone length as the detonation progressed up to a steady state.

Reaction Zone in PETN

Because PETN produces very little solid carbon when it reacts, the slower carbon coagulation phase of its reaction is expected to be absent [5]. Since carbon is also believed to slow down the initial fast reaction, the reaction zone of PETN is especially short, making it difficult to measure experimentally. Loboiko and Lubyatinsky [7] performed similar calculations using an indicator dye instead of Plexiglass. Lubyatinsky and Loboiko [6] found a weak density dependence of the reaction zone of PETN between 92 % and 98 % of TMD, whereas above 98 % the powder became agated and the reaction times dropped by an order of magnitude to less than the 5 ns resolution of the experiment. The reaction zone length went from 0.32 mm to 0.37 mm in the unagated material to $<$0.03 mm in the agated material. The agated material has much closer and wider intercrystal contact so the pressure rises much more sharply in response to the von Neumann spike. The densities of the present study are unlikely to extend to agated material.

2.2.4 Summary

Several models that describe detonation exist, however non-ideal behaviour manifests itself in experimental data. The initiation mechanism is an important factor in the transient behaviour. Wave curvature results in a velocity deficit – this in turn is dependent on material properties and confinement. A full treatment of the reaction zone is complex, and it can be difficult to measure, especially in fully oxidised explosives such as PETN.

2.3 Detonators

A detonator is a device used to initiate detonation within an explosive charge. Although it was already known that a spark could ignite gunpowder, the first true detonators were used by Nobel, and consisted of a fuse used to ignite gunpowder or mercury fulminate, which in turn initiated nitroglycerin. Most detonators work on a similar principle; since the output explosive is usually too insensitive to the input, a primary explosive is used as an intermediary. Pyrotechnic detonators use a fuse and ignition mix to heat the primary until it ignites. Electric match detonators function in a similar way, except resistive heating of a wire provides the input energy.

Some detonators do not initiate the explosive by directly heating it, but instead include an exploding electrical element. One advantage of this design is that it allows a sensitive secondary explosive to be used instead of the primary, making the detonators safer. Two examples of this type of detonator are the exploding bridgewire (EBW) and exploding foil intitiator (EFI). These detonators typically contain PETN so are highly relevant to this study.

2.3.1 Exploding Bridgewire Detonators

The exploding bridgewire detonator was invented within the Manhattan Project to be a safe way of initiating explosives with a high reproducibility in firing times [1]. An EBW detonator consists of a bridgewire connected to a fireset and embedded in an initial pressing (IP) of low density PETN. The bridgewire is made of a highly conductive and non-corrodible material such as gold. After the initial pressing, the next stage in the explosive train is an output pellet of either higher density PETN, or another high explosive with similar morphology such as HMX or RDX.

Bridge Burst

EBWs are fired using a fireset, a capacitor discharge unit (CDU) with a low inductance and hence a short rise time [80].

The fireset discharges through the bridge, heating it rapidly. The metal melts, vaporises and expands, and finally forms a plasma. The resistance of the wire increases as it is heated up to a maximum at the point of vaporisation

Varying the energy delivered to the bridge affects the firing time and the bridge efficiency. Lee et al. [81] found the electrical power of the bridgewire increased linearly with energy delivered while the time to burst decreased but asymptoted to about 50 ns due to a limit on the fireset rise time imposed by its reactance. As the fireset energy increased, a smaller fraction contributed to the burst, leaving more post-burst energy. This energy increases the kinetic energy of the bridge output [82], but its role in the initiation of the PETN is unclear.

Initiation Mechanism

The mechanism by which EBWs initiate detonation is disputed [4]. The conflicting theories are that either it is a) a shock to detonation transition from the bridge burst [83], b) a deflagration to detonation transition caused by heating from the bridgewire [84] [85] or c) direct thermal initiation without a deflagration [3]. The coupled nature of the temperature increase and shock strength from the bridge burst makes it difficult to reach a definitive conclusion. Although the shock produced in powdered PETN is difficult to measure, bridge bursts into water produce pressures of up to 1.5 GPa [86]. If the shock in PETN were the same strength, it would be strong enough to cause SDT, however at the porosities in EBW IPs it is likely to be weaker so SDT cannot be assumed [87]. The presence of factors such as shock duration and curvature also complicates the discussion.

Several authors [83] [2] have observed ‘lost time’ – a difference between the measured time the detonation takes to travel through the pressing and the calculated time assuming prompt initiation. This time decreases with increasing applied voltage, asymptoting to a minimum value when a much higher voltage than necessary was used. This behaviour may appear to be evidence for a rate limited DDT mechanism, since an SDT mechanism should not asymptote in this way. However, the authors agree that using existing Pop-Plot data to calculate the explosive time is tenuous at best, since the geometry and curvature are very different. Comparison with EFIs at the pressed to the same density showed similar lost times [2], indicating a possibility of a similar mechanism (i.e. SDT). Smilowitz et al. [88] observed reaction beginning some distance from the bridge, but without a deflagration wave, leading them to associate the lost time with self-heating within the proposed direct thermal initiation (DTI) model. Experiments

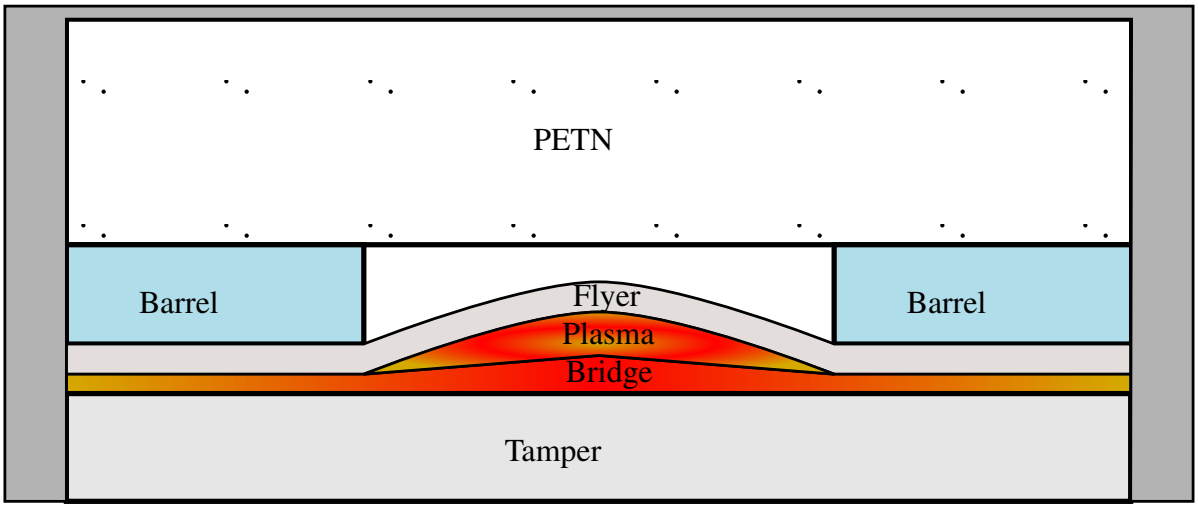

Figure 2.10 The EFI consists of a metal foil sandwiched between the dielectric flyer and tamper layers. The initial pressing is usually high density PETN, or hexanitrostilbene (HNS)

involving optical initiation [89] and spark initiation [90] indicate a similar relationship to EBWs between energy deposited and function time.

Roeski et al. [91] and Martin et al. [85] sectioned detonators at regular intervals along the charge and observed breakout. Both found ramp waves prior to detonation, further indicating that a direct SDT mechanism is not responsible for initiation. The effect of replacing air as the interstitial gas has a dramatic effect on the detonator function [92]. Using a gas that does not ionise easily, SF_6, detonation was very difficult to achieve, whereas with the readily ionised argon, detonation was achieved at all pressures. These results suggest that there is some sensitisation prior to detonation by the ionisation of the interstitial gas.

2.3.2 Exploding Foil Initiators

A new type of detonator, the exploding foil initiator (EFI) or slapper detonator, was invented by Stroud [93] in 1975 at Lawrence Livermore Laboratory. Like the EBW, slapper detonators use a high current to explode a metallic foil (usually copper), the bridge. Unlike the EBW, the bridge is not embedded in the explosive but separated by a film made of a dielectric such as Kapton, and an air gap made by the barrel, as shown in Figure 2.10. The bridge burst generates a bubble of plasma which pushes against the Kapton flyer film. Depending on the dimensions of the detonator, the flyer will blister or shear completely, and then accelerate down the barrel to impact the explosive initiator. The flyer is capable of reaching pressures of $15GPa$ in $200ns$ [94]. The slapper offers several safety advantages over the EBW, not least the physical separation of the explosive and the bridge.

Characterisation

EFIs can vary in the length of the bridge and diameter of the barrel. If the barrel diameter is greater than twice the bridge length it is termed an 'infinite barrel' [95]. Increasing the barrel length decreases the flyer velocity at the point of impact due to deceleration. Increasing the size of the bridge leads to a decrease in initial velocity. Another factor in performance is the density of the explosive – PETN in EFIs is typically pressed to around $1.6\,\mathrm{g\,cm^{-3}}$ compared to $1.0\,\mathrm{g\,cm^{-3}}$ in EBWs. Increasing the density decreases the sensitivity, however it also increases the power required to initiate by an order of magnitude. Mendes et al. [96] used a 3.5 kV fireset to launch a 25 µm Kapton flyer at speeds of up to $4\,\mathrm{km\,s^{-1}}$, measuring at several points to see the flyer curvature. As expected, the faster the flyer, the shorter the run-to-detonation distance. EFIs also exhibit lost time, although unlike the EBW this cannot come from a delayed onset DDT. Lost times for EBWs and EFIs were measured by Lee et al. [2] as 0.99 µs and 0.76 µs respectively, suggesting that much of the lost time may be due to a lower detonation velocity than predicted. Drake [66] produced an analytical model proposing wave curvature and the Wood-Kirkwood reaction zone length as parameters influencing this velocity deficit.

2.3.3 Summary

Two electrical detonators have been reviewed: the exploding bridgewire and exploding foil initiator. Both detonators have a longer function time than predicted with naive velocity calculations. This lost time may arise from an initiation delay or velocity deficit due to a finite reaction zone and wave curvature. The relevant importance of each factor is likely different between the two detonator types.

2.4 Diagnostics

A range of shock diagnostics can be applied to the study of detonation, however no single diagnostic gives a full picture. Three categories of diagnostic are discussed in this section:

- Velocimetry, where laser interferometry is used to obtain the velocity history of the rear surface of an explosive charge. Shock impedance calculations can then be used to calculate the detonation velocity.
- High rate X-ray imaging can produce cross-sectional pictures of detonation progress from which the structure and curvature of the detonation front can be seen. Synchotrons have been used as a source of radiation for this diagnostic.

- Various electromagnetic diagnostics have been developed which exploit the conductivity of the reaction to infer information about the particle velocity and reaction zone length.

2.4.1 Velocimetry

Velocimetry is a broad term given to any method which produces a velocity history for an interface or volume element of a fluid.

Several methods of velocimetry are based on analysis of the Doppler shift of a laser beam reflected from a moving interface. Since the shifted frequency is far in excess of the sampling rate of any digitiser, the beam must be interfered with a reference beam to extract useful information. In homodyne methods the beam is interfered with itself by means of an Fabry-Pérot etalon or, as in a VISAR (Velocity Interferometer System for Any Reflector), a Michelson-Morley interferometer. In heterodyne methods such as PDV (Photonic Doppler Velocimetry) the beam is interfered with a separate reference beam, which is usually the unshifted incident beam.

VISAR

The VISAR (Velocity Interferometer System for Any Reflector) was invented by Barker and Hollenbach [97] as an improvement to the earlier Sandia interferometer system [98]. The latter is based on a Michelson interferometer; the Doppler shifted light from the target is split into two legs. Light from the shorter leg is mixed with the slightly retarded light from the longer leg to form a series of interference fringes. Since the mixed light contains components originating from different times at the target, they have different degrees of Doppler shift. The two components have an associated beat frequency, which can be seen in the interference fringe pattern. The velocity history $v(t)$ for a free surface can be related to the fringe count $F(t)$, the laser wavelength λ and the time delay between the two legs τ:

$$v\left(t-\frac{\tau}{2}\right)=\frac{\lambda}{2\tau}F(t) \tag{2.16}$$

The Sandia interferometer only works well for target surfaces with a mirror finish, since diffusely reflective surfaces destroy the spatial coherence of the light. If the legs differ in length much more than the coherence length then a good interference pattern cannot be obtained. This problem is solved in a VISAR by using an etalon and mirror on a piezoelectric translation stage to make the legs appear equal length while still creating a delay Figure 2.11. The etalon is a block of transparent material with a high refractive index and partially mirrored surfaces whose effect is to delay the light without increasing the path length.

The other useful feature of the VISAR is the separation into S and P polarisations, so that two fringe patterns with a 90° phase difference are obtained. This phase shift is achieved with a quarter wave plate on one of the paths, and a polarising beam splitter on the path of the recombined light. By monitoring two fringe patterns it avoids the poor resolution at points where there is a small change in light intensity when the fringe count changes i.e. maxima and minima.

The velocity is calculated using a similar formula to Equation (2.16), except there is now a correction factor δ for the etalon dispersion [100]:

$$v\left(t-\frac{(1+\delta)\,\tau}{2}\right)=\frac{\lambda}{2\,(1+\delta)\,\tau}F\,(t) \tag{2.17}$$

The quantity $\frac{\lambda}{2(1+\delta)\tau}$ is known as the velocity per fringe (VPF) constant.

A further improvement to the VISAR was made by Bloomquist and Sheffield [101] by replacing the photomultiplier tubes with streak camera to record the fringes. Their system, known as ORVIS (Optically Recording Velocity Interferometer System) boasted an improved time resolution of 300 ps compared to a few nanoseconds for the conventional VISAR. Hemsing et al. [102] also used a streak camera in their line VISAR, which used a cylindrical lens to illuminate a line on a reflective surface to measure the velocity gradients across it.

Two VISARs were used by Gustavsen et al. [103] to measure the detonation profile of PBX-9501 (an HMX based explosive mixture) by applying impedance matching techniques between the product isentrope and window Hugoniot. They observed a short and narrow Von Neumann spike indicating a quick reaction rate, however the resolution of the VISARs limited the accuracy.

PDV

Improvements in digitiser sampling rate allowed Strand et al. [104] to use the heterodyne method to construct a velocimeter that could measure velocities over tens of microseconds and thus be useful for typical shock experiments. They used an optical fibre to transport laser light to a probe directed at the rear surface of a shocked material. The Doppler shifted light from the moving surface was mixed with unshifted light reflected from the end face of the fibre to produce beat frequencies. The mixed light was passed through a circulator Figure 2.12 and then through a detector, amplifier and digitiser to obtain the beat waveform.

Typical velocities in shock and detonation experiments are around $1\,\mathrm{km\,s^{-1}}$ to $10\,\mathrm{km\,s^{-1}}$, so according to the relativistic Doppler shift formula Equation (2.18) the size of the frequency shift is between 3×10^{-6} and 3×10^{-5}.

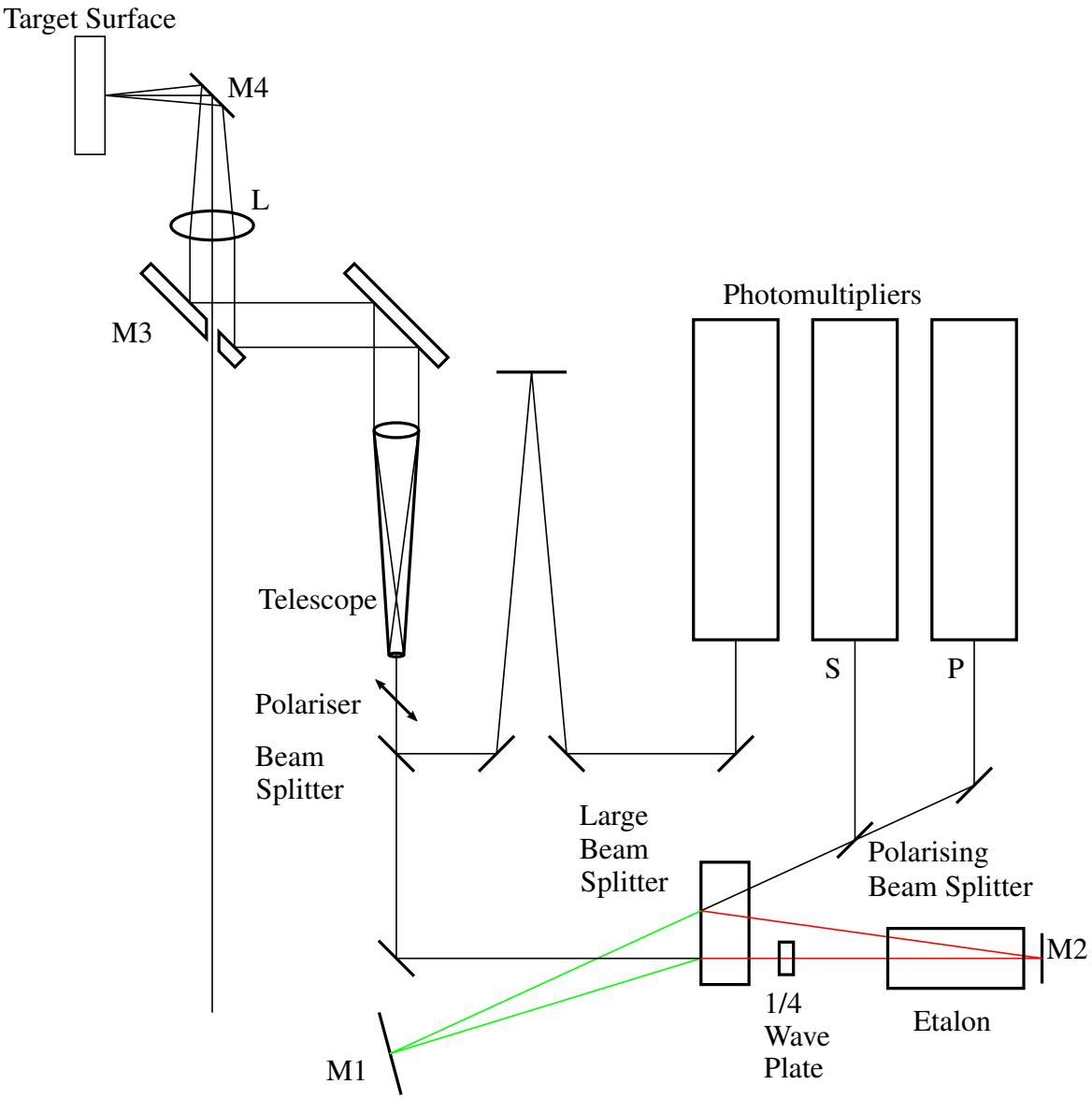

Figure 2.11 The VISAR system of Barker and Hollenbach [97]. Doppler shifted light is split into two paths (red and green) of the same apparent length, but a delay is introduced by the etalon on the red path. The mirror M1 is adjustable to match the path lengths, and M2 can be rotated for alignment. Photomultipliers measure the S and P polarised fringe patterns, and another is used to monitor changes in beam intensity. Hemsing [99] made the further improvement of using the light transmitted through the large beam splitter to drive another pair of detectors, in what is known as a push-pull VISAR.

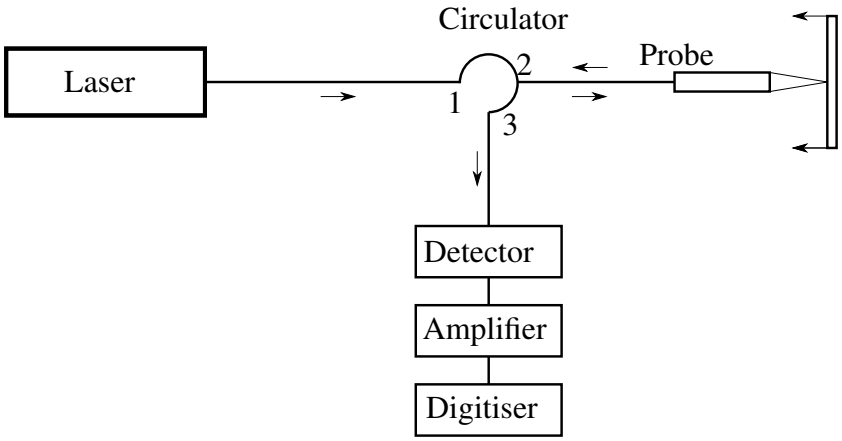

Figure 2.12 The heterodyne velocimeter constructed by Strand et al. [104]. The circulator is an optical component with three ports. Light which enters port 1 exits port 2, and light which enters port 2 exits port 3.

$$\omega_2 = \omega_1 \sqrt{\frac{c-u}{c+u}} \tag{2.18}$$

According to the Nyquist-Shannon sampling theorem a digitiser with a bandwidth of 20 GHz can reliably reconstruct frequencies under 10 GHz. To measure the largest frequency Doppler shifts the range of possible laser frequencies is limited; usually inexpensive infrared (1550 nm) telecoms lasers are used.

Once obtained, the beat waveform can be converted to a velocity history by means of a sliding Fourier transform. Dolan [105] calculated the uncertainties of PDV analysis, showing that velocity resolution is inversely proportional to time resolution and also depends on the analysis window and signal-to-noise ratio (SNR).

1550 nm PDV was used by Gustavsen et al. [106] on several HMX and TATB based explosives, but they were only able to resolve the relatively longer reaction zone of the latter. Bouyer et al. [107] used both PDV and VISAR on a TATB based plastic explosive and found similar detonation profiles with both techniques.

2.4.2 X-Ray Imaging

By measuring the attenuation of an X-ray beam it is possible to obtain areal density maps of the test subject. Rapid imaging can produce a number of frames, from which the transient properties of the detonation can be inferred.

Smilowitz et al. [3] used a suite of diagnostics including a flash X-ray source with a scintillator coupled camera to obtain time-resolved X-ray transmission images of an EBW

detonator. The X-ray imaging was done concurrently with a visible light camera and thermal imaging. They observed infrared emission associated with self-heating during the lost time discussed above. There was a lower X-ray transmission through the dense band at the front of the reaction zone.

An alternative way of using X-rays to image test subjects is to exploit the diffraction caused by crystalline materials. Guinier et al. [108] pioneered the use of small angle X-ray scattering (SAXS) to detect the shape and size of small particles. An important result from the analysis is that the scattered intensity from a group of identical particles is:

$$I_1 = I_0 N \left[F\left(\mathbf{h}\right)\right]^2 \tag{2.19}$$

where I_0 and I_1 are the initial and final intensities respectively, N is the number of particles and $F\left(\mathbf{h}\right)$ is the structure factor – the ratio of scattering amplitudes between the particle and a single electron (as a function of $\mathbf{h} = \frac{2\pi}{\lambda}\left(\mathbf{s} - \mathbf{s}_0\right)$ a vector proportional to the deviation between incoming and outgoing rays).

X-rays generated by synchotron radiation are suitable for this application – Ten et al. [109] used (SAXS) to examine nanoparticle formation behind the detonation front in TATB.

Gustavsen et al. [110] also used a SAXS method at the Advanced Photon Source (APS) to investigate carbon clustering behind the detonation front, a mechanism speculated to increase the length of the reaction zone.

Phase Contrast Imaging

Passing X-rays through a dense medium not only attenuates the intensity, but shifts the phase. Furthermore, the phase shift is usually more significant than the attenuation, meaning that phase-contrast imaging (PCI) is more sensitive to small variations in density than attenuation based imaging [111]. This method requires a strong source of spatially coherent radiation, such as that generated by a synchotron.

Application of X-ray PCI to dynamic shock experiments recently became feasible using the experimental capabilities of IMPULSE (Impact System for Ultrafast Synchotron Experiments) [112]. Features of the system include improvements to the synchronisation between the plate impact experiment and the 80 ps width X-ray bunch, as well as a multi-frame detection system.

Sanchez et al. [113] performed a range of experiments on detonators using IMPULSE. They observed a shock wave broadening from an EFI, providing further evidence for a prompt SDT mechanism. Improvements to IMPULSE allowed them to obtain images of the flyer microstructure including plasma instabilities [114].

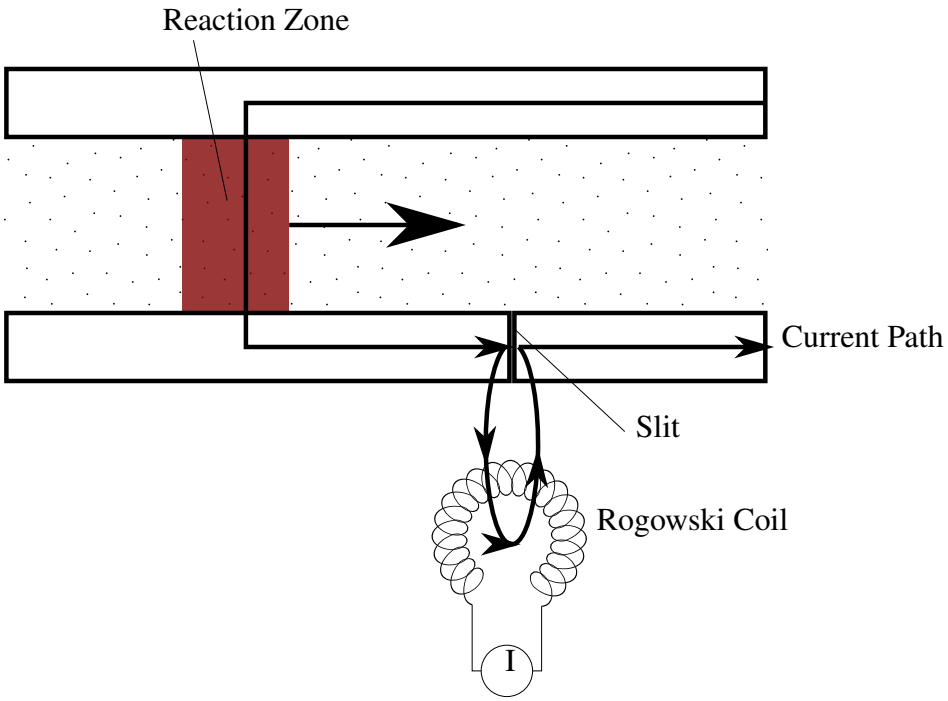

Figure 2.13 The experimental configuration of Ershov et al. [116] used to measure the conductivity profile of the reaction zone.

Shaw et al. [115] also used the improved IMPULSE to examine aged EFI detonators, looking at the ignitibility of PETN. They found the detonators were robust to temperature and humidity changes, but diminished performance after being subjected to γ-radiation.

2.4.3 Electromagnetic Diagnostics

The conductivity of the reaction zone ranges from $10^1\ \Omega^{-1}\,\mathrm{m}^{-1}$ to $10^3\ \Omega^{-1}\,\mathrm{m}^{-1}$ for different explosives [116]. The majority of electromagnetic diagnostics are contact methods, which measure the current through the reaction zone in response to an applied voltage across electrodes in contact with the material. Ershov et al. [116] used a coaxial electrode to measure the current passing through a reaction zone to the outer casing, which was split by an insulating section. When the reaction zone crossed the insulator the current switched on and could be measured with a toroidal Rogowski coil, as shown in Figure 2.13.

From Ohm's Law the time dependent current $I(t)$ through the reaction zone is:

$$I(t) = \frac{WDV}{h} \int_0^{\frac{x}{D}} \sigma(t)\, dt \tag{2.20}$$

where W is the width of the charge, h is the electrode separation, V the applied voltage and D the detonation velocity.

Since the voltage produced by a Rogowski coil with circumference l, loop are A and N turns is:

$$V(t) = -\frac{AN\mu_0}{l}\frac{dI(t)}{dt} \tag{2.21}$$

the output of the Rogowski coil in the conductivity experiment is:

$$V(t) = -\frac{AN\mu_0}{l}\frac{WDV}{h}\sigma(t) \tag{2.22}$$

The signal is therefore directly proportional to the conductivity profile. Tasker et al. [76] used the method of Ershov et al. [116] to measure the time-resolved conductivity of a reaction zone as well as separate experiments to measure the bulk resistivity in PBX-9501. The downsides of such a method are that it requires a high voltage, and it is sensitive to field distortion due to geometric effects.

Many authors have used embedded electromagnetic gauges to measure particle velocity [117] [118] [119] [120]. The commonly used 'stirrup' configuration allows for nanosecond resolution and simple data analysis, however the drawback is the difficulty of inserting it into the charge, and the question of whether embedding has implications for the detonation wave. Goff et al. [121] devised a correction method for the perturbation caused to electromagnetic gauges by conductive impactors but expressed uncertainty about the validity of using it for larger perturbations such as those resulting from explosive detonations.

Sheffield et al. [122] developed a particle velocity gauge based on Faraday's Law. Applying a magnetic field to the charge induced a voltage across the reaction zone. A castellated shock tracker then produced an alternating current as the reaction zone progressed. These shock trackers were used to obtain Pop plots for several explosives [119]. Millett and Bourne [123] used a similar particle velocity gauge to measure shock loaded PETN.

2.4.4 Summary

Different diagnostics are useful for measuring different parameters. Much information can be obtained from simple velocity measurements and impedance calculations, however these can rely on assumptions about the behaviour of the material under shock. Phase contrast X-ray imaging is a very powerful diagnostic, particularly for looking at the shape of the wavefront, however the infrastructure and equipment needed makes it inaccessible to most researchers. Electromagnetic diagnostics have been used in many creative ways to study the internal processes of detonation, particularly the reaction zone.

2.5 Literature Summary

- PETN is one of the most commonly studied explosives in the field of energetics due to its use in detonators and composites
- The behaviour of detonating PETN is highly dependent on its porosity and density.
- Detonators exhibit lost time due to a delay in initiation or diminished steady velocity. This study is principally concerned with the latter effect and its dependence on wave curvature and reaction zone length.
- The reaction zone length of PETN is short due to the absence of solid carbon, and therefore difficult to measure.
- The key parameters in a model of the reaction zone are likely to be density and surface area as well as the input shock.
- High resolution diagnostics are required to tackle the problem. Multiple techniques to measure different quantities will provide the best chance of success.

Chapter 3

Plate Impact Study

3.1 Introduction

The granular nature of PETN introduces additional complexity into an analysis of its reactive behaviour. This chapter describes experiments to investigate the behaviour of a non-reactive granular material (the inert simulant). By using a similar material to PETN which does not react, it is possible to identify behaviour which may be shrouded by the detonation, but nonetheless exists and affects the reaction zone.

It is useful to have an inert simulant for two reasons:

- To understand the response of a granular material to shocks. Since the explosive fill of a detonator has a length of several millimetres, the inert investigation will also focus on this scale. In particular, the question of whether there is a transition between steady and non-steady behaviour will be discussed. This transition is an important consideration for when chemical reactions are introduced, since it will affect the development of the reaction zone.
- To use when building and testing experimental initiation and diagnostic systems. While they do also have to be tested using the explosive, it would be costly, time consuming and potentially dangerous to introduce energetic materials immediately. Designing a procedure to press and prepare samples is also best done with a material that matches the behaviour of the powdered explosive.

The behaviour of granular materials under shock has been studied extensively, using subject materials such as sand [124], glass microspheres [125], fused silica [126] and sugar [127]. Granular materials exhibit behaviour under shock not seen in continuous materials. Irreversible compaction via pore collapse and particle fracture, means that the material does not unload

along the same path as it was loaded i.e. hysteresis. As will be seen there are also non-steady behaviours that arise due to mesoscale statistical effects.

Several phenomenological models have been developed to describe dynamic compaction of heterogeneous materials [126]. The simplest, the $P-\alpha$ model considers the separate volume changes due to compression and pore collapse. α refers to the porosity – the ratio of the solid material density ρ_S to the bulk porous density ρ. Other compaction models ($P-\lambda$, $\varepsilon-\alpha$, $\rho-\alpha$) rely on similar principles but still require fitting to experimental data.

The $P-\alpha$ model is limited to low pressure regimes, and even then fails to take into account mesoscale particle interactions such as fracture, friction, phase change or plastic deformation. Due to the low predictive power of this model, the best way to characterise granular materials is to gather experimental data.

The experiments described in this chapter were performed using a light gas gun to produce a planar plate impact shock, and beds of low density sugar between 0.5 mm and 4.0 mm in thickness.

3.2 Inert Simulant

Many materials have been used as inert stand-ins for PETN. Sucrose is a common choice, because it has a similar particle size and specific surface area (SSA) [90] besides being readily available. Others [128] have used acetaminophen (paracetamol).

The inert chosen was an ultrafine icing sugar 'Silk Sugar' obtained from British Sugar plc. It is a high purity, free flowing powder with a tightly controlled particle size around 8 µm. According to the manufacturer, 50 % of the particles were between 7.5 µm and 10.5 µm, and 90 % between 5 µm and 35 µm. The particle size and density makes it a good match for detonator grade PETN. The density used in these experiments was $1.0\,\mathrm{g\,cm^{-3}}$, or 63 % theoretical maximum density (TMD), making it similar to the PETN density used in EBWs. Sugar crystals are generally hexagonal prisms, although needle-shaped crystals can occur [129], whereas PETN can form needles, rods or tetragonal plates. The sugar used here has crystals with a low aspect ratio – in this regard it is most similar to the plate-like crystals in PETN. The morphologies are sufficiently similar for the scope of this experiment.

SEM (Scanning Electron Microscope) images of the sugar are shown in Figure 3.1.

3.3 Gas Gun

The Cavendish Plate Impact Facility [130] is a single stage light gas gun capable of firing projectiles at up to $1100\,\mathrm{m\,s^{-1}}$ and pressures of 350 bar. It has a 5 m long barrel and a 2" bore,

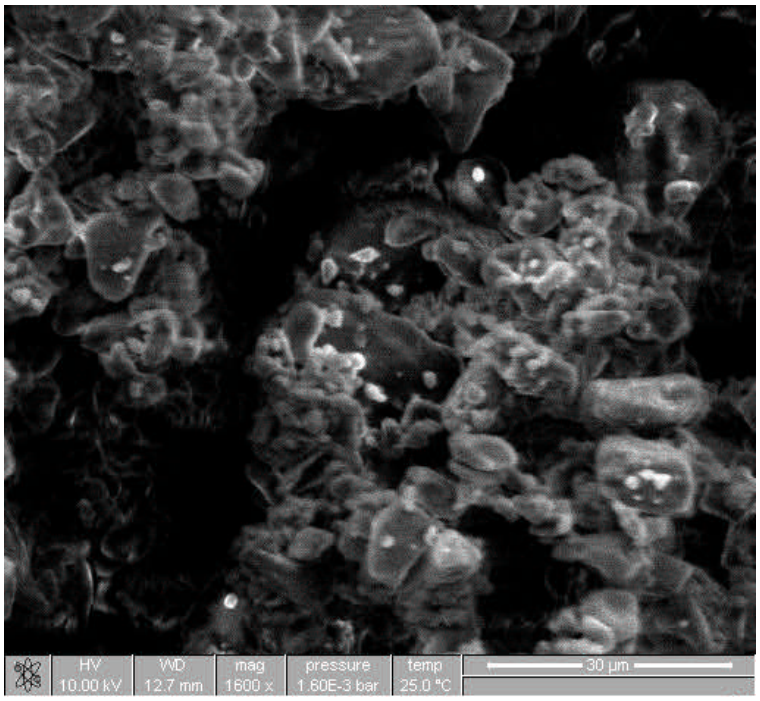

(a)

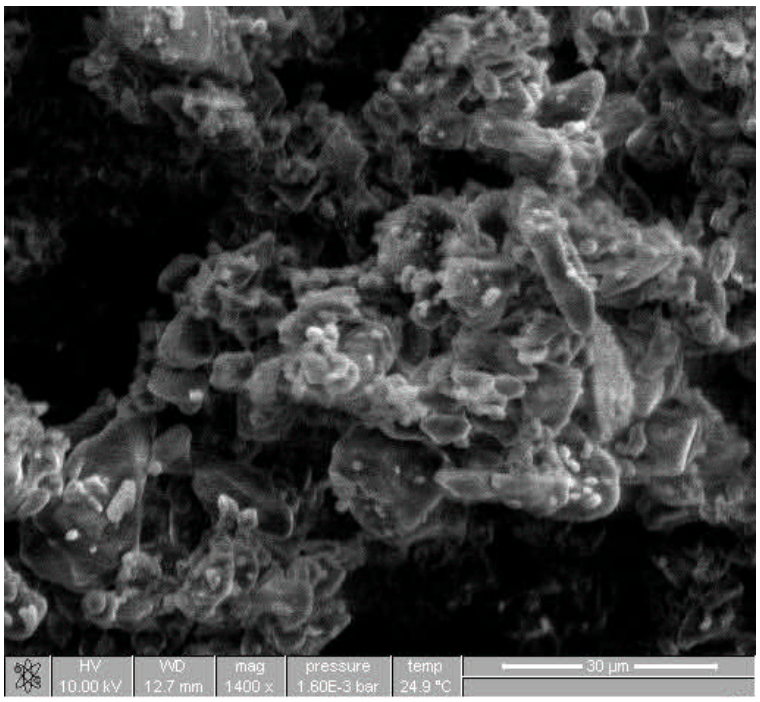

(b)

Figure 3.1 SEM images of sugar particles. Most of the particles are around the advertised $8\mu m$ and have a fairly rounded shape, however there are some smaller, more angular particles around $2-3\mu m$ which may have formed from fracture of the larger particles.

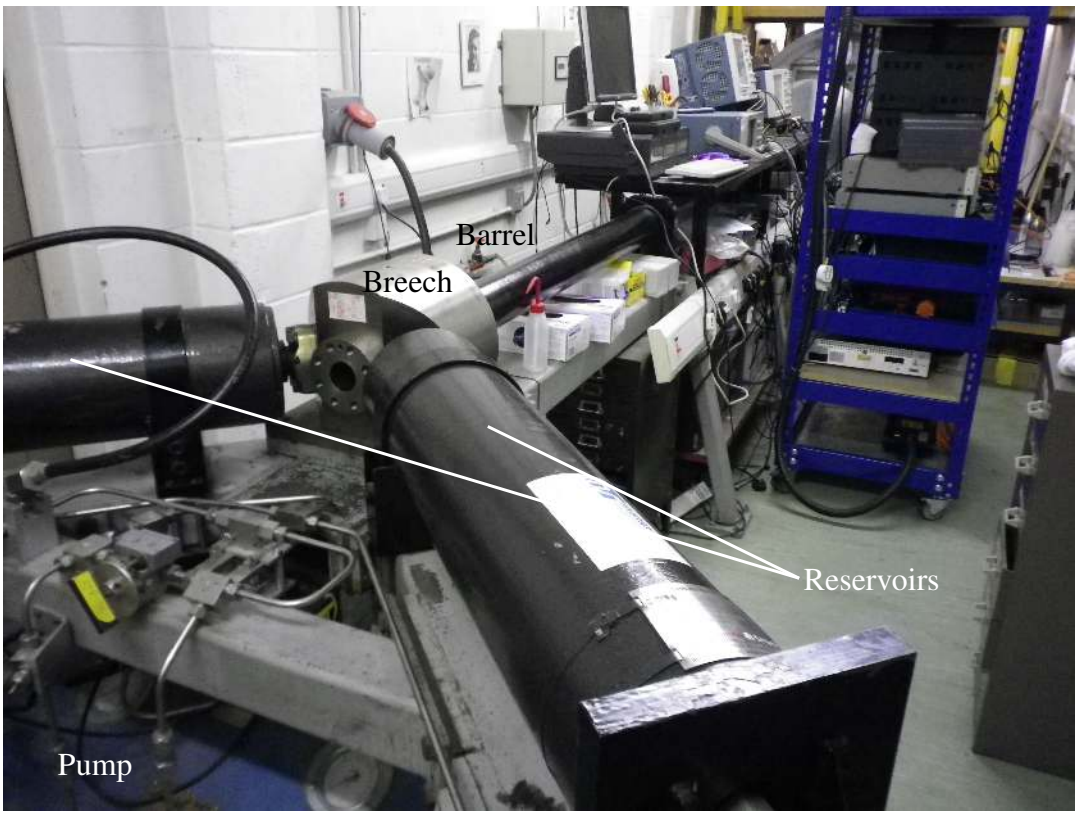

Figure 3.2 The single stage gas gun, showing the barrel, the (open) breech, the gas reservoirs and pump. The two reservoirs are fed from pressurised gas cylinders (not shown). The barrel of the gun is cleaned between each shot from this end.

and can use both compressed air and helium for lower and higher velocities respectively. The breech end of the gas gun is shown in Figure 3.2.

At the other end of the barrel is the sample chamber (Figure 3.3), where the target is held, and the expansion chamber, where the pressurised gas can expand to a safe pressure. To load the sample a section of the sample chamber can be raised and lowered using a winch.

In this investigation, the gun was fired using helium at 89 bar, resulting in a projectile velocity of around 500 $\mathrm{m\,s^{-1}}$.

3.3.1 Projectile

The projectile consists of a 10 mm thick high-purity copper (C101) 48 mm diameter plate glued onto a polycarbonate sabot, as shown in Figure 3.4. The total mass of the projectile plus the two rubber O-rings was 396 g. The projectile was loaded into the breech of the gun and sealed with vacuum grease.

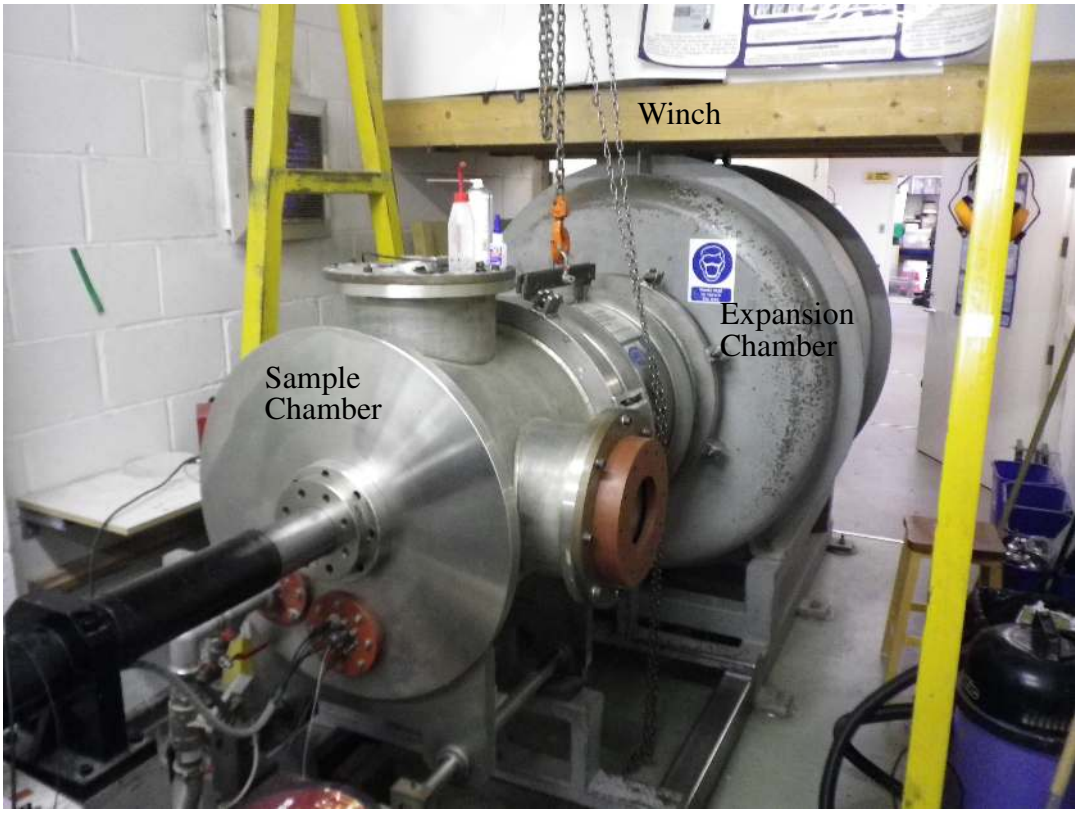

Figure 3.3 The sample and expansion chambers of the gas gun. A winch is used to raise a removable section of the chamber for loading the sample. At the bottom end of the sample chamber, the optical fibre for the PDV, and wires for other diagnostics, can be seen.

Figure 3.4 The projectile used in the gas gun has two rubber O-rings: the top one separates the barrel vacuum from the pressurised gas reservoirs and the bottom one separates the reservoirs from the rear holding vacuum.

Once the gun is loaded and the breech sealed, a small vacuum pump creates a high vacuum behind the rear O-ring of the projectile to hold it in place. A larger vacuum pump is then used to evacuate the barrel and sample chamber to a medium vacuum of below 20 mbar. In this way the air resistance in the barrel is minimised while ensuring the projectile does not prematurely move down the barrel due to a pressure differential. The gas reservoirs are then filled to the required pressure which is held between the projectile's two O-rings. To fire, the rear vacuum is released and the projectile moves forward, first from atmospheric pressure and then accelerates from the pressure of the gas reservoirs.

3.3.2 Velocity Pins

The velocity of the projectile can be measured using graphite shorting pins protruding into the path of the projectile at the end of the barrel (see Figure 3.5). When the projectile's copper plate makes contact with a pair of pins, it completes a circuit, triggering a pulse on the oscilloscope. There are four pairs of pins; each pair of pins is slightly offset from the previous so that they are not broken or prematurely triggered by a previous pin. The time between the pulses can be used to calculate the velocity. A delay generator was used to trigger the oscilloscope recording the outputs of the other experimental diagnostics.

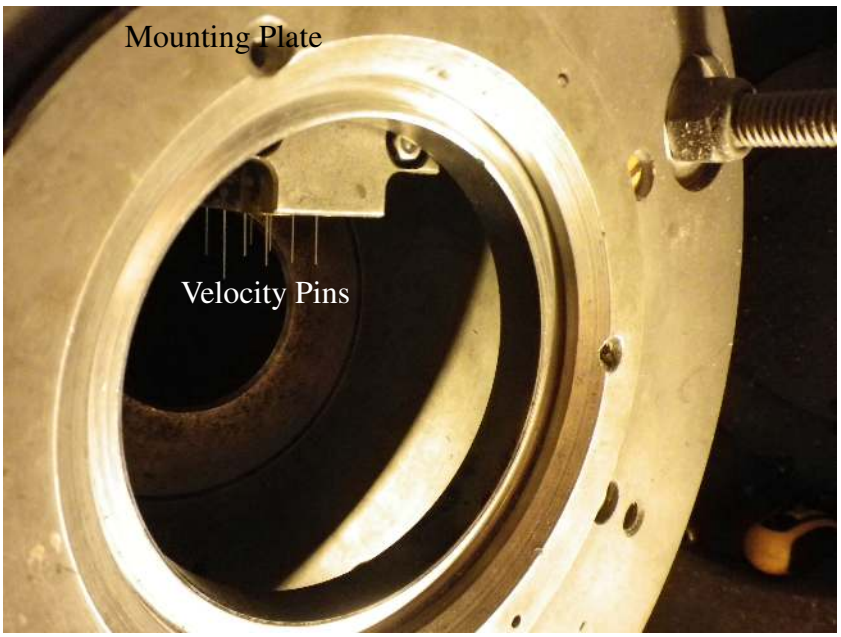

Figure 3.5 The graphite shorting pins used to measure the velocity and trigger the experiment. They are positioned immediately before the mounting plate so the measured velocity is as close as possible to the impact velocity

3.4 Sample Cell

The sample cells were adapted from a design originally used to investigate the properties of wet and dry sand under shock loading [124]. They have a cylindrical geometry and contain a bed of sugar with diameter of 70 mm and thickness 0.5 mm to 4.0 mm.

3.4.1 Cell Design

The sample cells have three main components. The aluminium holder ring provides an interface with the specimen holder at the end of the gun barrel, which holds it in place with solder tags. The PMMA (polymethyl methacrylate) cup holds the sugar and has a make-trigger diagnostic on the front surface. The thickness of the sugar bed can be varied by varying the depth of the cup. The lid, also PMMA, fits tightly onto the back of the cup, with an O-ring providing a seal between the two. The lid has a hole for the PDV fibre mount, which is a PMMA plug containing a 1 mm diameter hole for the fibre. The whole cell is held together with a fast-drying epoxy and eight M3 bolts through all three main parts. This seals the cell so it remains at atmospheric pressure even when the sample chamber is evacuated.

A small piece of copper sheet is glued over the inside of the fibre mount hole, which serves to contain the sugar and act as a reflective mirror for the PDV. In order to accurately represent

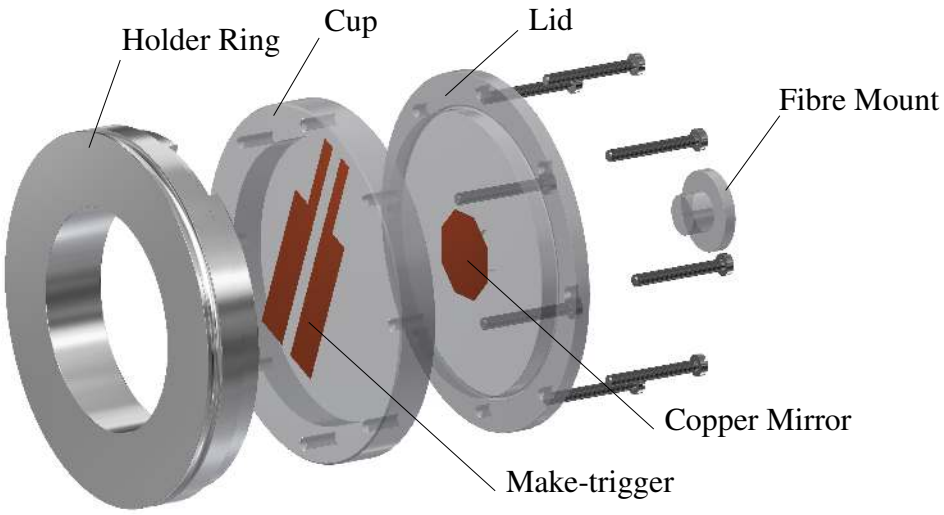

Figure 3.6 Expanded diagram of the sample cell. The holder ring has threaded holes for the bolts. The whole assembly is sealed with epoxy resin, and the fibre mount is glued in place.

the rear surface velocity the mirror needs to be in direct contact with the sugar so there is no air gap. Since it has higher impedance than the sugar, it will then stay in contact with the rear surface of the sugar bed when the latter is shocked [131]. The fibre mount inserts into a hole behind the copper mirror and is glued in place so that a seal is formed. In this way the pressure between the mirror and fibre mount remains the same as the pressure within the cell when the gas gun sample chamber is evacuated.

An expanded view of the cell is seen in Figure 3.6.

To ensure the bed has a constant thickness and the shock is coplanar with the bed, the faces of all parts were machined to a $10\mu m$ tolerance. The cell is made square with the end of the barrel by adjustment of the three mounting plate screws visible in Figure 3.7

3.4.2 Pressing

The sugar had a tendency to stick to containers and utensils, so in order to get the correct density, the sample cell cup was placed onto a high-precision scale, and the correct mass of sugar (as calculated from the measured volume of the cell interior) added directly. It was heaped into a conical shape in the middle of the cup, and then pressed down using the lid. to minimise the chance of air pockets forming directly behind the copper mirror. This process meant that air pockets would be pushed towards the edge and therefore interfere less with

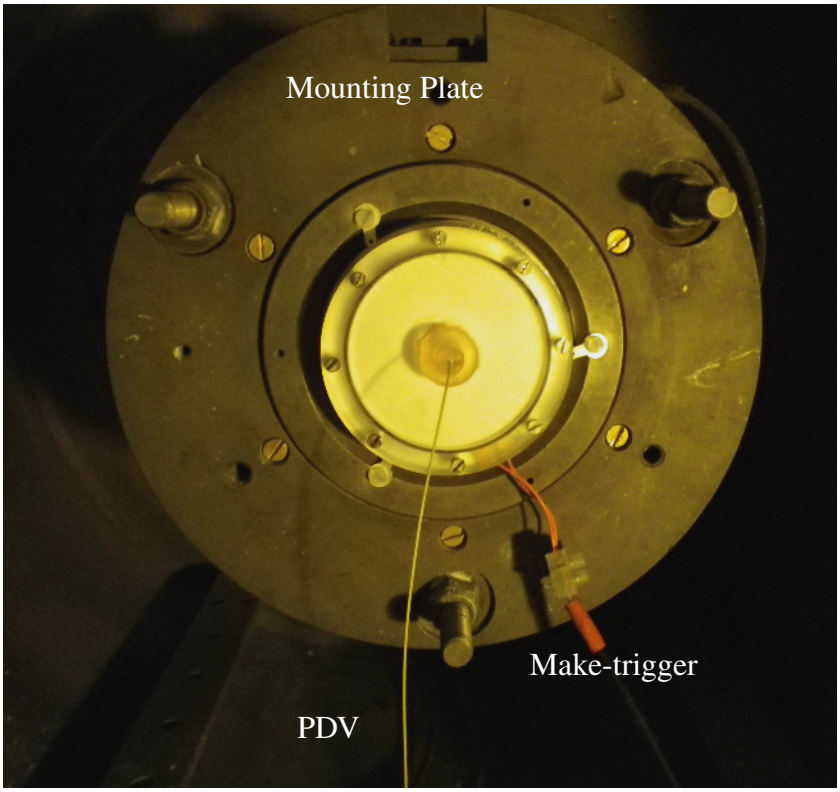

Figure 3.7 A sample cell affixed to the mounting plate inside the sample chamber. The make-trigger wiring and PDV fibre have been attached. The three adjustment screws on the mounting plate can be used to tilt the sample cell to be planar with the end of the barrel.

the shock wave in the centre part of the bed. This technique potentially introduces a radial density gradient which reduces the accuracy of the 'true' density. However, this was deemed less important than the need to eliminate air pockets which would have a much larger effect on density. The lid had an aluminium plug in the fibre mount hole to support the copper mirror against deformation during pressing.

The cell was then tapped, with more pressure applied evenly to the lid, until there were no visible cavities. The free flowing nature of the sugar meant that this was achieved fairly easily. Since the particle sizes are very tightly distributed around 8 μm, the effect of any size separation due to tapping is expected to be minimal [132]. Finally the PMMA parts were epoxied together and bolted to the aluminium holder ring.

The cells were weighed after being left for two days to confirm that there had been no exchange of moisture with the environment. Before loading into the gun, a visual inspection confirmed that there were no large voids or en masse movements.

3.5 Diagnostics

There were two diagnostic methods used in the experiments: a make-trigger on the front surface of the sample to measure the arrival time, and a PDV probe on the rear surface to measure its velocity history. The make-trigger and PDV were connected to separate channels of a Textronix 7254 Digital Phosphor Oscilloscope, which was triggered off the graphite pins discussed previously.

Figure 3.7 shows a sample cell installed into the sample chamber of the gas gun, with the diagnostics attached.

3.5.1 Make-trigger

The make-trigger consists of two pads of high purity copper evaporated onto the front surface of the cup to a thickness of about 100 nm. Wires were soldered onto two thin strips of copper sheet, which were in turn glued with silver conductive paste to the edges of the copper surfaces (outside the impact region of the projectile). These wires were then connected to a measurement circuit which triggers a pulse on the oscilloscope when the circuit is closed by the projectile hitting the two copper pads. The front of a complete sample cell with the make trigger visible is shown in Figure 3.8.

The make-trigger circuit of the cell was tested in situ before each shot. When the copper flyer hits the front of the cup, the measurement circuit is closed, and the pulse is seen on the oscilloscope (see Figure 3.9 for an example).

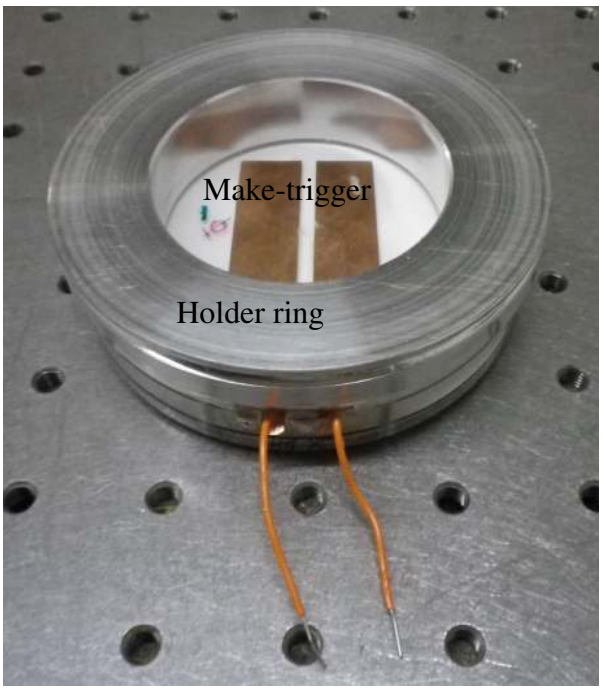

Figure 3.8 The make-trigger on the front surface of the sample cell cup. A shallow slot machined into the holder ring provides enough space for the wires.

3.5.2 Photonic Doppler Velocimetry

The PDV system essentially consists of an optical fibre, a 40 mW 1550 nm laser, and a digitiser. The fibre carries the light from the laser to the experiment. One end of the fibre is cleaved at 90° and pointed at the reflective copper mirror on the rear surface of the bed. The Doppler shifted light reflected from the copper surface mixes with the light reflected from the end of the fibre, producing beats. The amount of frequency shift depends on the instantaneous velocity of the copper mirror, according to the relativistic Doppler shift equation:

$$\frac{\omega_2}{\omega_1} = \sqrt{\frac{c-u_F}{c+u_F}} \tag{3.1}$$

Heterodyne mixing of the shifted and non-shifted light (of unit amplitude) gives rise to beat frequencies:

$$I(t) = \sin(\omega_1 t) + \sin(\omega_2 t + \phi) = 2\cos\left(\frac{\omega_1 t - \omega_2 t}{2}\right)\sin\left(\frac{\omega_1 t + \omega_2 t}{2}\right) + f(\omega_2, t, \phi) \tag{3.2}$$

The phase dependent term is treated as constant, while the summed frequency term is too high frequency for the sampling rate of the oscilloscope. The frequency difference term – the

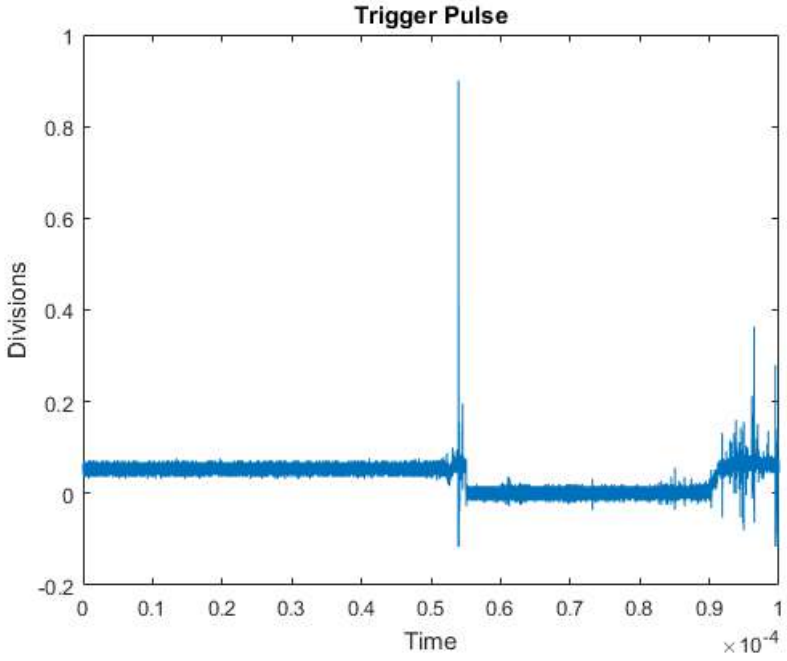

Figure 3.9 The sharp peak in the make-trigger output corresponds to the copper plate on the projectile hitting the make-trigger

beat frequency can be used to calculate the target velocity [104]:

$$\omega_b = \frac{\omega_1 - \omega_2}{2} = \frac{\omega_1}{2}\left(1 - \sqrt{\frac{c-u_F}{c+u_F}}\right) \approx \frac{v}{2c}\omega_1 \tag{3.3}$$

The mixed light returns back down the optical fibre, but a device called a circulator prevents it from going back into the laser, and instead directs it towards a digitiser, which converts it to an electrical signal. Within the shifted light there will be a range of beat frequencies since light reflected from multiple parts of the target can reenter the fibre. There will therefore be a distribution of velocities given by the spectrum of frequencies present in the PDV signal. Fourier transforming the signal gives the velocities present and their relative intensities.

3.5.3 Data Processing

Raw data from the make-trigger and PDV are recorded onto separate channels of the same oscilloscope. The impact time is taken to be the time at which the voltage first rises on the make-trigger channel, as seen in Figure 3.9.

The raw trace from the PDV channel contains a time-varying beat frequency that is proportional to the back surface velocity. Since the velocity changes over time, the data is divided into segments – each segment is analysed to give the velocity at that particular time. The signal of

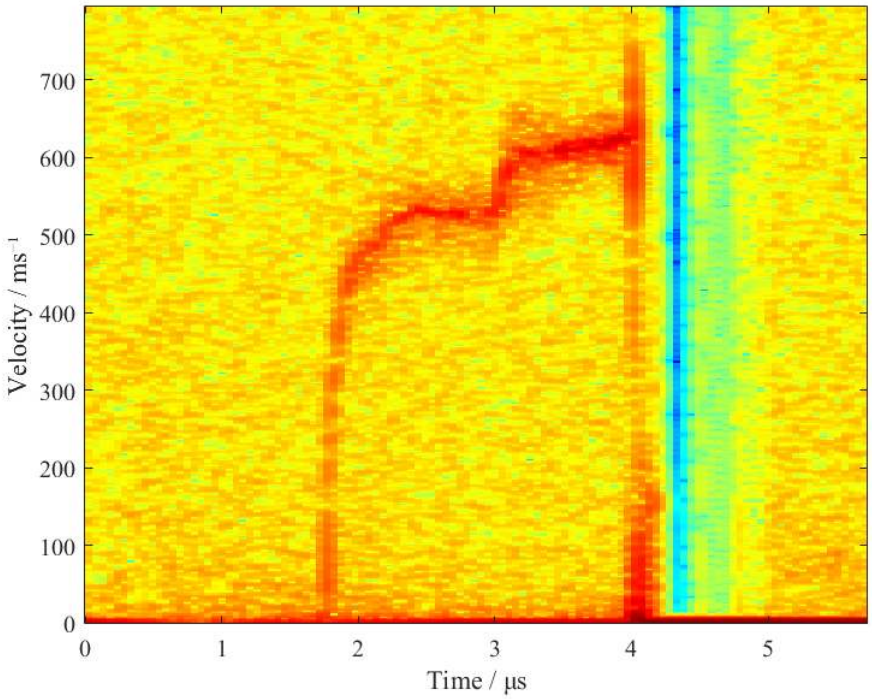

Figure 3.10 PDV velocity history from one of the shots. The initial rise marks the arrival of the shock at the copper mirror and the velocity of the first plateau is the free surface velocity u_F. There is also a second rise and plateau which occurs due a second shock reflected from the PMMA-sugar interface. The velocity drops to zero and then the data cuts off when the copper mirror hits the cleaved end of the fibre and breaks it.

each segment is multiplied by a Gaussian window function before being Fourier transformed – this process is called a Gabor transform. Each segment overlaps with the next by a factor of $\frac{7}{8}$. Choosing a shorter window gives a better time resolution, but since each window contains less of the signal, the resolution of the velocity is reduced.

A longer window of 8192 data points was used to for a better resolution of the velocity plateau, while a shorter window of 512 data points was used for a better temporal resolution to measure the arrival time and rise time. The window length in both cases is a power of 2 so a computationally efficient radix-2 fast Fourier transform can be used. The data processing was performed using a MATLAB routine and can be used to extract the velocity history from the background. The processed data for one shot is seen in Figure 3.10.

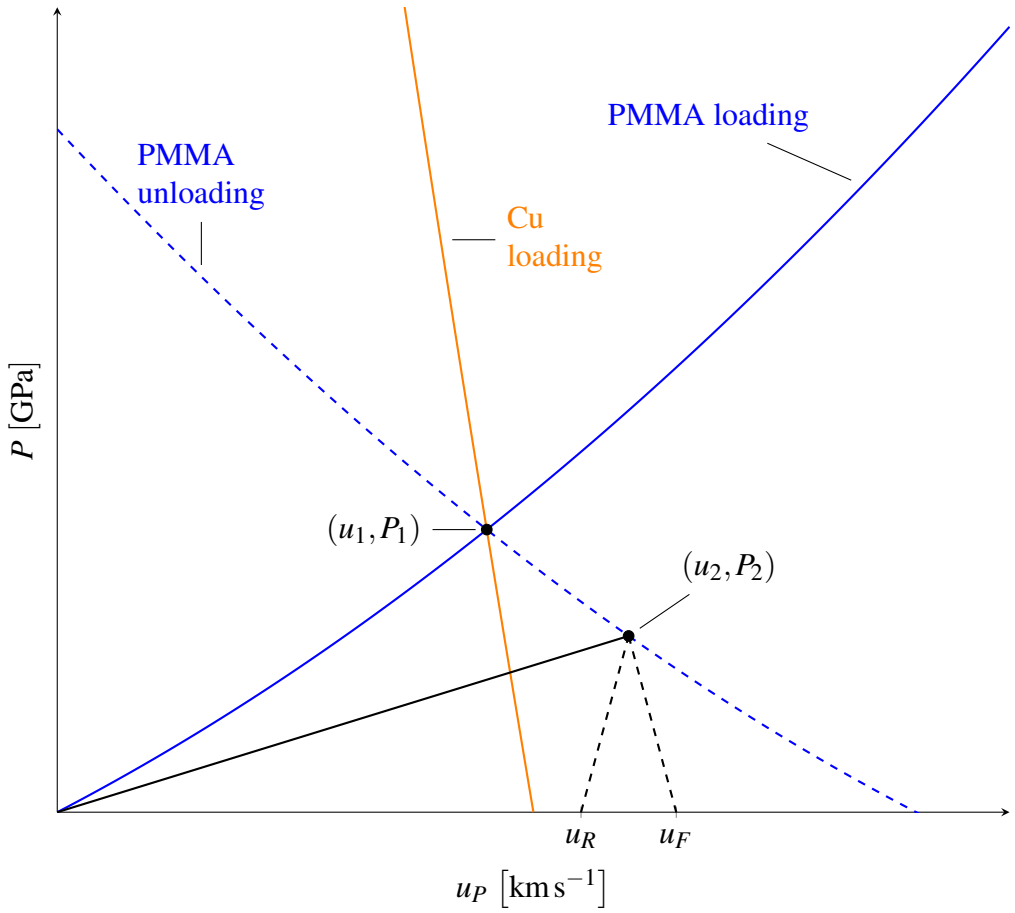

Figure 3.11 Schematic of the impedance matching technique used by Chapman [126] and Perry [124]. The shock states (u_1, P_1) and (u_2, P_2) refer to the Cu-PMMA interface and PMMA-sugar interface respectively. It is assumed that the materials either side of each interface remain in contact (i.e. there is no spalling).

3.6 Impedance Matching

When the projectile hits the PMMA sample cell, a shock is created in both materials. The shock travels through the PMMA and into the sugar, at which point a release wave travels back through the PMMA. By considering the loading and unloading of each material between states, the behaviour of the sugar under shock can be determined. The following impedance matching analysis describes how to find the pressure, particle velocity and shock velocity in the sugar from the quantities that are actually measured: the projectile velocity u_0, the impact time and the rear free surface velocity u_F.

A graphical representation of the analysis in this section is shown in Figure 3.11

The incoming copper flyer hits the front PMMA surface at velocity u_0, and both are shock loaded to the state (u_1, P_1). The equations for the PMMA and copper Hugoniot curves are given by:

$$P = \rho_0 c_0 u + \rho_0 s u^2 + \rho_0 r u^3 + \rho_0 q u^4 \tag{3.4}$$

$$P = \rho_0 c_0 (u_0 - u) + \rho_0 s (u_0 - u)^2 \tag{3.5}$$

Note that the two curves begin from the initial velocity of each material and are oriented in opposite directions because the shocks travel in opposite directions. A quadratic fit is sufficient for copper, however a quartic fit has been made for PMMA because of its irregular behaviour in the low pressure regime [133]. The numerical Hugoniot fits used in this analysis are for PMMA [134]:

$$P = 2.9u + 8.03u^2 - 24.45u^3 + 25.64u^4 \tag{3.6}$$

and for copper [135]:

$$P = 35.18 (u_0 - u) + 13.30 (u_0 - u)^2 \tag{3.7}$$

where in both cases the pressure is in GPa and velocities in kms^{-1}.

These equations can be solved to find (u_1, P_1) the interface state in terms of the projectile velocity u_0.

Now that the state (u_1, P_1) of the shocked PMMA is known it is possible to calculate the velocity V_S of the shock in the PMMA using:

$$P_1 = \rho_0 V_S u_1 \tag{3.8}$$

where the initial density of the PMMA is $\rho_0 = 1.18\,\mathrm{g\,cm^{-3}}$. Since the thickness of the PMMA layer is also known, the time for the shock to cross into the sugar can also be calculated.

The time at which the PMMA is first shocked is known from the make-trigger signal, so the time at which the shock exits the PMMA and enters the sugar can be inferred. The PDV trace can be used to obtain the time at which the shock reaches the end of the sugar bed – it is taken to be the point when the velocity reaches 50 % of its value on the first plateau. The difference between the shock's entry and exit times, along with the bed thickness can be used to calculate an average shock velocity in the sugar U_S.

To proceed, the reflected shock approximation can be used [136], which means that the left-going release adiabat of the PMMA can be approximated by the Hugoniot reflected about

u_1, with the equation:

$$P = \rho_0 c_0 (2u_1 - u) + \rho_0 s (2u_1 - u)^2 + \rho_0 r (2u_1 - u)^3 + \rho_0 q (2u_1 - u)^4 \tag{3.9}$$

The same coefficients as above are used. The sugar Hugoniot is unknown, but because the shock velocity U_S has already been calculated, the Rayleigh line can be expressed in terms of known quantities:

$$P = \rho_0 U_S u \tag{3.10}$$

The release wave in the PMMA and the shock wave in the sugar must have the same state at the PMMA-sugar interface (u_2, P_2). This point represents a possible shock state of the sugar, so lies on its Hugoniot, and can be found by solving Equation (3.9) and Equation (3.10).

The shock wave travels through the sugar and densifies it until it reaches the rear surface. Here a release wave starts to travel back through the sugar, causing the free surface to move with a (lab frame) velocity u_F. This velocity is the velocity of the first plateau seen on the PDV trace.

Release waves move in the opposite direction to the particle velocity, so the velocity of the release wave is the negative of the free surface velocity. Since the sugar is already moving at u_2, the inversion must be done in this reference frame:

$$u_R - u_2 = -(u_F - u_2) \tag{3.11}$$

A perfectly elastic sample would release to u_2 whereas a perfectly inelastic sample would have a release velocity of zero i.e. there would be no release and the material would remain fully densified. The sugar is neither fully elastic nor inelastic so there is a partial release $0 < u_R < u_2$.

3.7 Results

Seven shots with a projectile velocity of approximately $500\,\mathrm{m\,s^{-1}}$ were performed into sugar beds with a range of thicknesses. They are summarised in Table 3.1.

The data for the average shock velocity is presented in Figure 3.12 as a function of bed thickness.

d/mm	u_0/m s^{-1}	U_S/m s^{-1}	u_2/m s^{-1}	u_F/m s^{-1}	t_r/ns
0.5	507	358	828	880	N/A
1.0	493	831	726	715	N/A
1.0	503	546	787	785	45
1.5	505	650	772	610	123
2.0	502	823	740	530	169
3.0	496	690	752	540	309
4.0	498	694	754	530	303

Table 3.1 Summary table of the experiments performed. The columns are: the thickness d of the bed, the velocity u_0 of the projectile, the shock velocity U_S, the particle velocity u_2 in the sugar, the velocity u_F of the free surface and the rise time t_R. Two measurements were taken for d =1.0 mm because the first produced unusual results.

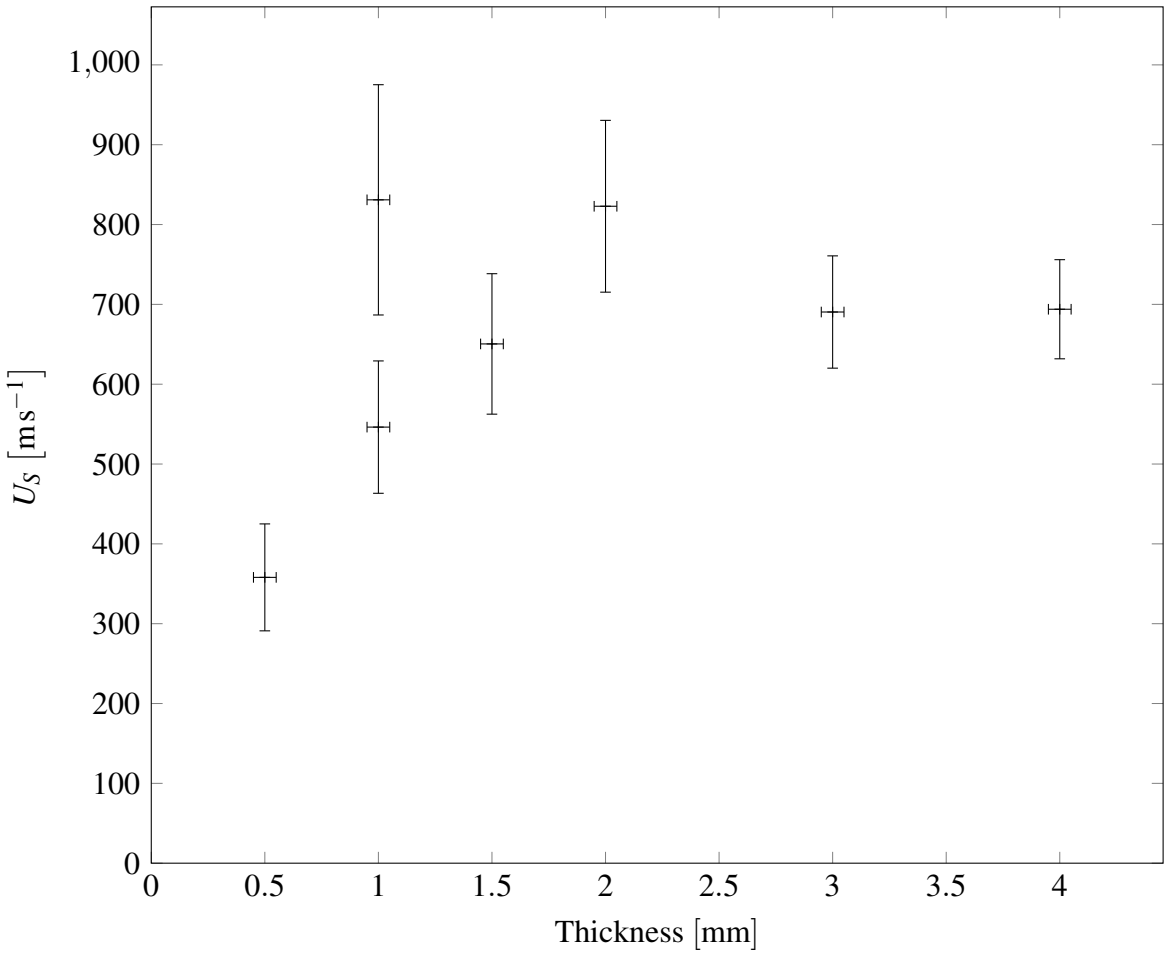

Figure 3.12 The average shock velocity increases with bed thickness until 2.0 mm after which it flattens off. The experiment was repeated at 1.0 mm because of the outlier

3.7.1 Release

Using the argument described above for calculating the release behaviour from the free surface velocity, the results shown in Figure 3.13 were obtained

Since approximately the same impact velocity was used in each shot, the points are very close together in $P - u_P$ space. The release behaviour, however, is significantly different. The (inverse) gradient of each shot's release path was calculated and is shown in Figure 3.14.

The release gradient has the same dimensions as shock impedance, and can be interpreted as the pressure released from unit decrease in particle velocity. Shock impedance, which is the pressure built up from a unit increase in particle velocity, is given by:

$$Z = \rho U_S \tag{3.12}$$

A positive gradient is indicative of a partially elastic release, with the bed's specific volume increasing as the pressure drops to zero. An infinite gradient (zero inverse gradient) corresponds to a totally inelastic response, and the bed density staying as the shocked density even after the pressure is removed. Finally a negative gradient suggests negative release i.e. further densification as the pressure drops. Since there is unlikely to be a physical mechanism leading to this phenomenon it is more likely that one or more of the assumptions made do not apply for these results.

In thinner beds, a greater relative fraction of the shock energy goes into thermoelastic compression, whereas in thicker beds the energy goes into compaction. During the unloading phase, the elastic compression energy can be partly recovered, allowing for greater release, hence a smaller release gradient in thinner beds. the results in Figure 3.14 suggest that the elastic compression stops being significant for beds thicker than 1.0 mm. Chapman [126] noted that porous beds do not typically reach thermal equilibrium over the rise time of the shock, although some energy may also go into heating the bed.

3.7.2 Rise time

For five of the seven shots the velocity rise had a strong enough signal to noise ratio to be distinguished from background at a sufficiently high time resolution. The rise times (defined as the time for the measured free surface velocity to rise from 10 % to 90 % of its plateau value) are displayed in Figure 3.15 against the bed thickness. For the two shots where a rise time was not recorded there was no window length that provided both the temporal and velocity resolution to read off the 10 % and 90 % points. The rise time exhibits a dramatic increase with bed thickness, before levelling off at around 300 ns.

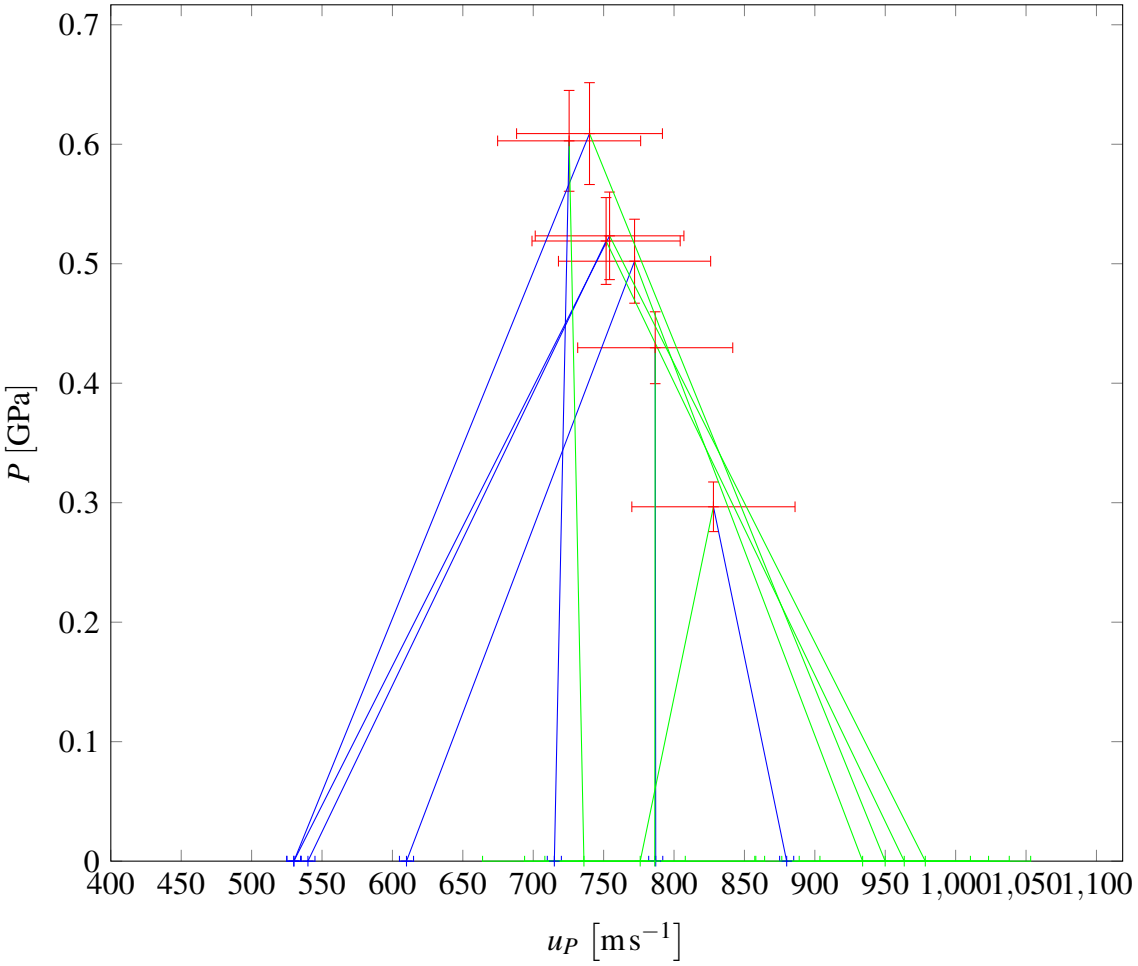

Figure 3.13 The release paths (green) in $P - u_p$ space. The release is highly inelastic for the thinner beds, while for the thicker beds the calculated release is not physical since the free surface velocity (blue) is significantly lower than the particle velocity (red). The bed releasing laterally instead of axially would mean that the copper mirror could lose contact with the rear surface of the bed.

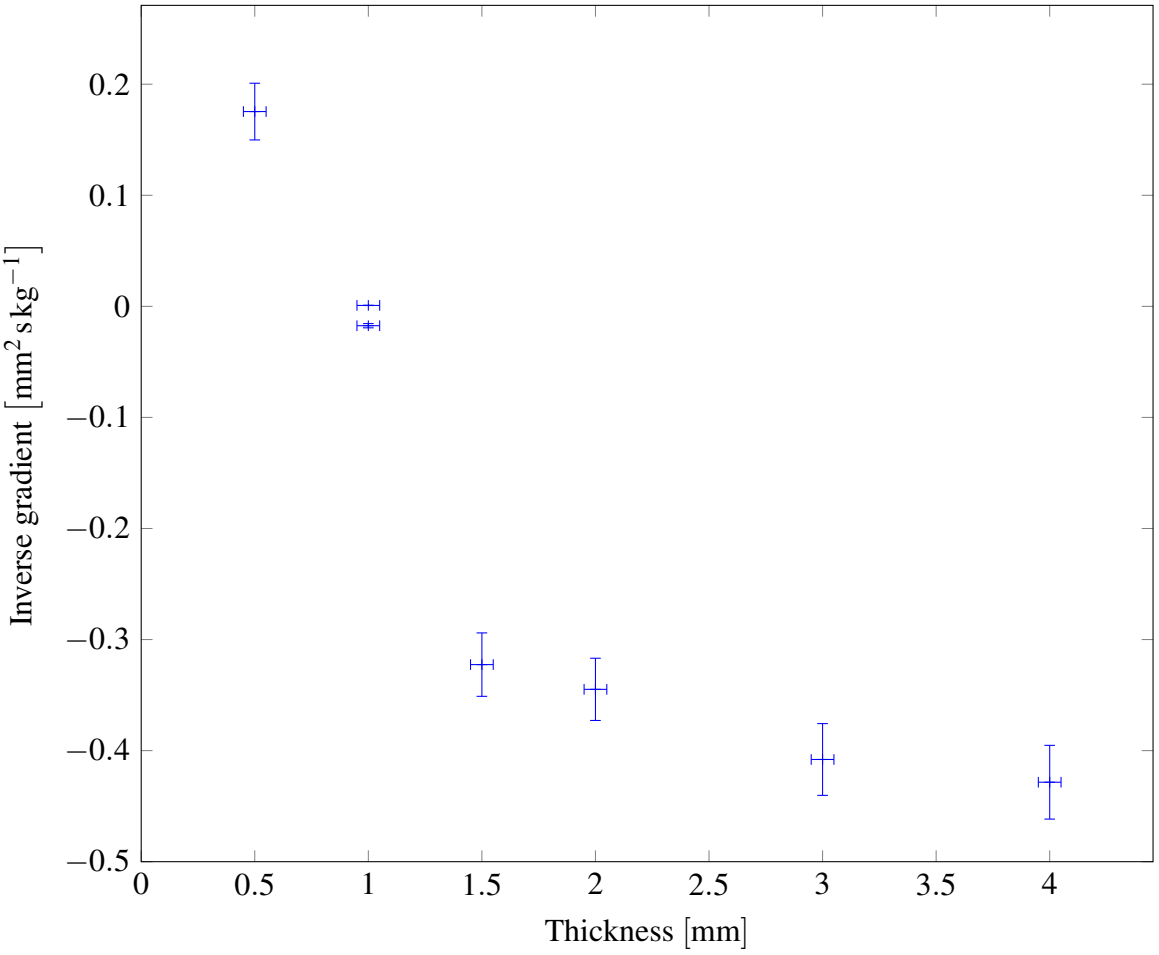

Figure 3.14 The inverse gradient has been plotted since some of the release paths are close to vertical. There is a noticeable change at around 1.0 mm.

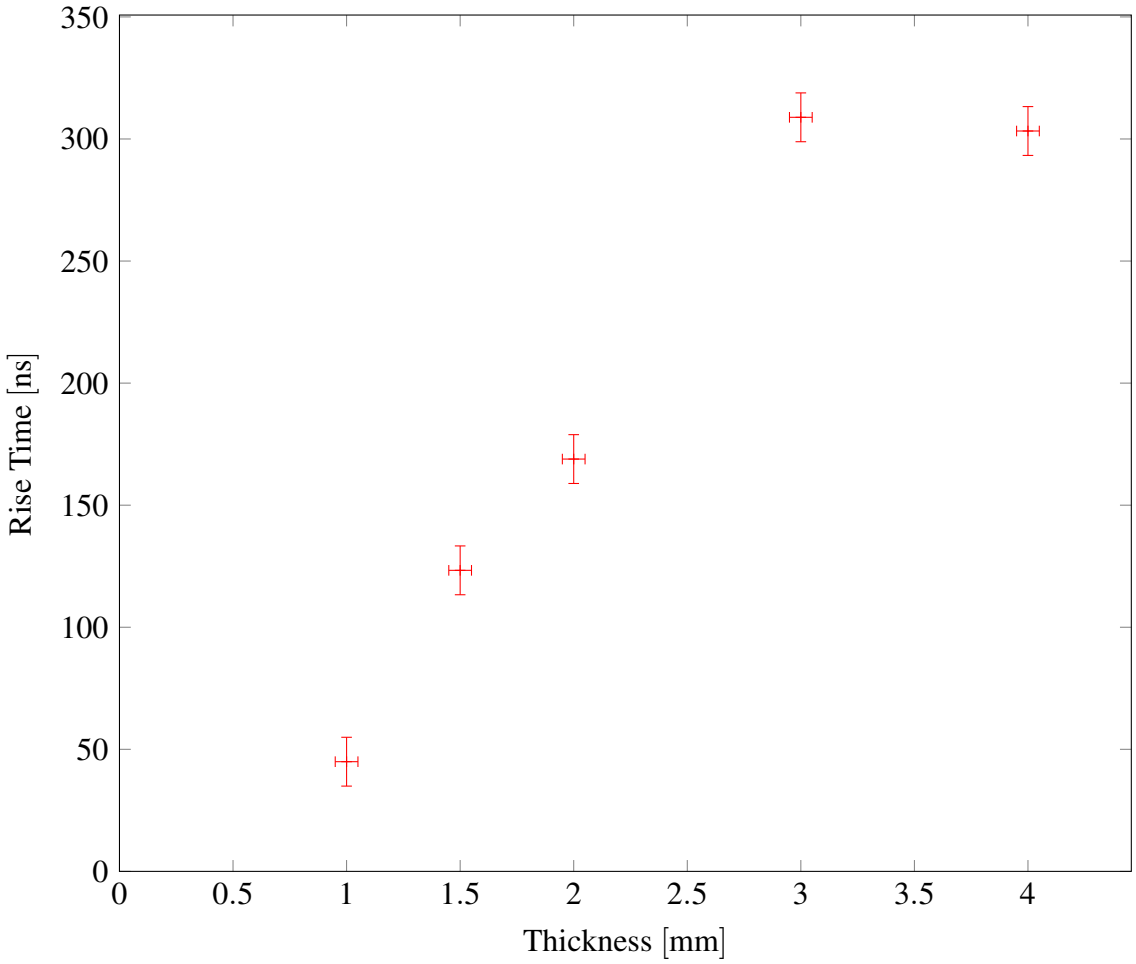

Figure 3.15 The time for the free surface to rise from 10 % to 90 % of its peak value increases with bed thickness up to about 3.0 mm, where it then plateaus at about 300 ns.

3.8 Errors

Errors are introduced for each quantity that is measured, that is: the projectile velocity, the timing points from the make-trigger and PDV, the velocity of the plateau on the PDV trace and the thickness of the sugar bed. The impedance matching conditions mean that the errors accumulate in a complex way as detailed below:

The largest source of error in the shot velocity is due to uncertainty in the velocity pin spacing, since the timing of the pulses can be measured very precisely. The angular deviation from vertical of the graphite pins gives the largest contribution, estimated at ± 1 %.

The alignment of the cell with the barrel was determined to be planar to within 10 µm across the width of the barrel. Given that this is the same order of magnitude as the sugar particles themselves, this uncertainty is neglected.

The uncertainty in bed thickness was estimated as ± 0.05 mm from combining uncertainties in the digital callipers used to measure the initial thickness and error from machining. The error in pinpointing times from the oscilloscope trace was estimated to be ± 100 ns. Combining the sources of error from the cell and the traces led to an error in shock velocity of ± 7 %. It should be noted that this could theoretically be reduced by decreasing the size of the Fourier transform window, however there is then the risk of misattributing the arrival time entirely due to increased noise drowning out the signal. Perry [124] notes the non-trivial aggregation of error arising due to the impedance matching technique. Chapman [126] estimated the error in the stress state to be ± 8 % when using this technique.

Reading off the plateau velocity carries an error of $\pm 5\,\mathrm{m\,s^{-1}}$ when using a Gabor window of 8192 data points.

Although the average density had a small error (± 1 %) it is likely that there was greater error in the density distribution due to the pressing technique described above, despite the measures taken to avoid this. In future experiments it may be possible to quantify this effect by measuring the attenuation of light through the bed due to the translucency of the sugar.

The above analysis does not include the uncertainty arising from the literature Hugoniots for copper and PMMA – since these are themselves empirically derived there will be some experimental error. Furthermore the reflected shock assumption introduces some systematic error due to the difference between the reflected Hugoniot and the true unloading curve [137]. This error becomes significant at high pressures, or for large impedance mismatches. It is possible to apply a correction function which derives from a theoretical equation of state treatment. Chapman [126] calculated a 2.7 % difference between the reflected Hugoniot and true release curve.

Finally, there will inevitably be variation between beds arising due to random microstructural differences e.g. void distribution. Given the small particle size it is expected these

differences would largely average out, so that this variation would not be significant if the experiments were repeated.

3.9 Discussion

There are two possible effects that could cause the observed dependence of rise time on bed thickness. Since the shock wave is a combination of individual wavelets there may be a simple statistical explanation. Across the bed there will be slight random variations in wavelet propagation speed which accumulate with distance. A thicker bed has accumulated more variation so the overall shock has a gentler ramp.

Another possible explanation is the existence of force chains, or stress bridges – sets of particles held in contact by pre-existing compressive forces that span the samples. The bridges follow a random path through the bed, therefore their length increases non-linearly with bed thickness [138]. Stress transmitted through these force chains will cause particle movement at the far end of the bed before the main shock does. This precursor wave travels faster than the compaction wave and so will lead it by more time in thicker samples,can give the appearance of the latter ramping up more gradually. In thin beds there is smaller variation in the length of force chains, so the precursor wave is narrow. For thick beds the variation in force chain length is greater, which broadens the precursor wave, potentially blending it into the compaction and leading to the appearance of a gentler rise. An illustration of this effect is shown in Figure 3.16.

Others have found a similar effect. Trott et al. [127] also experimented on low density sugar, looking for non-steady behaviour under gas gun impact. They instead used VISAR for a velocity history, but otherwise the calculation for rise time was the same. Their results showed that the rise time was approximately constant for thicker beds, but noticeably shorter for the thinner beds. The onset of steady waves were observed for 4.0 mm thick beds, but below this thickness there was evidence of non-steady behaviour. Neal et al. [125] measured similar behaviour in a bed of glass microspheres, and suggested that with better spatial resolution it might be possible to observe individual force chains.

The onset of steady behaviour occurs when the beds are thick enough such that there is no significant degree of stress bridging. At this point the precursor becomes indistinguishable from the compaction. The rise time variation is effectively a statistical phenomenon that arises from accumulation of variation, both in the paths of stress bridges and compaction wavelets.

If there is a precursor wave present in PETN, it could have a desensitising effect on the explosive. By collapsing voids and releasing pre-existing stresses, but with insufficient energy to initiate reaction, the explosive is less sensitive to the subsequent shock wave. The results of Setchell [139] indicated that until the precursor was overtaken by the shock, there was

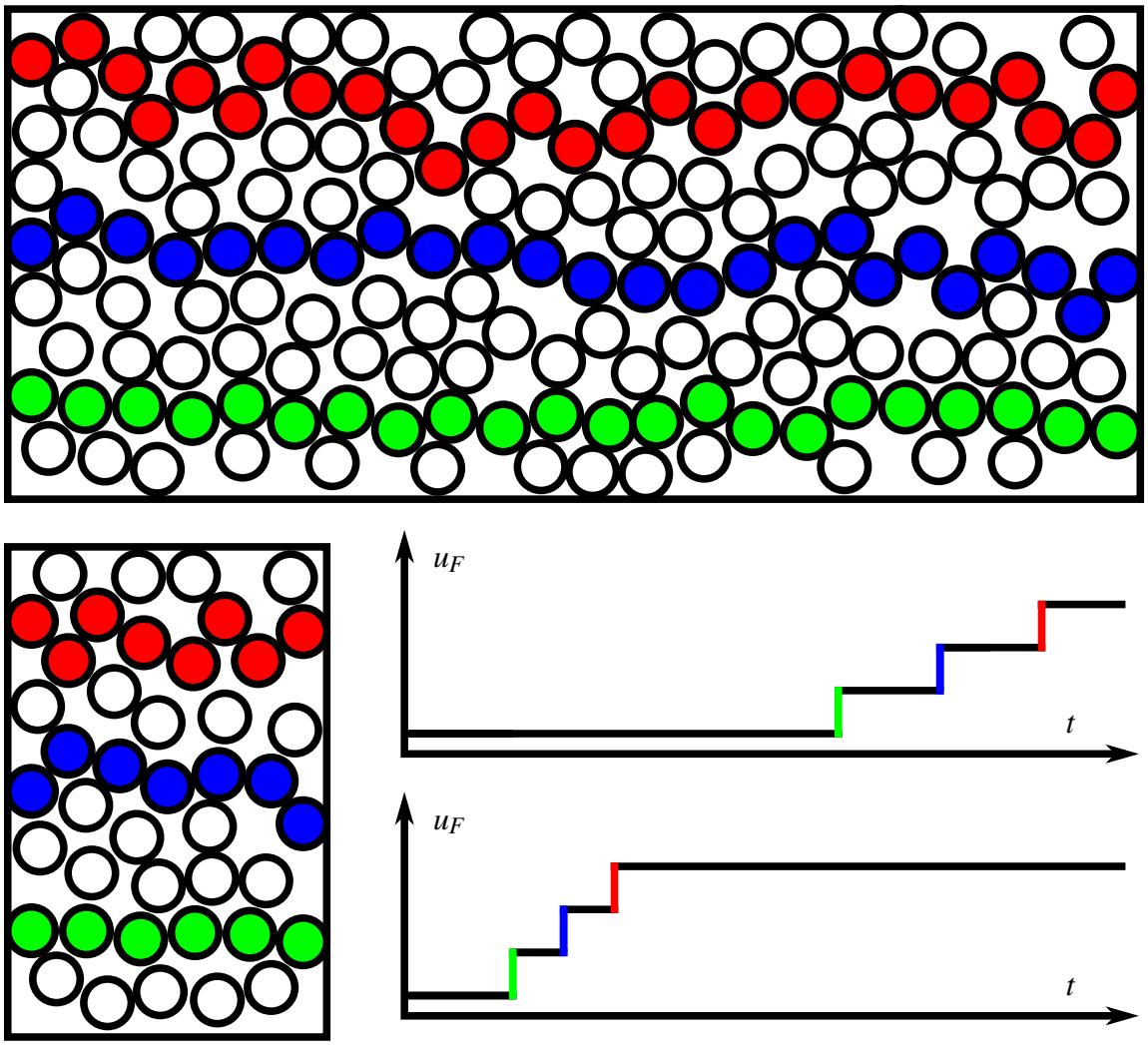

Figure 3.16 Demonstration of the force chain effect. Three force chains of different lengths have been highlighted for a long and short bed of a loosely dispersed granular material. The impulse through the longer red force chain arrives after the impulse through the shorter green one. In the longer bed there is greater variation in the length of force chains so the shock front will have a greater variation in arrival. Given a large distribution this will result in a larger rise time.

a significant decrease in particle velocity in PBX-9404 when a ramp precursor wave was artificially introduced. If experimentation finds that the detonation velocity in PETN suddenly increases, then it is possible that this marks the point at which the detonation passes the precursor, should one exist.

As seen in Figure 3.12, the average shock velocity in thinner beds is significantly lower than in thicker beds, indicating that the shock undergoes a run up phase before reaching a steady state. It is generally accepted that shocks travel faster in granular materials when the density is increased [140], so a mechanism that led to compaction increasing with distance would cause the shock velocity to also increase with distance.

It is proposed that as the precursor wave becomes blended with the compaction ramp the amount of compaction increases. This mechanism can be justified by the reasoning that the longer the ramp the more time is available for particles to rearrange to a closer packing configuration. Furthermore, due to force chain branching, more particles will be affected further into the bed. Some particles near the end of the bed may be in multiple force chains, whereas particles near the beginning of the bed may not be in any. This introduces a density gradient, increasing with distance. The average velocity is therefore greater in thicker beds, where the wave travels at a higher steady speed for a greater fraction of the distance.

The densification effect plateaus and so does the shock velocity. Eventually it will diminish as release waves from the edges of the cell catch up to the shock. Trott et al. [141] identified an approximately constant shock velocity for samples between 2.27 mm and 8.03 mm.

If the same densification mechanism is present in detonating PETN it will affect the reaction zone. Denser compacts exhibit a sharper and shorter conductivity profile [6] [77]. If the reaction zone length is found to decrease with distance then this could be an explanation. Evidence for an increase in conductivity would be further evidence towards this theory. The detonation velocity would also increase with density, in addition to the expected run up. A possible additional effect is that the usual divergence of the detonation front may be slower if the centre of the wave is moving through denser material in the middle than at the edges and therefore travelling faster. Depending on the significance of this mechanism the curvature may actually increase, or at least decrease less quickly.

With regards to the release behaviour, there appear to be three categories. The 0.5 mm bed is shown to exhibit a small amount of elastic release, since the free surface moves faster than the calculated particle velocity. The only feasible mechanism for this behaviour is the decompression of the sugar crystals, since other compaction mechanisms are entirely inelastic. The bed is thin enough that there is noticeable reassertion of the compressed crystals in the axial direction that occurs alongside rearrangement and fracture. In the 1.0 mm beds the release

is entirely inelastic since the release velocity is the same as the free surface velocity within error. It is clear that the shock loading is completely irreversible.

The third category, which applies for all the beds thicker than 1.0 mm, has the free surface velocity significantly less than the particle velocity, implying that the beds continue to get denser even after the pressure is released. Since this is unphysical, there must be a different explanation. A lateral release velocity much higher than the shock velocity would result in a decreased free surface velocity since the release waves from the edges of the sample would have had time to catch up to the shock wave in the centre before it reached the end [126]. It is also possible that the assumption that the copper mirror matches the rear surface velocity does not hold all of the time.

In a detonation, there is unlikely to be any measurable elastic release, since the reaction products are gaseous and do not reassert. However, the effect of lateral compaction may be important. Compaction could lead to faster ignition via void collapse, frictional heating or plastic deformation. Without lateral movement of particles, the mechanisms by which the reaction spreads from the centre to the edges are limited to thermal conduction and jetting. These additional mechanisms brought about by lateral movement may increase the speed at which the reaction reaches the edge, meaning that the rarefaction waves are created earlier.

3.10 Summary

Plate impact experiments on an inert bed have identified a non-steady phase at the millimetre scale. Non-elastic compaction has been suggested as one mechanism for the effects seen.

- The shock velocity initially increases, potentially due to a densifying precursor wave, but then decreases as lateral release waves catch up.
- In beds thinner than 1.5 mm there was an inelastic release. In thicker beds the results suggest that the material has already begun to unload due to the lateral release before the shock reaches the end.
- In beds thinner than 3.0 mm the rise time becomes longer as the thickness is increased. Above 3.0 mm the rise time reqaches a plateau of 300 ns. A possible explanation is the variability in force chain length.
- There are several inert effects that could impact the reactive behaviour of PETN. In particular the existence of precursor waves or a densification effect would complicate the relationship between initial density, reaction zone length and curvature.

While the plate impact experiments described in this chapter are useful for characterising the inert simulant, it would not be feasible to use the same amount of explosive. Therefore it is necessary to perform new experiments where a much smaller volume of material is used – on the scale of a detonator. The next chapter describes efforts to design and build such an apparatus.

Further experiments on energetic materials will need to be capable of distinguishing between the inert effects observed here and other complications arising from the reactive nature of the detonation wave. The results of this chapter will be applicable to the very early stages in detonation – before any significant chemical reaction has occurred.

Chapter 4

Experimental Configuration

4.1 Introduction

In order to investigate the reaction zone of PETN it is necessary to be able to initiate it in a way that is reproducible, inexpensive and time efficient. Since the motivation behind this work is to measure the reaction zone in a detonator environment, the experimental apparatus should be capable of producing a similar shock profile.

This chapter describes the construction and testing of a laser flyer system, and the characterisation of slapper detonators fired with an adapted capacitor bank. These two alternatives both produce shocks capable of detonating PETN, however the laser flyer system does not produce an electrical discharge which may disrupt certain diagnostics.

4.2 Laser Flyer System

Pulsed lasers can provide the energy to initiate explosives with low cost and high repeatability. The deflagration to detonation mechanism occurs when the configuration allows direct heating, while a shock to detonation transition can be achieved using a thin flyer driven by plasma produced by laser ablation.

4.2.1 Direct Laser Initiation

Direct laser initiation occurs when laser heating of an explosive leads to a DDT process. A metal film on the surface of the explosive of sufficient thickness can change the mechanism to SDT, as plasma generation at the surface leads to a shock in the metal and then the explosive. Yang and Menichelli [142] first demonstrated that high power laser pulses from a Q-switched laser could initiate the secondary explosives PETN, RDX and tetryl. In some cases the detonation

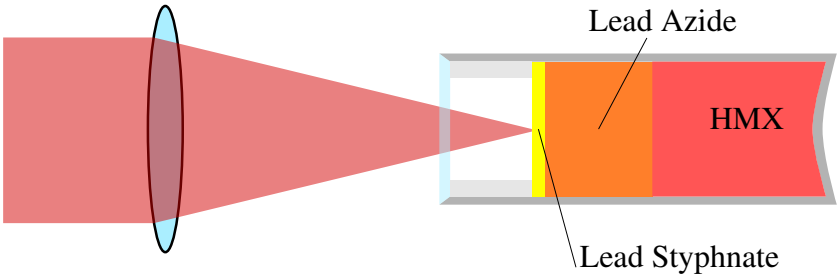

Figure 4.1 The microdetonator designed by Yang [143]. The threshold initiation energy was observed to be 15 mJ

ramped up to steady state within 0.5 µs. They found detonations could be achieved at higher densities (and therefore higher detonation velocities) than in the initial fill of an EBW detonator. A 100 nm aluminium film deposited on the window enhanced the sensitivity to detonation of RDX and tetryl but in PETN detonation could be achieved regardless. This principle was later used in the construction of a laser microdetonator [143], consisting of a lead styphnate primary followed by lead azide and HMX. The total function time was close to the theoretical values for the lead azide and HMX, indicating an almost instantaneous initiation of the lead styphnate.

Using a pulsed laser focused through a transparent plate onto low density ($0.9\,\mathrm{g\,cm^{-3}}$) PETN, Volkova et al. [144] found only a weak dependence of initiation threshold on the shape or length of a laser pulse of a given energy, suggesting that pulse energy was the important quantity, as opposed to power. They suggested a two-stage model of initiation, namely a high pressure reaction wave developing into a detonation wave. Renlund et al. [145] also performed experiments of direct laser initiation of PETN and found the detonation took longer to pass through the explosive than a naive calculation using time-of-arrival and detonation velocity would predict. The two possible mechanisms they suggested to explain the excess function time are an induction time at the front surface followed by immediate detonation, or a slower deflagration transitioning to a full detonation. A delay in light generation until after the end of the laser pulse suggested that the second mechanism was correct in agreement with Volkova et al. [144]. A third possible mechanism is that the detonation velocity was reduced by wave curvature effects, although this was not considered by the authors. The induction distance was between 0.4 mm and 2.5 mm and the deflagration velocity was between $1.5\,\mathrm{km\,s^{-1}}$ and $3.0\,\mathrm{km\,s^{-1}}$. It is possible that there is some similarity in the mechanism causing excess function time here as in EBW detonators.

Tarzhanov et al. [146] used a 40 ns 1064 nm pulsed laser to initiate PETN with a wide range of densities and porosities. Their results also supported a two-stage initiation model. They also found that the light absorption into the PETN abruptly increased following initial photoionisation in the surface layer. Further work was done [147] using laser light to explode

metal films adjacent to PETN charges. There was a dependence of initiation energy on the film material and thickness. Different metals had different optimal thicknesses – if the film was too thin a fraction of light passed straight through while for thicker than optimal films there was unnecessary heating of additional material. The products of the exploding film were speculated to act as a shock-generating piston on the explosive, with numerical models estimating the shock strength as around 0.1 GPa.

More work using metal films was done by Kennedy et al. [89], who observed that PETN became more sensitive to laser initiation when coated with a 235 nm titanium film, and that it was less sensitive at higher densities. They hypothesised that the organic explosive molecules allowed a significant degree of scattering and transmission before a plasma was formed. The plasma then absorbs energy and heats the explosive. By using a metal foil, the laser energy is either reflected (aluminium) or absorbed (titanium), rapidly forming a highly absorptive plasma in either case. They also drew a comparison with exploding bridgewire (EBW) detonators, noting that the minimum initiation threshold energy of 10 mJ was similar to that of a small bridgewire.

4.2.2 Laser Flyers

Rather than coating the explosive with a metallic film, the film can be deposited on an optical substrate and separated from the explosive. The expanding plasma formed by an incident laser pulse then punches a high velocity disc – the flyer – out of the film and towards the target. The shock formed in the explosive by the impact of such a flyer can be sufficient to initiate detonation.

Paisley [148] used a Nd:YAG (Neodymium doped Yttrium Aluminium Garnet) laser to produce miniature ($<$5 µm thick, $<$1 mm diameter) flyer plates which were studied with a streak camera and a VISAR.

A common method for delivering the output of a laser to a flyer is via an optical fibre. Trott and Meeks [149] used an optical fibre to deliver light from a 1064 nm laser to a 25 µm thick aluminium foil target with a 25 % efficiency (optical energy converted into kinetic energy). Frank and Trott [150] used a similar method to launch flyers with thicknesses from 0.25 µm to 2.6 µm produced by physical vapour deposition on the polished surface of the fibre. The advantages of fibre coupling include mixing of modes, which produces a smoother beam profile, and therefore flatter and more stable flyers.

Hatt and Waschl [151] used a light based time-of-arrival (TOA) method to measure the average velocity of single layer and multi-layer flyers with a range of metals (Al, Mg and Cu) and dielectrics (Al_2O_3, MgF_2 and ZnS). The most efficient flyers were those with Al/Al_2O_3 and $Mg/MgF_2/Cu$ layers which travelled at velocities of 3.6 $\mathrm{km\,s^{-1}}$ and 4.4 $\mathrm{km\,s^{-1}}$ respectively.

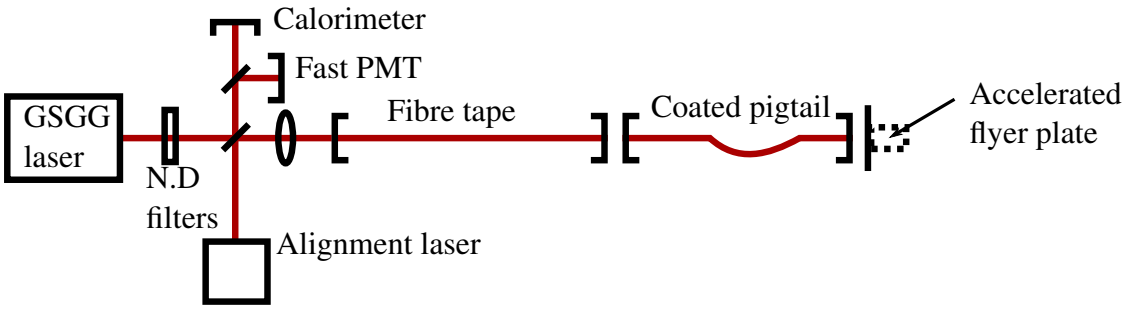

Figure 4.2 The laser flyer system of Frank and Trott [153] used a gadolinium scandium gallium garnet (GSGG) laser with a tapering optical fibre.

These multi-layer flyers have several different layers which each serve a different role, allowing greater coupling efficiency and better overall performance. The purpose of each layer is discussed in more detail later in the chapter.

Bowden [152] developed a laser flyer system with the aim of optimising the coupling efficiency into the fibre. Polishing the fibre end face increased the fibre's damage threshold to $50\,\mathrm{J\,cm^{-1}}$. A tapered optical fibre was used to inject higher energy pulses into the main fibre. The structure of multilayer flyers was optimised with a parameter study of materials and thicknesses.

A generic fibre coupled laser flyer system from Frank and Trott [153] is shown in Figure 4.2.

4.2.3 Flyers in Shock Experiments

Laser flyers have been used for shock compression experiments as an alternative to more traditional methods such as plate impact, because of their high reproducibility and firing rate and low cost. They are particularly suited for use with small samples, which may be the case if material supply is limited or there are other experimental constraints. Laser flyers are not suited to polycrystalline targets with a large crystal size, because the small lateral size of the flyer and short shock duration do not produce behaviour that is representative of the whole sample. Single layer aluminium flyers were used by Brown et al. [154] to calculate the Hugoniot equation of state (EOS) of a polymer film . Shaw et al. [155] observed an oscillating velocity history as measured by PDV due to shock reverberation between the front and rear faces of the flyer. They also recorded the shock response of PMMA using the spectrographic redshift of an embedded emissive dye.

Relatively thick ($50\,\mu\mathrm{m}$ to $250\,\mu\mathrm{m}$) and slow ($<1\,\mathrm{km\,s^{-1}}$) flyers were used by Swift et al. [156] to investigate the dynamic properties of the flyer material (Cu). The flyer was impacted onto a PMMA window and the deceleration as measured using VISAR was used to deduce the Hugoniot. By far the most common application of laser flyers in shock experiments is as an

initiator for energetic materials, either as an investigation into the flyers themselves or into the properties of the explosive.

4.2.4 Flyers as Initiators

Watson et al. [157] investigated the sensitivity of PETN with different grain sizes to laser flyers. Ultrafine PETN (grain size 1 µm) was initiated far more readily than coarse PETN (grain size 106 µm). The explanation is that the flyers are very thin and shock duration very short, so only in the ultrafine PETN are grains and voids completely encompassed by the shock. In the coarse PETN the grains are larger than the shock width, so there are fewer initial impact sites, and only the surface of the grains is heated. The greater number of smaller voids in the ultrafine material also meant that there were more possible sites for hot spot formation via void collapse.

Bowden and Maisey [158] used a fibre coupled laser flyer system to initiate PETN with a range of surface areas, finding lower initiation thresholds at higher surface areas. The flyer velocity was up to $4\,\mathrm{km\,s^{-1}}$ and they produced shocks over 30 GPa with sub-nanosecond durations.

4.2.5 Theory

The action of laser launched flyers lends itself to theoretical analysis using an energy-balance treatment, as was carried out by Lawrence and Trott [159]. Energy from the laser is deposited into the flyer plate causing some material, the blowoff, to ablate. The remaining material is launched as the flyer. By considering the energy flow within the material, it is possible to derive a relationship between flyer velocity and launch energy. Starting from the Gurney equations [160] for explosive fragment velocities, the explosive energy is replaced with the energy deposited by the laser.

$$\underbrace{\rho x_d E}_{\text{Energy deposited into material}} = \underbrace{\frac{\rho}{2}\left(x_0 - x_d\right) v_0^2}_{\text{Kinetic energy of flyer}} + \underbrace{\frac{\rho}{2}\int_0^{x_d}\left(\frac{v_0 x}{x_d}\right)^2 dx}_{\text{Kinetic energy of blowoff}} \tag{4.1}$$

It has been assumed that the velocity of the blowoff varies linearly with distance such that $v(x) = \frac{v_0}{x_d}x$ for vaporisation depth x_d as shown in Figure 4.3. x is the distance from the start of the flyer: the first layer has velocity v_0 and this decreases linearly down to the start of the flyer.

Solving Equation (4.1) for the flyer velocity gives:

$$v_0 = \sqrt{\frac{3E}{\frac{3x_0}{2x_d} - 1}} \tag{4.2}$$

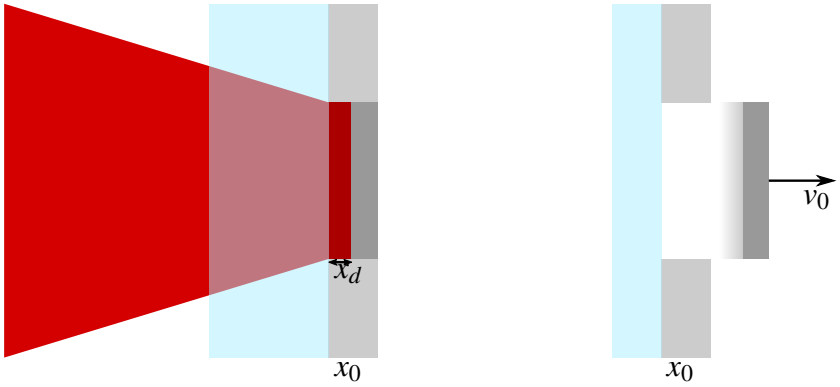

Figure 4.3 A laser vaporises material to a depth of x_d and launches a flyer of thickness $x_0 - x_d$ at a speed of v_0

To calculate the Gurney energy E it is assumed that energy is deposited following a Lambert Law exponential relationship as shown in Figure 4.4.

The Gurney energy E is then:

$$E = \frac{1}{x_d}\int_0^{x_d} [\varepsilon(x) - \varepsilon_d]\, dx = \underbrace{\frac{\varepsilon_0}{\rho\mu x_d}}_{\text{Total deposited energy}} - \underbrace{\varepsilon_d}_{\text{Vaporisation energy}} - \underbrace{\frac{\varepsilon_d}{\rho\mu x_d}}_{\text{Energy deposited beyond } x_d} \tag{4.3}$$

In the regime where the energy deposited is high compared to the vaporisation energy, and the blowoff distance x_d is small compared to the foil thickness x_0, the flyer velocity follows a square root relationship with the deposited energy:

$$v_0 = \sqrt{\frac{2\varepsilon_0}{\rho\mu x_0}} = \sqrt{\frac{2F_0(1-r)}{\rho x_0}} \tag{4.4}$$

where F_0 is the laser fluence and r is the fractional energy loss. r varies between materials and must be determined empirically with velocity measurements. Lawrence and Trott [159] tested this relationship using copper, magnesium and aluminium flyers, and were able to reliably predict the behaviour of flyers with a broad range of parameters.

4.3 Laser

The laser used in the flyer system is a Big Sky/Quantel CFR (Compact Folded Resonator) 400 mJ Nd:YAG lamp pumped pulsed laser with Q-switching. The key elements of the laser head are the flashlamp, the laser rod, and the Q-switch. The laser is powered by an Big

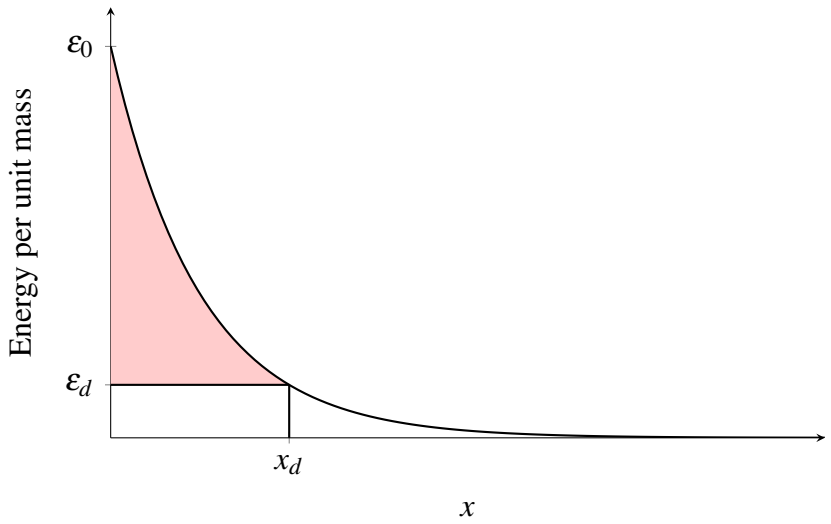

Figure 4.4 The energy is assumed to be deposited into the flyer material according to $\varepsilon(x) = \varepsilon_0 e^{-\mu\rho x}$. The blowoff depth x_d is the depth at which the deposited energy is equal to the vaporisation energy ε_d. The shaded area represents the energy per unit mass deposited into the material $x_d E$.

Sky/Quantel ICE (Integrated Cooler and Electronics) 450 power supply. The timings for the flashlamp and Q-switch can be externally controlled by TTL (Transistor-Transistor Logic) inputs and outputs to synchronise the laser pulse with the rest of the experiment.

4.3.1 Q-switching

The CFR400 uses a variable attenuator consisting of a polarising prism and a Pockels cell to control the optical resonator. A Pockels cell is a wave plate made of an electro-optic material. When a voltage is applied the birefringence of the material changes to produce a 90° rotation of the polarisation. This effect along with the polarising prism can be used to turn the lasing in the gain medium on and off. A Q-switched pulse can be formed by pumping the gain medium to saturation (maximum population inversion) with the resonator closed, then opening it using the Q-switch, increasing the quality factor of the resonator. A high power pulse is formed since the stored energy is released very quickly once optical feedback begins.

By directing the synchronisation outputs of the flashlamp and Q-switch triggers to an oscilloscope, it was possible to tune the Q-switch delay to the optimum value of 135 µs. When tested using this delay the maximum laser output was in excess of 350 mJ, easily sufficient for the laser flyer system.

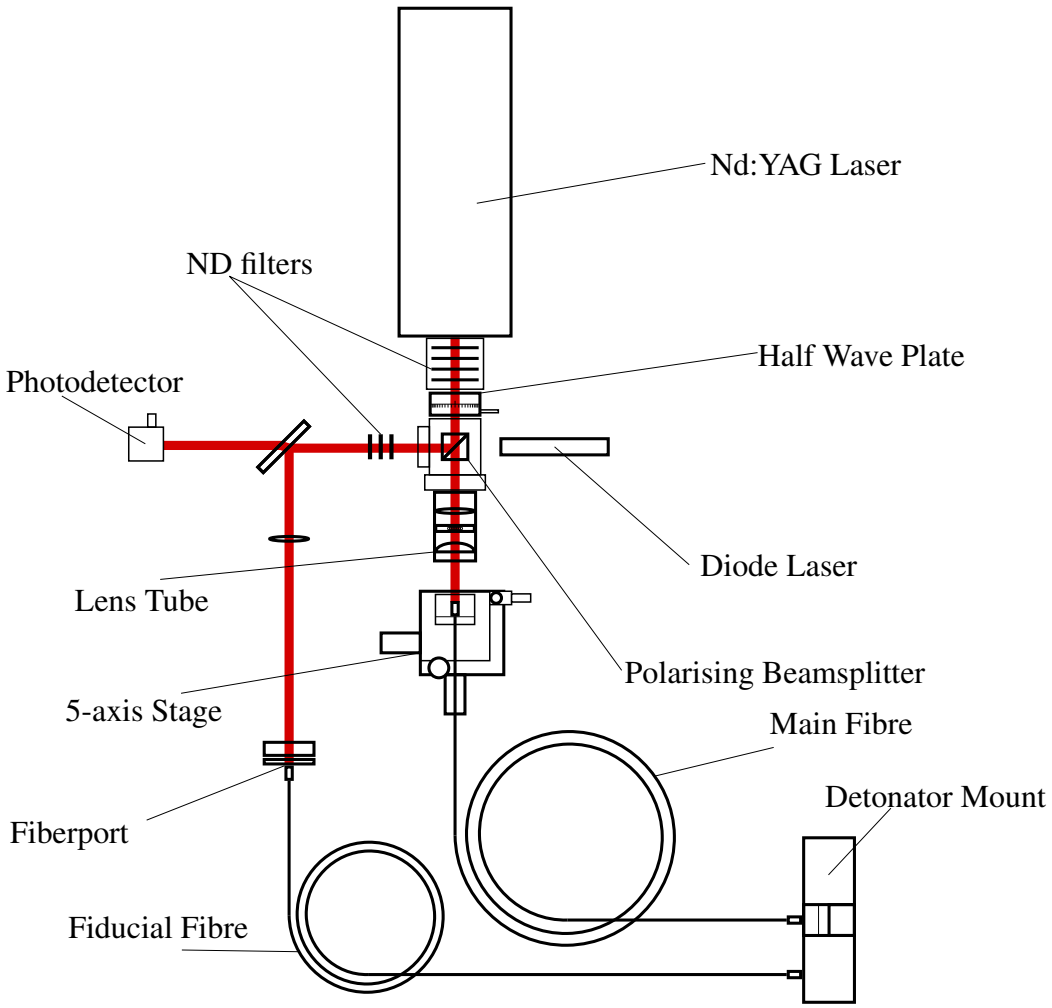

Figure 4.5 The full laser flyer system. All components were bolted to an aluminium breadboard to minimise travel. When firing, the system was enclosed with black aluminium panels to protect users from the risk of stray radiation.

4.4 Beam Forming

The laser pulses are passed through an optical fibre to deliver them to the coated substrate. This section describes the arrangement of optical components used to achieve this coupling. The full layout is shown in Figure 4.5. The main laser was bolted to the aluminium breadboard, and the other components aligned approximately along the optical path. Most components were mounted on Thorlabs posts and post holders to allow the height and position to be changed easily. Where it was important to have components more precisely aligned, for example the focusing lenses, a threaded lens tube was used. The two main elements of the beam forming system are the attenuation section, which reduces the beam's power and the focusing section, which couples it to the fibre.

4.4.1 Alignment Beam

A continuous wave 532 nm 0.9 mW laser diode (Thorlabs CPS532-C2) was used to align the optical components for safety and convenience. The laser was positioned at 90° to the main laser, and directed through the beam splitter so that it split and followed the same paths as the split beam from the main laser. Photographic Polaroid film was used as an alignment target since the main laser left a visible burn mark [94]. By using both paths and two different target locations on each path it ensures that the beam alignment is good. The diode laser was first aligned with the Nd:YAG laser using the four steps shown in Figure 4.6. Once the two beams were aligned, the main laser was turned off to complete the assembly of the system.

4.4.2 Beam Attenuation

Three methods can be used to reduce the energy of the laser beam. Firstly, adjusting the voltage supplied by the power supply to the laser head directly affects the pulse energy. This method was not used due to possible side effects on the spatial profile of the beam. Secondly, neutral density (ND) filters placed immediately after the laser output were used to reduce the light intensity to levels that avoid damage to optical components. Using this method only allowed for step changes in intensity based on the number and strength of the filters placed on the beam line The pulse energy could be continuously varied using a half-wave plate and polarising beam splitter placed immediately after the ND filters [94]. A half wave plate is a disc of birefringent material such that it introduces a phase shift of π between the fast and slow polarisation components of the laser. The phase shift has the effect of inverting the polarisation axis around the wave plate fast axis.

In the (x,y) lab coordinate system, the initial laser polarisation can be described by components $(\cos(\phi),\sin(\phi))$. If the fast axis of the half-wave plate is at angle θ to the x axis then the effect of its Jones matrix on the polarisation vector is:

$$e^{-\frac{i\pi}{2}}\begin{pmatrix}\cos(2\theta) & \sin(2\theta)\\ \sin(2\theta) & -\cos(2\theta)\end{pmatrix}\begin{pmatrix}\cos(\phi)\\ \sin(\phi)\end{pmatrix} = e^{-\frac{i\pi}{2}}\begin{pmatrix}\cos(2\theta-\phi)\\ \sin(2\theta-\phi)\end{pmatrix} \tag{4.5}$$

A polarising beam splitter then separates these two components. The primary beam line takes the p-polarised component which is parallel to the splitter plane and the secondary beam line takes the s-polarised component which is perpendicular (senkrecht) to the splitter plane. The primary beam is coupled into a fibre and used to launch the flyer plates, while the secondary beam is used for all accessory functions, including diagnostics and producing a fiducial beam for streak photography.

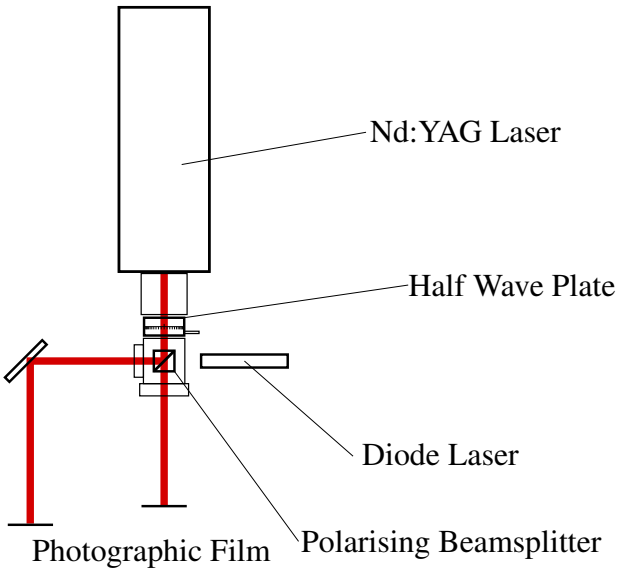

(a) The main laser was fired at a high energy to produce burn marks on pieces of photographic film placed along the primary and secondary beams

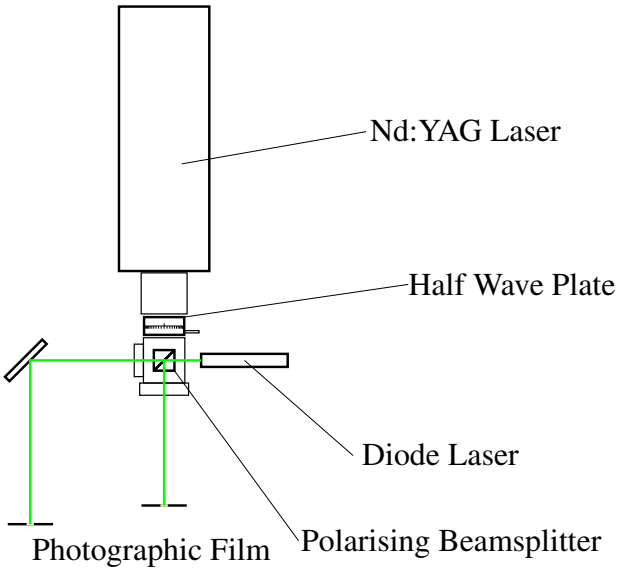

(b) The diode laser was coarsely positioned so that the laser spot coincided with the two burn marks

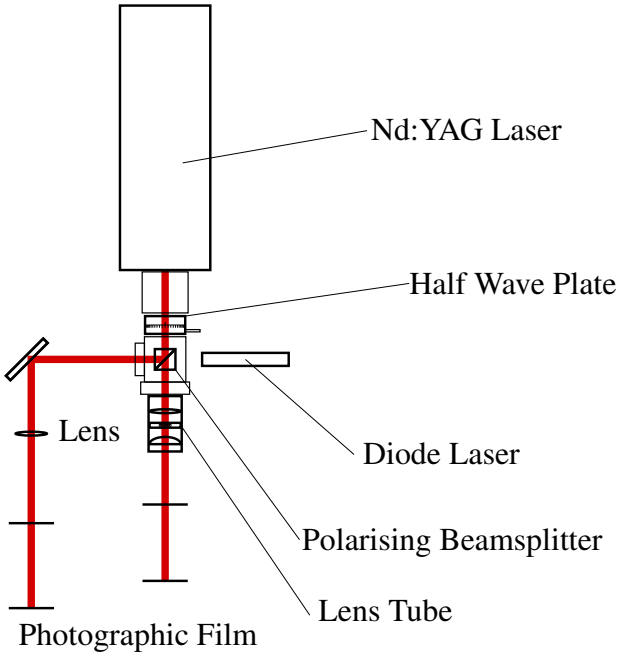

(c) Lenses were placed along the primary and secondary beam to focus them. Several high power pulses were fired to burn holes in the photographic film and produce smaller marks on more pieces of film placed further back

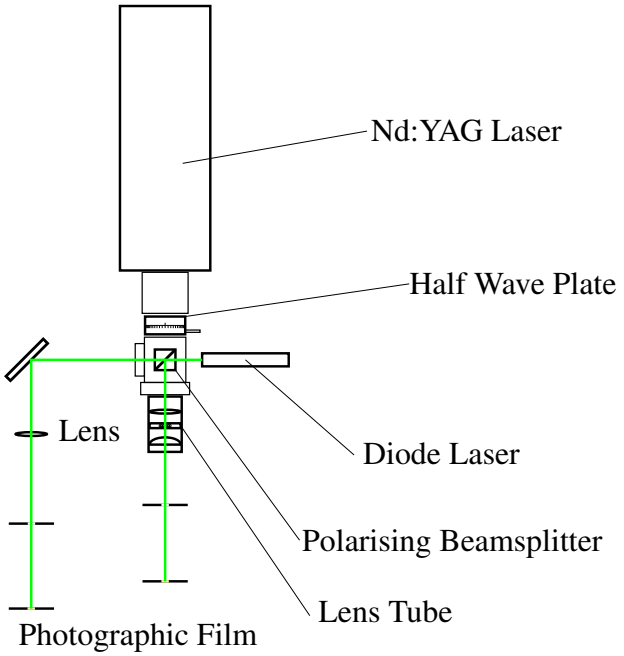

(d) The diode laser was finely positioned so that the laser spot passed through the holes and aligned with the smaller marks

Figure 4.6 The four stage process of aligning the diode laser with the Nd:YAG laser

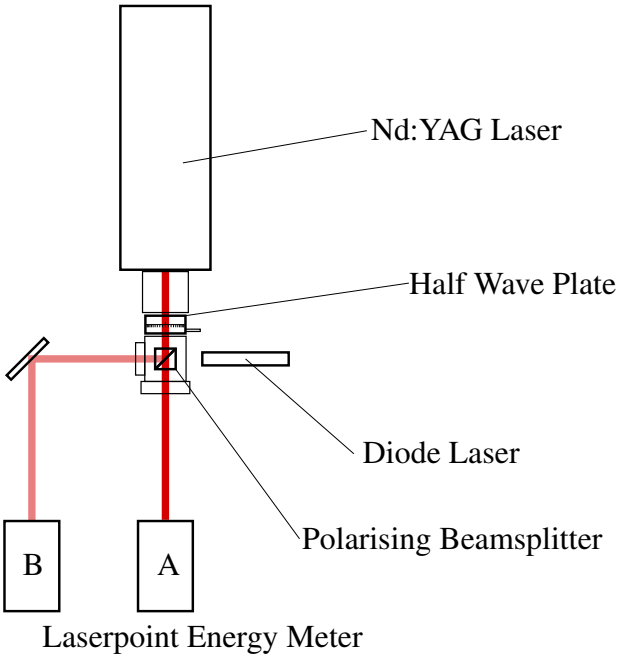

Figure 4.7 The laserpoint energy detector was placed at position A while the waveplate was rotated incrementally through 180°. A beam block was used to terminate the beam not being measured

Combining the initial beam polarisation ϕ, the offset between the wave plate and the graduated rotation axis, and any possible misalignment of the beamsplitter into one constant δ, the output energy of the primary beam line can be fitted to:

$$E_1 = E_0 \cos^2(2\theta - \delta) \tag{4.6}$$

and the secondary beam line to:

$$E_2 = \alpha E_0 \sin^2(2\theta - \delta) \tag{4.7}$$

where α encompasses the additional energy losses incurred by reflection off the mirror and transmission through the lens.

A Laserpoint 10-BB detector and PLUS energy meter were used to measure the pulse energies for the primary and secondary beams over a range of half-wave plate angles. The detector head was placed at positions A and B as shown in Figure 4.7, and the energy reading recorded for 2° intervals between 0° and 180°.

The data is shown in Figure 4.8. Fitting to Equation (4.6) and Equation (4.7) gives E_0 =245.5(5) mJ, δ =−62.8(1)° and α =0.877(3).

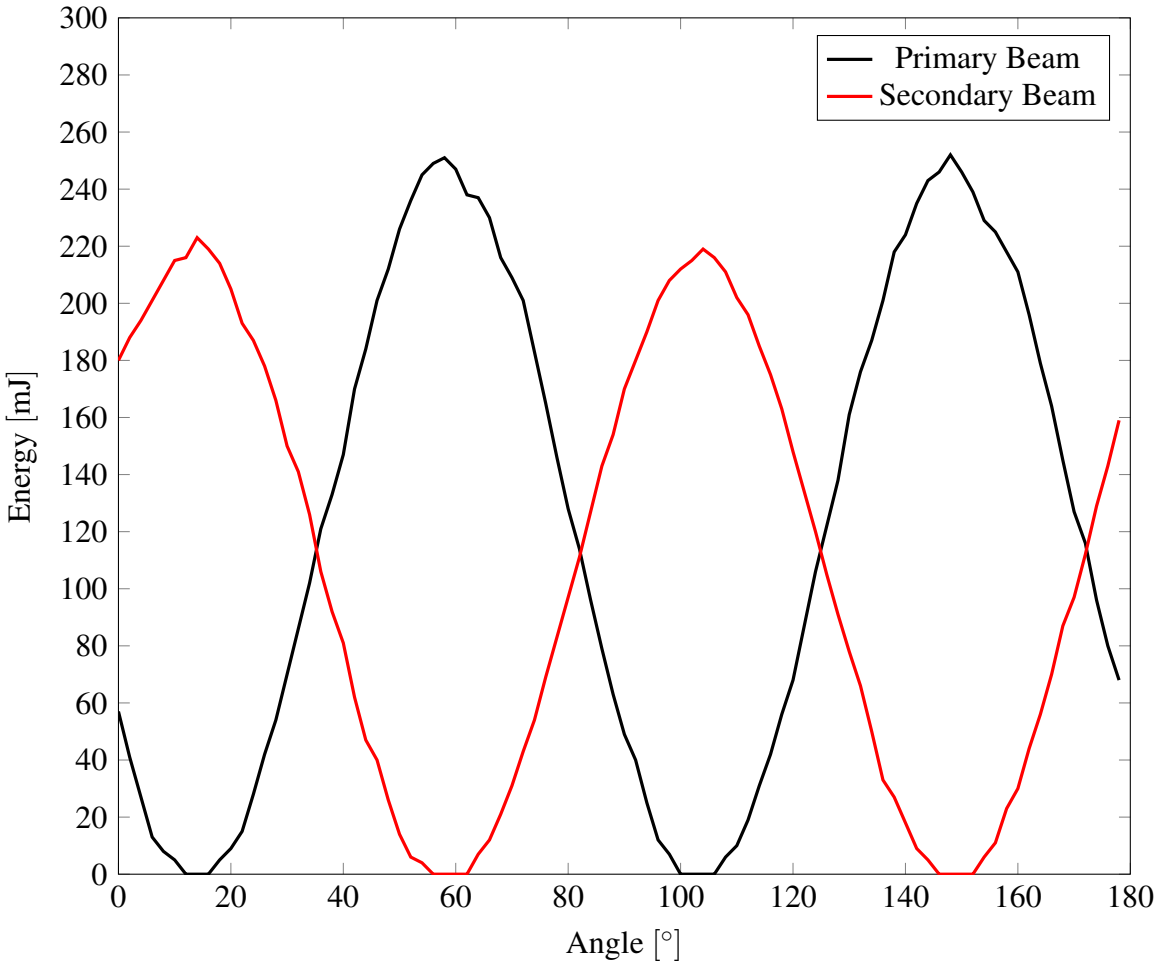

Figure 4.8 The effect of rotating the wave plate on the beam energies. Since the energy meter does not trigger for energies less than 4 mJ, these are recorded as 0 mJ

Errors

The rotation stage for the half-wave plate is subject to reading error, with a corresponding angular error. The reading error in aligning the graduated scale is assumed to be half the width of each graduation (250 µm). Since the error in the stage radius R =49.0 mm is negligible, $\delta\theta = \frac{\delta x}{R}$, meaning the angular error in each measurement is about 0.3°.

The energy meter has a resolution of 1 mJ, and there is also a calibration error which Laserpoint quote as ±5 %. Assuming these are the only errors, the combined error for a single energy measurement is:

$$\delta E = \sqrt{(0.05E)\,2 + (0.5mJ)^2} \tag{4.8}$$

For all but the smallest energies the error is dominated by the calibration error.

When using the beam attenuator to choose an energy in conjunction with Equation (4.6) and Equation (4.7) the error in the coefficients and the error in the chosen angle must be considered. It can be shown that the error in the angle measurement is the largest source of error, giving a total error of approximately (with θ and δ in radians):

$$\delta E_{1,(2)} = 2\,(\alpha)\,E_0\,|\sin(4\theta - 2\delta)|\,\delta\theta \tag{4.9}$$

This equation has a straightforward interpretation – the errors are greatest when the sensitivity of the energy to angle is greatest.

In the region of interest this corresponds to errors of around ±1 mJ.

4.4.3 Beam Focusing

In order to couple the attenuated primary beam into an optical fibre it is necessary to produce a tightly focused spot which can be finely adjusted to line up with the fibre surface. It is also desirable to homogenise the spatial profile to reduce the chance of optical damage caused by localised regions of high energy fluence, and to produce uniform flyers. A ⌀1″ lens tube (Thorlabs SM1L20) placed after the polarising beam splitter contained 3 components to focus and homogenise the beam, as shown in Figure 4.9. The microlens produces multiple images, which are then focused to a single spot by the aspheric lens [152].

Aligning the end of the fibre with the focal spot of the primary lens was done with a five axis translator, capable of moving the fibre in the x, y, and z directions, as well as adjusting the pitch and yaw. The fibre mount was first positioned approximately using the alignment laser, which was then turned off for the fine adjustment. The end of a spare fibre ferrule was painted black, and the energy of the primary beam tuned such that it just left a mark on the

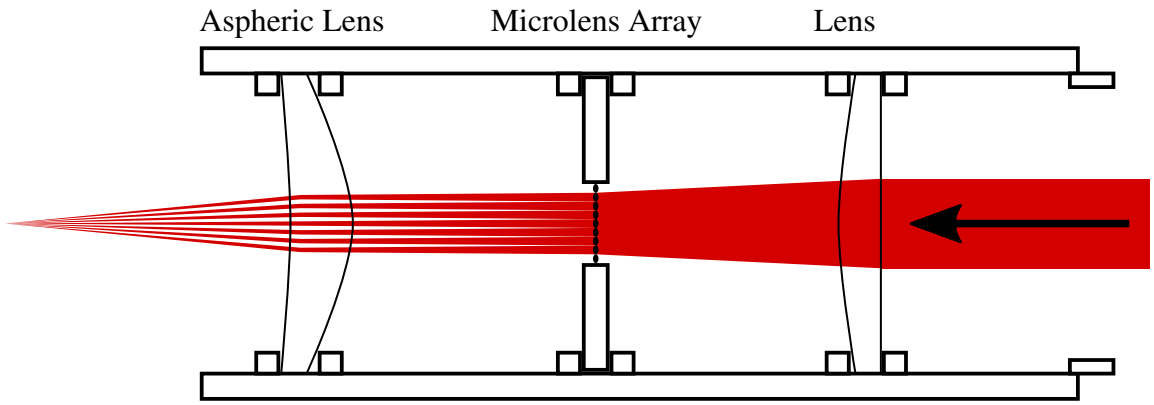

Figure 4.9 The lens tube contains a lens, a microlens array (Thorlabs MLA150-5C-M), and an aspheric lens (Thorlabs AL2520-C). Each lens is held in place with a pair of retaining rings (Thorlabs SM1RR)

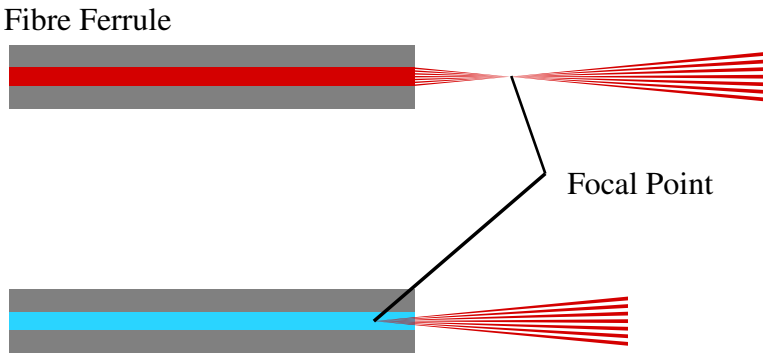

Figure 4.10 The beam is focused outside the fibre, and diverges into it. If the beam focuses inside the fibre the risk of optical damage is greatly increased.

painted surface. The stage was then adjusted to move the fibre face closer to the focal point. This process was repeated, repainting the ferrule each time, until the spot was central and as small as possible. The painted fibre was then replaced with the unpainted one. The third step in the alignment process was to make very fine adjustments using the main fibre and a Thorlabs pyroelectric energy meter. The laser frequency was set to 1 Hz and the energy reading monitored. The stage was adjusted along all five axes to maximise the transmitted energy.

The fibre face was shifted slightly past the point of maximum energy in the z direction; this is beneficial as it avoids the beam focusing inside the fibre and potentially causing optical damage – see Figure 4.10. The energy densities required to launch flyers are close to energy densities that cause optical damage. Focusing outside the fibre does however reduce the transmitted energy since some higher order modes are lost [152].

An important parameter of an optical fibre is the numerical aperture (NA), which is defined (for a fibre in air/vacuum) by $NA = \sin(\alpha)$ for acceptance angle α: the largest angle that light can be accepted and totally internally reflected. Having a high NA increases the amount of light that can be coupled into the fibre, however it also requires a higher core refractive index which can cause greater scattering losses. The main fibre has a numerical aperture of 0.22, corresponding to an acceptance angle of 12.7°.

4.5 Beam Diagnostics

A suite of diagnostics were used on the secondary beam to analyse the pulses delivered to the coated substrate. It is assumed that the only difference between the primary and secondary beam is the polarisation direction, and therefore that they have the same spatial and temporal profiles. The energy of the secondary beam was attenuated using ND filters, as these diagnostics are very sensitive and easily damaged. The use of the secondary beam for diagnostic purposes was used by Frank and Trott [153] in their laser flyer system.

4.5.1 Spatial Profile

The spatial profile of the beam is an important characteristic since it ultimately determines the shape of the flyer produced. If there are hot spots in the beam these can cause corresponding points of plasma breakthrough, which leads to the flyer breaking apart prematurely [161]. It is also important to know the spatial profile of the beam before it enters the fibre, since hot spots here can lead to optical damage. The optimal spatial profile for the beam is a top-hat function, since the desired flyer shape is flat and uniform.

A figure-of-merit used in beam profile analysis is the M^2 parameter, or beam quality factor [162]. The M^2 parameter is a measure of how tightly the beam can be focused relative to a zero order mode Gaussian beam profile. In terms of the divergence Θ_σ of the beam and the divergence $\Theta_{\sigma 0}$ of the ideal Gaussian beam:

$$M^2 = \frac{\Theta_\sigma}{\Theta_{\sigma 0}} = \frac{\pi}{\lambda}\frac{d_{\sigma 0}}{\Theta_\sigma}4 \tag{4.10}$$

The M^2 value can be calculated in practice by measuring beam profiles at several different axial locations as shown in Figure 4.11. The data obtained are fitted to the hyperbolic function:

$$d_\sigma(z) = \sqrt{a + bz + cz^2} \tag{4.11}$$

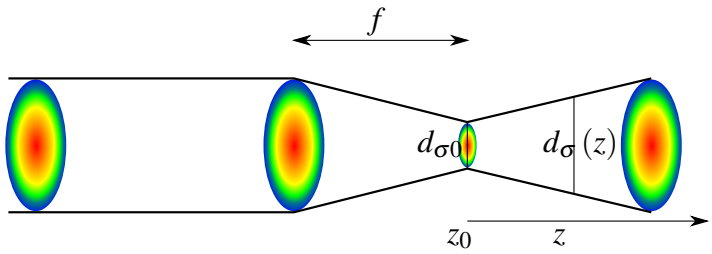

Figure 4.11 By taking measurements of the 4σ beam width at several locations and fitting the results to Equation (4.11) it is possible to obtain the value of M^2, as well as the minimum waist size possible

where $d_\sigma(z)$ is the width measured at axial position z, $d_{\sigma 0}$ is the width of the focal spot and z_0 its position. The widths in this equation are defined as 4 standard deviations in intensity. More details of measuring the beam widths and calculating M^2 are given in Appendix A.

A DataRay WinCamD CCD (Charge Coupled Device) camera was used with its accompanying software to analyse the beam. The software can be used to produce heat maps of the beam and calculate its width. The camera sensor consists of an array of photoactive capacitors which are charged when exposed to light. The capacitors then sequentially discharge and the resulting signal is decoded to form the image of light intensity. An example of such an intensity image is shown in Figure 4.12.

4.5.2 Temporal Profile

A high speed battery biased InGaAs (Indium Gallium Arsenide) photodetector (Newport 818-BB-30) connected to an oscilloscope was used to measure the temporal profile of the pulse. Due to its high sensitivity the photodetector was placed behind a mirror on the secondary beam in order to capture the small portion of light transmitted through. The rise time of the detector is quoted as $<$175 ps. The temporal profile is shown in Figure 4.13. The FWHM of the pulse is 28.5 ns, although this may be a slight overestimate due to the rise time of the detector.

This profile is less symmetric than lasers used by other authors [94], however the rise time is the important feature for launching flyers – this parameter is similar to other works. The extended tail results in a feature seen on streak records as shown later in the chapter.

4.6 Fibre Delivery

The primary beam was delivered to the target assembly using a 2 m long, ⌀550 µm high power optical patch fibre (Thorlabs FG550LEC). There are several advantages of fibre delivery over focusing directly onto the flyer. Firstly, separating the flyer system from the target mitigates any

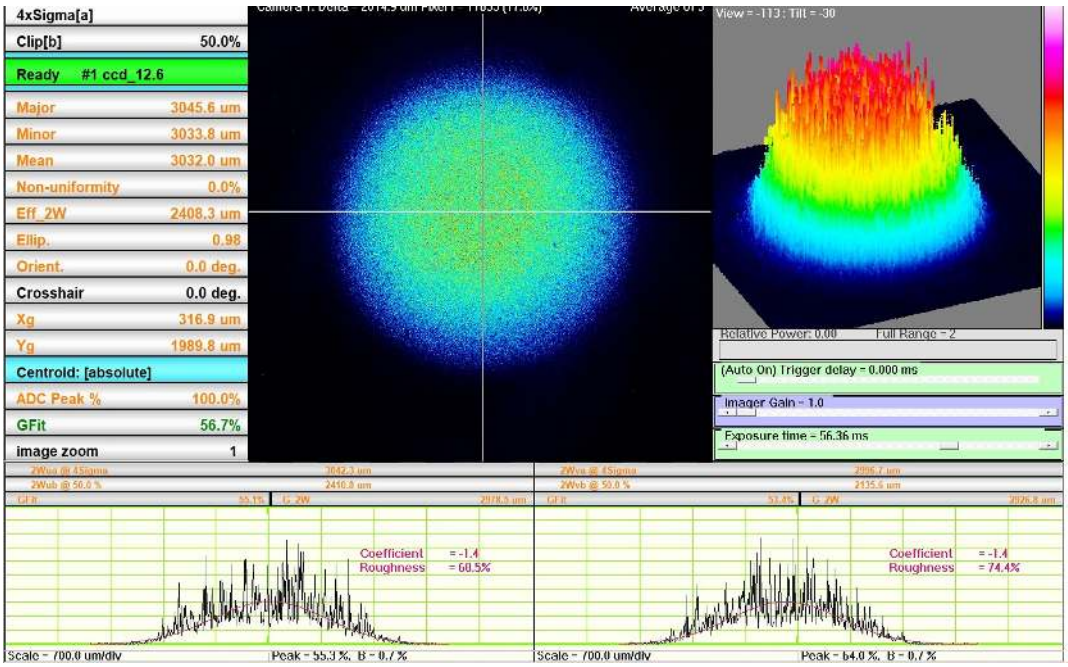

Figure 4.12 The spatial profile of the laser beam as measured using a CCD camera. The profile has good symmetry in the x and y directions with no obvious hot or cold spots. There is some shot noise which causes the spikiness of the profile at higher intensities.

chance of the explosive output damaging optical components. Secondly, by having 2 m long fibre, the front of the pulse cannot reflect from the surface of the flyer and back propagate to interfere with the end of the same pulse. This interference could potentially cause a reduction in the pulse energy and distortion of the beam profile [94]. The pulse intensity peaks after 14 ns and the fibre introduces an extra 10 ns delay each way (the refractive index is about 1.45) so the pulse has been fully formed by the time the reflected pulse returns to the laser. Finally, passing the pulse through a fibre improves the spatial profile by the process of optical smoothing. Zhao et al. [163] also reported that fibre delivery resulted in a more top-hat beam profile resulting in better flyer integrity.

4.6.1 Optical Smoothing

The incident laser beam has high spatial coherence, which means that the irregularities in the beam profile persist over a long distance. A dispersive element such as an optical fibre can be used to destroy this spatial coherence [164]. Light entering a fibre of length L at an angle θ will travel a path length of $Ln/\cos(\theta_r)$ where θ_r is the angle of refraction with $\sin(\theta) = n\sin(\theta_r)$.

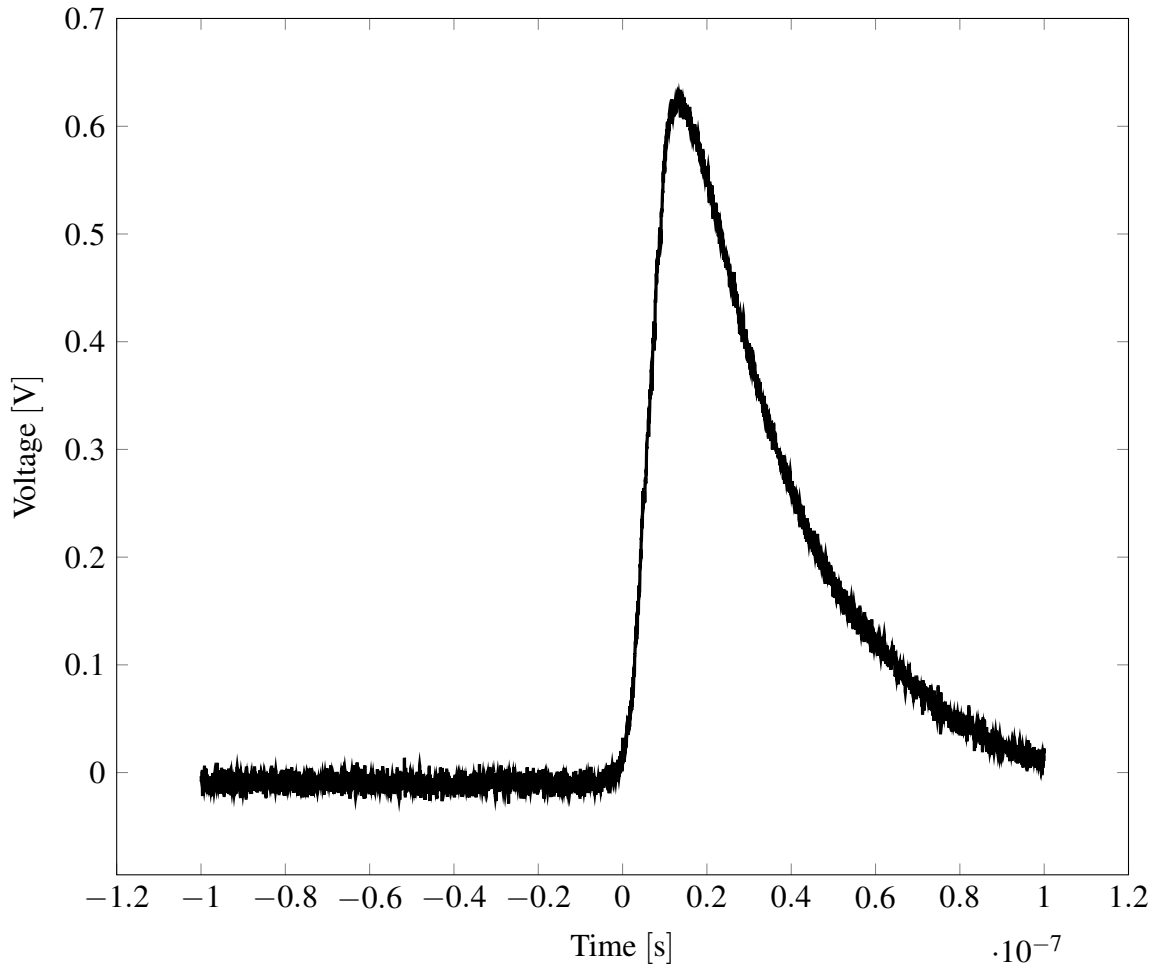

Figure 4.13 The temporal profile of the laser pulse as measured using a photodetector. The intensity rises to its maximum over approximately 14 ns, and then falls back to baseline over about 100 ns

The delay relative to direct transmission is therefore for small angles:

$$\Delta t = \frac{Ln}{c\cos(\theta_r)} - \frac{Ln}{c} \simeq \frac{L\theta^2}{2nc} \tag{4.12}$$

Using the 2 m fibre with a numerical aperture of 0.22 the time delay is ∼100 ps. Since the coherence length of the laser is ∼10 mm, the time delay introduced by the fibre is sufficient to exceed the coherence time.

Even better optical smoothing can be achieved when the fibre carries a 360° loop [149] due to the energy being more distributed throughout the fibre volume. The fibre used in this system was looped twice.

4.6.2 Energy Loss

There is an energy loss associated with passing the beam through the optical fibre. A Thorlabs pyroelectric sensor in conjunction with an energy meter console (Thorlabs PM100D) was used to measure the energy before entering and after emerging from the fibre. The results are shown in Figure 4.14. Transmission through the fibre results in a 50 % energy loss. Bowden [152] tested a wide range of fibre configurations, including tapered fibres and different polishing methods, reporting a range of transmissions from 31 % to 86 %. The efficiencies were not strongly correlated to fibre length, but were highly dependent on the nature of the input and output faces. A high fibre transmission is useful but not essential, since laser energy can be increased to meet the launch criteria – however, using a higher energy may result in optical damage which can in turn reduce the efficiency.

4.6.3 Beam Divergence

Upon exiting the fibre the laser beam diverges. To quantify this the WinCamD beam profiler was used to measure beam profiles at ten positions a distance away from the fibre end face. The z =0 point does not mark the end face but the closest it was physically possible to place the camera to the end face (about 1 cm) due to the various mounts and the camera's protective ND filter. Five laser pulses were fired at each position and the average profile recorded. Beam diameters were then calculated using the methods in Appendix A. The beam diameters and divergence are shown in Figure 4.15.

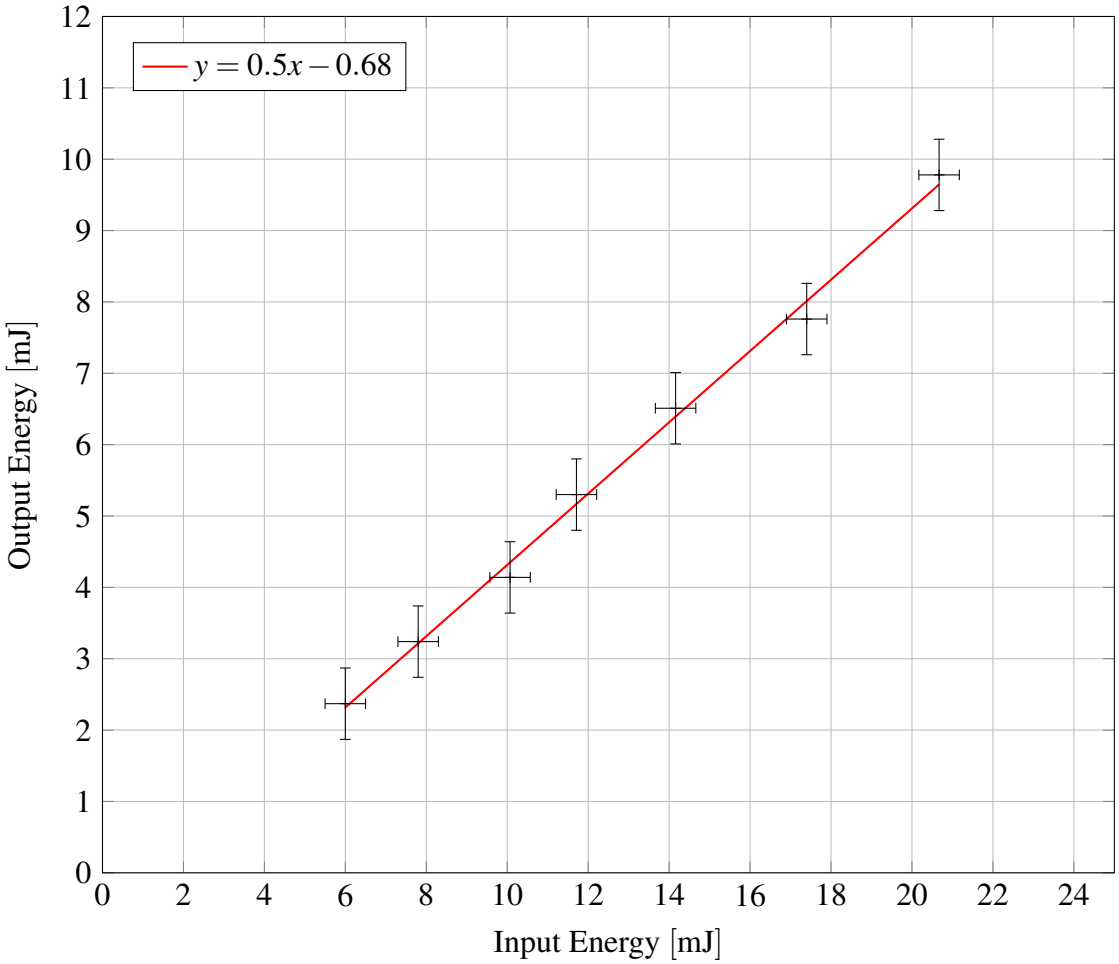

Figure 4.14 The transmission of energy through the optical fibre. Approximately 50 % of the energy is transmitted. A linear relationship produces a reasonable fit over this range of energies – at higher energies damage mechanisms mean this may not be the case.

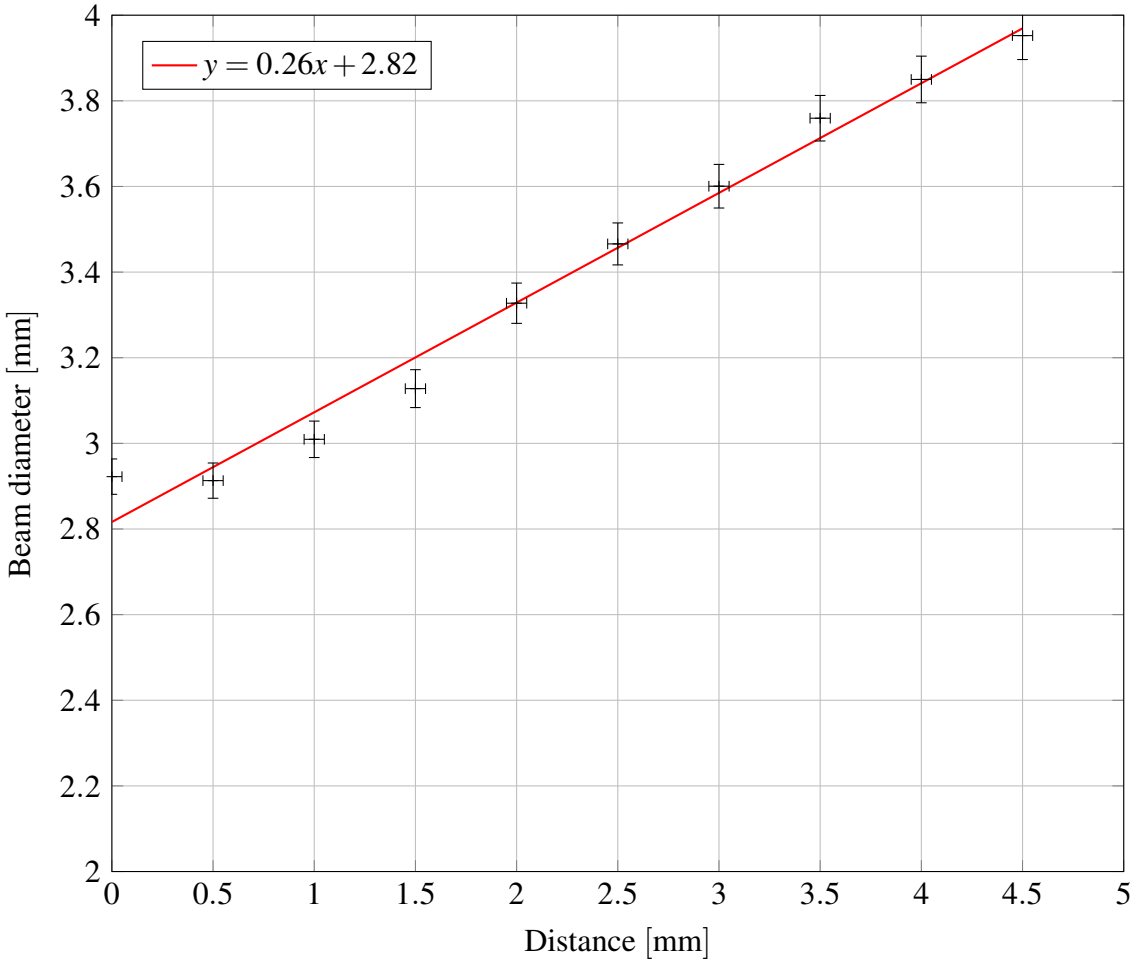

Figure 4.15 The diameter of the beam emerging from the fibre. The 0 mm distance is about 1 cm from the fibre end face due to the physical constraints of the experiment. The divergence angle was calculated as 14.8°. The upper limit on beam divergence due to the fibre's numerical aperture would be 25.4°.

4.6.4 Optical Damage

All of the optical components in the system can potentially be damaged due to the high power fluxes caused by focusing the laser beam. The most susceptible point is the entry face of the primary fibre. Allison et al. [165] described two possible damage modes to fused silica optical fibres: damage to the input surface due to over-focusing; and linear longitudinal fractures just inside the fibre caused by non-uniformity or misalignment. Trott and Meeks [149] reported that a ⌀400 µm core fibre could transmit a 25 ns pulse of 97 mJ 1064 nm light. Scaling this to a 10 ns pulse through a ⌀550 µm core fibre as used in this system gives a safe transmission energy of 76 mJ. Bowden [152] found a fluence of 20 $J\,cm^{-2}$ was required to launch flyers, which, with a ⌀550 µm fibre corresponds to a pulse energy of 48 mJ.

4.6.5 Fibre Polishing

The output end of the fibre needed polishing between experiments due to mechanical damage from the explosive. The ferrule was also damaged and so was replaced each time. After each experiment, the damaged ferrule was cut off, and the fibre buffer removed using a stripping tool (Thorlabs T28S46). The end of the fibre was inserted into an SMA ferrule connector (Thorlabs 10640A) and fixed in place using epoxy. Once the epoxy had dried the excess fibre was cleaved off, and the end of the fibre was polished in a two step process. Using a polishing disc (Thorlabs D50-SMA) to keep the surface flat and level, the fibre was first polished using a 3 µm grit aluminium oxide lapping sheet (Thorlabs LF3P) and then a 0.3 µm grit calcined alumina sheet (Thorlabs LF03P). The polishing disc was moved by hand in a figure-of-eight pattern over the wetted polishing sheets, with regular inspection of the end face.

4.7 Flyer

Shock properties such as strength, duration and rise time are dependent on the structure of the flyer plate. A single layer flyer suffers from the need for the material to perform several different roles and therefore cannot be optimal for all of them. Flyers with multiple layers can have each layer optimised for the individual application. A schematic of a multi-layer flyer is shown in Figure 4.16.

The role of each layer is:

- (a) The absorption layer maximises efficient conversion of laser energy to heat by minimising reflection. Carbon and titanium are good materials for this layer: the former due to its very low reflectivity and the latter due to its low vaporisation energy.

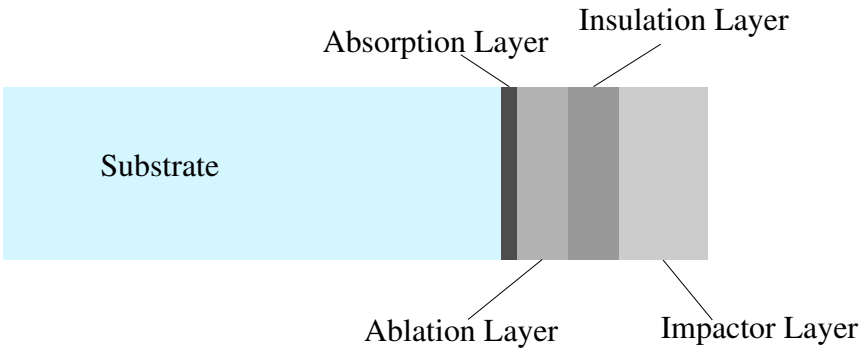

Figure 4.16 A flyer with multiple layers designed for optimal performance [166] – not to scale.

- (b) The ablation layer is converted to plasma by the increase in temperature. Good ablation materials therefore have a low vaporisation energy, but also good thermal diffusivity so the temperature increases across the layer. Magnesium and germanium exhibit better properties relative to aluminium [166].
- (c) The insulation layer protects the impactor layer from the ablating plasma to improve flyer uniformity and efficiency [148]. Typically this is a metal oxide such as alumina.
- (d) The impactor layer determines the shape and strength of the shock. Low density materials such as aluminium generate higher pressures for a given laser fluence since they are less dense and therefore accelerate to a higher velocity. Even though aluminium has a lower shock impedance than denser materials such as copper, the greater velocity results in a stronger shock.

The flyers used were predominantly composites consisting of several deposited layers of varying metals and thicknesses.

The coated substrate was held in front of the fibre exit face by a PMMA washer as shown in Figure 4.17.

4.8 Streak Photography

A Cordin digital streak camera was used to verify the planarity and velocity of the laser flyers. The camera was positioned facing the back of the detonator mount, and the slit position adjusted to line up with the main and fiducial beams. The flyers were fired into a glass window inside the charge cavity of the detonator mount and along the path of the flyer. The glass window was held within a PMMA cylinder slightly off axis so the same window could be used for multiple shots simply by rotating as shown in Figure 4.18.

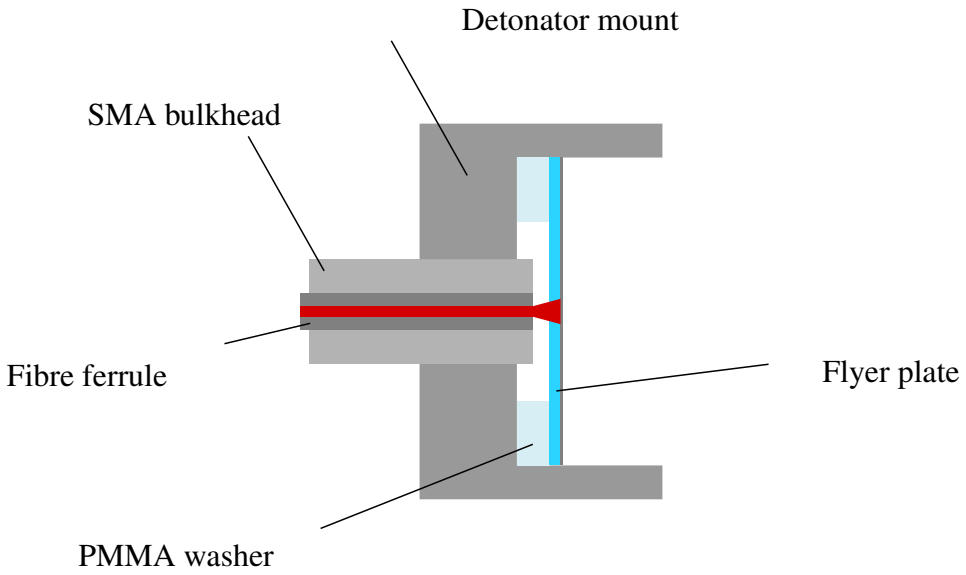

Figure 4.17 The optical fibre is held by an SMA bulkhead inserted into the detonator mount. A PMMA washer separates the end of the fibre ferrule from the coated substrate.

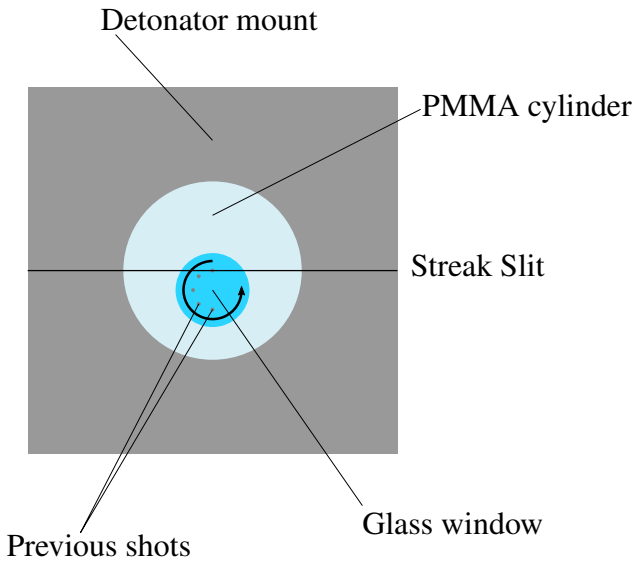

Figure 4.18 By rotating the glass window in its PMMA holder, multiple shots can be fired onto the same window. This procedure avoids the need to replace the window each time so ensures the stand-off distance does not change.

The flyer travels for a certain distance, the stand-off distance, before impacting into the glass window. The impact releases a flash of light which is observed on the streak record. The average velocity over this distance can be calculated from the stand-off distance and the time between the fiducial mark and the impact mark. This calculation makes two assumptions:

- The flyer plate is launched simultaneously with the arrival of the fiducial beam
- The impact flash coincides with the moment of impact.

Using calculations based on these assumptions produces results similar to previous work [166] [161]. While this does not give a complete velocity history it was justified on the basis that the acceleration phase is likely to be brief, followed by a relatively long period of approximately constant velocity [161].

In order to capture the image, the laser and camera must be triggered with precise timings. In particular the camera must be triggered slightly before the laser pulse is formed, since there is an in-built delay which cannot be changed between triggering and image capture. A delay generator is used to control the sequence. Initially the camera was triggered off the flashlamp, with the Q-switch triggered internally by the laser, however this method had too much intrinsic jitter so the firing event was not always captured on the streak record. The solution was to trigger the flashlamp from the delay generator, and then return the output signal from the laser to the delay generator. This signal could then trigger the camera and Q-switching with minimal jitter. The sequence of operations in the triggering process is shown schematically in Figure 4.19.

4.8.1 Fiducial Beam

A fiducial beam was produced from the secondary beam line using a Thorlabs fiberport (PAF2S-11C) to couple light into a 2 m long, 200 µm diameter fibre (Thorlabs M38L02). The fiberport had an anti-reflective coating tailored to the wavelength of the light (1064 nm). The energy of the beam was attenuated to very low levels with a 0.001 transmission coefficient ND filter to avoid damaging the fibre or camera CCD. The purpose of the fiducial beam is to mark the $t = 0$ position on the streak record at the point in time at which the laser light reaches the end of the fibres. Later features due to flyer impacts or breakup can then be assigned a time coordinate. The two optical paths are sufficiently similar in length that the laser pulse arrives at the end of each fibre at the same time; a streak record taken without a flyer (and with the main beam heavily attenuated) verified this assumption.

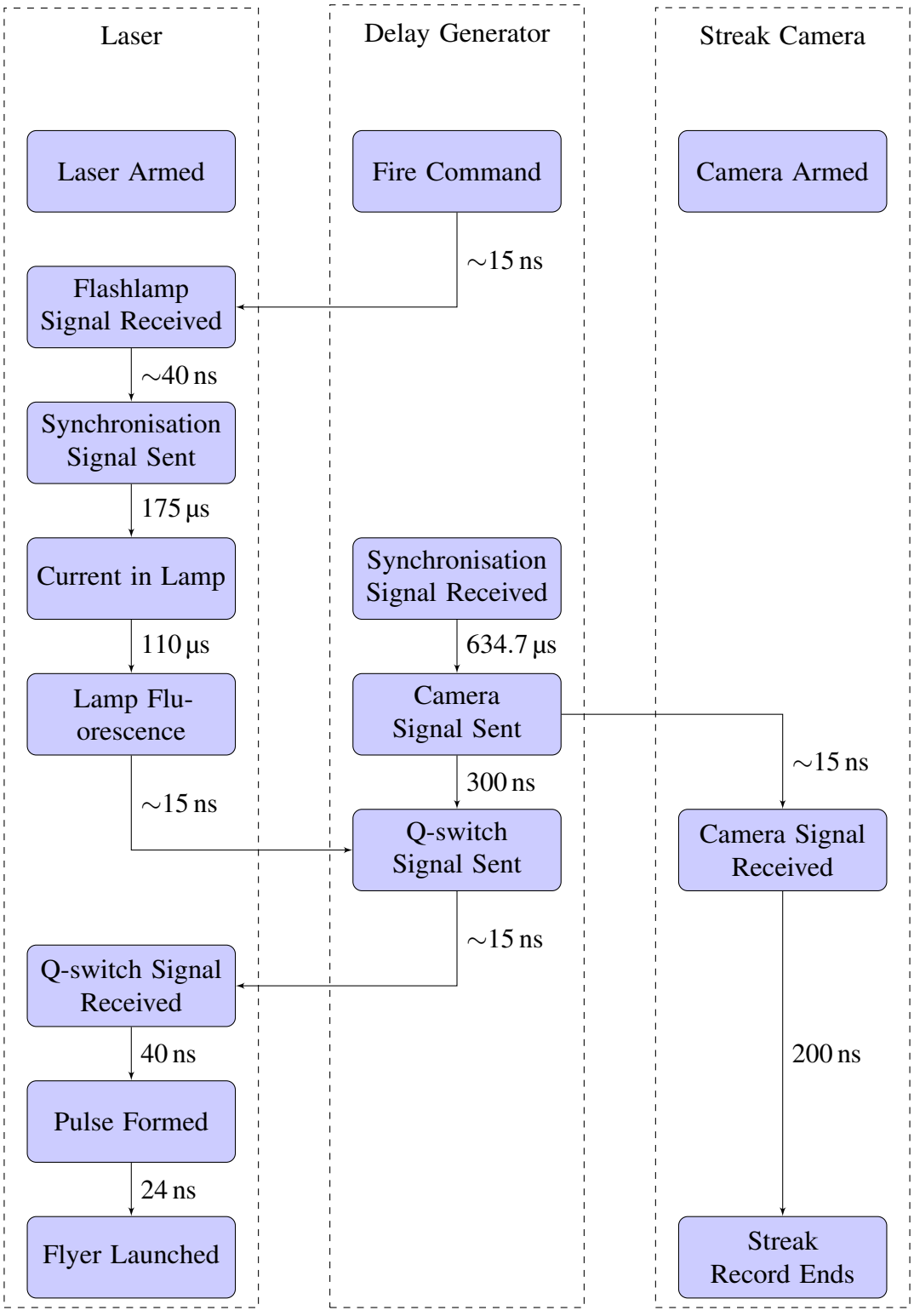

Figure 4.19 Schematic of the triggering sequence for the streak camera. The coaxial cable between the three main components introduces a delay of a few nanoseconds since the signal travels at $\frac{2c}{3}$

4.8.2 Results

An example of a 200 ns streak record is shown in Figure 4.20. The flight time is calculated from the temporal separation between the fiducial mark and the impact mark. The stand-off distance was measured using a micrometer as 170(7) µm. Velocities were calculated for a range of launch energies – the results are shown in Figure 4.21. The streak images all indicated high flyer planarity since the impact time was consistent across the width of the flyer to within around 2 ns. There was also good flyer integrity as shown by the lack of any plasma leaking through before impact. This performance is likely due to the presence of the insulation layer.

Watson and Field [161] imaged flyers with poor integrity and observed plasma penetration and a high degree of curvature – see Figure 4.22.

4.8.3 Errors

Sources of uncertainty in the velocity measurement arise from uncertainty in the stand-off distance and the time coordinates of features on the streak record. The stand-off distance was measured differentially using a micrometer – each reading has a 5 µm error. The error in the flight time is harder to calculate owing to the difficulty in determining the point of impact. The time was calculated as the separation between the midpoint of the fiducial mark and the first inflection point of the intensity profile averaged over the flyer width. This method results in a 3 ns error in the flight time.

The energies were varied using the half wave plate, therefore the errors in the energies can be calculated using Equation (4.9).

The errors in the velocities and energies are shown in Figure 4.21.

4.9 Exploding Foil Initiator (EFI) System

For ease of experimentation and producing meaningful comparisons the laser flyer system was designed to be interchangeable with a exploding foil initiator (EFI) system. The main components in this system are the EFI itself (the slapper), a capacitor bank to generate the necessary high voltage, and a remote firing unit to charge the capacitor bank and trigger the discharge.

4.9.1 Firing System

A firing system consisting of a capacitor bank and remote firing unit was used to fire the slapper detonators. The capacitor bank has a total capacitance of 5 µF and an inductance of 50 mH, and

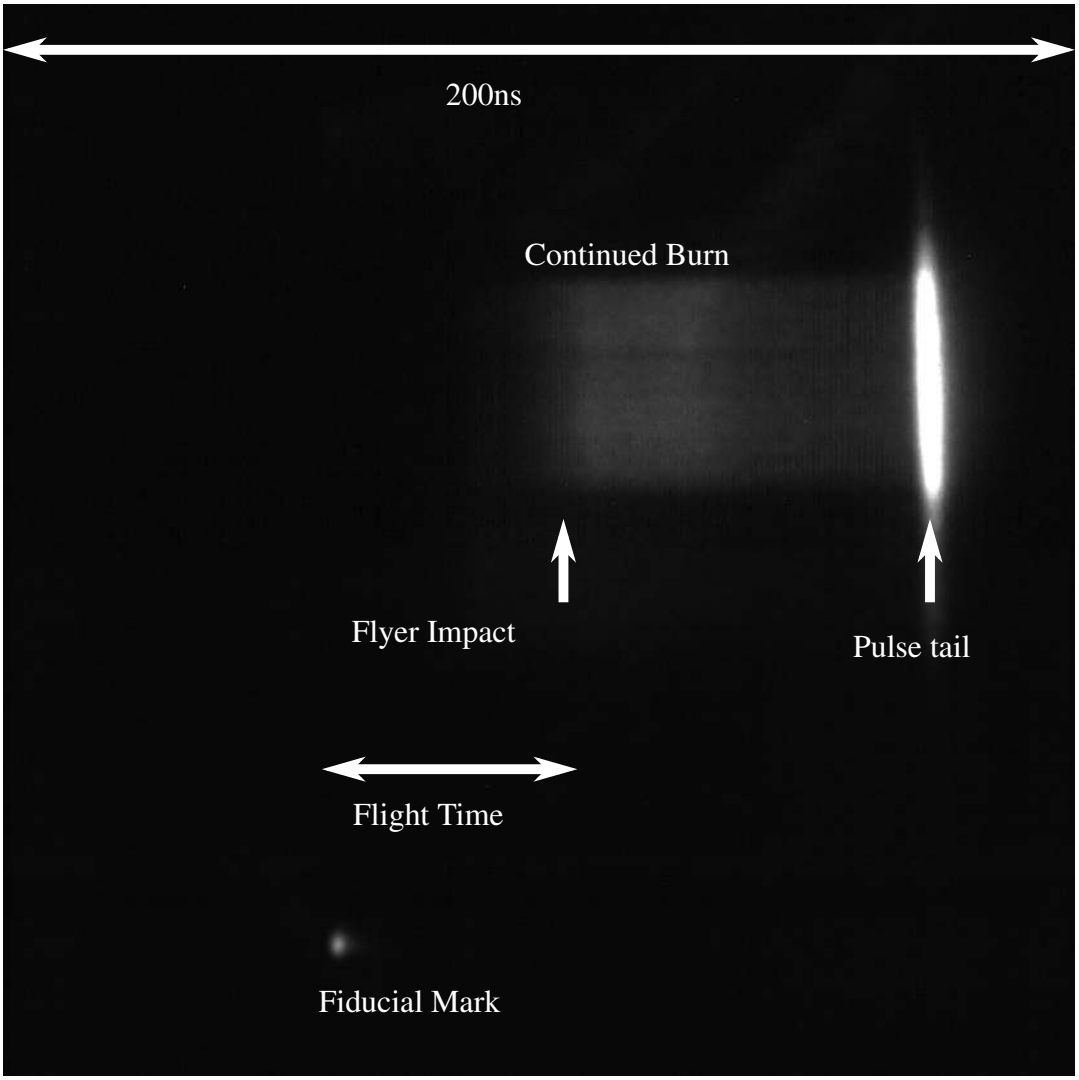

Figure 4.20 An example of a streak record of a laser flyer launch and impact. The flyer is assumed to launch at the same temporal coordinate as the fiducial mark. When it hits the window, some light is released. The flyer continues to burn on the window and emit light – the intensity decreases over time. When the flyer burns up completely, a bright mark is seen due to the tail end of the pulse no longer being occluded by the flyer. At higher energies there are also diagonal marks due to plasma escaping around the edges of the flyer.

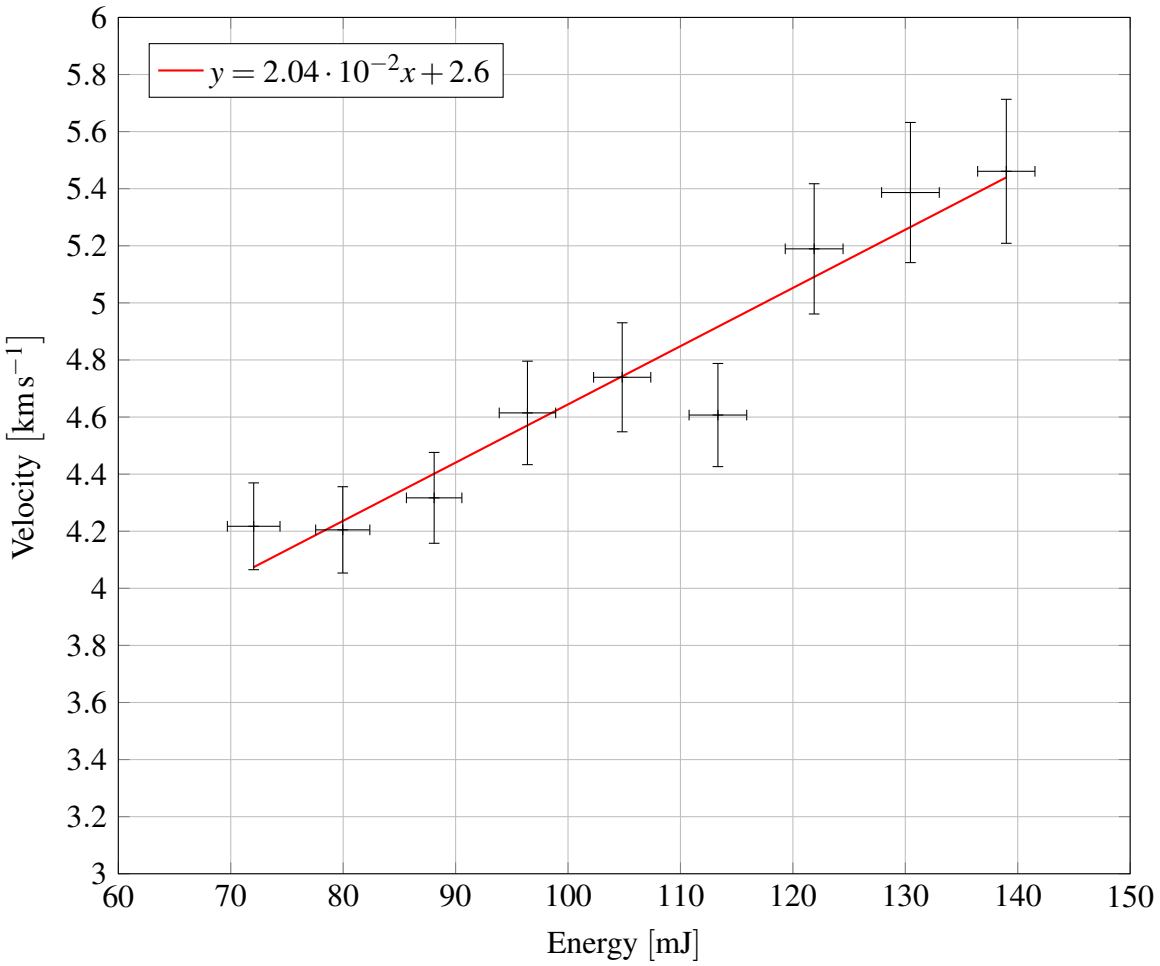

Figure 4.21 The average velocities of the flyer are dependent on the energy of the laser. Here they are shown plotted against the energies as calculated via Equation (4.6)

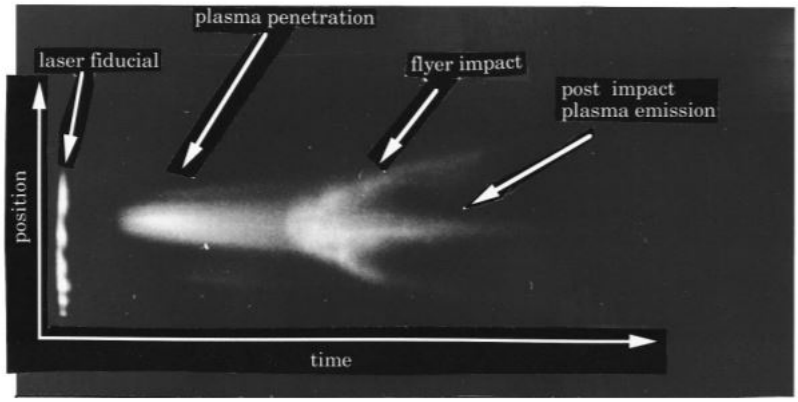

Figure 4.22 A streak image of a curved flyer with pre-impact plasma penetration [161].

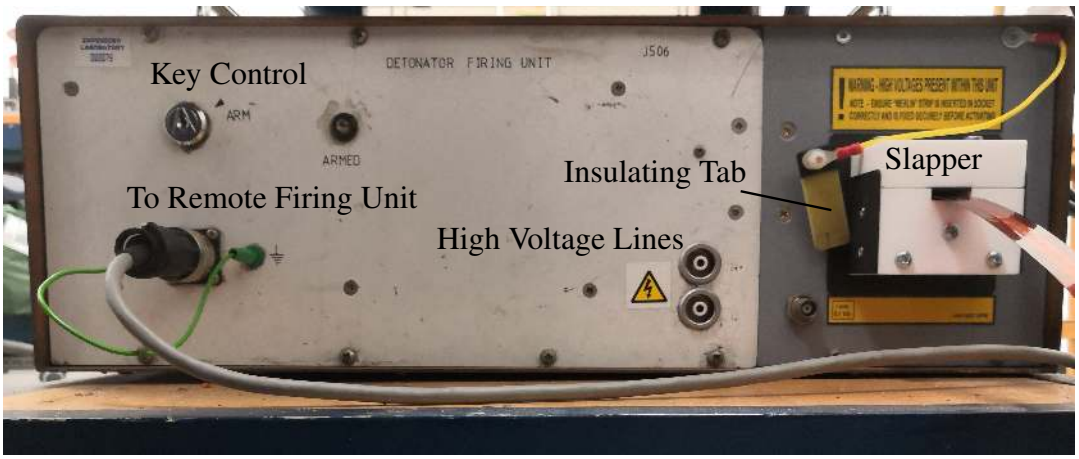

Figure 4.23 The front panel of the capacitor bank. The unit is first armed by turning the key, then charged from the remote firing unit. The slapper connection block (right) was added to fit the striplines of the supplied slapper cables

it could be charged to a maximum voltage of 4.5 kV. It is shown in Figure 4.23 with a slapper stripline inserted into a custom-made slapper connection block.

The custom-made slapper connection block added to the capacitor bank allows it to fire the flat slapper detonators without significantly increasing the inductance. The block contains a slot into which the exposed tails of the slappers' striplines could be inserted. The two sides of the stripline then make contact with a pair of internal electrodes. The capacitor bank can still discharge through the high voltage lines; when an insulating tab is inserted in between the internal electrodes the current is redirected to the original output.

The slapper connection block of the capacitor bank is shown in Figure 4.24

4.9.2 Slappers

The slapper cables consist of two layers of copper stripline which form the outward and return paths of the circuit. The two layers are connected at the head by plated through holes (PTH). One of the striplines narrows to a bridge – typically 200 µm × 200 µm, which is covered by a thin Kapton (polyimide) layer. Kapton is also used to separate and cover the copper layers of the stripline, except for a small section at the end of the tail where the slapper is inserted into the capacitor bank. A slapper head is shown in Figure 4.25 before and after a bridge burst event.

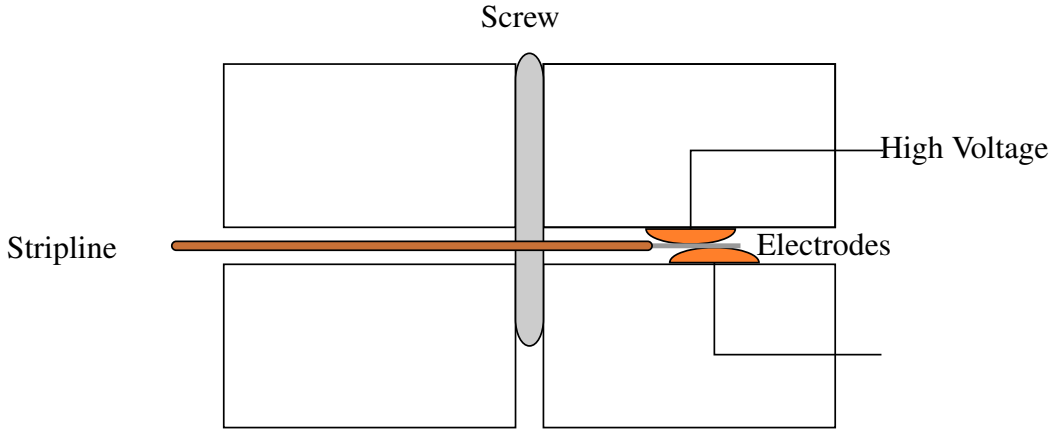

Figure 4.24 The stripline is held between the two electrodes by two screws. The electrodes are slightly offset from each other so contact is ensured. Firing the capacitor bank without a slapper or the circuit stop in place could severely damage the unit due to dielectric breakdown of air between the electrodes.

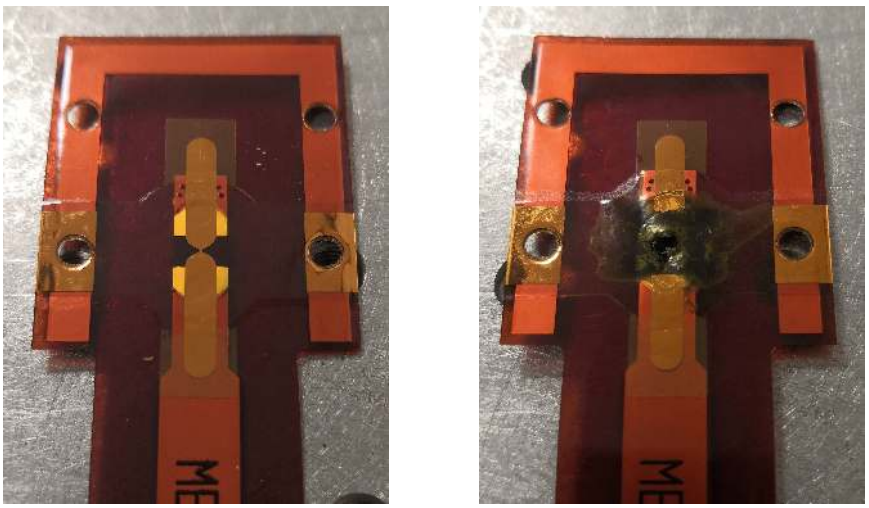

(a) (b)

Figure 4.25 A slapper head (a) before and (b) after burst. The bridge can be seen through the transparent Kapton layer. The deformation of the Kapton layer following firing is clearly visible.

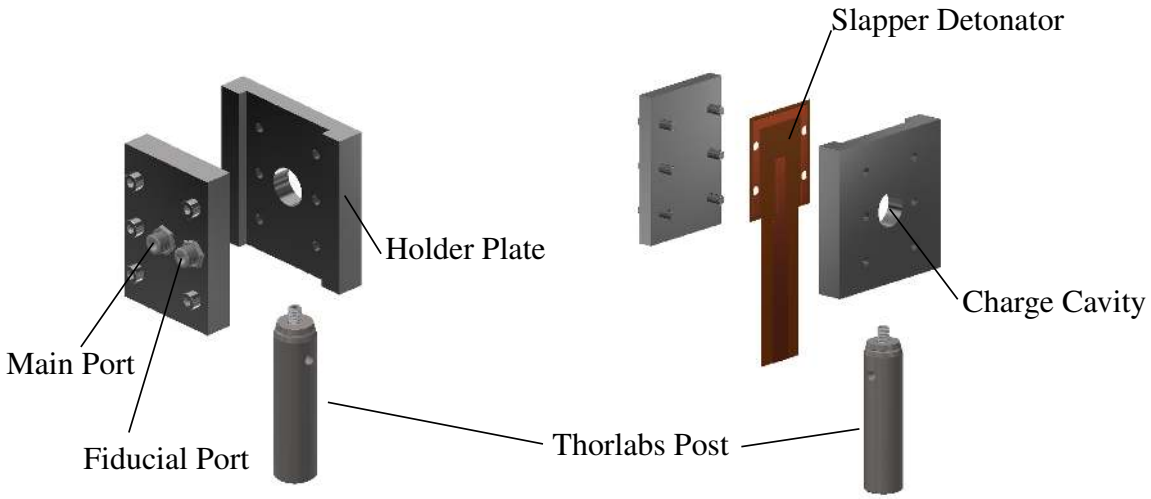

(a) Flyer Configuration (b) Slapper Configuration

Figure 4.26 The mount can hold either the coated substrate and optical fibre ends (a) or a slapper detonator (b). In both cases the detonator is aligned with the explosive charge cavity

4.10 Detonator Mount

Both the laser flyer system and slapper detonator can be interchangeably integrated into a custom-made mount made out of mild steel (Figure 4.26). The flyer backing plate has two SMA threaded ($1/4" - 3/16$) bulkhead adaptors (Thorlabs HASMA) for the main and fiducial optical fibres. The main port connects to the charge cavity in the holder plate, while the fiducial port aligns with one of the threaded holes. The backing plate for the slapper detonator has holes which line up with holes on the detonator head to ensure the bridge is on-axis.

The flexibility afforded by the optical fibre or stripline allows the detonator mount and explosive charge to be contained in a detonation chamber with the remaining apparatus outside.

4.11 Diagnostics

High speed diagnostics were used to characterise the detonators' outputs to assess the suitability for detonation experiments. A high speed framing camera was used to image a slapper burst into air and PETN. Photonic Doppler Velocimetry (PDV) was also used for both laser and slapper detonators, however the signal from the laser flyers was not strong enough to calculate a velocity.

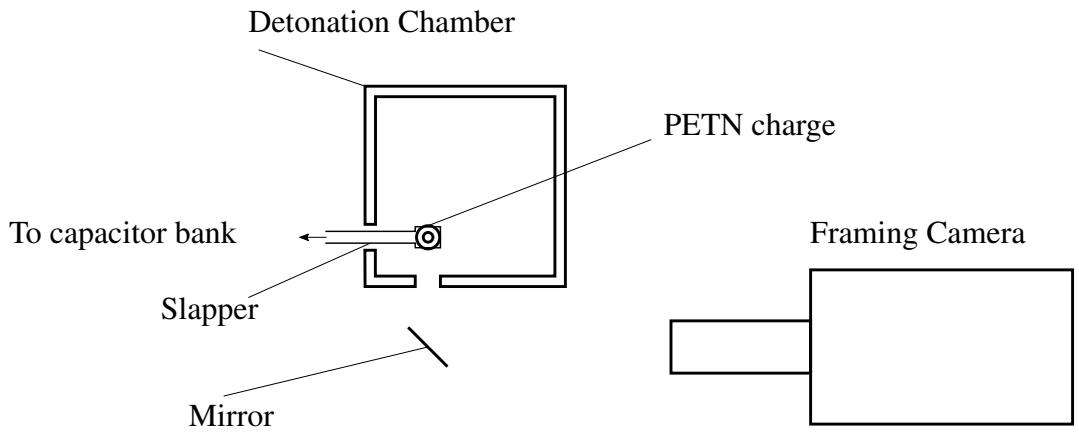

Figure 4.27 The apparatus used to image a slapper initiation of PETN. The detonation is initiated at the bottom of a 5 mm × 5 mm charge of 1.0 g cm^{-3} PETN. A plane mirror reflects the emitted light into the framing camera.

4.11.1 Framing Camera

High speed photography is a useful way of determining what happens during a slapper burst, even if it does not provide as precise quantitative data as more indirect methods such as PDV. Frame sequences were captured first for an unconfined burst into air, and then for a cyclindrical column of PETN in a PMMA casing. The camera used to image the slapper detonator was an Invisible Vision UHSi framing camera. The experiment was first roughly aligned in the camera's viewing plane, and then the camera lens was focused onto the slapper.

For the experiments involving explosive, the slapper head was inserted into a detonation chamber with a window and a plane mirror used to direct the light into the camera. The setup is shown in Figure 4.27.

Frames for the slapper firing into air are shown in Figure 4.28 and frames for the slapper initiating 1.0 g cm^{-3}, coarse grained PETN are shown in Figure 4.29. The PETN underwent complete reaction and totally destroyed its PMMA casing. Coarse PETN was chosen for the tests since it should be the hardest to initiate owing to the smaller number of potential initial ignition sites.

4.11.2 PDV

The bare PDV fibre was cleaved at 90° and glued into a ⌀1 mm hole in a PMMA holder. The holder was inserted into the charge cavity in the detonator mount and aligned with the bridge of the slapper. The Doppler shifted light from the moving slapper bridge mixes with the unshifted light reflected from the end of the fibre to form the beat frequency for the PDV signal. The

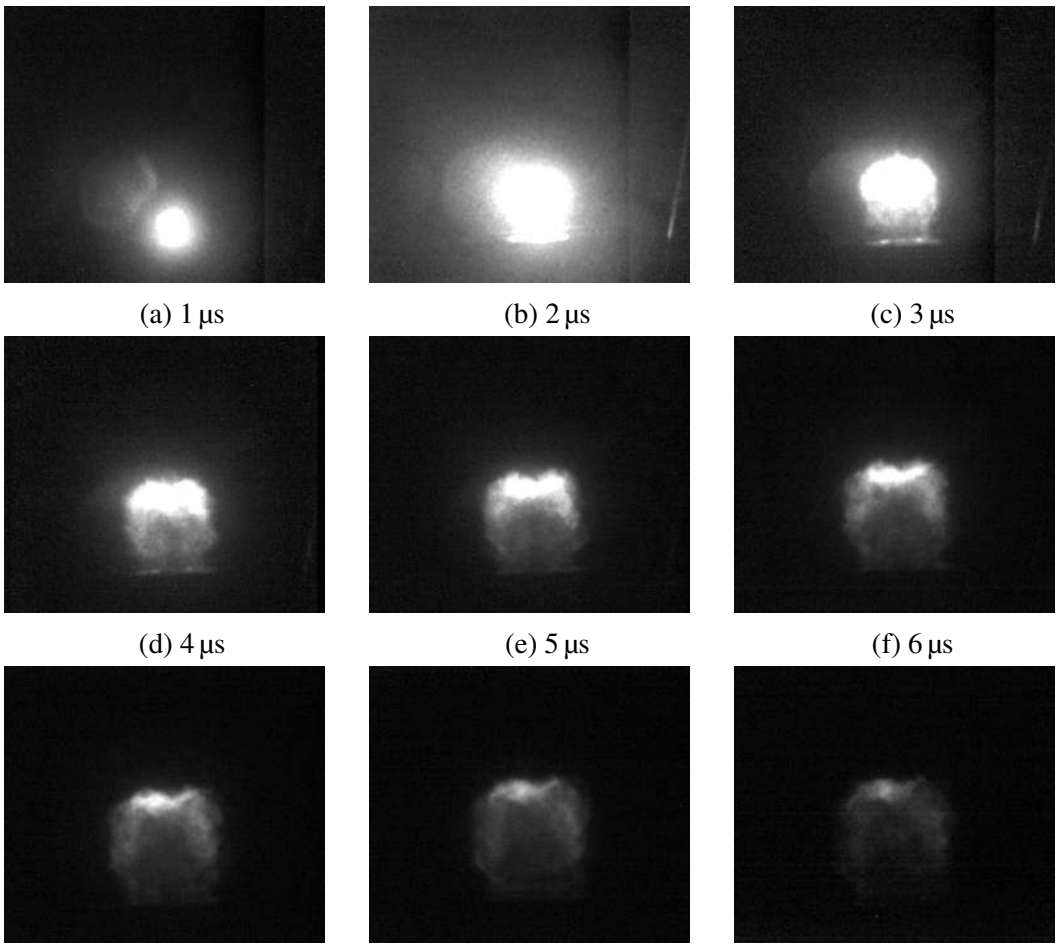

(a) 1 µs (b) 2 µs (c) 3 µs

(d) 4 µs (e) 5 µs (f) 6 µs

(g) 7 µs (h) 8 µs (i) 9 µs

Figure 4.28 High speed photography of a slapper detonator fire. The frame rate is 1 μs^{-1}. The exposure is 200 ns. The 'infinite' barrel used causes the flyer to have more curvature. Less luminous plasma can be seen behind the flyer after the first few frames

PDV system is the same as was used in Chapter 3 – a 40 mW 1550 nm laser with a digitiser and high bandwidth oscilloscope. Figure 4.30 shows a PDV trace of a slapper firing event.

Based on the velocity measured with PDV and the initiation imaged with the framing camera, it can be concluded that the slapper detonators and fireset are suitable for initiating PETN.

4.12 Summary

Two detonator systems have been built and characterised by a range of diagnostics: a laser flyer system and an EFI system.

- The laser flyer system uses a pulse from a Q-switched Nd:YAG laser coupled into an optical fibre to launch laser flyers.
- Several optical components were used to produce suitable pulses; a suite of diagnostics were used to check that the pulse energy was high enough to launch the flyers, without causing optical damage, and that the spatial profile would not lead to badly formed flyers.
- The laser flyer system can reliably launch planar flyers at velocities greater than $5\,\mathrm{km\,s^{-1}}$ – sufficient to initiate detonation.
- A capacitor bank has been adapted to fire slapper detonators, which reach a velocity of $3.8\,\mathrm{km\,s^{-1}}$ in 200 ns. These results are congruent with existing work on characterisation of slapper detonators.
- The slapper detonators were tested on $1.0\,\mathrm{g\,cm^{-3}}$ coarse grained PETN and found to initiate detonation, therefore should also initiate finer PETN.
- Both detonator systems can be used interchangeably in the same location to facilitate comparison.

Achieving reliable detonation is the first step in solving the overall problem. A new technique for measuring the reaction zone of these detonations is described in the next chapter.

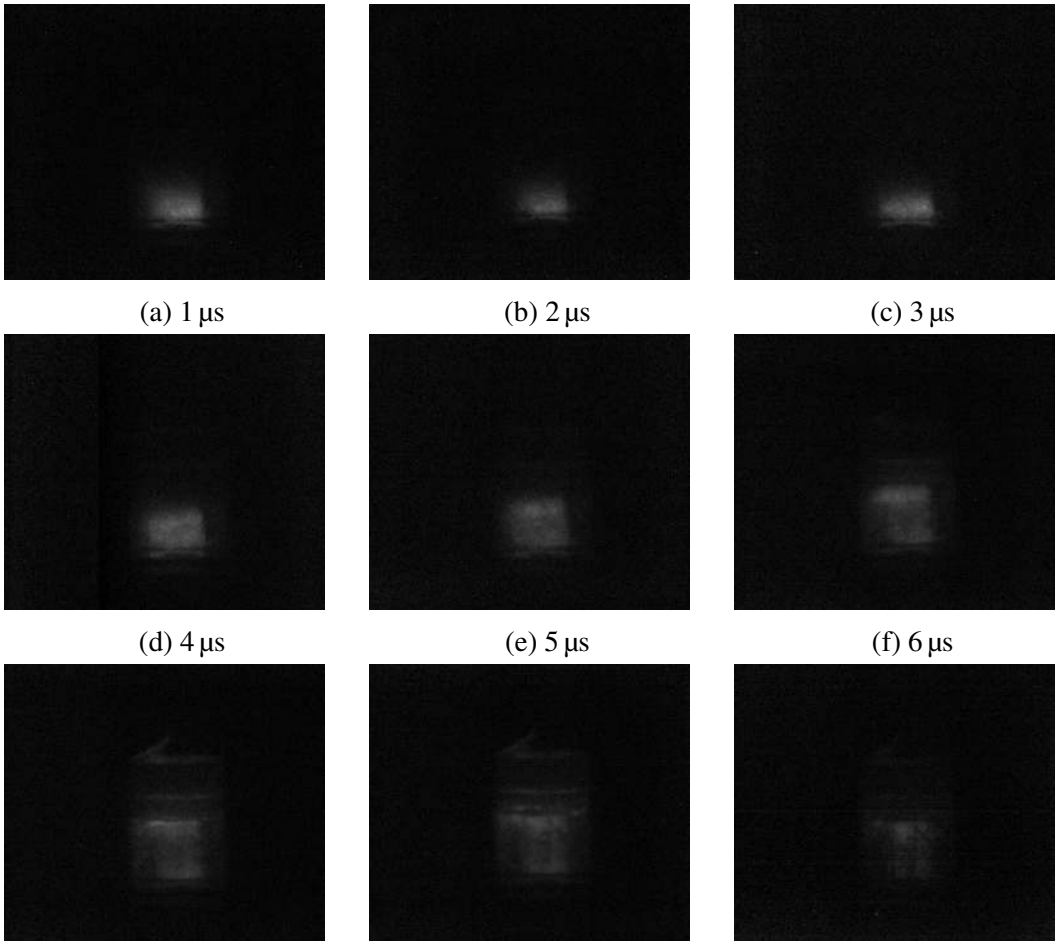

(a) 1 µs (b) 2 µs (c) 3 µs

(d) 4 µs (e) 5 µs (f) 6 µs

(g) 7 µs (h) 8 µs (i) 9 µs

Figure 4.29 Detonation of a column of coarse PETN. The detonation front is indicated by a faint thin line above the brighter emission from the detonator. The frame rate is 1 μs^{-1} and the exposure is 300 ns. The PMMA casing attenuates the light levels somewhat relative to the initiation in air, and the camera gain was significantly reduced compared to the burst into air shown in Figure 4.28.

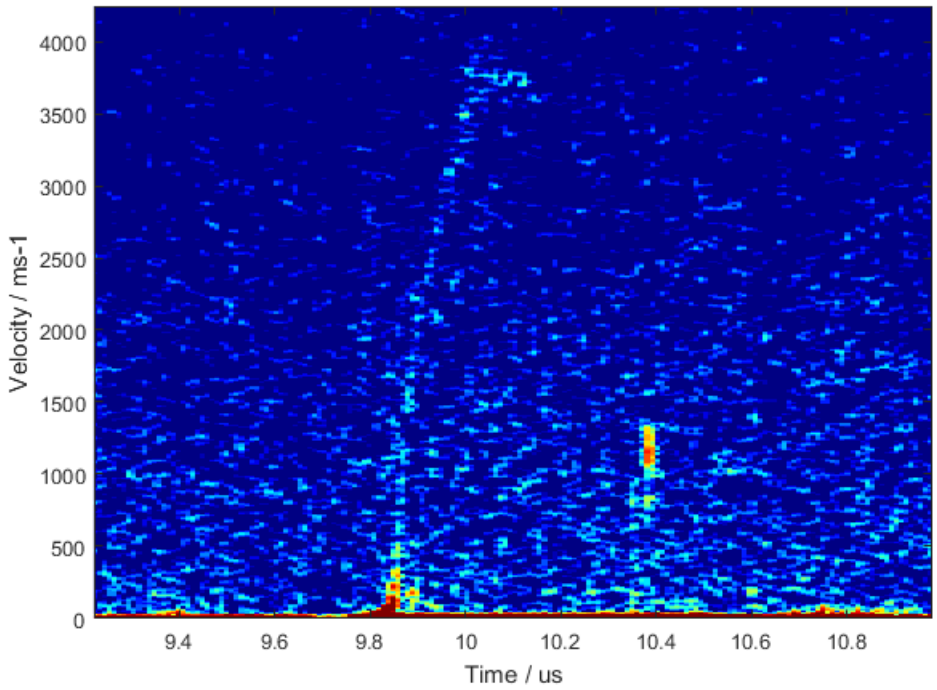

Figure 4.30 The velocity history of an slapper exploding into air. The detonator had a bridge size of 200 µm × 200 µm and was subjected to a 4 kV discharge from the capacitor bank. The peak velocity of 3.8 km s^{-1} is reached in approximately 200 ns

Chapter 5

Capacitive Sensing

5.1 Introduction

This chapter describes the development of capacitive sensors for measuring the reaction zone of a detonating explosive. The underlying principle behind these sensors is that a conducting object – in this case the reaction zone – will capacitively couple to electrodes and alter their response to a microwave frequency signal. Capacitive sensing has many commercial applications, including touchscreens and humidity sensors. It has also been used in a range of research applications as a substitute for optical sensing. There is generally a trade off between spatial resolution, temporal resolution and capacitance resolution [167]; the nature of the research determines the particular focus.

Many authors have used sensing systems with a high spatial and capacitive resolution for detection and localisation of small objects – however the applications were not ones which required a particularly high time resolution (at least in the context of detonation waves). Romani et al. [168] used a 320×320 array of 20 µm CMOS (Complementary metal oxide semiconductor) capacitive sensors to detect the location of 50 µm bioparticles on a 2D plane. Ghafar-Zadeh et al. [169] developed an even smaller CMOS chip with interdigitating electrodes for microfluidics. Guha et al. [170] also utilised CMOS technology to fabricate sensors for particle sensing in a dynamic fluid. Using a phase-locked loop demodulator to measure the frequency shift of an oscillator circuit due to a capacitance change, they demonstrated a measurement time as low as 3 µs. Shin et al. [171] used a delta-sigma modulator – a device which converts an analogue signal to a train of digital pulses whose frequency is proportional to the size of the analogue signal – to build a self-calibrating capacitive sensor circuit. A digital-to-analogue converter (DAC) was used to apply the compensation to the sensor capacitors.

Various electrode geometries and patterns have been invented to maximise the effectiveness of capacitive sensing for applications such as touch sensing [172] [173] and humidity detection [174]

Present capacitive sensing methods rely on contemporaneous data processing – each data point requires an actuation phase, sensing phase, and readout phase. The sensor is first activated by the on-cycle of the oscillator which charges the capacitive element. During the off-cycle of the oscillator the charge then changes in response to the object being measured. This charge change is then measured and digitised to produce the data point. This process significantly limits the time resolution of sensing, since each sensor cannot simultaneously be actuated and read. Improvements to the time resolution can be made by sacrificing the capacitance resolution and performing post-experiment processing. The technique described in this chapter does not explicitly measure the capacitance; it instead measures the transfer function – a function of the capacitance.

5.1.1 Transfer Function

The transfer function is the property of an electrical network which describes the mapping of an input signal to an output. Mathematically, if an input signal is described by the function $u(t)$ and the output by $v(t)$, then the transfer function is given by:

$$H(s) = \frac{V(s)}{U(s)} = \frac{\mathscr{L}\{v(t)\}}{\mathscr{L}\{u(t)\}} \tag{5.1}$$

where $X(s) = \mathscr{L}\{x(t)\}$ denotes the Laplace transform:

$$X(s) = \mathscr{L}\{x(t)\} = \int_{-\infty}^{\infty} x(t)\, e^{-st} dt \tag{5.2}$$

The conjugate variable s is a complex number $s = \sigma + i\omega$. In non-transient applications, σ can be set to 0 and the Laplace transform reduces to the Fourier transform with ω as the conjugate variable.

In a generalised RLC circuit the transfer function will be a function of the impedances of each component: $H(s; R_i, L_i, C_i)$. The circuit can be designed to maximise the effect of changing any one of these.

An equivalent circuit is shown in Figure 5.1

The magnitude of the transfer function for a fixed frequency input signal is called the frequency response $|H(i\omega)|$. An input signal containing different frequency components will therefore also change shape as well as size in response to a change in the transfer function.

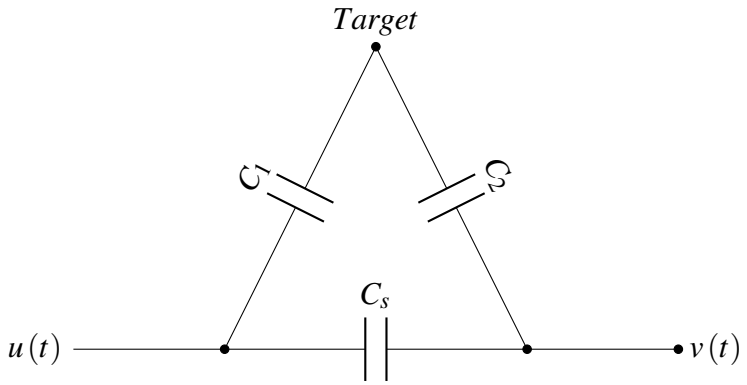

Figure 5.1 The capacitive sensor can be represented by an equivalent circuit. When a target is detected the transfer function changes to include C_1 and C_2 as well as the original sensor capacitance C_S

5.2 Implementation

This section describes the construction of an apparatus for measuring the capacitive shift of the chemical reaction zone of a detonation wave. The apparatus works by measuring the transfer function of the electrical network consisting of the reaction zone and the sensor. By comparison with the transfer function of the sensor alone, it is possible to deduce the size and spatiotemporal coordinates of the capacitive shift, and therefore the properties of the reaction zone. The input signal is a pulse train produced by an arbitrary waveform generator (AWG), while the output is the same pulse train having been modified by the sensor. The output is read with a high bandwidth oscilloscope and compared to the input to obtain the transfer function.

The sensor is a flexible printed circuit (FPC) containing coupling electrodes and connection pads. The head section containing the electrodes is inserted into a charge of explosive, while the tail is connected to a junction box connected to the other instruments.

The components of the sensor system are listed below.

5.2.1 Waveform Generator

A Tektronix AWG70002A Arbitrary Waveform Generator was used to produce the input signal for the sensor system. This two channel instrument can output user defined waveforms. Each channel has a positive and negative output which have equal and opposite potential at all times. While in theory any waveform would work, a square wave was chosen due to its shape – a square wave contains multiple frequencies, and therefore changes shape and amplitude when filtered by an RC circuit while a sine wave only changes its amplitude. The data processing method relies on calculating the misfit of the output signal compared to a baseline so the

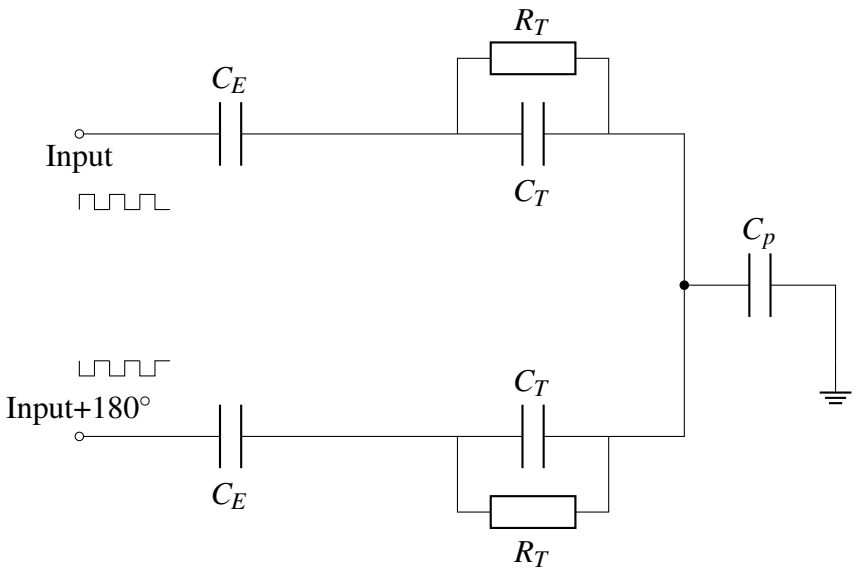

Figure 5.2 By making the shield electrodes symmetric to the sensing electrodes, the voltage across parasitic capacitance is approximately constant, limiting the effect the parasitic capacitance has on the signal.

best waveform is one which changes significantly in response to small changes in the transfer function.

5.2.2 Active Shielding

In order to maximise the signal-to-noise ratio (SNR) of the sensors it is necessary to maximise their capacitive coupling to the reaction zone, while minimising coupling to other objects. A technique known as active shielding is used to reduce this unwanted interference [175].

The shielding channels carry a signal of the same magnitude and shape as that sent to the transmitter electrode, but 180° out of phase. In this way, the voltage at the centre of symmetry is constant, as therefore is the voltage difference across the stray (parasitic) capacitance (see Figure 5.2). This destructive interference prevents the parasitic capacitance from contributing to the output signal.

This out-of-phase technique only works for stray capacitances that enter between the shield and sensing electrodes. It is still important to reduce other interferences, which is done by using coaxial cables to connect the sensor to the instruments, and within the junction box. The active shielding also improves the focus of the sensing zone on the area of interest, therefore reducing the edge effects – these are considered in more detail below.

5.2.3 Sensor Head

The sensors themselves are double layer flexible printed circuits produced by P. W. Circuits. There is a layer of 65 µm thick copper etched on each side of 25 µm thick polyimide by a photolithographic process. The sensor has six channels; each channel consists of a transmitter electrode, a receiver electrode and a pair of shield electrodes. The five short 0.5 mm × 0.5 mm channels share a transmitter electrode, while the adjacent long 0.5 mm × 4 mm channel has its own transmitter electrodes. Both transmitter electrodes are connected to the same input source. Each channel also has a pair of adjacent active shielding electrodes; the five short channels also share one shielding pair.

The electrodes in the sensor head are connected to the pads via 0.1 mm wide tracks and ⌀0.1 mm plated through holes (PTH). The tracks are approximately 4 cm long: any shorter and it would risk more components needing to be replaced after each shot; any further and the tracks' own capacitance would become influential.

A view of the Gerber file for the design of both layers of the PCB is shown in Figure 5.3 and a close-up of both sides of the sensor head is shown in Figure 5.4.

5.2.4 Junction Box

The tail of the sensor inserts into a 14 pin FPC connector mounted on a junction box. A small piece of tape over the tail end of the sensor prevents it from moving within the connector thus improving the signal reliability. Within the junction box the sensor connector is wired to eight SMA coaxial bulkheads (two inputs and six outputs). The connections within the junction box are shown schematically in Figure 5.5. The inputs are connected to the AWG and the outputs to the oscilloscope using coaxial cables (Thorlabs CA2948). The two inputs are attached to the same channel on the waveform generator: Input 1 is connected to the transmitter electrode and attached to the positive AWG output; Input 2 is connected to the shield electrodes and attached to the negative AWG output.

For experiments, the junction box is mounted immediately adjacent to the detonator mount. The flexible sensor then extends from the junction box to the explosive charge, as shown in Figure 5.6.

The junction box is filled with putty in order to protect the circuitry. A steel cover is placed over the FPC connector to provide additional protection as shown in Figure 5.7.

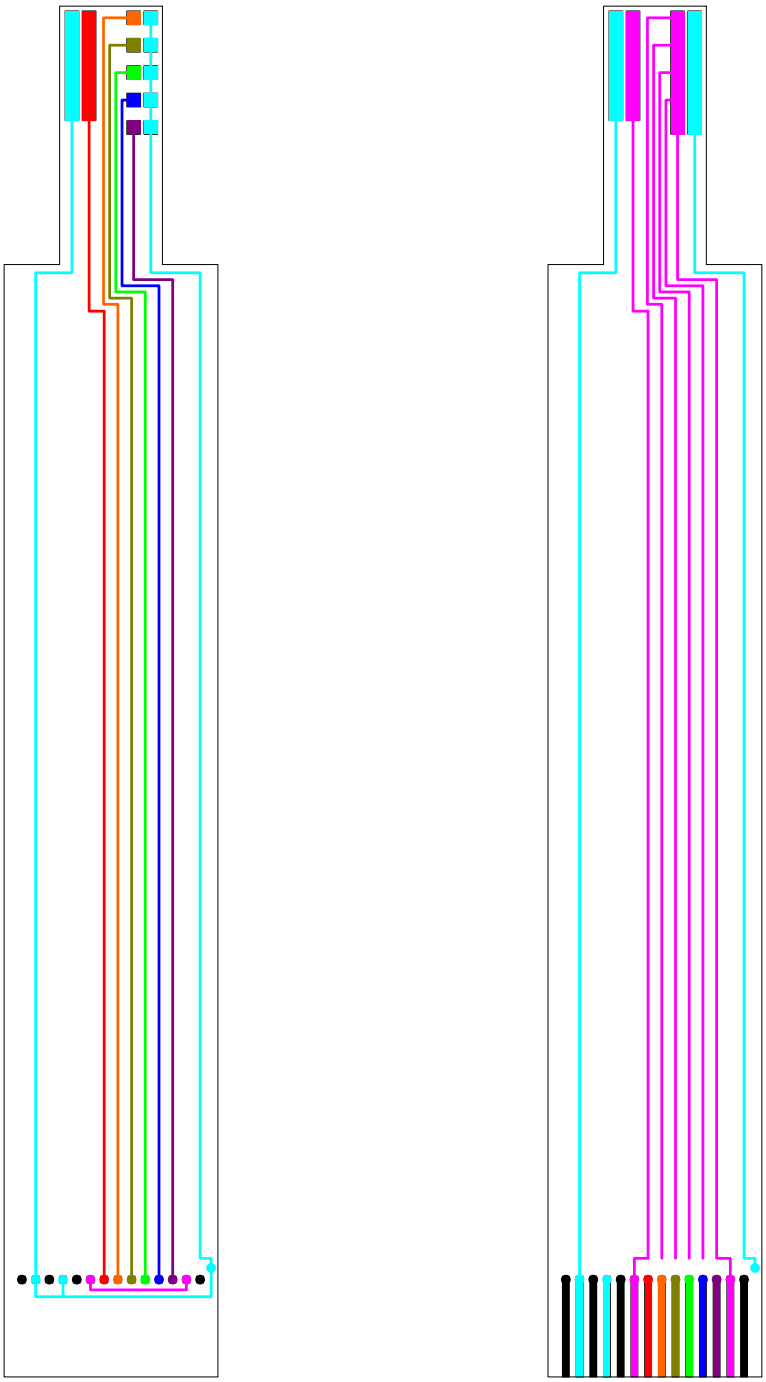

(a) (b)

Figure 5.3 The front layer (a) of the sensor contains the individual channel receiver electrodes (five short and one long), while the back layer (b) contains the shared transmitter electrodes and 14 connection pads. For clarity each electrical net is a different colour: Channel 1, Channel 2, Channel 3, Channel 4, Channel 5, Channel 6, Transmitter, Shield, Ground.

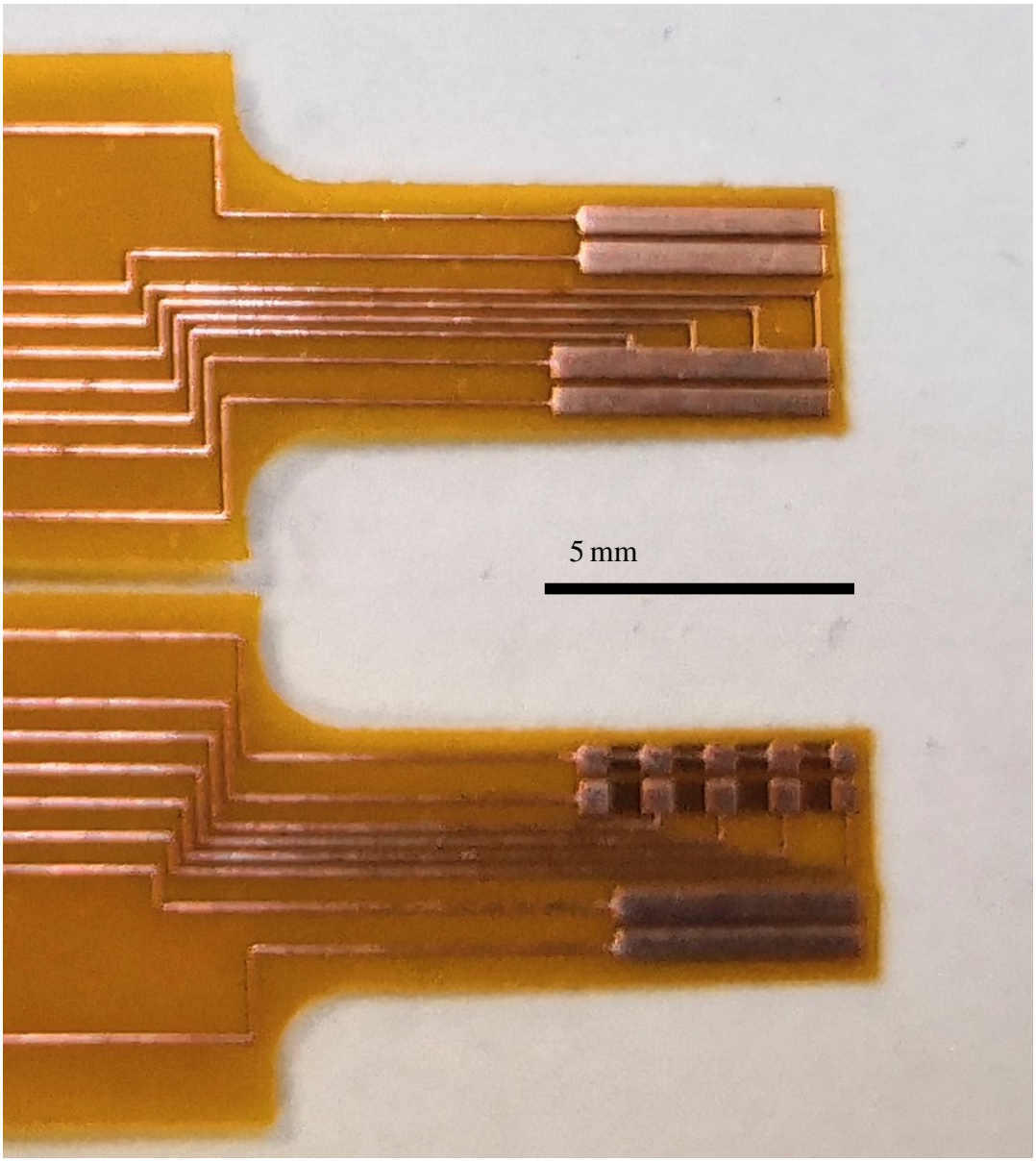

Figure 5.4 Both sides of the sensor head

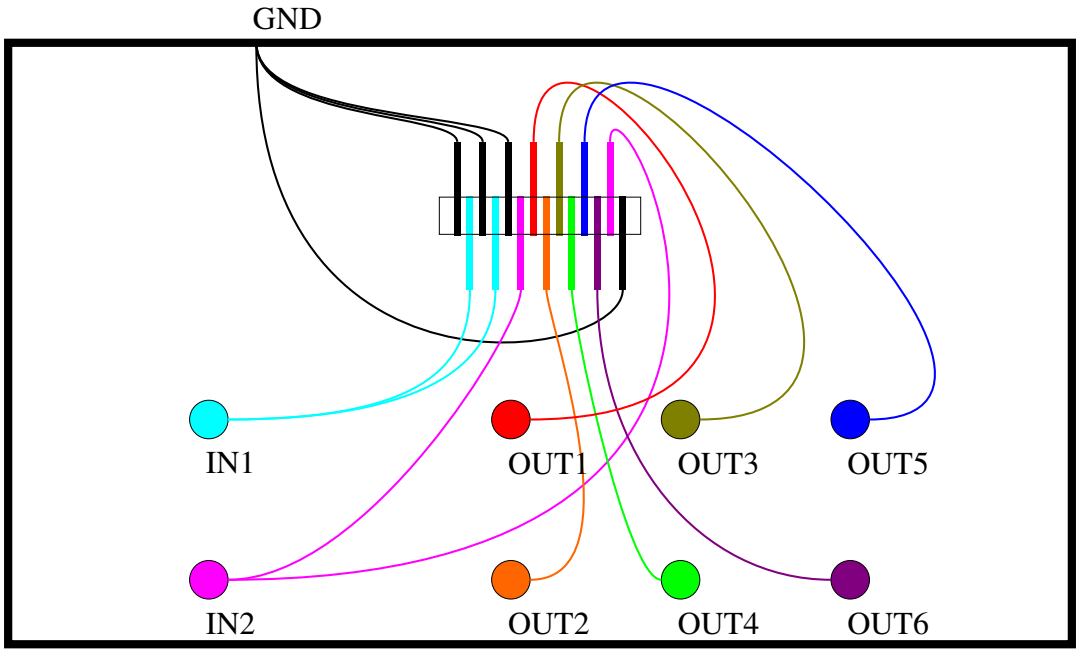

Figure 5.5 A schematic of the junction box showing the connections between the 14 pin FPC connector and the six SMA ports. The colour scheme is the same as in Figure 5.3.

5.2.5 Oscilloscope

The oscilloscope (Tektronix DPO7254) record window is triggered by a TTL signal from the delay generator in order to synchronise with the detonator (either the laser flyer system or the capacitor bank discharge for slapper detonators). The oscilloscope has a bandwidth of 2.5 GHz, which from the general rule of thumb that an oscilloscope should have a bandwidth 5 higher than the fundamental frequency it measures [176], puts a soft upper bound on the signal frequency of 500 MHz. With four channels in use, the sampling rate is 10 G§/s, therefore the oscilloscope makes 20 voltage measurements for each signal time period.

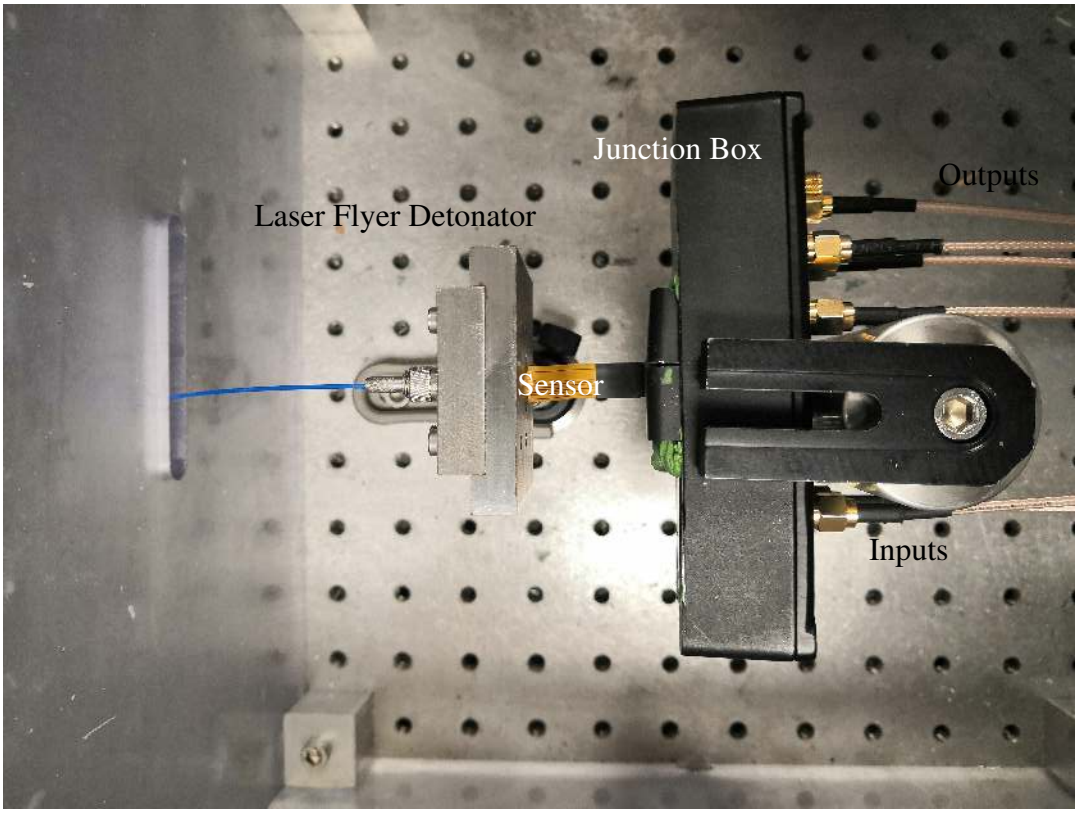

Figure 5.6 The configuration of the sensor and junction box when used with the laser flyer detonator

(a)

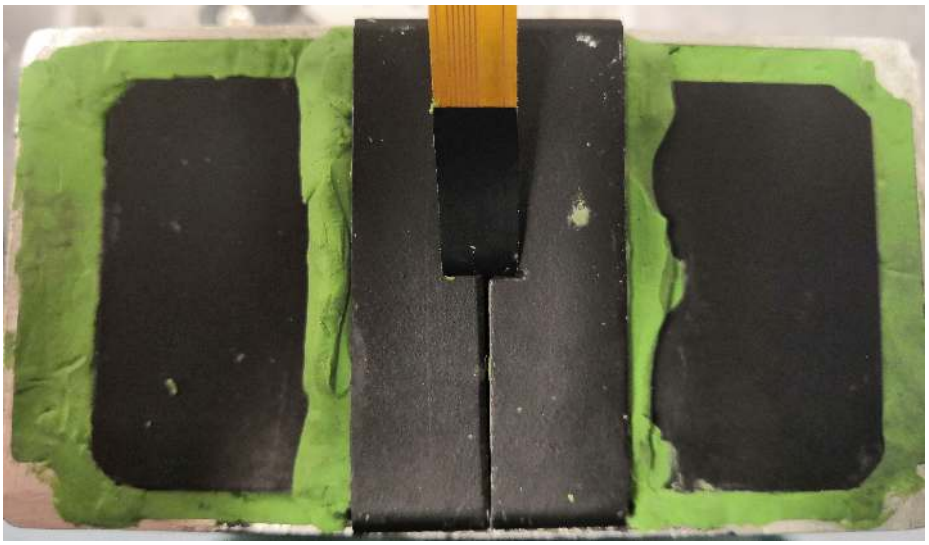

(b)

Figure 5.7 Putty and a steel plate protect the circuit board from being damaged during experiments.

5.3 Data Processing

The oscilloscope data is processed in Matlab. The purpose of the data processing is to turn the raw data into a time series of the change in the transfer function, which therefore reflects the strength of the capacitive signal at each point in time.

First the raw oscilloscope data is imported into the Matlab workspace and the region of interest defined. A baseline region before the detonation event is also defined. The baseline time series $g_b(t)$ is shifted forward in time by t_b such that it remains in phase with the unshifted version of itself, and its extent covers the region of interest. It is then left to calculate the time-varying degree of 'difference' between the two signals The algebraic difference between the two is simply:

$$D(t) = g(t) - g_b(t - t_b) \tag{5.3}$$

however, this drops to zero when the two signals cross, so a more complex analysis is required that reflects the possibility that both the phase and spectral composition could change. The technique used is the continuous wavelet transform (CWT).

5.3.1 Continuous Wavelet Transform

When converting a time series into a time-frequency representation, one way is to divide the series into (possibly overlapping) windows, perform a Fourier transform on each window, and submit the resulting spectral decomposition at each point in time. This method is commonly used but has the downside that there is a trade-off between frequency and time resolution.

The CWT is a more sophisticated tool, where a function is transformed via:

$$W(t,f) = \sqrt{\frac{2\pi|f|}{\omega_0}} \int_{-\infty}^{\infty} g(\tau)\, \psi^* \left(2\pi f \frac{\tau - t}{\omega_0} \right) d\tau \tag{5.4}$$

The time series $g(t)$ is convolved with a series of wavelet functions $\psi(t)$ scaled by the frequency f. Intuitively, the CWT represents the different contributions to a signal from wavelets with different amounts of scaling (by the frequency parameter f) and translation (by the time parameter t).

The wavelet function itself must have certain mathematical properties – a suitable function is the Morlet wavelet:

$$\psi(t) = \frac{1}{\pi^{\frac{1}{4}}} e^{i\omega_0 t} e^{-\frac{t^2}{2}} \tag{5.5}$$

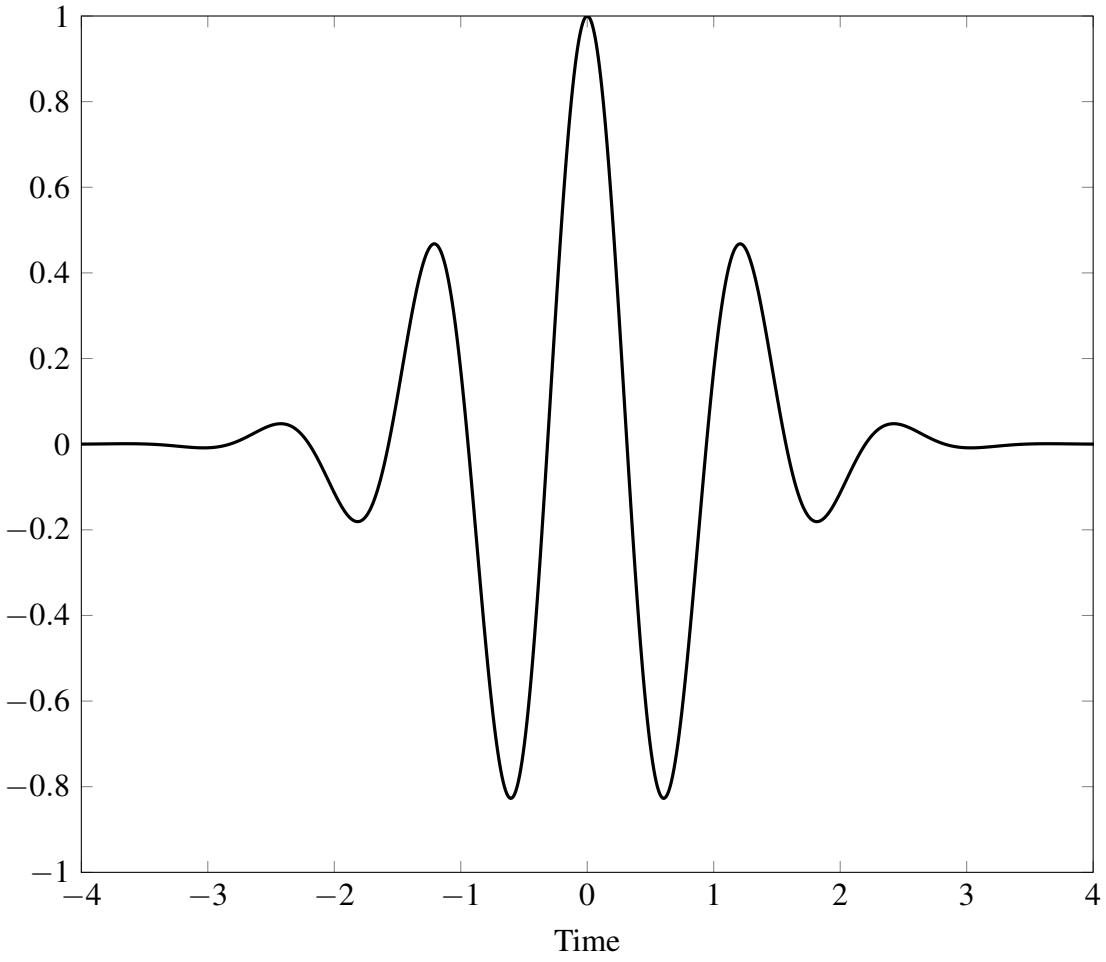

Figure 5.8 The Morlet wavelet

This function is a complex exponential bounded by a Gaussian – ω_0 sets the number of oscillations that fit under the Gaussian envelope. The Morlet wavelet is plotted in Figure 5.8.

5.3.2 Signal Comparison

From the time-frequency representation, one can quantitatively describe the phase and amplitude difference by using the 'misfit' functions of Kristeková et al. [177]. The amplitude misfit M_A is:

$$M_A(t,f) = \frac{|W(t,f)| - |W_b(t,f)|}{|W_b(t,f)|} \tag{5.6}$$

and the phase misfit M_ϕ is:

$$M_\phi(t,f) = \frac{1}{\pi} Arg\left(\frac{W(t,f)}{W_b(t,f)}\right) \tag{5.7}$$

This technique encompasses both phase and amplitude/envelope information, which can be conveyed in a two-dimensional $t-f$ plane. Individually they can be conveyed as one-dimensional time series by summing over the frequency:

$$M_A(t) = \frac{\sum_f |W_b(t,f)| M_A(t,f)}{\sum_f |W_b(t,f)|} \tag{5.8}$$

$$M_\phi(t) = \frac{\sum_f |W_b(t,f)| M_\phi(t,f)}{\sum_f |W_b(t,f)|} \tag{5.9}$$

Since the baseline signal differs between channels, in order to make meaningful comparisons between channels, the misfit is normalised by the envelope of the baseline analytic signal $\sum_f |W_b(t,f)|$. This local definition means that the misfit at a particular time can be determined using only data at that time.

5.3.3 Noise

Noise in the context of capacitive sensing is unwanted random fluctuations in the signal measured by the oscilloscope. These contributions can enter the system at several points.

The sensor or junction box can act as an antenna and pick up external radiation. The 50 Hz AC noise from the mains ought not to affect the signal since the frequency of the noise is orders of magnitude lower than the signal. Mobile and WiFi transmitters may pose a larger problem, since they typically operate in the 900 MHz to 5 GHz range, which is comparable to the wave generator. Fortunately, the bands they operate in are known and have a relatively small bandwidth ($\sim$20 MHz) so can be removed with a notch filter if necessary. Furthermore the detonation box should effectively act as a Faraday cage and block the noise from entering at the most vulnerable point – the sensor.

Environmental noise such as temperature or humidity variations is very unlikely to affect the signal due to the time scale.

The usual sources of electrical noise will be present; given the frequencies involved thermal white noise will be more significant than $1/f$ noise.

5.3.4 Summary

A summary of the data processing step is as follows:

- The raw oscilloscope data is converted to numerical arrays
- A section of reference data is designated from before the initiation to act as a baseline. The baseline is then shifted to the region of interest.
- Both signals are converted to a time-frequency representation using a continuous wavelet transform.
- The amplitude and phase misfit functions are calculated as time series.

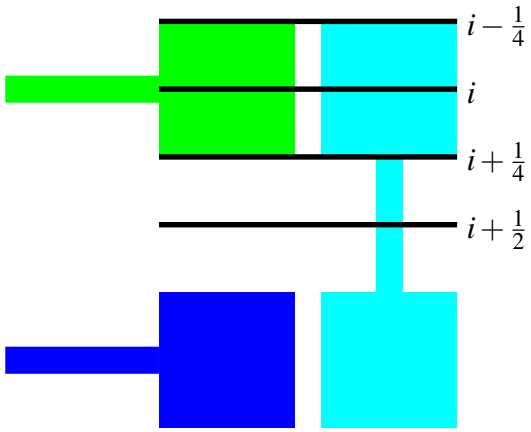

Figure 5.9 The detonation velocity D, Chapman-Jouguet velocity V and reaction zone length ξ are evaluated at discrete intervals denoted by subscripts.

5.4 Data Analysis

The processed data consists of a phase and amplitude time series for each channel, with features corresponding to changes in the transfer function of the sensor circuit. This section describes how these time series can be analysed to obtain information about the detonation wave and reaction zone. There are two configurations that are considered: firstly with the sensor aligned axially along the direction of propagation to measure detonation velocity and reaction zone length; and secondly with the sensor aligned radially along the rear face of the explosive pellet to measure breakout time and wave curvature.

Each electrode is indexed $i = 1,2,3,4,5$. The timing points $\alpha_i, \beta_i, \gamma_i, \delta_i$, $i = 1...5$ refer to the start of the rise, the end of the rise, the start of the fall, and the end of the fall respectively for the signal of each channel. Quantities are calculated by reference to the edges of the channel electrodes and are assigned a subindex based on the closest edge or midpoint. The notation for this indexing is shown in Figure 5.9. In some cases it is more useful to know the quantities as a function of time – this can be done by simple interpolation between the two timing points used in the calculation.

5.4.1 Axial Alignment

The processed data contains useful information about the detonation, which can be extracted by considering a conducting reaction zone crossing an electrode. The detonation velocity, Chapman-Jouguet velocity, and reaction zone length can all be calculated in this way.

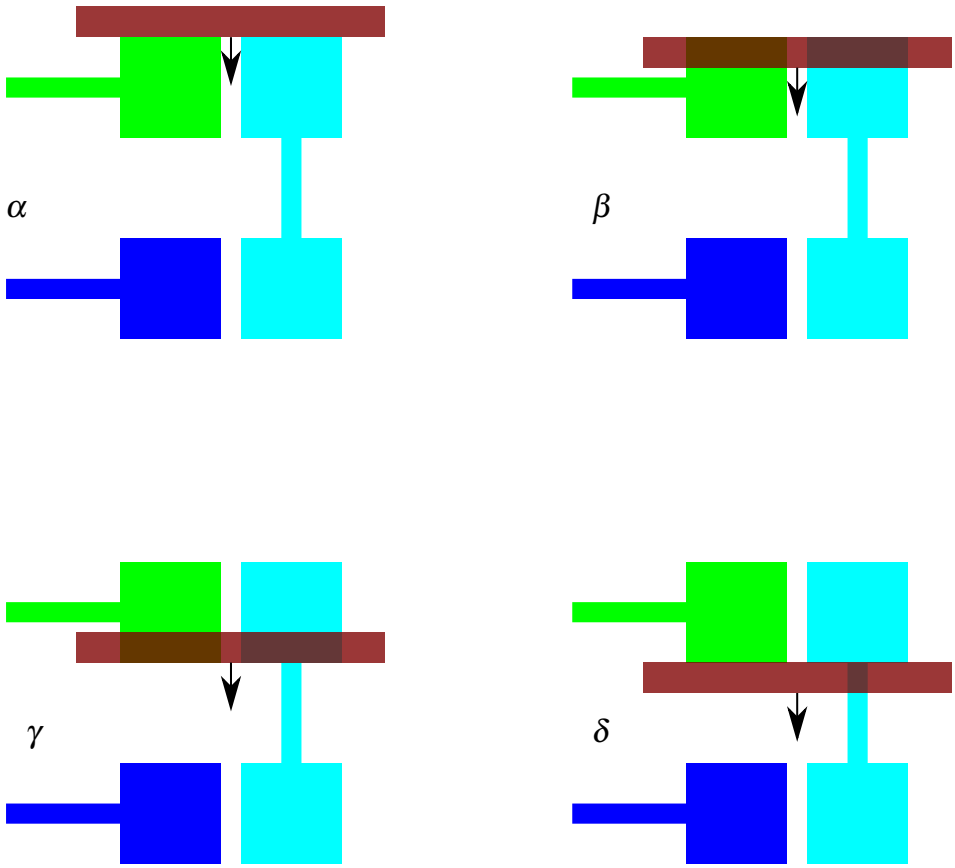

Figure 5.10 In the case that $\xi < w$, the i^{th} capacitance starts to rise when the front edge of the reaction zone crosses into the i^{th} electrode (α) and levels off when the rear edge crosses into the electrode (β). It starts to fall when the front edge of the reaction zone crosses out of the electrode (γ) and finishes falling when the rear edge of the reaction zone crosses out of the electrode (δ). Since the reaction zone has not entered the $(i+1)^{th}$ electrode by this point, the traces are separated.

There are two cases which need to be considered which differ slightly in their analysis: the reaction zone length ξ is either larger than the width w =0.5 mm of a short channel electrode, or it is smaller.

Case 1: $\xi < w$

If the reaction zone length is smaller than 0.5 mm, it only interacts with one electrode at a time. A typical sequence of events arising from such a reaction zone is shown in Figure 5.10 and the resulting trace shown in Figure 5.11.

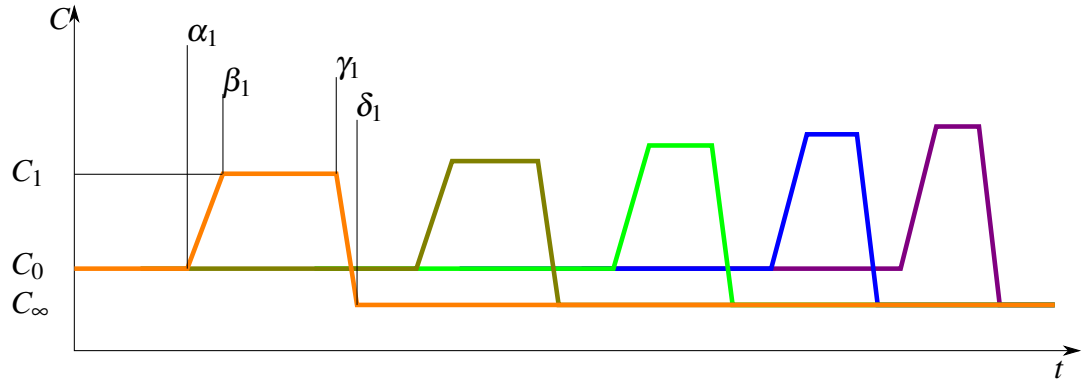

Figure 5.11 Idealised trace for a reaction zone shorter than 0.5 mm. The peaks for each channel are completely separate.

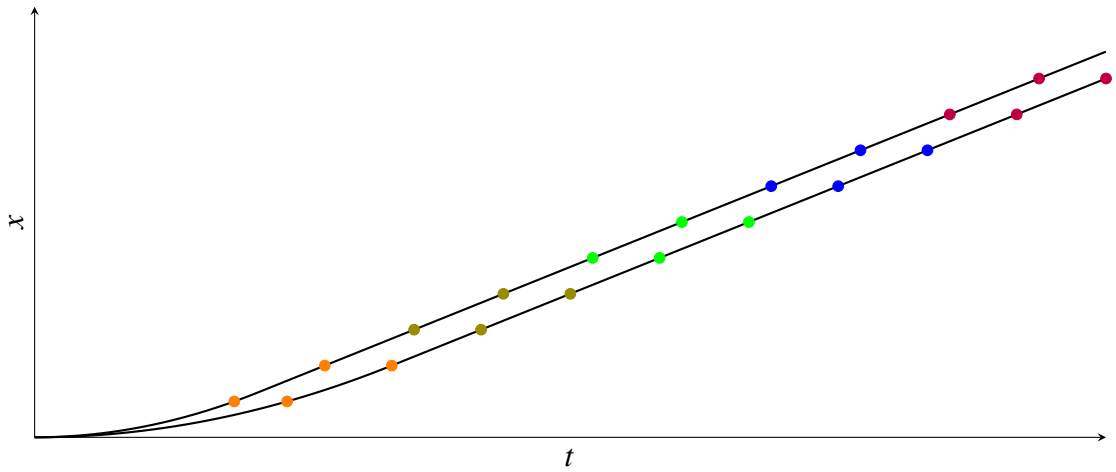

Figure 5.12 Illustration of how the timing points $\alpha_i, \beta_i, \gamma_i, \delta_i$ can be used to give a position-time graph for the detonation front (top branch) and Chapman-Jouguet plane (bottom branch)

Detonation Velocity

For this analysis the detonation velocity is considered to be the velocity of the front edge of the reaction zone. There are two ways that this can be obtained from the traces. The detonation velocity across the electrode can be calculated from the time between the front entering the electrode and leaving the electrode. Interpolating to the centre of the electrode gives:

$$D_i = \frac{w}{\gamma_i - \alpha_i} \tag{5.10}$$

The detonation velocity in the gap between two adjacent electrodes can be calculated from the time between the front leaving one electrode and entering another. Interpolating to the midpoint between the two electrodes (using the indexing notation in Figure 5.9) gives:

$$D_{i+\frac{1}{2}} = \frac{w}{\alpha_{i+1} - \gamma_i} \tag{5.11}$$

Chapman-Jouguet Velocity

The Chapman-Jouguet velocity is here taken to be the velocity of the rear of the reaction zone. In the same way as with the detonation velocity, it can be calculated from the time between the rear entering the electrode and leaving the electrode:

$$V_i = \frac{w}{\delta_i - \beta_i} \tag{5.12}$$

Likewise, between electrodes it is:

$$V_{i+\frac{1}{2}} = \frac{w}{\beta_{i+1} - \delta_i} \tag{5.13}$$

Reaction Zone Length

Firstly, at time α_i the front of the reaction zone has just entered the electrode, and the back of the reaction zone is a distance $\xi_{i-\frac{1}{4}}$ behind and moving at a velocity $V(\alpha_i)$. At time β_i the back edge enters the electrode at velocity $V(\beta_i)$ having travelled the distance $\xi_{i-\frac{1}{4}}$. $\xi_{i-\frac{1}{4}}$ can therefore be expressed as:

$$\xi_{i-\frac{1}{4}} = \int_{\alpha_i}^{\beta_i} V(t)\, dt \tag{5.14}$$

At time β_i the rear edge enters the electrode and the front edge is a distance $w - \xi_i$ away from leaving and travelling at $D(\beta_i)$. At time γ_i it leaves at a velocity of $D(\gamma_i)$. Integrating gives:

$$\xi_i = w - \int_{\beta_i}^{\gamma_i} D(t)\,dt \tag{5.15}$$

Using the same analysis in the gap between electrodes gives:

$$\xi_{i+\frac{1}{4}} = \int_{\gamma_i}^{\delta_i} V(t)\,dt \tag{5.16}$$

and:

$$\xi_{i+\frac{1}{2}} = w - \int_{\delta_i}^{\alpha_{i+1}} D(t)\,dt \tag{5.17}$$

Case 2: $\xi > w$

If the reaction zone length is greater than 0.5 mm, it interacts with multiple electrodes simultaneously. A typical sequence of events arising from such a reaction zone is shown in Figure 5.13 and the resulting trace shown in Figure 5.14.

Detonation Velocity

The detonation velocity is again taken to be the velocity of the front edge of the reaction zone. Since the front now leaves the electrode before the rear enters, the timing points β and γ correspond to different events than in the $\xi < w$ case. The detonation velocity at the centre of the electrode is then:

$$D_i = \frac{w}{\beta_i - \alpha_i} \tag{5.18}$$

Similarly, the detonation velocity at the midpoint between the electrodes is:

$$D_i = \frac{w}{\beta_i - \alpha_i} \tag{5.19}$$

Chapman-Jouguet Velocity

The Chapman-Jouguet velocity at the centre of an electrode when $\xi > w$ is:

$$V_i = \frac{w}{\delta_i - \gamma_i} \tag{5.20}$$

Between two electrodes it is:

$$V_{i+\frac{1}{2}} = \frac{w}{\gamma_{i+1} - \delta_i} \tag{5.21}$$

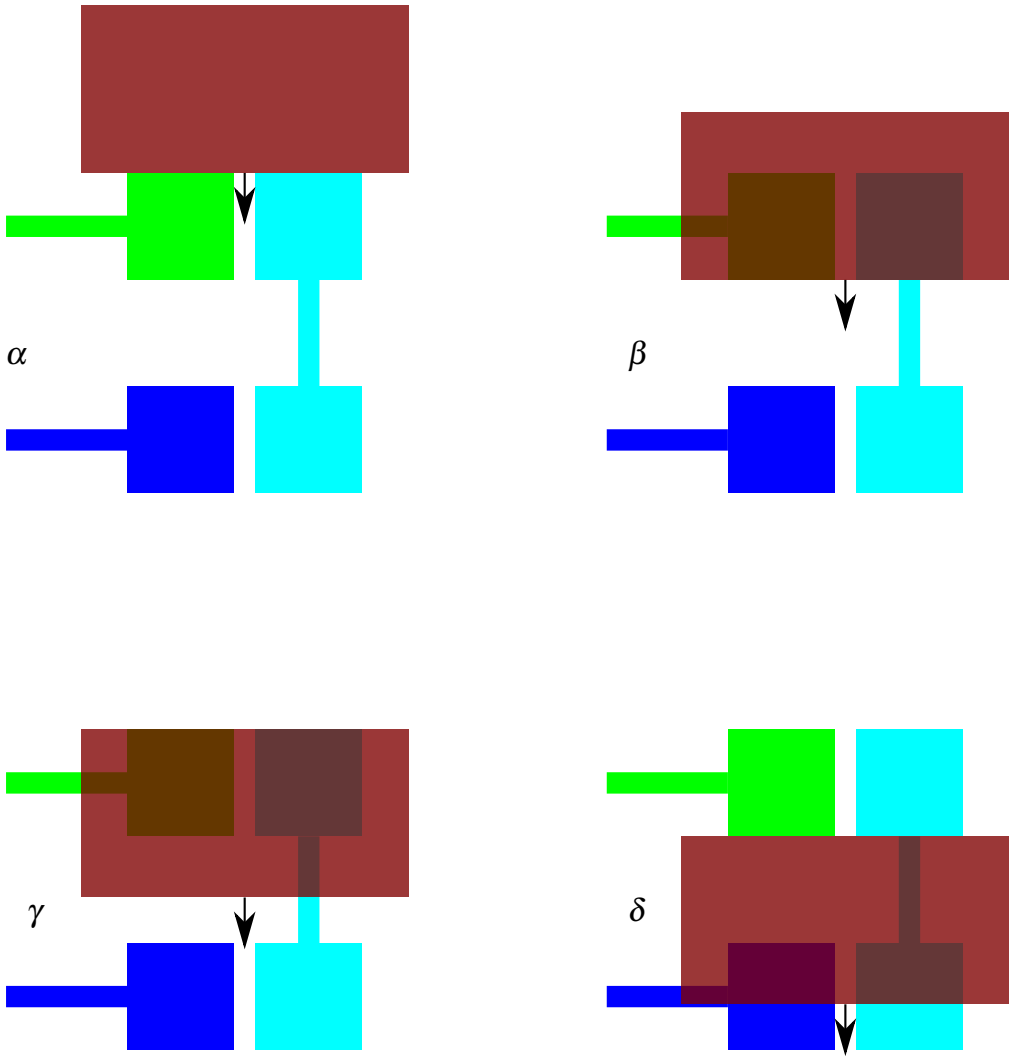

Figure 5.13 In the case that $\xi > w$, the i^{th} capacitance starts to rise when the front edge of the reaction zone crosses into the i^{th} electrode (α) and levels off when the front edge crosses out of the electrode (β). It starts to fall when the rear edge of the reaction zone crosses into the electrode (γ) and finishes falling when the rear edge of the reaction zone crosses out of the electrode(δ). Since the reaction zone has entered the $(i+1)^{th}$ electrode by this point, the traces overlap.

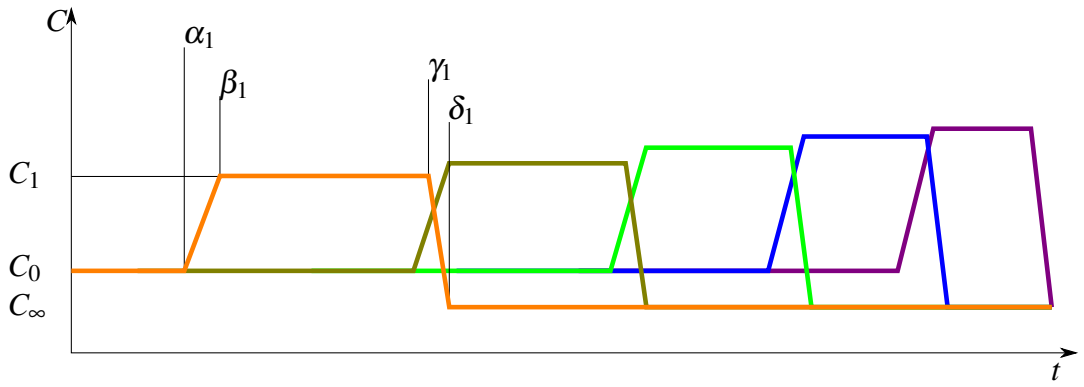

Figure 5.14 Idealised trace for a reaction zone longer than 0.5 mm. The peaks for each channel overlap with adjacent channels.

Reaction Zone Length

At time β_i the detonation front is leaving the i^{th} electrode, and the rear of the reaction zone is a distance $\xi_{i-\frac{1}{4}}$ behind and travelling at velocity $V(\beta_i)$. At time γ_i the rear of the reaction zone crosses into the i^{th} electrode at $V(\gamma_i)$ having travelled a distance $\xi_{i-\frac{1}{4}} - w$. The reaction zone length can then be written as:

$$\xi_{i-\frac{1}{4}} = w + \int_{\beta_i}^{\gamma_i} V(t)\,dt \tag{5.22}$$

At time γ_i the rear of the reaction zone enters the i^{th} electrode, while the front is moving at $D(\gamma_i)$ and is $2w - \xi_i$ away from entering the $i+1^{th}$. At time α_{i+1} the detonation front enters the $i+1^{th}$ electrode at velocity $D(\alpha_{i+1})$. Therefore:

$$\xi_i = 2w - \int_{\gamma_i}^{\alpha_{i+1}} D(t)\,dt \tag{5.23}$$

At time α_{i+1} the detonation front enters the $i+1^{th}$ electrode, and the rear is $\xi_{i+\frac{1}{4}} - w$ away from leaving the i^{th}. Therefore:

$$\xi_{i+\frac{1}{4}} = w + \int_{\alpha_{i+1}}^{\delta_i} V(t)\,dt \tag{5.24}$$

At time δ_i the rear of the reaction zone leaves the i^{th} electrode, while the front is moving at $D(\delta_i)$ and is $2w - \xi_{i+\frac{1}{2}}$ away from leaving the $i+1^{th}$. At time β_{i+1} the detonation front leaves the $i+1^{th}$ electrode at velocity $D(\beta_{i+1})$. Therefore:

$$\xi_{i+\frac{1}{2}} = 2w - \int_{\delta_i}^{\beta_{i+1}} D(t)\,dt \tag{5.25}$$

Table 5.1 The method of calculating reaction zone properties based on the above analysis. The continuum approximations are made by interpolating the discrete measurements from the sensor's measurement zones. The two sets of formulae (for ξ <0.5 mm and ξ >0.5 mm) differ depending on whether the reaction zone is shorter or longer than w =0.5 mm. In the first instance the signal plateaus when the reaction zone is completely covered by the measurement zone, while in the second case the signal plateaus when the reaction zone completely covers the measurement zone.

Property	$\xi < w$	$\xi > w$	Continuum Approximation
Detonation Velocity	$D_i = \frac{w}{\gamma_i - \alpha_i}$ $D_{i+\frac{1}{2}} = \frac{w}{\alpha_{i+1} - \gamma_i}$	$D_i = \frac{w}{\beta_i - \alpha_i}$ $D_{i+\frac{1}{2}} = \frac{w}{\alpha_{i+1} - \beta_i}$	$D(t)$
Rear Velocity	$V_i = \frac{w}{\delta_i - \beta_i}$ $V_{i+\frac{1}{2}} = \frac{w}{\beta_{i+1} - \delta_i}$	$V_i = \frac{w}{\delta_i - \gamma_i}$ $V_{i+\frac{1}{2}} = \frac{w}{\gamma_{i+1} - \delta_i}$	$V(t)$
Reaction Zone Length	$\xi_{i-\frac{1}{4}} = \int_{\alpha_i}^{\beta_i} V(t)\,dt$ $\xi_i = w - \int_{\beta_i}^{\gamma_i} D(t)\,dt$ $\xi_{i+\frac{1}{4}} = \int_{\gamma_i}^{\delta_i} V(t)\,dt$ $\xi_{i+\frac{1}{2}} = w - \int_{\delta_i}^{\alpha_{i+1}} D(t)\,dt$	$\xi_{i-\frac{1}{4}} = w + \int_{\beta_i}^{\gamma_i} V(t)\,dt$ $\xi_i = 2w - \int_{\gamma_i}^{\alpha_{i+1}} D(t)\,dt$ $\xi_{i+\frac{1}{4}} = w + \int_{\alpha_{i+1}}^{\delta_i} V(t)\,dt$ $\xi_{i+\frac{1}{2}} = 2w - \int_{\delta_i}^{\beta_{i+1}} D(t)\,dt$	$\xi(t)$

5.4.2 Properties Table

The formulae for each property in the two cases are summarised in Table 5.1.

In the edge case that $\xi = w$, the two columns are equivalent since $\gamma_i = \beta_i$ and $\alpha_{i+1} = \delta_i$

5.4.3 Radial Alignment

If the sensor is positioned on the face of the explosive charge farthest from the initiator the data can be used to measure the variation in breakout time across the width of the charge. The analysis is broadly similar to the axial alignment, except the reaction zone length ξ is replaced with its radial equivalent $\xi\tan(\theta)$ and the velocities replaced with their radial equivalents $D\tan(\theta)$ and $V\tan(\theta)$. Again there are two possible cases, although Case 1 is unlikely to occur

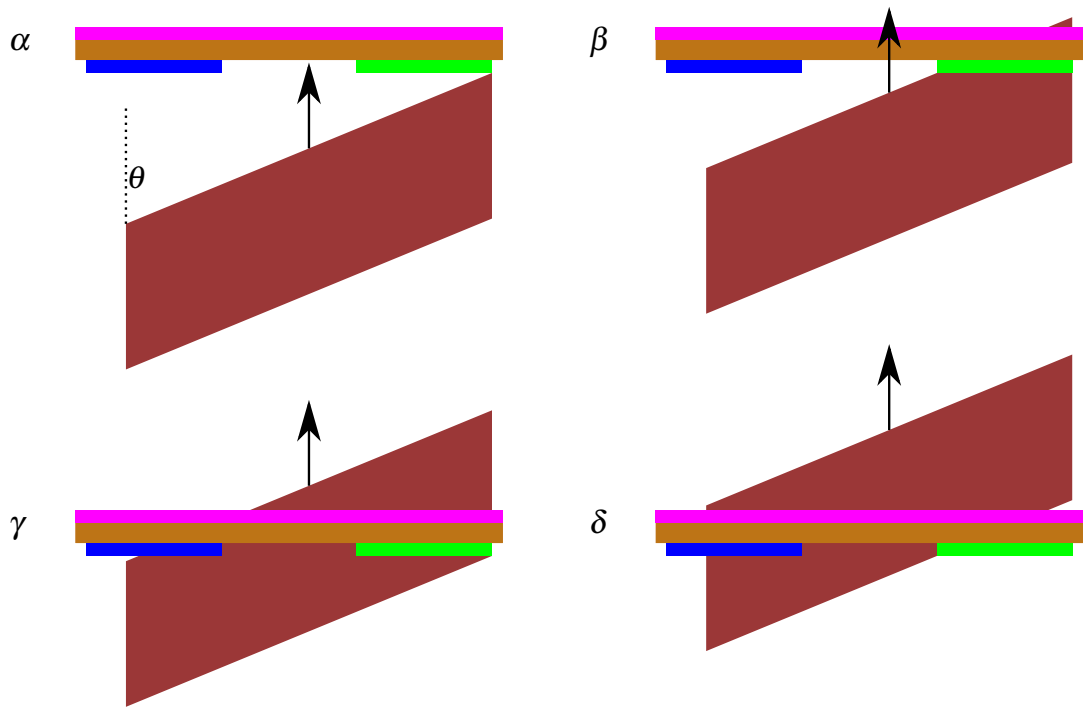

Figure 5.15 The front makes an angle θ to the axial direction. The timing points for the green channel are shown. The effective reaction zone is much wider due to the angle of the front relative to the sensor. In a real experiment the charge would end at the sensor so the reaction zone would not continue past it.

since it would require an extreme front angle of $>45°$. A section of the wavefront passing over a channel is shown in Figure 5.15

Since the sensor occupies a single plane, the data from a single experiment using the radial alignment of the sensor does not represent a single snapshot in time. A full picture of the time evolution of the curvature can be developed by performing multiple experiments with different charge lengths.

5.4.4 Edge Calibration

While the sensors are most effective when the reaction zone is directly above the receiver electrodes, there may be a small degree of detection slightly outside the extent of the electrode. This effect, illustrated by Figure 5.16 could lead to slightly inaccurate timing points. To correct for this effect, the timing points must first be assigned to points in space that do not exactly correspond to electrode edges and then corrected so that the above analysis and formulae in Table 5.1 are accurate.

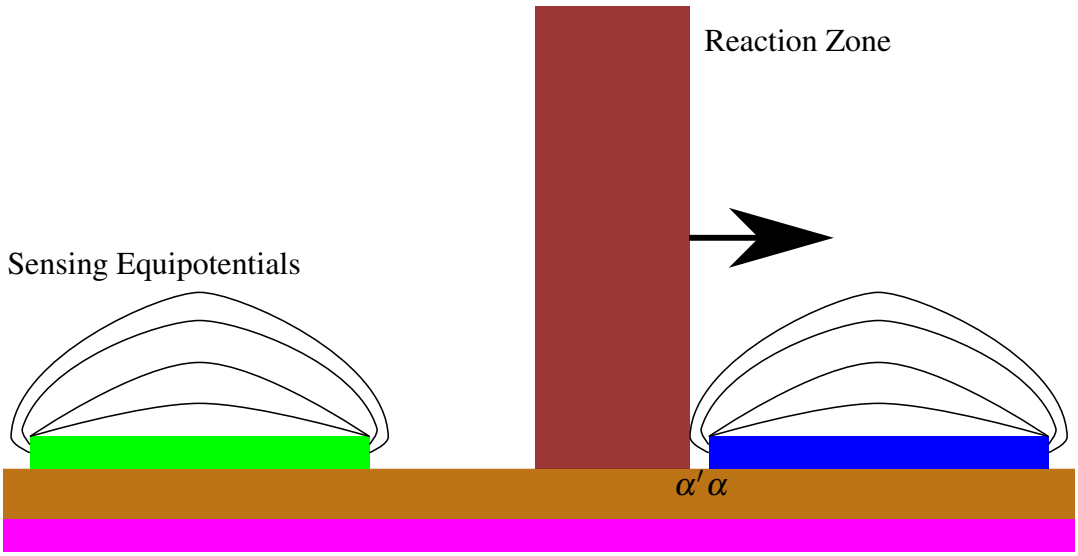

Figure 5.16 Cross-section of a reaction zone passing over a receiver electrode. While the sensing field is strongest directly above the receiver electrodes, there is inevitably some leakage. The sensor first detects the reaction zone at time α', whereas the reaction zone crosses the sensing zone slightly later at time α

The consequence of these shifts is that the wave will appear to move faster in between electrodes and slower while directly over them.

The symmetry of the sensor can be exploited to compensate for this effect. It is assumed that the stray fields are symmetric on each edge of the electrodes, and therefore that α_i and β_i (γ_i) (for $\xi < w$ ($\xi > w$)) need to be corrected forward in distance by the same amount that γ_i (β_i) (for $\xi < w$ ($\xi > w$)) and δ_i respectively need to be corrected backwards in distance. The corrections are shown in Table 5.2

An algorithm implemented in Matlab has the following steps:

- Start with w =0.5 mm and ε_D =0 mm
- Calculate the total velocity variation

$$S = \sum_i \left(\frac{w + 2\varepsilon_D}{\gamma'_i - \alpha'_i} - \frac{w - 2\varepsilon_D}{\alpha'_{i+1} - \gamma'_i} + \frac{w + 2\varepsilon_D}{\gamma'_{i+1} - \alpha'_{i+1}} - \frac{w - 2\varepsilon_D}{\alpha'_{i+2} - \gamma'_{i+1}} \right) \tag{5.26}$$

- Increment the value of epsilon
- Recalculate the total velocity variation
- Iterate until the total velocity variation is minimised and ε_D is found

Table 5.2 The corrections made to the timing points under the edge calibration technique. ε_D and ε_V are the corrections for the front and rear of the reaction zone respectively.

$\xi < w$	$\xi > w$
$\alpha_i = \alpha_i' + D(\alpha_i)\,\varepsilon_D$	$\alpha_i = \alpha_i' + D(\alpha_i)\,\varepsilon_D$
$\beta_i = \beta_i' + V(\beta_i)\,\varepsilon_V$	$\beta_i = \beta_i' - D(\beta_i)\,\varepsilon_D$
$\gamma_i = \gamma_i' - D(\gamma_i)\,\varepsilon_D$	$\gamma_i = \gamma_i' + D(\gamma_i)\,\varepsilon_V$
$\delta_i = \delta_i' - V(\delta_i)\,\varepsilon_V$	$\delta_i = \delta_i' - V(\delta_i)\,\varepsilon_V$

This algorithm is correct for $\xi < w$ – an equivalent for $\xi > w$ has the relevant replacements from Table 5.1. Equivalent algorithms can be used to find ε_V.

The timing points are then corrected as in Table 5.2

5.4.5 Errors

There are two categories of experimental uncertainty in the capacitive sensing apparatus – spatial uncertainty in the position of the sensing elements, and temporal uncertainty in the timing points.

The manufacturing process for the sensors uses a highly accurate photolithographic machine with a tolerance of $\pm 5\,\mu m$, or $\pm 1\,\%$ of the small electrode width w. The positioning of the sensor in the charge may also reduce the spatial accuracy if it is inserted at an angle, or is not flush to the surface. By aligning the shoulders of the sensor to be parallel with the face of the charge during insertion, the angular uncertainty can be reduced to approximately $\pm 1^\circ$, corresponding to a spatial uncertainty of around $\pm 17\,\mu m$.

The minimum uncertainty in continuous wavelet transforms is half a wave period, however with noisy data it is more typically 1-2 wave periods. For this analysis the temporal uncertainty is taken to be one period of the input signal. For a 500 MHz signal, with a 2 ns time period, the equivalent spatial uncertainty for a steady detonation wave in low density PETN is around $\pm 10\,\mu m$.

Furthermore, the oscilloscope has a rise time of 160 ps, so signal rise time accuracy is limited to around five times this, 800 ps.

All together, the errors amount to no more than a few multiples of the particle size. The most important experimental consideration is ensuring that the sensor is glued properly within the charge, and does not become damaged or dislodged during the pressing of the explosive. The sensor can be placed accurately to within $100\,\mu m$, but for the differential measurements on which most data are based the manufacturing error of $5\,\mu m$ is used. The pressing apparatus and procedure are described in the next chapter.

5.4.6 Summary

A summary of the data analysis process

- The timing points $\alpha_i, \beta_i, \gamma_i, \delta_i$, $i = 1...5$ are extracted via gradient analysis.
- The rise and fall times seen in the CWT misfit represent the reaction zone crossing the edges of the receiver electrodes
- Straightforward analysis is used to infer the position of the front and rear of the reaction zone over time, and therefore its detonation velocity, Chapman-Jouguet velocity and length.
- Corrections are made to $\alpha_i, \beta_i, \gamma_i, \delta_i$ by smoothing out any velocity zig-zagging using an iterative process.
- The temporal resolution of the system is approximately 2 ns and the spatial resolution is approximately 10 µm. Further spatial uncertainty may arise from the positioning of the sensor relative to the explosive.

5.5 Testing

Before using in a detonation experiment, the apparatus was tested for validation and calibration purposes. First the response of the sensors to a conducting probe was used to confirm that they did produce a signal, then they were tested with a shock tube

5.5.1 Probe Test

The testing data consisted of four 10 µs records, each with a different channel activated, and 10 µs with no activation. The activation was done using a metal needle tip brought close to the receiver electrode of channels 1 to 4 (the oscilloscope only has four input channels).

Figure 5.17 shows a subset of the raw data from one of the records where channel 2 was activated, showing the significant difference in signal shape and size. Not only is the amplitude approximately twice as large, there is a phase shift of around 180°, and a reduction in the contribution from higher frequency modes.

The five 10 µs records were joined together, and each channel processed using the continuous wavelet transform misfit method. The time-frequency representation of each channel is shown in Figure 5.18.

The jumps when each channel is activated can clearly be seen. In addition to the primary signal on the correct channel, small signals were also registered on the other channels.

5.5.2 Shock Tube Test

A second test was performed to check that the sensors could detect the change in conductivity created by an explosive reaction over fast time scales. A sensor was spliced into a 40 cm length of shock tube – a hollow plastic tubing lined with a thin layer of explosive. The shock tube used had an outer diameter of 3.0 mm, an inner diameter of 1.2 mm and an explosive load of 12.7 $\mathrm{mg\,m^{-1}}$ of HMX/aluminium. It was fired by using a capacitor bank to pass a high current through a resistor taped to the other end of the shock tube to the sensor. When the resistor explodes it creates a shock which initiates the explosive. The wave travels through the shock tube at a velocity slower than the detonation would be in bulk material, but still fast enough to be a worthwhile test. The apparatus is shown in Figure 5.19.

The shock tube velocity was measured in two ways – firstly using a straightforward time-of-arrival method, and secondly using the sensor. The first velocity provides a benchmark against which the second velocity can be compared. The benchmark velocity as measured over the whole length of the shock tube from the resistor burst to the time-of-arrival was $1.60(5)\,\mathrm{km\,s^{-1}}$. The velocity as measured using the interval between the signals from the first two sensing

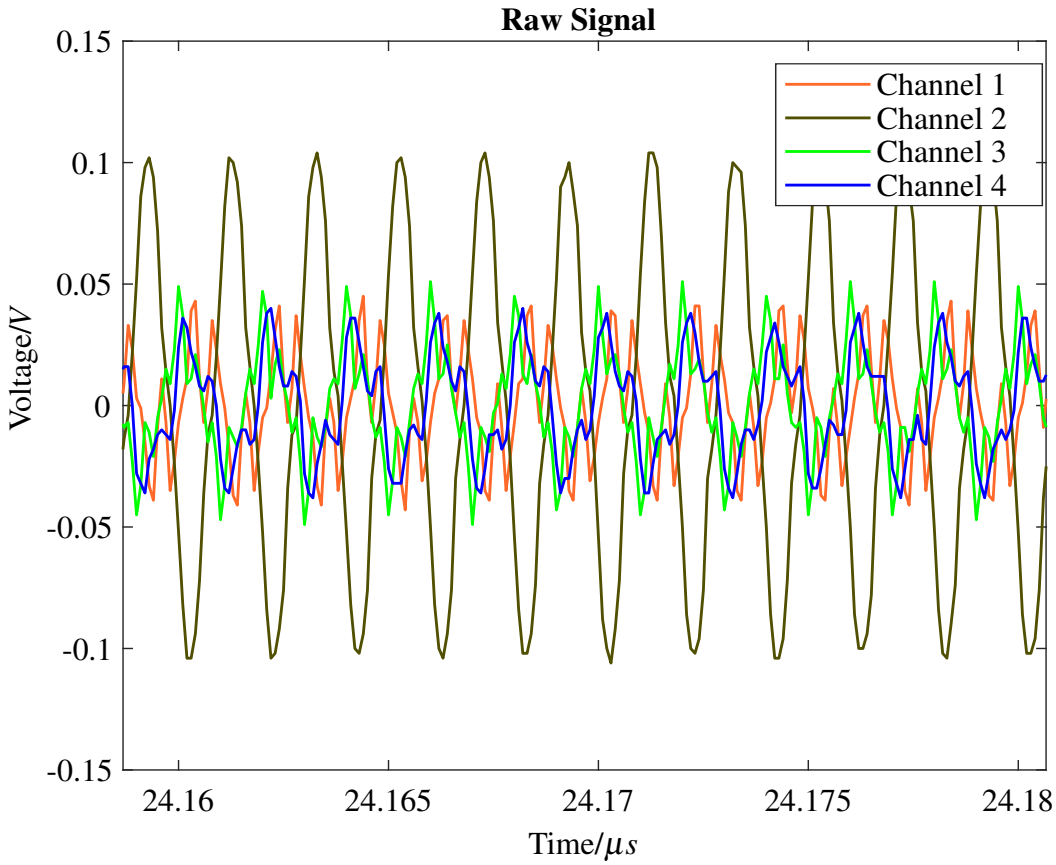

Figure 5.17 The raw signal while channel 2 was activated. Its signal is considerably larger than the other channels'.

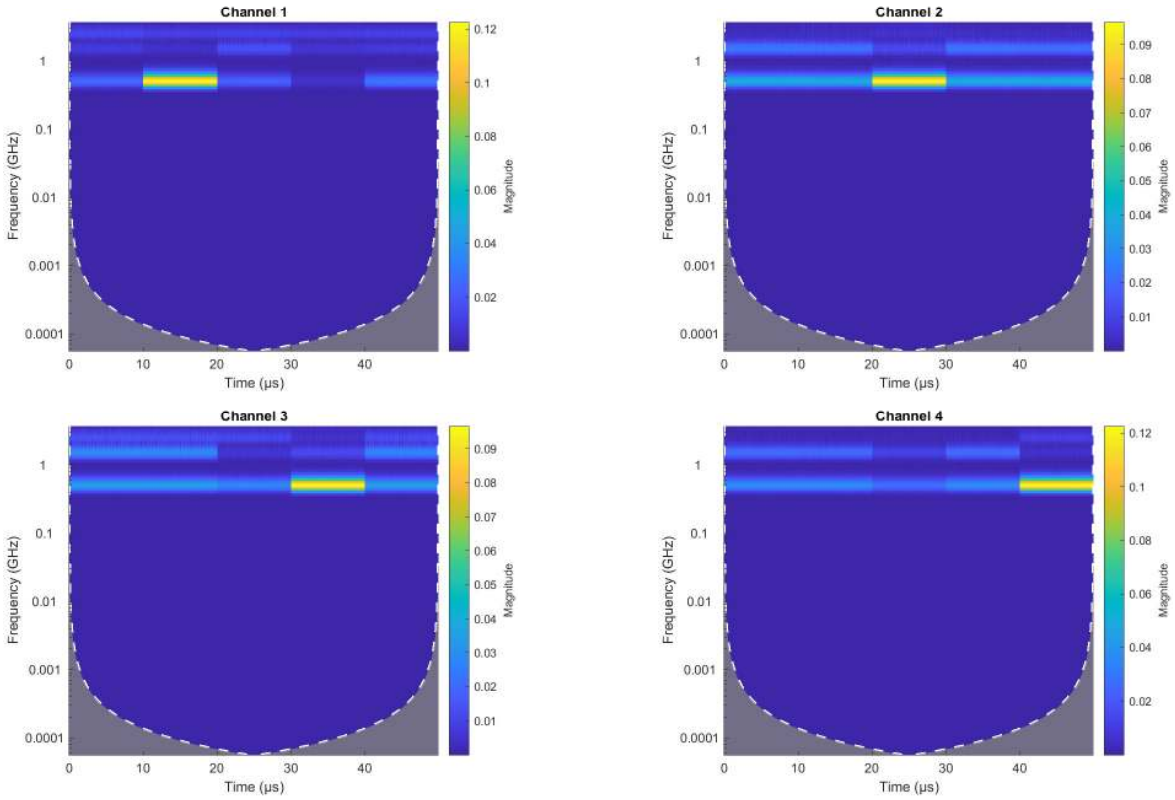

Figure 5.18 The amplitude spectrograms from the validation testing. The activated channels clearly stand out from the baseline (first 10 µs). There is some cross-activation where activated channels affect the signal from non-activated channels, however this effect is not significant. The largest frequency contribution is at the generator frequency 500 MHz, and more of the signal power is in this frequency during activation. Higher frequencies contribute less during activation – indicating the signal becomes more sinusoidal. The grey region at low frequencies is the cone-of-influence where edge effects become important, but this does not affect the region of interest.

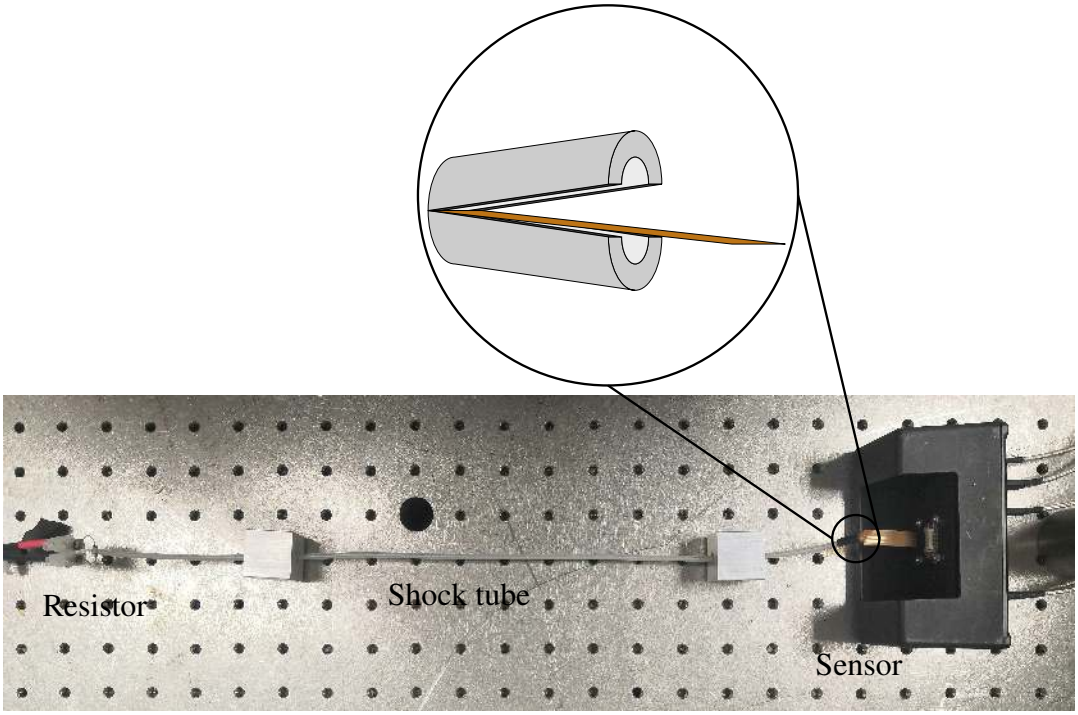

Figure 5.19 The apparatus used to test the sensors' response to an explosive reaction. 40 cm of shock tubing was initiated by an exploding resistor. The output of the tube was measured using a capacitive sensor spliced into a shock tube as shown, with the short channels in line with the inner surface. Electrical tape was used to hold both the sensor and resistor in place. Two aluminium blocks hold the shock tube in position.

zones was $1.67(2)\,\mathrm{km\,s^{-1}}$, however this quickly reduced at later sensing zones as the reaction expanded out of the end of the tube. The 4 % difference between the measured value and the 'true' value is probably due to the former being an averaged value while the latter is a more instantaneous measurement.

Several shots were performed using this apparatus. Raw traces from a typical shot are shown in Figure 5.20. Across all shots the common features were the resistor blowing and the initial shock front. The subsequent hot gas and alumina particles elicit a somewhat variable sensor response, however in all cases it lasts for around 200 µs. Brent et al. [178] observed light emission in a shock tube from a secondary combustion behind the initial shock – this may be the cause of the prolonged signal. The peak at the end of the trace did not appear for all shots, and is probably due to the sensor being damaged in a way that fundamentally changed the transfer function. The sensor was visibly damaged by some shots so this explanation is plausible.

These tests confirm that the sensors produce a signal when exposed to a reacting explosive. In contrast, detonating PETN should produce a stronger, sharper signal than the output of a shock tube.

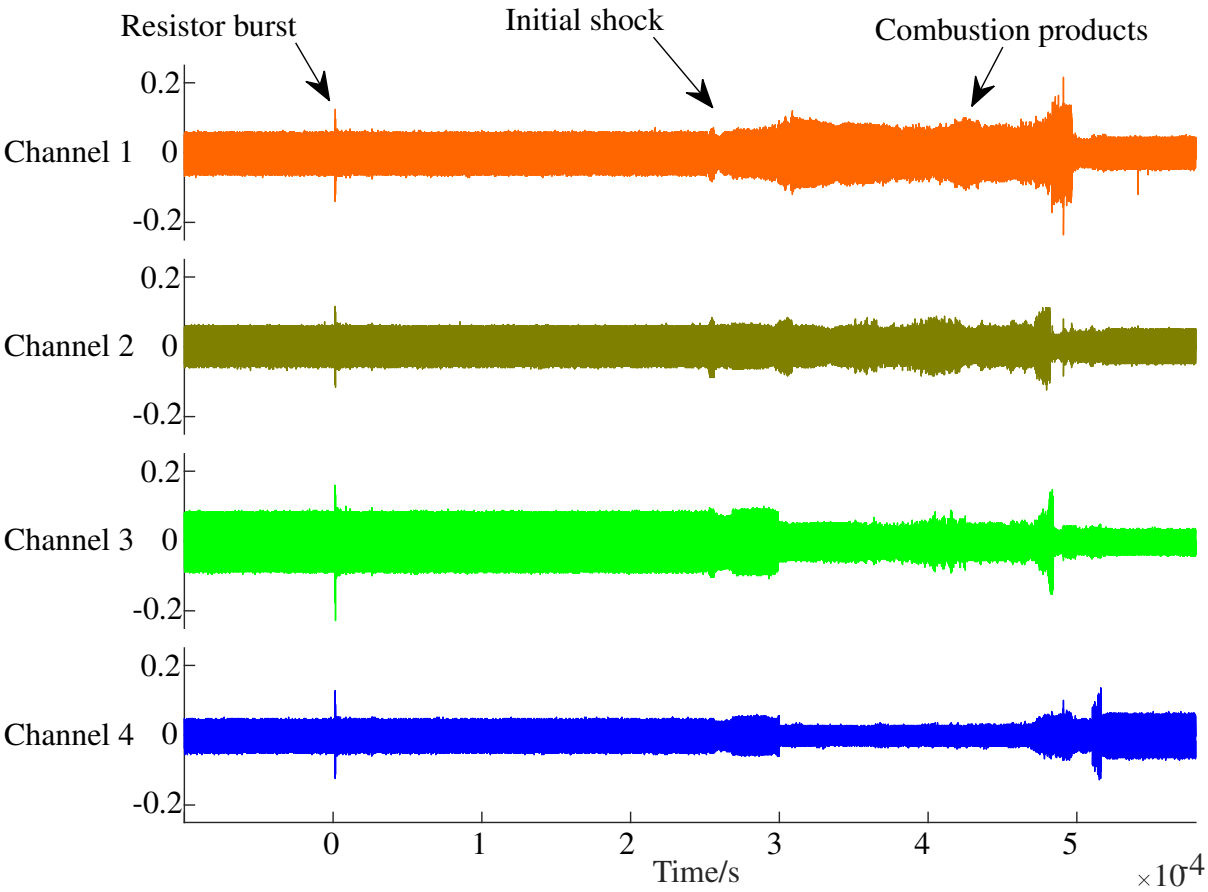

Figure 5.20 A typical signal from the shock tube. The shock reaches the end of the shock tube about 250 µs after the resistor burst. This time includes the initiation time and propagation time. Then follows a small but sudden change in the signal due to the shock front. This pulse lasts approximately 50 µs. Finally a larger change in the signal is produced by the hot reacting gas and solid particles which follow the shock and are more conducting. This phase lasts around 200 µs and varies over time and across channels, likely due to its turbulent nature.

5.6 Summary

A novel measurement system based on capacitive sensing has been designed and built for integration into small-scale detonation experiments.

- Capacitive sensing allows for non-intrusive detection of conducting objects.
- The extra capacitance introduced by the reaction zone changes the transfer function of the circuit to the signal produced by a high frequency wave generator.
- The strength of the signal depends on the conductivity and proximity to the sensor.
- Data is processed post-experiment to achieve a temporal resolution of 2 ns.
- The apparatus consists of flexible printed circuits connected to a wave generator and high bandwidth oscilloscope.
- Data is compared with a baseline signal via a continuous wavelet transformation and time-frequency to obtain the transient points of the transfer function.
- The capacitance history is then used to reconstruct the position-time graph of both edges of the reaction zone.
- The sensors were tested by measuring the velocity in a length of shock tube, and comparing this value against the velocity as measured by a conventional time-of-arrival method.

The next chapter describes experiments incorporating this new apparatus into the detonator systems described previously.

Chapter 6

Experimental Results

6.1 Introduction

Experiments were carried out to determine the effects of material and geometric properties upon the reaction zone length of PETN, and its evolution in time alongside the wave curvature. The research into this area to date has been very limited, and the diagnostic technique described here has not been used to study detonations before.

The apparatus for this investigation was a combination of the detonator systems described in Chapter 4 and the capacitive sensing system described in Chapter 5. A schematic of the full experimental apparatus is shown in Figure 6.1.

Two series of experiments were performed: firstly to determine the effect of density on the reaction zone and secondly to measure wave curvature and reaction zone length simultaneously at different points along the detonation axis.

For the first series, a capacitive sensor was placed on the outside edge of a PETN pellet, and used to measure the times at which the conductivity rose and fell at several points along the axis. These measurements were used to calculate the reaction time and reaction zone length. The data also allowed values for the detonation velocity and lost time to be calculated. Since there is significantly more existing literature data on these properties, these measurements served as a useful validation tool for the method as a whole.

For the second series, a sensor was used to measure the breakout times along a radius on the back surface of the pellet; these timing points gave the shape of the detonation front. For a small range of densities, these lag curves were produced at regularly spaced pellet lengths. By fitting analytical functions to the curves it was possible to derive values for the curvature. The reaction time and reaction zone length were also calculated in this configuration.

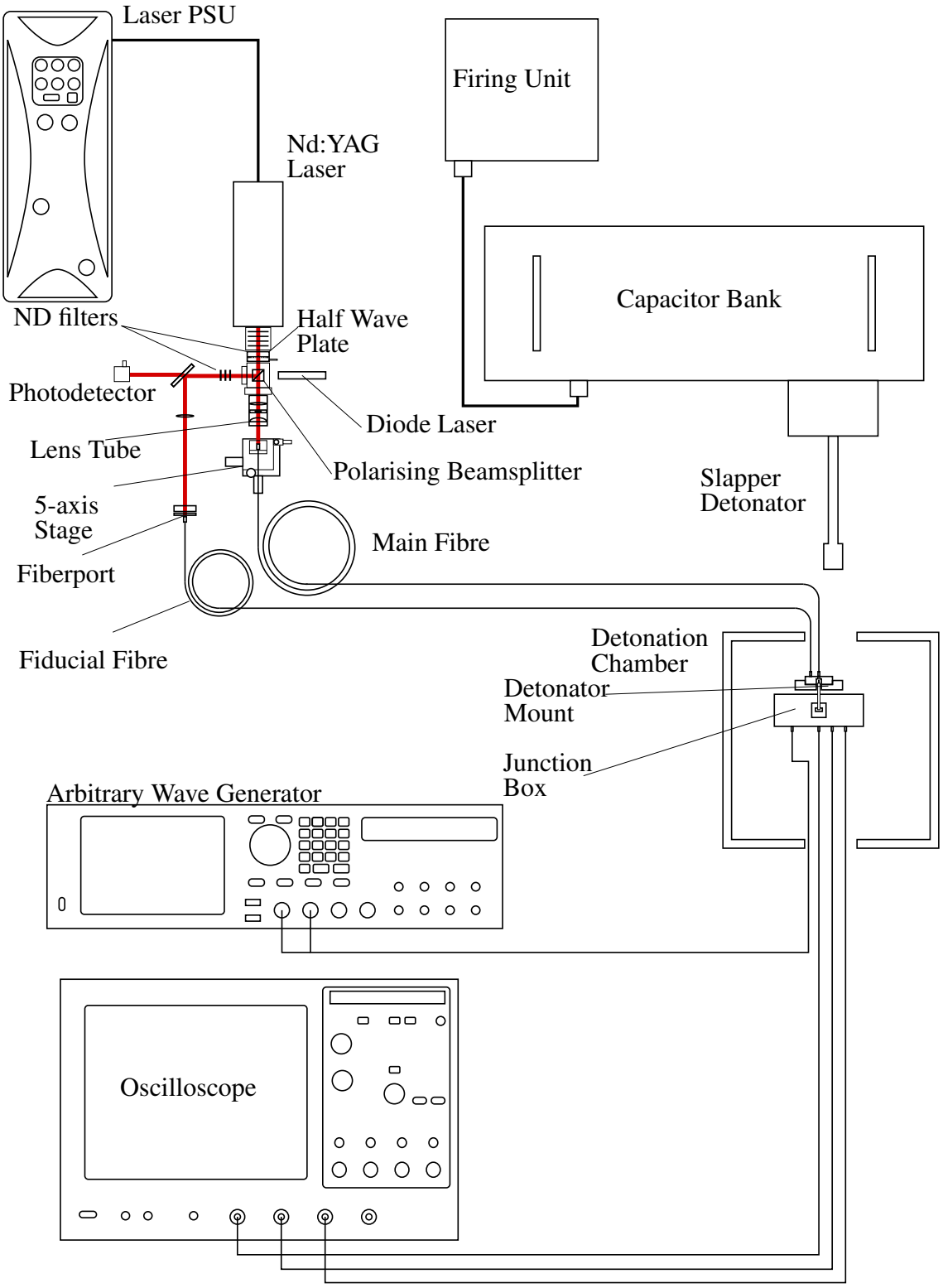

Figure 6.1 The two interchangeable detonator systems and the capacitive sensing system. Not shown is the delay generator which synchronises the initiation and diagnostics

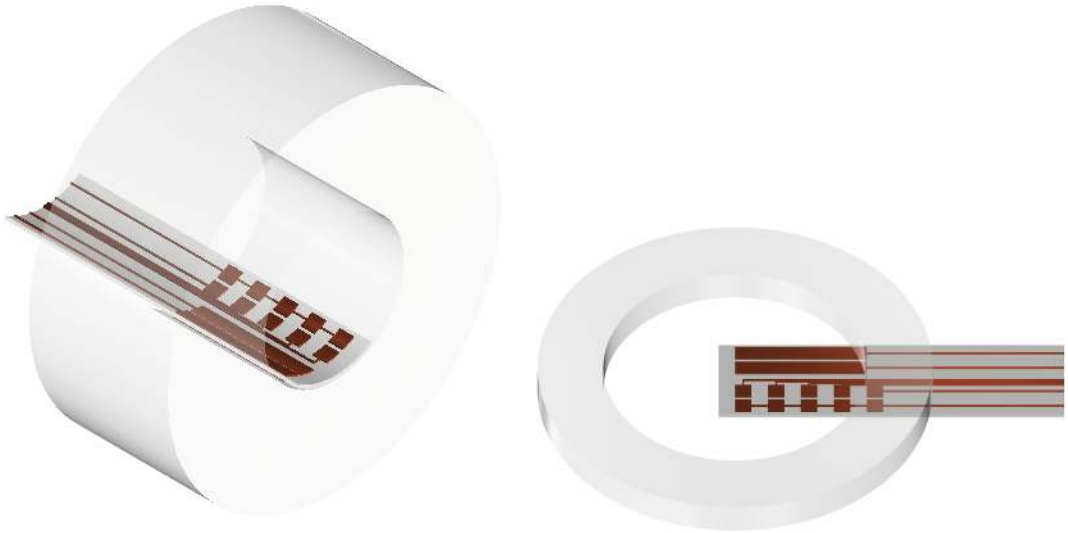

(a) (b)

Figure 6.2 The position of the sensor in the density (a) and curvature (b) experiments.

6.1.1 Material

The material used in these experiments was an ultrafine PETN powder originally produced for Gifford et al. [179]. SEM imaging of the powder (Figure 6.3) shows that it predominantly consists of tetragonal crystals 1 µm to 2 µm in size. The observed crystal habit suggests that it was prepared by a rapid crystallisation of concentrated PETN in acetone poured into water [19]. The loose powder has a density of $\approx 0.3\,\mathrm{g\,cm^{-3}}$. The powder is known to initiate for densities between 70 % ($1.24\,\mathrm{g\,cm^{-3}}$) and 76 % ($1.35\,\mathrm{g\,cm^{-3}}$) TMD for a laser flyer velocity of $5.3\,\mathrm{km\,s^{-1}}$, but not at 89 % ($1.58\,\mathrm{g\,cm^{-3}}$) TMD [157].

The small particle size means that it will reliably initiate, since the surface will have fewer deviations following pressing, providing many possible sites of initiation (see Figure 6.4 for an illustration). Another consequence, however, is that the reaction time will be small [180]. This effect occurs because smaller particles require less time for the reaction to travel from the shock initiated hot spots to reaction in the bulk material. The other available powders had particle sizes of $\approx 100\,\mu\mathrm{m}$, which were tested and found not to be reliably initiated by a laser flyer.

The size and shape of the particles means they are less vulnerable to fracture than larger, needle-shaped particles. They also have better flow properties than the needle-shaped particles, so they are more likely to retain their size and shape during pressing as they can move into gaps rather than be forced to break. Another consequence is that the initiation mechanism is likely to be dominated by pore compression and plasma heating as opposed to fracture stresses [42]. In the pore compression mechanism, interstitial gas is compressed, while viscoplastic work in

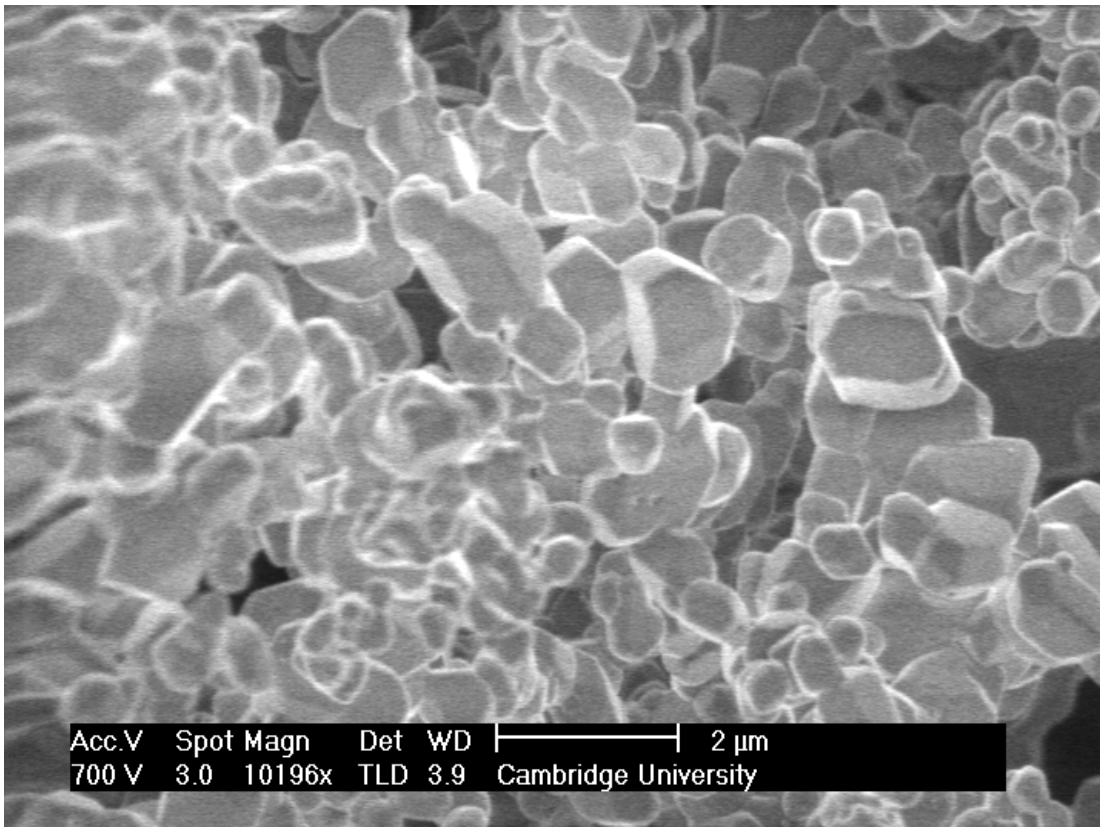

Figure 6.3 Scanning electron microscope image of the 'Ultrafine' powder, which has an average particle size of 1 µm to 2 µm. The surfaces of the individual particles appear to be smooth and free of cracks or cavities.

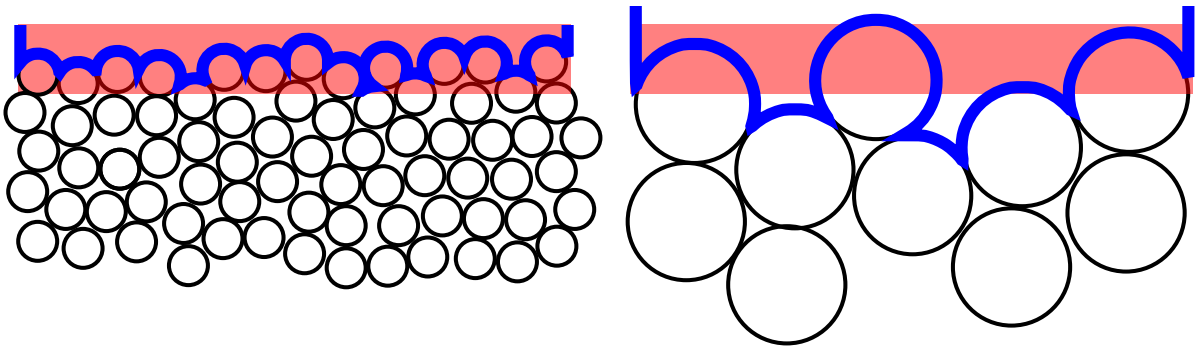

Figure 6.4 The effect of particle size on the surface metrology of a pressed pellet. For a given particle shape, smaller particles (left) result in fewer surface deviations and thus more potential sites of initiation. The blue line represents the exposed surface in each case, and the pink area represents the shockwave imparted by the flyer. Many more voids and points of particle contact are under shock when the particles are smaller.

the surrounding explosive further increases the temperature. Adiabatic shear banding is another possible contributor, although unlikely to be as significant as pore compression due to the short shock duration of a laser flyer.

6.2 Density Study

The investigation into how the density of PETN affected the reaction zone width was performed using a capacitive sensor placed longitudinally along the edge of a PETN pellet confined by PMMA. The densities studied varied between $0.90\,\mathrm{g\,cm^{-3}}$ and $1.40\,\mathrm{g\,cm^{-3}}$. For each shot, the laser flyer system was used with a pulse energy of 150 mJ, which corresponds to a flyer velocity of about $5.5\,\mathrm{km\,s^{-1}}$. The standoff distance between the flyer and the front surface of the PETN was 100 µm. The PETN pellet had a 5.0 mm diameter and was 5.0 mm long for all the experiments in the density study. These dimensions are close to those of common EBW detonators such as the Teledyne RP-80 [4].

6.2.1 Sample Preparation

Preparation of the PETN pellet is an important process to optimise in order to obtain consistent and useful experimental data. Two vital aspects of preparation are to minimise density gradients in the powder caused by the pressing process and to ensure the sensor is accurately positioned relative to the pellet. These two concerns are the biggest contributors to experimental uncertainty in the data.

Sensor Placement

In order to obtain accurate data, it is important that the sensor is well aligned within the cylindrical explosive charge. This alignment was complicated by the small size of both components. The alignment was done by eye, but with several optical aids. The charge was placed in a mount fixed to an optical table with the axial direction horizontal. The apparatus was illuminated to provide contrast between the translucent PMMA casing and opaque sensor. A lens was used to magnify the components and a plane mirror gave two simultaneous views: end-on and side-on. A small drop of glue was placed on the back of the sensor head, which was then placed into the casing. Using the edges and copper tracks as guides, the flat surface of the sensor was bent to fit the inner cylindrical surface of the casing and held in place while the glue dried. The side-on view ensured that the angular alignment was correct, while the end-on view was used to check that the sensor was flush with the surface. With careful placement it was possible to reduce the uncertainty in the axial placement of the sensor to 100 µm. Since most measurements rely on differential measurements between sensing zones, the sensor's manufacturing error is used instead, which was taken to be 5 µm. The arrangement is shown in Figure 6.5.

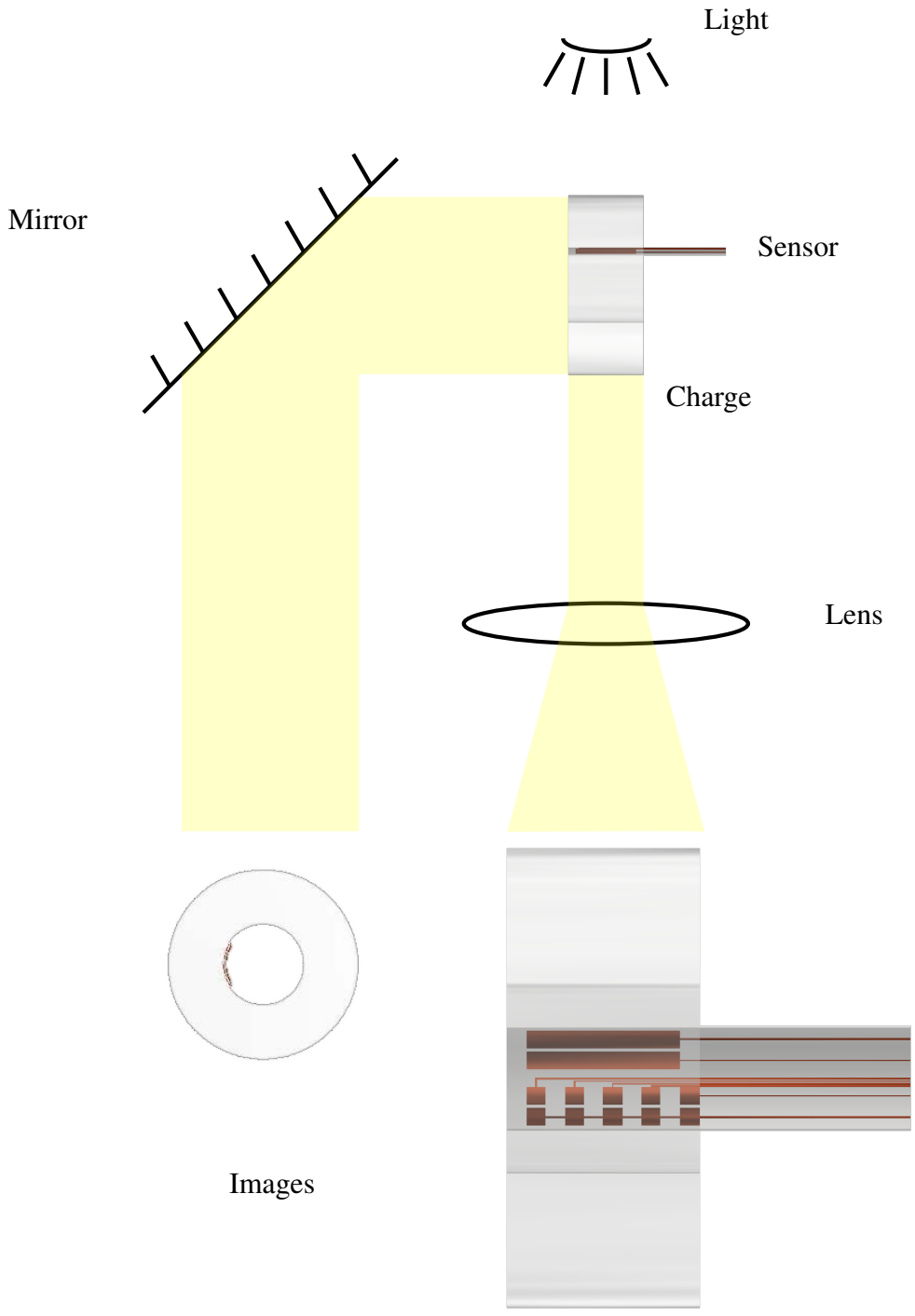

Figure 6.5 The cylindrical casing is viewed from two different angles while the sensor is inserted. Magnification improves the positional accuracy that can be achieved by eye.

With the sensor attached to the empty PMMA casing as in Figure 6.2(a), it was then placed inside the die of the powder press described in the next section.

Powder Press

In preparing the sample, it is desirable to reduce inhomogeneities that could introduce experimental variation. While the granular nature of the material inevitably produces some mesoscale variation between samples, proper preparation can reduce the density gradients that occur on the scale of the whole sample.

Friction between the powder and the wall of the die can lead to radial and axial density variation [181]. The normal outcome for a unidirectionally pressed cylindrical charge is for the top of the charge to have a low density region at the centre and a high density region at the outer circumference. At the bottom of the charge, the reverse occurs, and there is lower density at the outer circumference than in the centre, as illustrated in Figure 6.6. A density variation of this nature would cause the detonation at the centre of the charge to accelerate more than in a homogeneous pellet, whereas the acceleration at the edge of the pellet would be smaller than would otherwise occur. In extreme cases, these density gradients can lead to 'sombrero curves', where the centre and edge both lag behind some intermediate point [182].

Kumar et al. [183] developed a double action pressing process with which the axial density variations of a shaped charge were reduced from 3 % to 0.25 %. They used removable spacers to control the amount of press movement in each direction. The same principle has been applied here, but the process differs in that wall friction is exploited to balance the two directions and regulate the pressing action.

This novel approach was applied using a specially designed pressing apparatus. The design involving a free floating outer die containing two pistons and inner dies, as opposed to conventional powder presses which just have a single die and piston. The pistons, dies and casing cylinder are all free to move axially relative to each other, but have relatively tight tolerances to reduce non-axial movement. The design exploits the principle that the friction between the wall and powder is transmitted better through denser powder. As pressure is applied to both pistons, the one which moves relative to the die is the one which faces least resistance from the powder, and therefore also the one at the less dense end. As the piston moves, the powder at its end densifies and resistance increases until it exceeds the force required to move the other piston. In this way the pistons alternately compress the powder in a way that reduces the effect of having a preferential pressing direction.

The bottom piston of the press is modified to allow it to accommodate the capacitive sensor. The sensor is glued to the inside of the cylindrical casing using the technique detailed in the previous section. A small indent is machined into the cylindrical surface of one of the pistons,

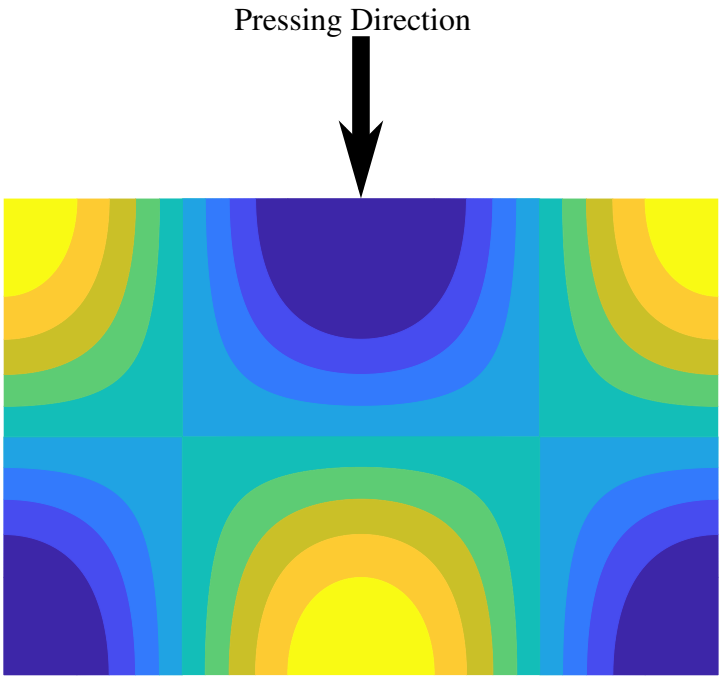

Figure 6.6 Qualitative illustration of the density variations that arise from single directional pressing. When a cylindrical charge of powder is pressed with a single pressing direction, regions of high density (yellow) occur along the outer circumference of the top end and in the centre of the bottom end. This effect is more pronounced with higher powder-wall friction.

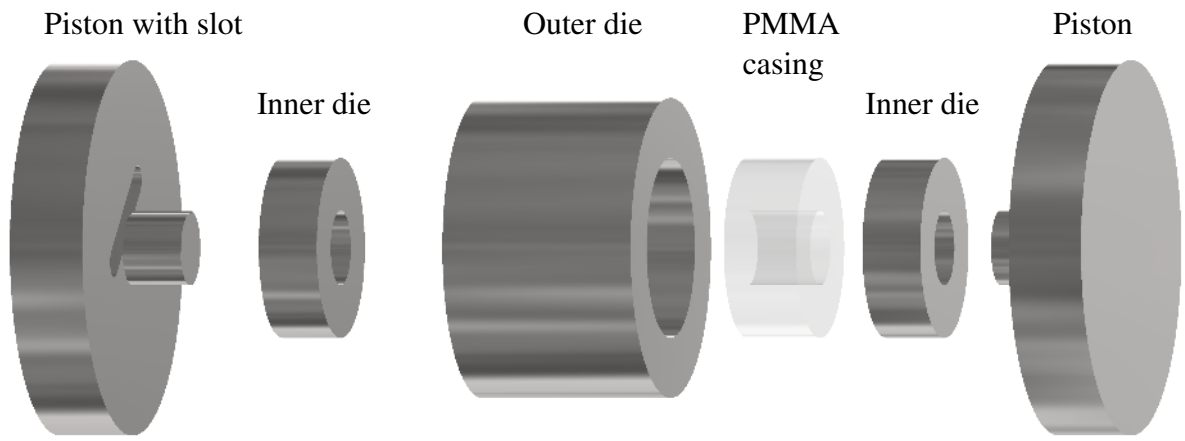

Figure 6.7 The press consists of two pistons (one of which is adapted to accommodate the sensor), two inner dies and an outer die.

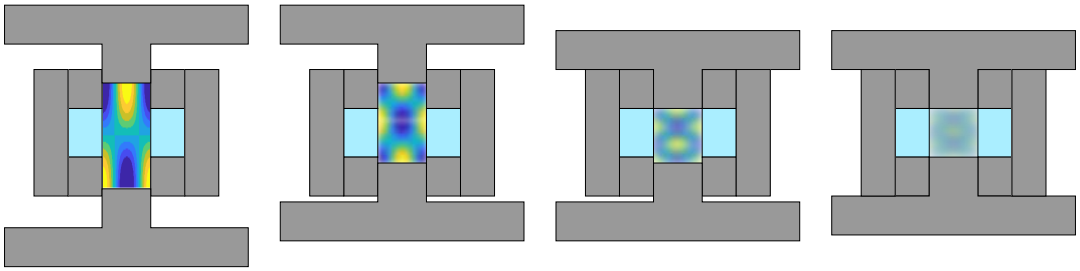

Figure 6.8 In the double action floating die press, the pistons alternate according to which faces the least resistance. The density variation seen in Figure 6.6 is applied alternately from each end, each time reducing the magnitude of the variation. In this way the density gradients are smoothed out.

allowing it to pass over the sensor. A slot in the top part of the same piston allows the sensor tail to protrude so it does not become damaged during pressing. An expanded view of the press is shown in Figure 6.7 and its double action mechanism is shown in Figure 6.8.

Experimental Procedure

With one of the pistons removed, the casing was carefully filled with the powdered explosive using a paper funnel until the desired mass was reached. The piston was then placed inside its inner die and the assembly was placed in a manual press machine. The pistons were brought together until they were flush with the outer die, indicating that the volume was correct. The press was left in situ for two minutes to prevent reassertion upon release – it was then transferred to the detonation chamber. Inside the detonation chamber, the charge was extracted

from the press and loaded into the detonator mount, which had already been attached to the laser flyer system. The tail end of the capacitive sensor was inserted into the junction box, and the detonation chamber sealed.

The experiment was triggered remotely – a sharp audible sound indicated that the detonation was a success. The gaseous products were removed from the detonation chamber via extractor fan between shots.

6.2.2 Results

The raw data was in the form of voltage traces for four channels, the relevant portion of which spanned approximately 1 µs. This data was then processed using a custom-made continuous wavelet transformation method detailed in Chapter 5. An example of the raw oscilloscope data, as well as its processed form is shown in Figure 6.9

The processed data provided a sequence of timing points that mark the rise and fall of conductivity at the relevant edge of each sensing zone. Each sensing zone edge provides two timing points – one as the detonation front passes over, and another as the sonic locus passes over. These timing points are plotted in distance-time coordinates (Figure 6.10).

Several features of these plots are immediately evident. The gradient of the front position with respect to time increases up to a constant value, indicating the expected increase in detonation velocity to the steady state velocity. The exception is the $1.30\,\mathrm{g\,cm^{-3}}$ experiment where the opposite occurs. This anomaly is probably due to the sensor detaching at some point before or during the experiment. The denser the pressing, the greater the steady velocity.

The detection time also becomes earlier as the density increases. This trend is a function of both the theoretical transit time and lost time shrinking with increasing density. The lost time is explored in more detail in a later section.

The gap between each pair of points gives the reaction time at that position along the sensor. While there are several anomalous pairs with greater separation (for example the second pair at $1.05\,\mathrm{g\,cm^{-3}}$ and the fourth pair at $1.10\,\mathrm{g\,cm^{-3}}$) this value is generally of the order of 10 ns.

A final observation is that at higher densities the gradient seems to be less consistent within each sample, indicating variation in the wave velocity. While best efforts were made to avoid it, the most likely cause for this effect is density variation. Such variation would be a more significant effect at higher densities since being further from the loose powder density means the amount by which the local density at a particular point could deviate from the desired density is greater.

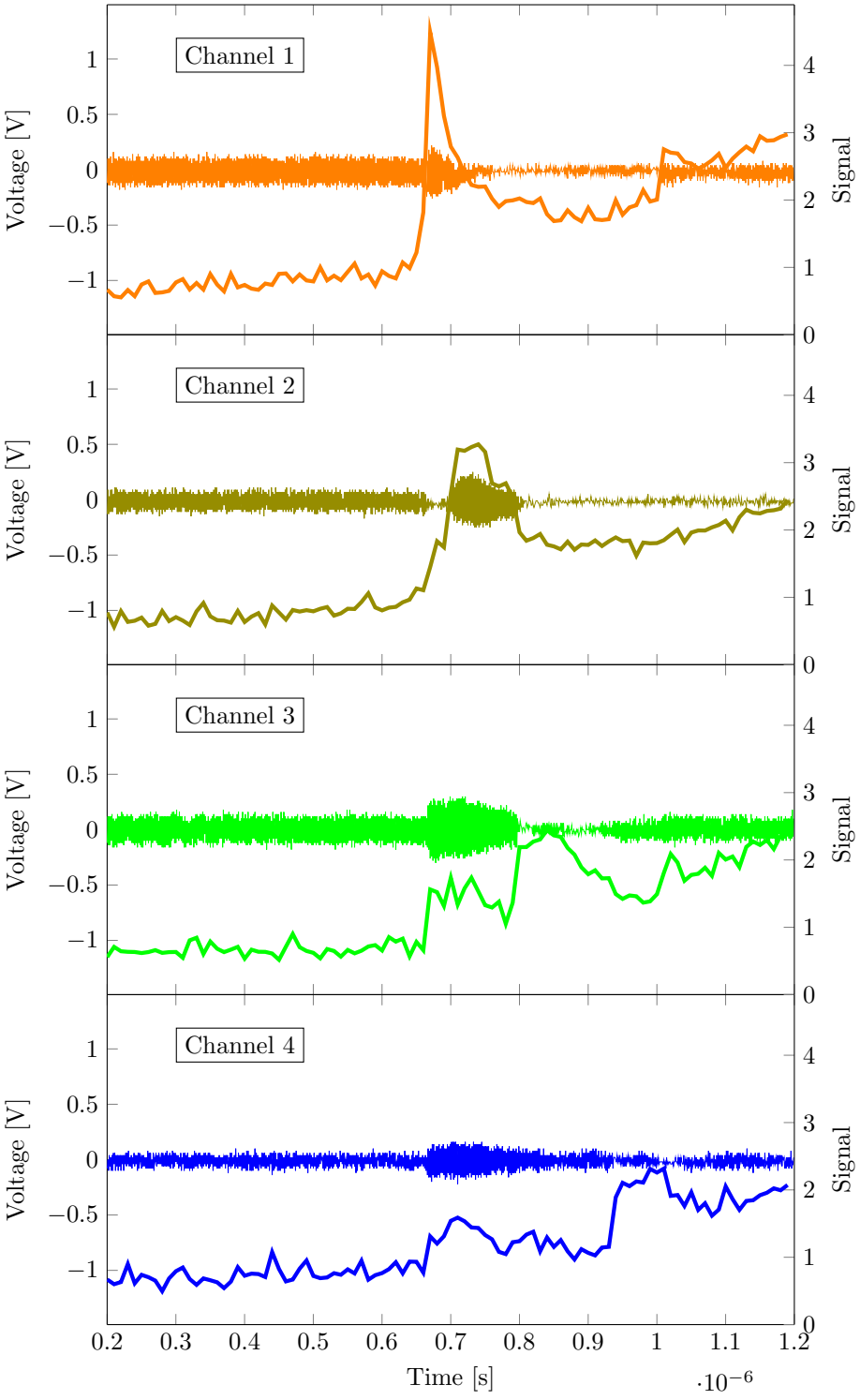

Figure 6.9 Raw data produced by the capacitive sensing system (thin line) and the transformed signal (thick line). Shown is ultrafine PETN at 1.05 g cm^{-3}.

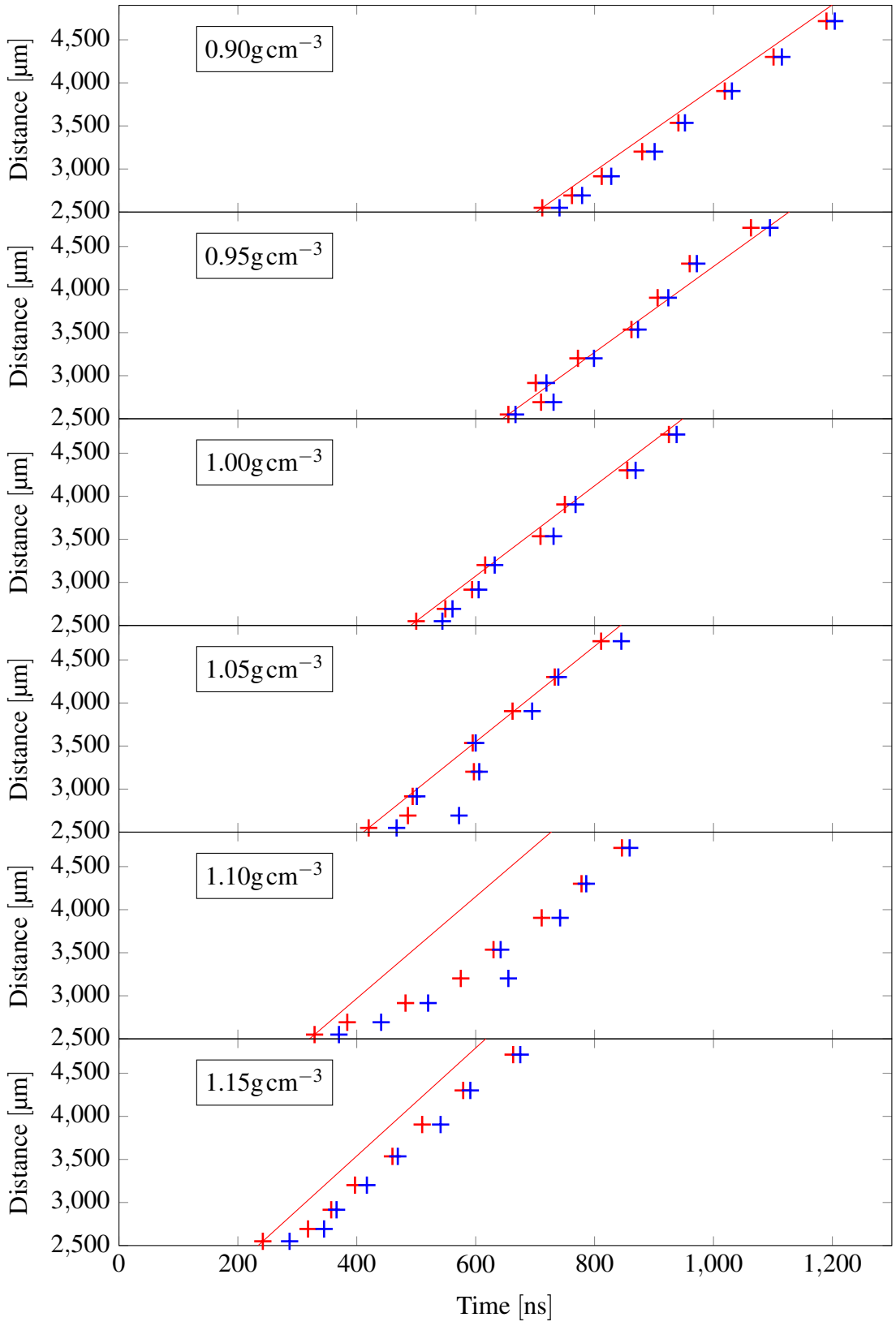
0.90g cm−3
0.95g cm−3
1.00g cm−3
1.05g cm−3
1.10g cm−3
1.15g cm−3
Distance [µm]
2,500
3,000
3,500
4,000
4,500
0
200
400
600
800
1,000
1,200
Time [ns]

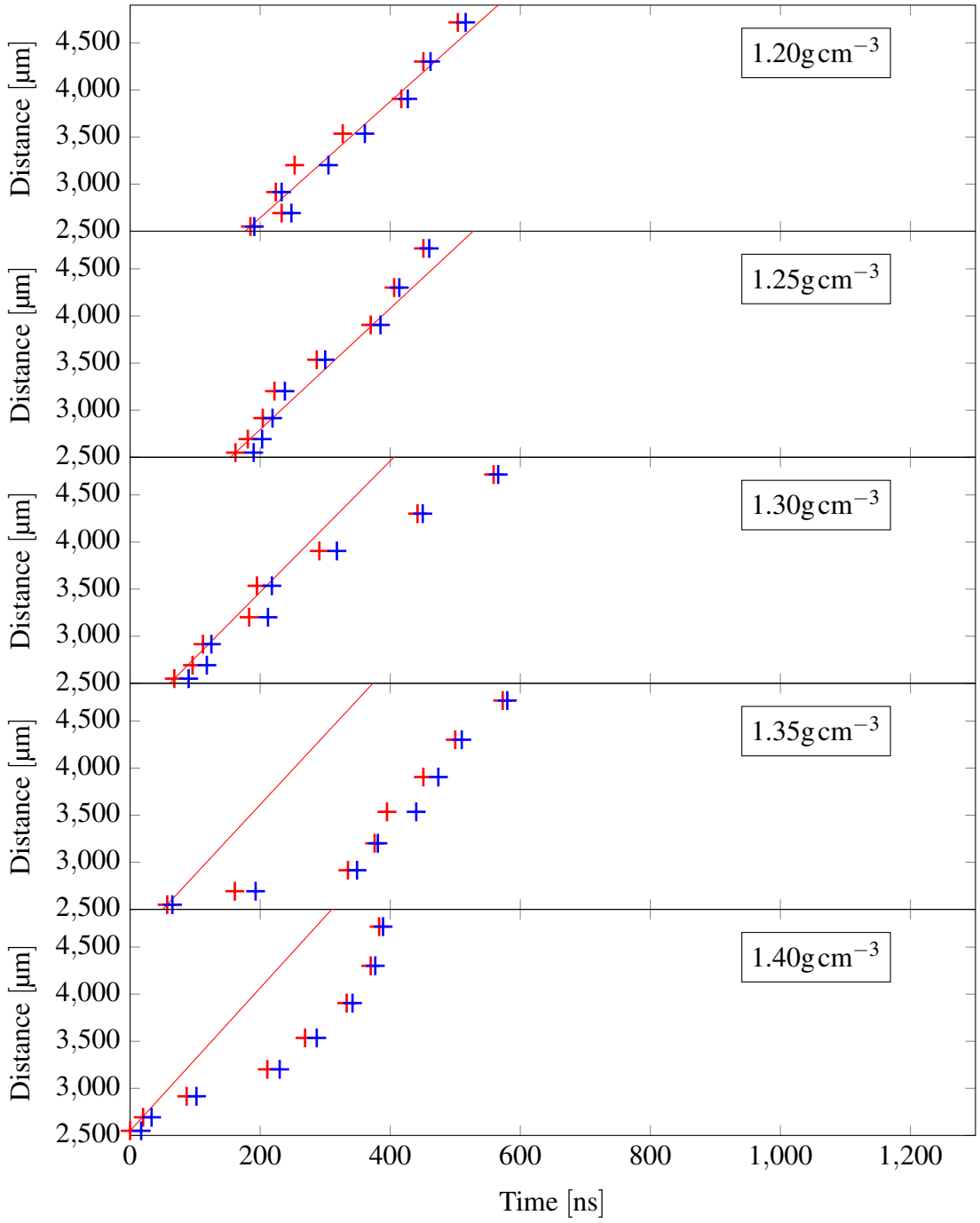

Figure 6.10 Distance-time plots for the density study. The red marker indicates the front of the conducting zone and the blue marker indicates the rear. For easier comparison the times have been shifted so that the detection time of the densest sample is at zero. In this shifted coordinate system the laser pulse occurred at −500 ns. The red line shows the position of the detonation front assuming the wave travels at the steady state velocity from the point of first detection. As can be seen by the difference between the red line and the red data, the wave is generally not yet at the steady state velocity when it is first detected.

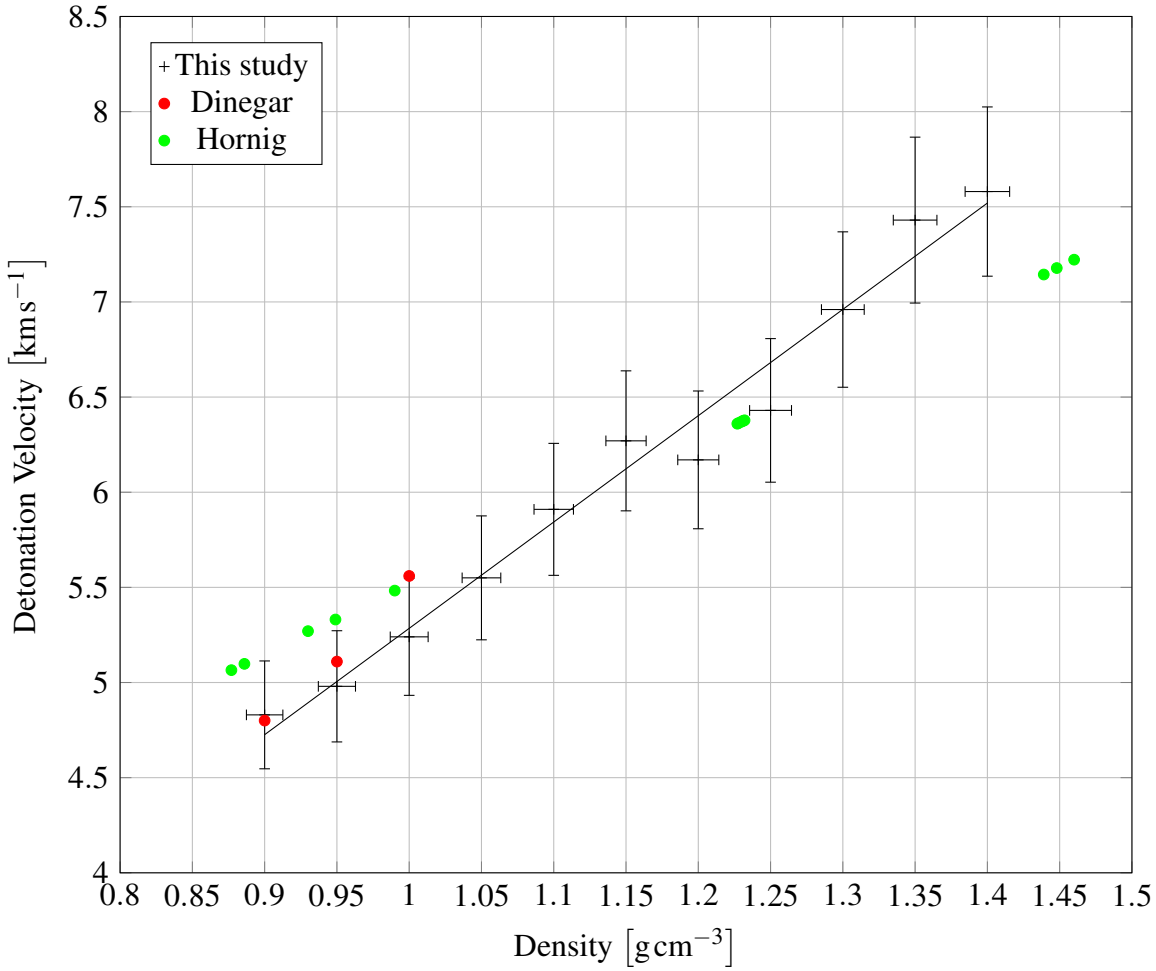

Figure 6.11 The detonation velocities measured using the last sensing zone of the capacitive sensors. Also shown are values from Dinegar [184] and Hornig [185]. The experimental results differ from those of Hornig [185] at higher densities

Detonation Velocity

The detonation velocity at each density was calculated using the gradient of the timing points for the front of the conducting zone. It is therefore possible to directly see the evolution of the detonation velocity as the wave moves through the explosive.

In general the detonation velocity ramped up from a smaller value at the first sensing zone, to a larger steady value for the later sensing zones. These steady velocities are shown in Figure 6.11. Anomalous points were ignored for the purpose of calculating these velocities. The calculated steady state velocities are in reasonably close agreement with the literature values [184, 185]. There is however some small discrepancy, which may be explained by differences in experimental setup – Dinegar [184] used a larger diameter charge. The diameter effect would

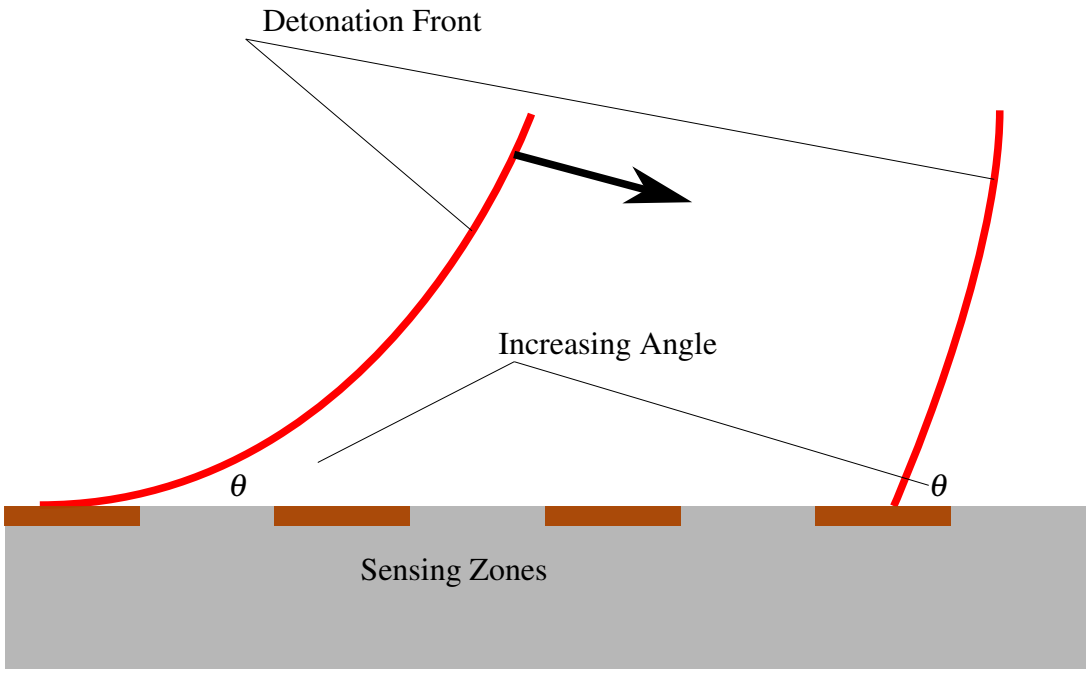

Figure 6.12 As the angle between the detonation front and sensor increases, the timing points are further apart, so the percentage uncertainty in the velocity decreases.

be expected to increase the detonation velocity for larger diameters, hence the discrepancy at lower densities. At higher densities the experiments yield detonation velocities that are larger than those in [185]. The experimental error was large for these measurements, and it is possible that there were additional uncertainties that were not considered here. Steady state detonation velocity follows an approximately linear relationship with density over the range tested, although extrapolating this gradient would slightly overestimate the TMD detonation velocity – therefore the gradient is expected to flatten at higher densities.

The errors shown arise from uncertainty in identifying the timing points and uncertainty in the position of the sensing zone edges. Due to the high temporal resolution of the diagnostic and the process used in sensor positioning the overall error is small. The uncertainty in the measurement decreases for later sensing zones as the angle between the front and the edge of the charge increases and the detonation direction becomes more aligned with the sensor (see Figure 6.12).

The calculated velocity midway between two sensing zone edges is given by:

$$D = \frac{w \sin(\theta)}{t_2 - t_1} \tag{6.1}$$

where t_1 and t_2 are the times of arrival at each edge, w =0.5 mm is the distance between the edges, and $\tan\theta = \frac{z}{R}$ with z being the axial position of the midpoint and R the radius of the charge. The uncertainty in D is then:

$$\frac{\sigma_D^2}{D^2} = \frac{\sigma_\theta^2}{\tan^2\theta} + \frac{2\sigma_t^2}{(t_2-t_1)^2} = \frac{R^2\sigma_z^2}{R^2 z + z^3} + \frac{2\sigma_t^2}{(t_2-t_1)^2} \tag{6.2}$$

The second term is small and constant, but the first term becomes large for small z.

While this method is not the most accurate technique for obtaining a steady state detonation velocity due to small charge length, it does provide credibility to the capacitive sensors as a method for measuring detonation features.

Lost Time

Since the laser pulse timing was recorded for each shot, the data can also be used to infer some information about the detonation prior to detection by the first sensing zone.

The detection time was taken as the time between the laser flyer impact and the first sign of detection at the first sensing zone. The detection time was measured by subtracting the laser flyer flight time from the interval between the laser pulse and the first sign of detection. The flight time is assumed to be constant between experiments since the same flyer launch parameters were used for each shot. With a flyer velocity of 5.5 $\mathrm{km\,s^{-1}}$ and a standoff of 100 µm, the flight time is approximately 18 ns.

The theoretical transit time was the time that a detonation travelling at the previously calculated steady state velocity would take to travel from the initiation point to the first sensing zone. The lost time (also called excess transit time in literature) was then calculated to be the difference between the detection time and theoretical travel time. The lost times for each density are shown in Figure 6.13.

At higher densities the lost time decreases, indicating that the detection time more closely matches the theoretical travel time. There was about 520 ns of extra delay in the shot at 0.90 $\mathrm{g\,cm^{-3}}$ relative to the shot at 1.40 $\mathrm{g\,cm^{-3}}$. The lost time has two possible sources to consider: a delay between flyer impact and initiation, and the wave velocity between the initiation site and sensing zone being smaller than the steady velocity.

The first explanation – that there is a delay between impact and initiation – may feasibly cause variation with density and is worth consideration. In order for a detonation to develop, there must be chemical energy release before the end of the imparted shock, otherwise the release wave will quench the hot spots and they will not grow [157]. Since the thickness of the flyer plates is only ≈4 µm, the imparted shock is very brief – of the order of 1 ns and the release wave from the rear of the flyer follows soon after. The shock from the flyer does not penetrate

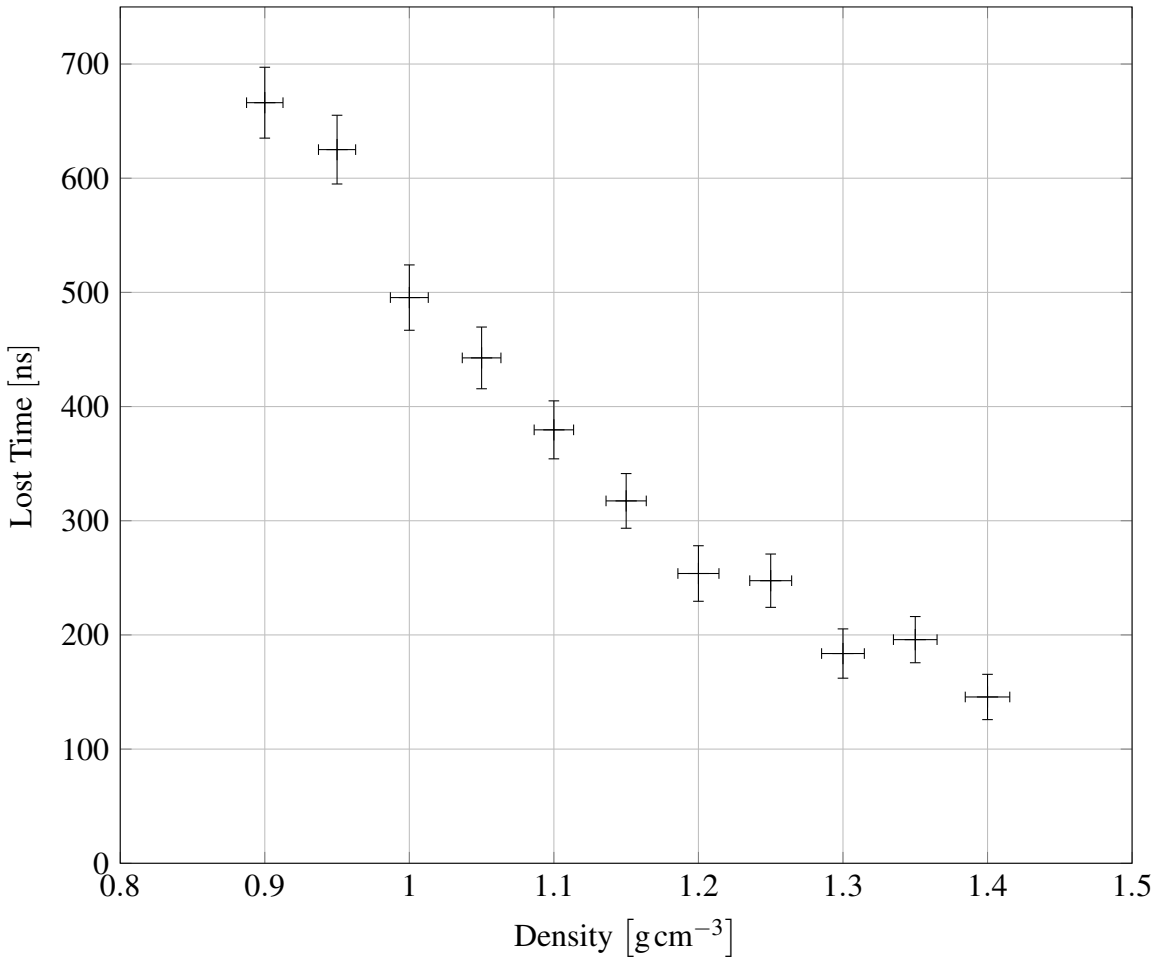

Figure 6.13 The lost time vs. density. 18 ns of laser flyer flight time has been subtracted from these measurements.

far into the powder before detonation commences, otherwise the release wave will overtake it. The run to detonation time is therefore very short, so it is not possible for a significant part of the lost time to be due to the run to detonation and it can effectively be ignored.

The second, and most significant contribution to the lost time is the velocity deficit. Since the wave is travelling from the centre to the edge of the pellet, its curvature is changing, and therefore the velocity D will be smaller than the steady state velocity D_∞. Post-detection ramping up is seen explicitly in Figure 6.10; this analysis attempts to capture the behaviour before detection.

Wood and Kirkwood [8] made the following approximation for how the velocity deficit depends on curvature:

$$\frac{D}{D_\infty} = 1 - \beta \frac{\xi}{S} \tag{6.3}$$

S and ξ are the radius of curvature and reaction zone length respectively. β is a state-dependent constant approximately equal to 3.5. This approximation is less valid for small radii of curvature, and clearly does not work at all for $S < \beta\xi$. A slightly more complex model introduces a cut-off S_c to avoid this divergence [69].

$$\frac{D}{D_\infty} = 1 - \beta \frac{\xi}{S - S_c} \tag{6.4}$$

Integrating between two general distances x_1 and x_2, and subtracting the theoretical transit time $\frac{x_2 - x_1}{D_\infty}$ gives:

$$t = \frac{\beta\xi}{D_\infty} \ln\left(\frac{x_2 - S_c - \beta\xi}{x_1 - S_c - \beta\xi}\right) \tag{6.5}$$

This time is generally of the order of 100 ns, indicating that the velocity deficit makes up the majority of the lost time. However, a more elaborate model is needed to account for the lost time between initiation and the cut-off distance.

The lost time found here at $1.00\,\mathrm{g\,cm^{-3}}$ (0.51 µs) is shorter than that found by Lee et al. [2] for both EFIs (0.76 µs) and EBWs (0.99 µs). The decrease in lost time with increasing density also exists in EFIs – a $1.6\,\mathrm{g\,cm^{-3}}$ pressing had a lost time of 0.16 µs [2]. The powder used here has a smaller particle size and therefore the reaction zone length and velocity deficit are smaller.

The input shock pressure from a laser flyer is ≈1.5 greater than that of an EFI for equal densities [186][2], so the run to detonation distance will be similar – of the order of a few microns, and the run to detonation time will be a few nanoseconds. Bowden [152] tested flyer-initiated PETN of different specific surface areas at $1.6\,\mathrm{g\,cm^{-3}}$ and found very little lost

time, with no dependence on flyer energy. Therefore it can be concluded that the contribution to lost time from the run to detonation is minimal.

Extrapolating from Figure 6.13 implies that lost time would fall to zero at approximately $1.50\,\mathrm{g\,cm^{-3}}$. In reality it would level out, and even at TMD there would still be a small amount of lost time, since the wave cannot accelerate to the steady state velocity instantaneously. For general shock initiated detonations, zero or negative lost time could be observed if the detonation was overdriven, with the initial shock velocity exceeding the steady state detonation velocity. However, in this case the short shock duration means that release waves from the rear of the flyer would almost immediately reduce the velocity, so it is very unlikely that a wave could remain overdriven for long enough to significantly reduce the lost time in this scenario.

The conclusion is that the increasing lost time at lower densities must be due to variation that occurs after detonation is achieved, such as the velocity deficit due to curvature.

Reaction Time

The calculated timing points also made it possible to calculate the width of the conductivity peak. There is a question of how closely the rise and fall in conductivity match the Von Neumann point and sonic point respectively – if they do match then the length of the conductivity zone is a good proxy for the reaction zone length. This matter was discussed by Ershov et al. [187], who found strong correlation between the width of the main conductivity peak and the reaction zone length as measured by optical methods. They also found a distinct long tail of lower conductivity behind the main peak, which decreased with distance and corresponds to the rarefaction wave. The conductivity of this tail was attributed not to reaction but to the presence of free carbon which gradually becomes oxidised and loses its conductivity. With the assumption that the conduction zone can be equated with the reaction zone, the progression of the reaction time with distance is shown in Figure 6.14

The data presented here is quite sensitive to the anomalous results, since the limited supply of material only permitted a single shot to be performed for each density. However there is a general trend for the reaction time to decrease as the detonation moves through the charge.

The reaction time also has a density dependence – the steady state is around 14 ns at $0.90\,\mathrm{g\,cm^{-3}}$ while at $1.40\,\mathrm{g\,cm^{-3}}$ it is around 6 ns. Most of the variation in reaction time with respect to density occurs above $1.10\,\mathrm{g\,cm^{-3}}$, whereas below this density there is very little variation. Utkin et al. [188] found a reaction time of 50 ns using $\approx$500 µm particles, suggesting a dependence on particle size. Other studies [75][7] found values closer to the ones here, but did not specify the particle size. Figure 6.15 shows the steady state reaction time for the different densities.

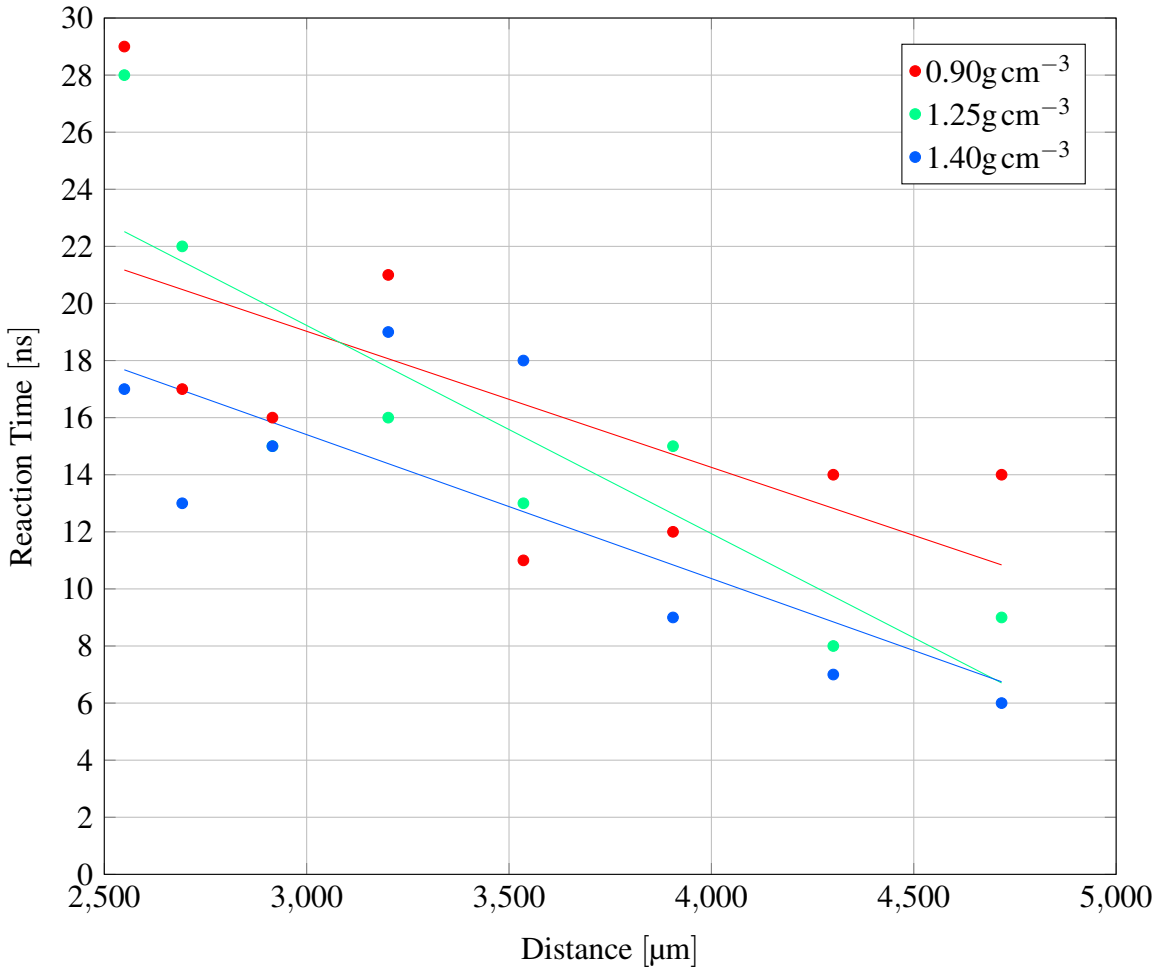

Figure 6.14 The reaction time progression for selected densities. The reaction time decreases with distance from the initiation point and also with density

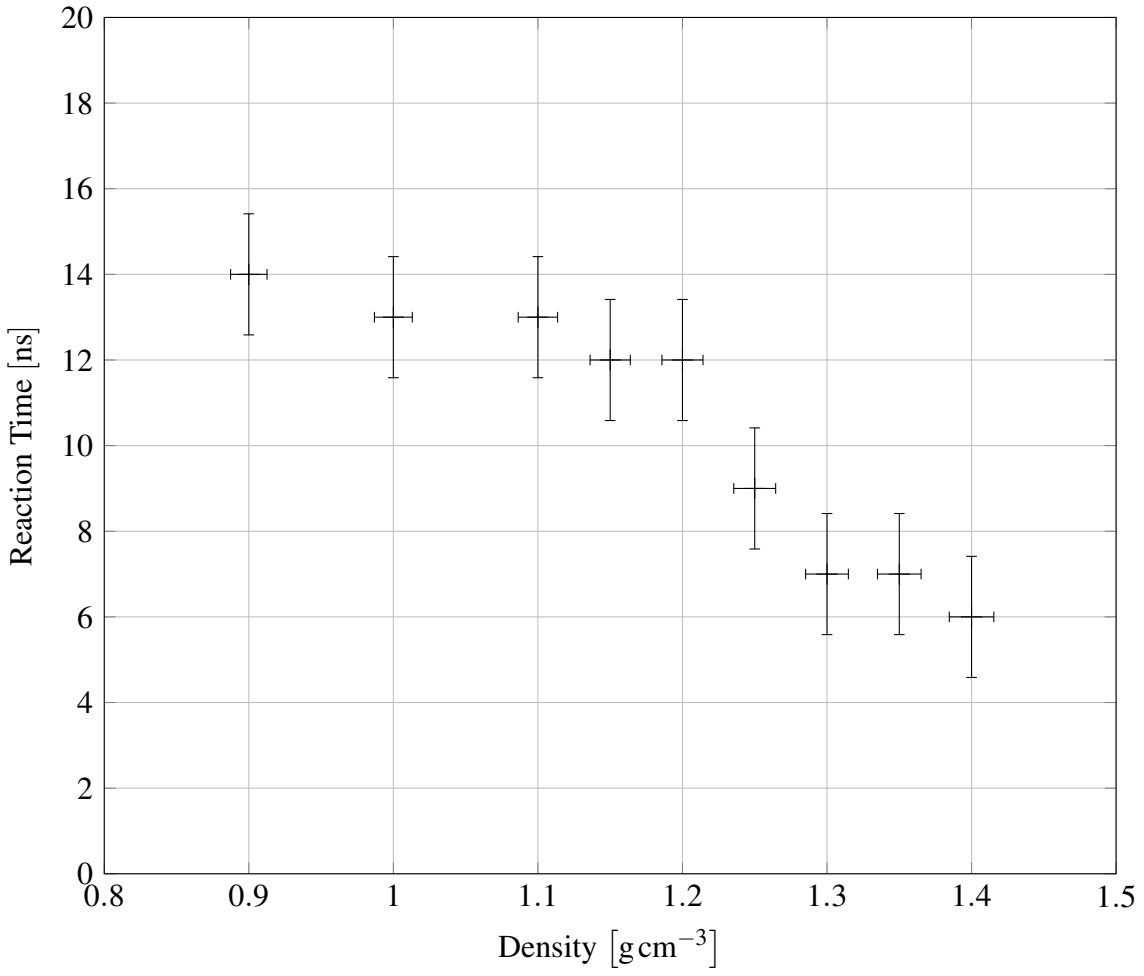

Figure 6.15 The final reaction time vs. density. Denser pressings exhibit shorter steady state reaction times, particularly above $1.10\,\mathrm{g\,cm^{-3}}$.

An explanation for the anomalous points where the reaction time is larger than expected may lie in the assumption made about the equivalence between the conduction zone and the reaction zone. As can be seen from Figure 6.9, the signal strength rise is faster than the fall due to the rarefaction tail. Therefore the uncertainty in determining the rear of the reaction zone is greater than the uncertainty in determining the front. The conductivity of the reaction zone is more similar to the conductivity of the rarefaction tail than it is to the conductivity of the unreacted explosive, therefore it is harder to identify the CJ point than the VN point. A CJ point misattributed to somewhere in the rarefaction tail would cause an anomalously large reaction time.

Reaction Zone Length

By combining the timing points with the velocity profiles according to the relationships in Table 5.1, the reaction zone length ξ was calculated. The steady state lengths are shown in Figure 6.16.

As with the reaction times there is a decreasing trend for densities higher than $1.10\,\mathrm{g\,cm^{-3}}$, however for lower densities the reaction zone is also shorter. This behaviour is a consequence of the trends exhibited by both detonation velocity and reaction time. While the reaction time is greater at lower densities, the detonation velocity is smaller. Below $1.10\,\mathrm{g\,cm^{-3}}$ the smaller detonation velocity is more important, so the reaction zone length is smaller. As the density is increased up to $1.10\,\mathrm{g\,cm^{-3}}$ the reaction time trend becomes more important, and the detonation velocity trend becomes less important.

At higher densities the gradient of the detonation velocity with respect to density decreases (Figure 6.11) while the gradient of the reaction time with respect to density increases (Figure 6.15). The reaction zone length therefore decreases with increasing density above $1.10\,\mathrm{g\,cm^{-3}}$.

Most literature deals with reaction zone time, so the comparison with these results is the same as discussed above, since the detonation velocity is well-known. Lubyatinsky and Loboiko [6] measured reaction zone lengths of less than 30 µm in agatised PETN, close to TMD, but the non-agatised samples had much longer reaction zone lengths. The difference was explained as being due to the non-planarity of the shock causing slower compression and reaction in some crystals. That the results here were closer to the agatised samples suggests that the ultrafine powder supports a relatively planar shock.

The higher density effect is expected, and agrees with literature [7], however the decreasing reaction zone length with density at lower densities is somewhat unexpected. It can be rationalised using the above argument of a trade-off between reaction time and detonation velocity.

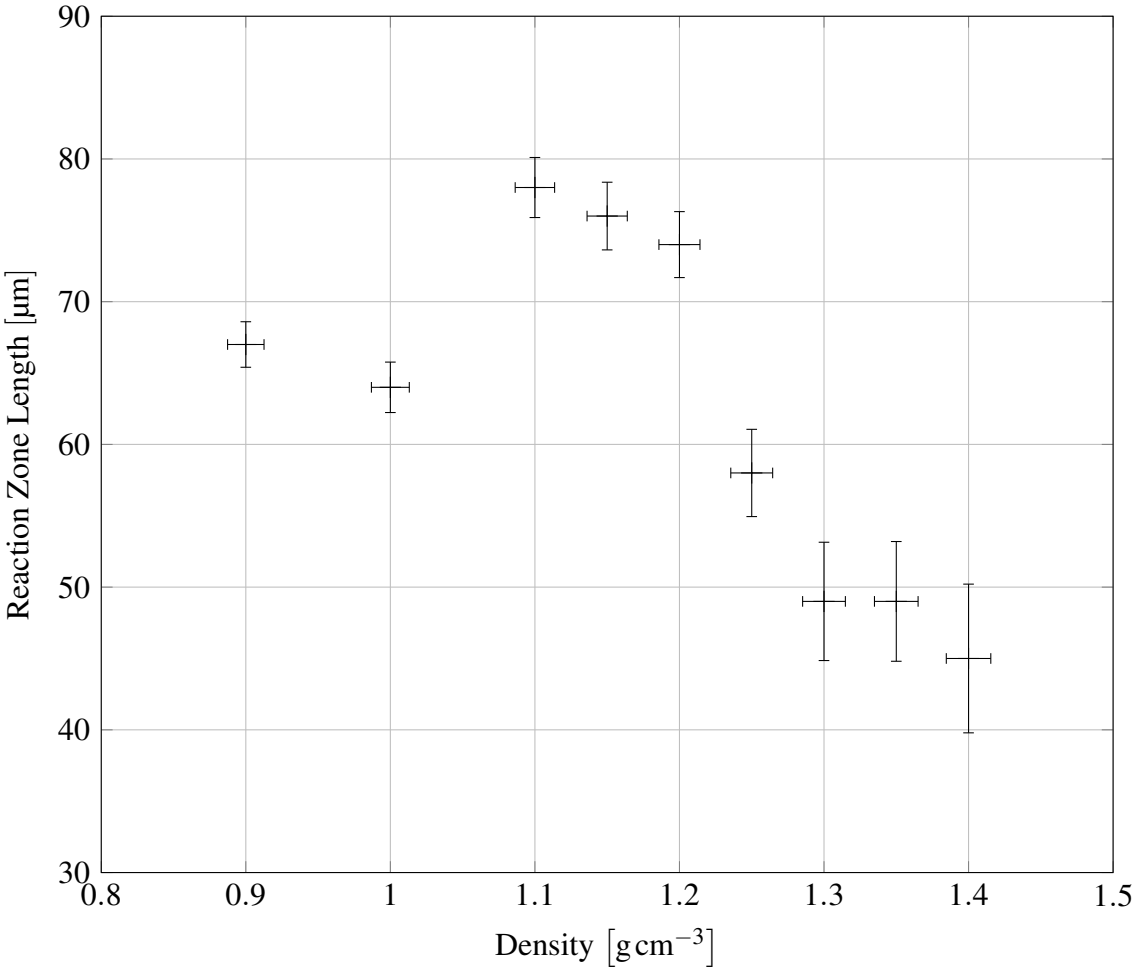

Figure 6.16 The final reaction zone length vs. density. The reaction zone length is greatest at $1.10\,\mathrm{g\,cm^{-3}}$, and decreases with density above this value. For the lowest densities, the smaller detonation velocity results in a smaller reaction zone length.

6.2.3 Density Study Summary

ρ/g cm^{-3}	D/km s^{-1}	τ/ns	ξ/µm	t_L/ns
0.90	4.83	14	67	670
0.95	4.98	(32)	(146)	630
1.00	5.24	13	64	500
1.05	5.55	(34)	(185)	440
1.10	5.91	13	78	380
1.15	6.27	12	76	320
1.20	6.17	12	74	250
1.25	6.43	9	58	250
1.30	6.96	7	49	180
1.35	7.43	7	49	200
1.40	7.58	6	45	150

Table 6.1 Summary of the results from the density study, showing the (steady) detonation velocity (D), reaction time (τ) and reaction zone length (ξ). Also shown is the calculated lost time. Suspected anomalous results are enclosed by parentheses.

6.3 Curvature Study

The purpose of the second series of experiments was to establish the relationship between curvature and reaction zone width, and how they evolve during the first few millimetres of detonation. The experiments were performed using a capacitive sensor positioned radially on the back face of the explosive pellet. The length of the pellet was varied in increments of 0.5 mm between 0.5 mm and 4.0 mm, and the diameter was fixed at 8.0 mm. A slightly larger diameter allows more sensing zones to be used, and therefore more data with which to calculate curvature. The sensor was positioned with four sensing zones spanning a radius of the back face of the pellet as shown in Figure 6.2(b), so the first sensing zone's front edge was at the centre and the last zone's back edge was at the outer circumference.

By varying the length of the pellet it is possible to infer what the properties of the detonation would be at that distance into a hypothetical longer charge. This 'cutback' technique in combination with a diagnostic on the rear face has been extensively used to study detonations [91][4]. It avoids the need for intrusive gauges where the explosive is opaque to optical methods, although it does require multiple experiments to be performed with a high degree of consistency.

The laser flyer system was used with the same pulse energy (150 mJ) and standoff distance (100 µm) as for the density study.

6.3.1 Sample Preparation

The explosive pellets were prepared in a similar way as for the density study, with several modifications made to the powder press and sensor placement procedure.

Sensor Placement

To place the sensor on the back face of the pellet it was first aligned with a circular cross-hair target printed on paper, to which it was then affixed, with the sensing elements facing up. A small drop of glue was placed on the neck of the sensor. The PMMA casing was also aligned with the paper target, then pressed onto the sensor and held in place until the glue dried. The cross-hair target was then removed from the assembly and sticking paper was applied over the sensor and glue to provide additional structural integrity. The sensor placement is shown in Figure 6.17.

Press Modification

For the curvature experiments, a similar press design was used to the density experiments with a few modifications. The bottom piston was replaced with a plate with a recessed face and a slot

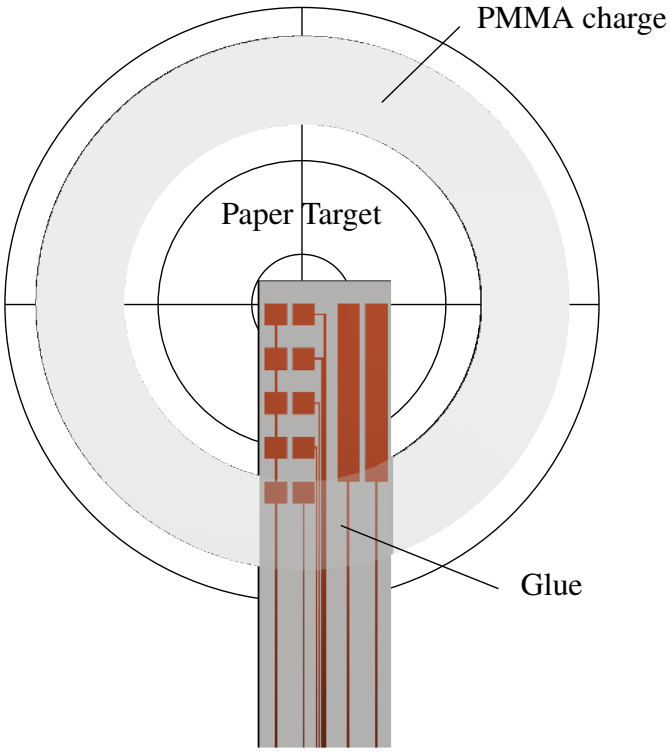

Figure 6.17 The sensor is positioned so that the sensing zones are aligned with a radius

to hold the sensor tail during pressing. Several outer dies of different lengths were produced to match the different lengths of PMMA casing. The modified press is shown in Figure 6.18.

Since in this configuration the sensor blocks one end of the casing, the powder was pressed from one direction rather than from both directions. The density variation is still expected to be minimal due to the short length of the charge compared to its diameter. Besides these changes the preparation and experimental procedure was the same as for the first series of experiments.

6.3.2 Results

The raw data was processed in the same way as before, yielding timing points for arrival of the detonation front and sonic locus at the sensing zone edges. The front at the edge of the charge lags behind the front in the middle of the charge, indicating that it has a curvature. This curvature changes with the length of the pellet, which implies that the curvature would evolve as the wave passes through a charge of greater length.

There are three missing experiments from the complete set: the longest charge length for $1.35\,\mathrm{g\,cm^{-3}}$ and $1.50\,\mathrm{g\,cm^{-3}}$ were omitted because of insufficient supply of the explosive. The 1 mm charge at the lowest density ($0.90\,\mathrm{g\,cm^{-3}}$) was attempted several times but was prone to collapsing while loading into the detonator mount. A different procedure would be required

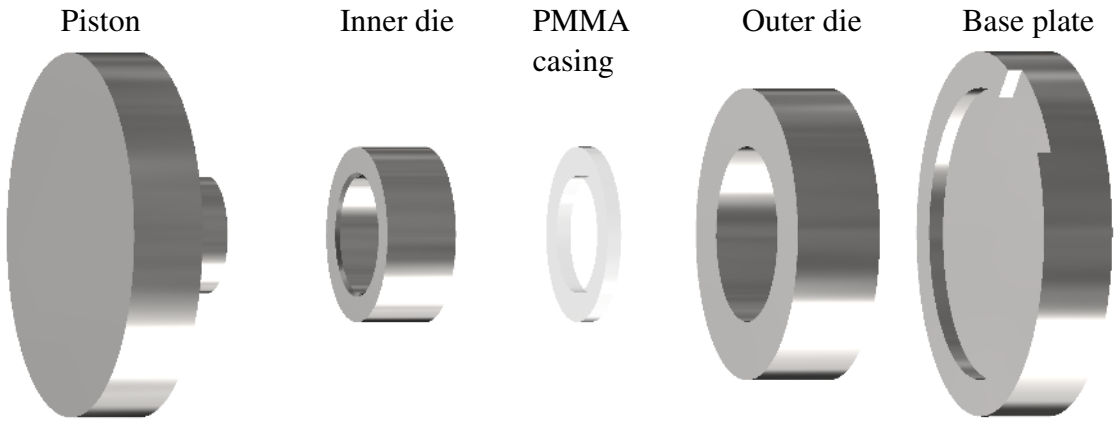

Figure 6.18 The modified press can accommodate casings of varying length by using different length outer dies.

for thinner or less dense experiments as the limit was reached for the powder to maintain a compact shape.

For each experiment, the time by which the wave lagged the central point at each sensing zone edge was recorded. Lag data for both the detonation front and CJ plane were obtained.

Curve Fitting

In order to reduce the dimensionality of the results, the data were fitted to curves described by a semi-phenomenological model. In this way it is possible to extract a smaller set of parameters from each experiment which can then be compared. If there were no interaction with the casing and the detonation wave spherically propagated from the surface impacted by the flyer plate, then the lag function would have the form:

$$L_0(r) = \begin{cases} 0 & r < \frac{d}{2} \\ \frac{\sqrt{C^2+\left(r-\frac{d}{2}\right)^2}-C}{D} & \frac{d}{2} < r < R \end{cases} \tag{6.6}$$

Here C is the length of the charge, d the diameter of the flyer and L the time by which the front lags at a radius r from the centre. The geometrical justification for this form is shown in Figure 6.19:

On the other hand, as the detonation reaches a steady state far from the flyer impact, the shape derives only from the interaction with the PMMA casing and not the nature of the initiation. For this case the lag is written in a phenomenological form [189]:

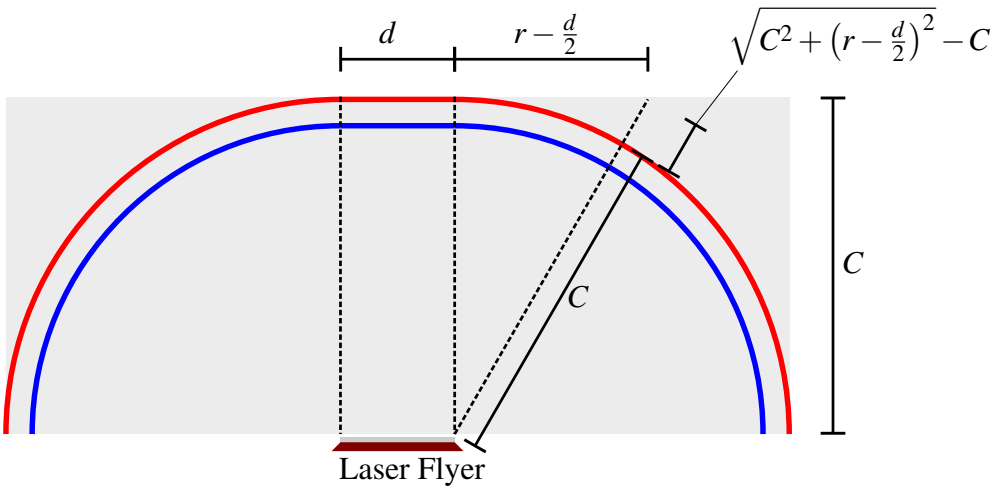

Figure 6.19 Waves are assumed to spread out spherically from each point that the laser flyer impacts.

$$L_\infty(r) = -A \ln\left[\cos\left(\eta \frac{\pi}{2} \frac{r}{R}\right)\right] \tag{6.7}$$

The parameters A and $0 \leq \eta \leq 1$ determine the curvature. A is an overall scaling factor, while η controls the relative size of the edge lag.

Unlike in the experiments done by Catanach and Hill [189], the approximation $z(r) = D_0 L(r)$ does not hold, since the wave has not yet reached a constant shape.

For the experiments in this study, the detonation front has not reached its steady state shape, although there is some confiner interaction. Therefore the overall shape must be a combination of L_0 and L_∞. A common sigmoid switching function – the logistic function – is used to weight the two constituent functions as follows:

$$L = \frac{1}{2}\left(1 - \tanh\left(\frac{C - C_0}{\delta}\right)\right) L_0 + \frac{1}{2}\left(1 + \tanh\left(\frac{C - C_0}{\delta}\right)\right) L_\infty + B \tag{6.8}$$

The switching function means that if the charge length C is less than the transition length C_0, then L_0 dominates, whereas if it is greater than the transition length then L_∞ dominates. The transition length marks the point at which the general function switches from L_0 to L_∞, while δ is a fixed parameter controlling the smoothness of the transition – as $\delta \to 0$, the switching function tends to a step function. The choice of δ did not significantly affect the outcome of the fitting – a value of $\delta = 100\,\mu\text{m}$ led to good convergence for all curves.

Equation (6.8) has three tunable parameters: A and η, as well as the y-intercept constant B. A curve of this form is fitted to each set of data.

To fit the curve the total least squares (TLS) regression method is used. This technique is similar to the common ordinary least squares method, except that the error function to be minimised is the sum of a more generalised squared residual. In ordinary least squares, the residual is the difference between the curve and the point along the dependent variable axis (i.e. it is assumed that there is no error in the independent variable). In total least squares the residual takes account of errors in both the independent and dependent variables. TLS is used here because there is uncertainty not only in the dependent variable (the lag times) but also in the independent variable (the positions of the sensing zone edges). The objective function S is the sum of the squared residuals for both dependent and independent variables weighted by their respective errors as follows:

$$S = \sum_i \left[\frac{\left(L_i - L^*\left(A, \eta, B, r_i^*\right)\right)^2}{\sigma_L^2} + \frac{\left(r_i - r_i^*\right)^2}{\sigma_r^2} \right] \tag{6.9}$$

(r_i, L_i) are the measured data points, L^* is the function to be fitted, and σ_L and σ_r are the errors in the data, which are not necessarily equal. In the special case that the errors are equal the residual is the orthogonal distance between the data point and the fitted curve. S is minimised by an iterative gradient descent on the parameters A, η and B, as well as the 'true' values r_i^*. From the starting values $A = 0$, $\eta = 0.5$, $B = 0$, $r_i^* = r_i$, the gradient of S with respect each variable is calculated, and the variables are reduced by an amount proportional to the gradient. This process is repeated until the minimum of S is found.

The lag data for five different densities are shown in Figures 6.20 to 6.24, along with the curves that were fitted using the above method. The red and blue points correspond to the front and back of the reaction zone respectively, while the fitted curves are shown in the same colours. The reaction zone between these curves is coloured brown.

Since the D in Equation (6.6) is the steady state velocity, L_0 can be identified with the theoretical transit time described in the discussion about lost time. The L_∞ term can therefore be identified with the lost time.

Curvature

A value for the curvature can also be extracted from the fitted model. A general expression for the (unsigned) curvature is:

$$\kappa = \frac{L''}{\left(1 + L'^2\right)^{\frac{3}{2}}} \tag{6.10}$$

However, because the slope of the fitted curve is zero along the axis, it is simpler to use the on-axis curvature, which is just the second derivative L'' of the lag function. Furthermore, because L_0 is a piecewise function that is flat for $r < \frac{d}{2}$, the second derivative $L_0''(0)$ is zero.

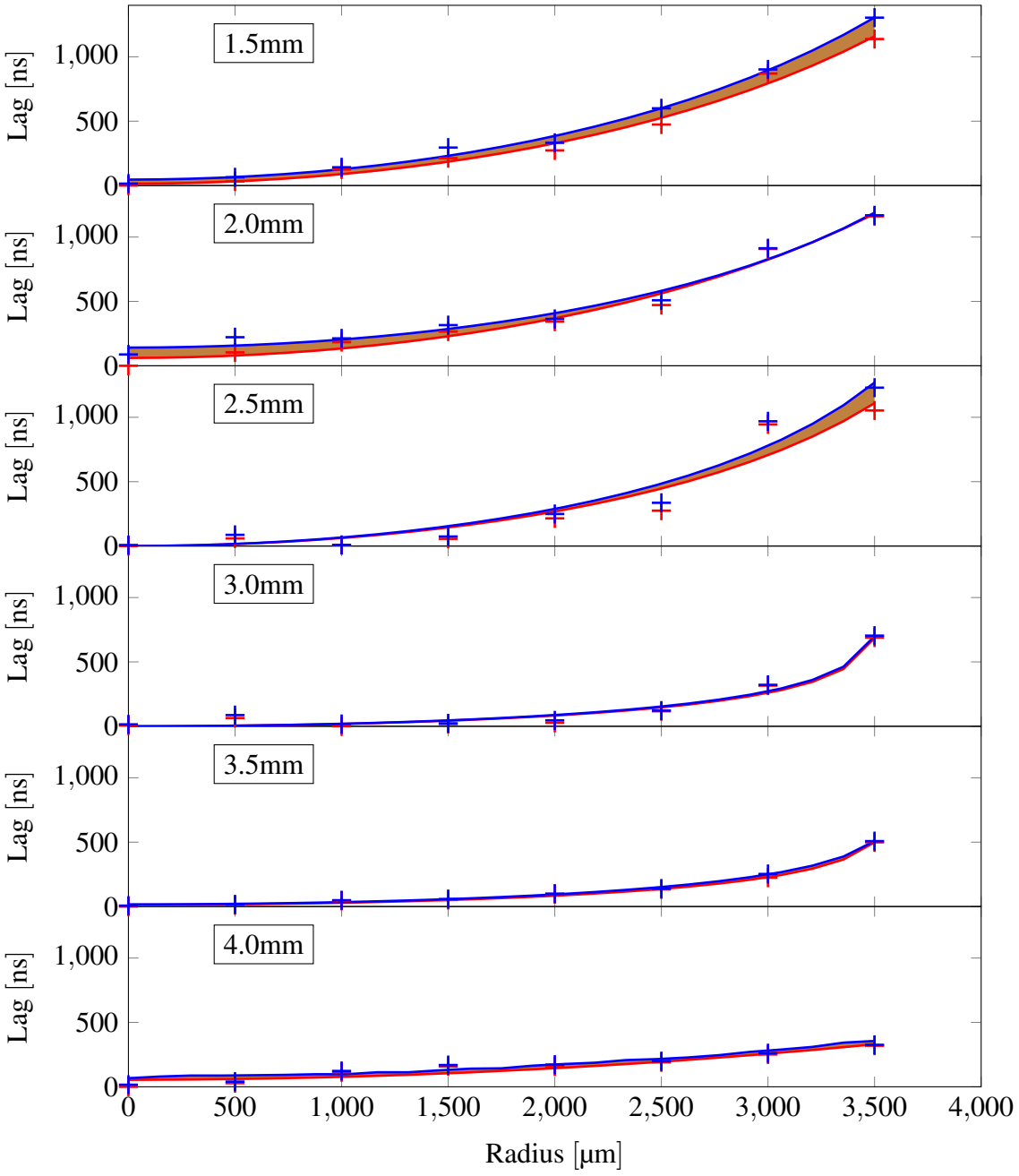

Figure 6.20 Lag curves for 0.90 g cm^{-3} PETN

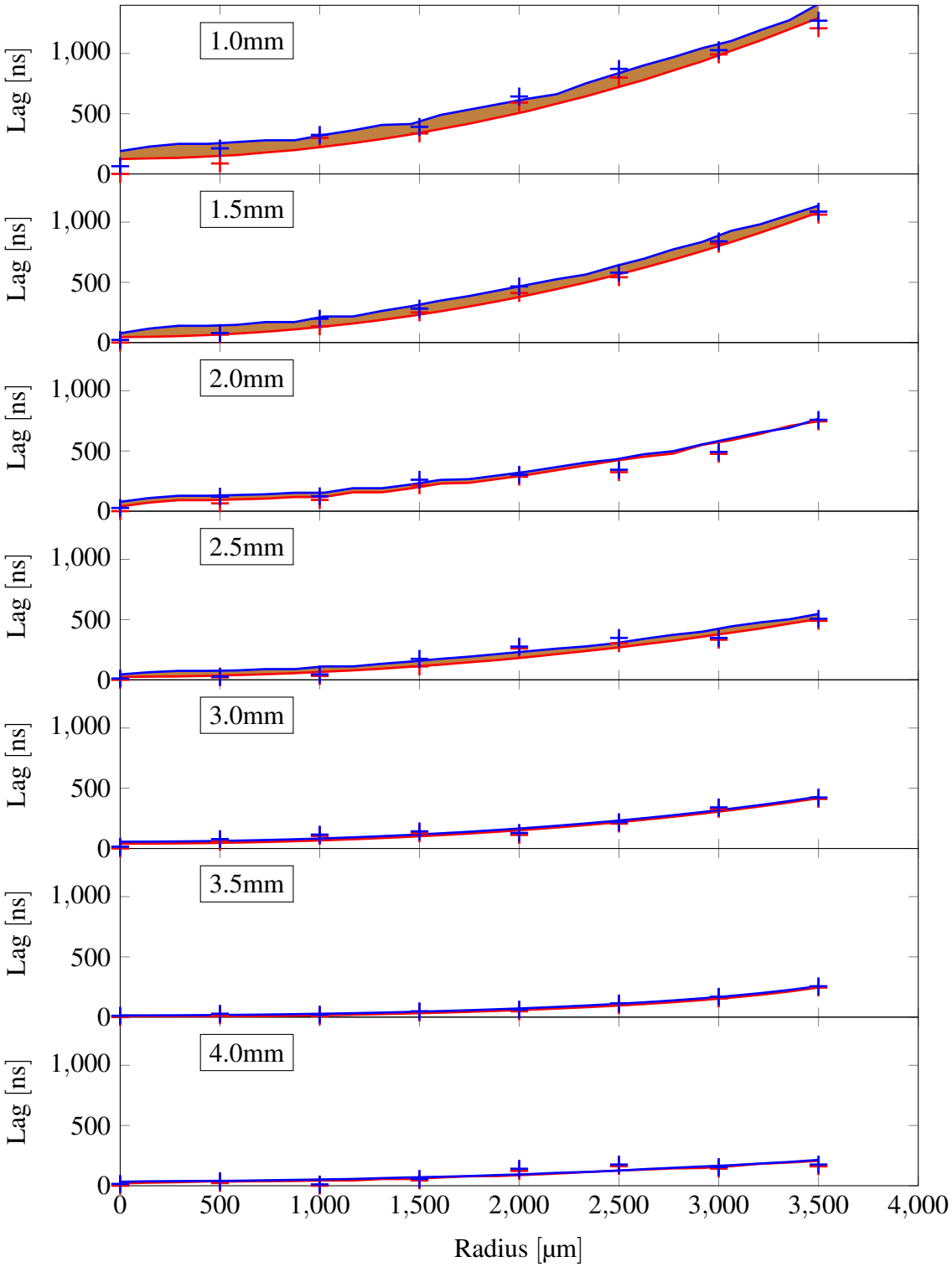

Figure 6.21 Lag curves for 1.05 g cm^{-3} PETN

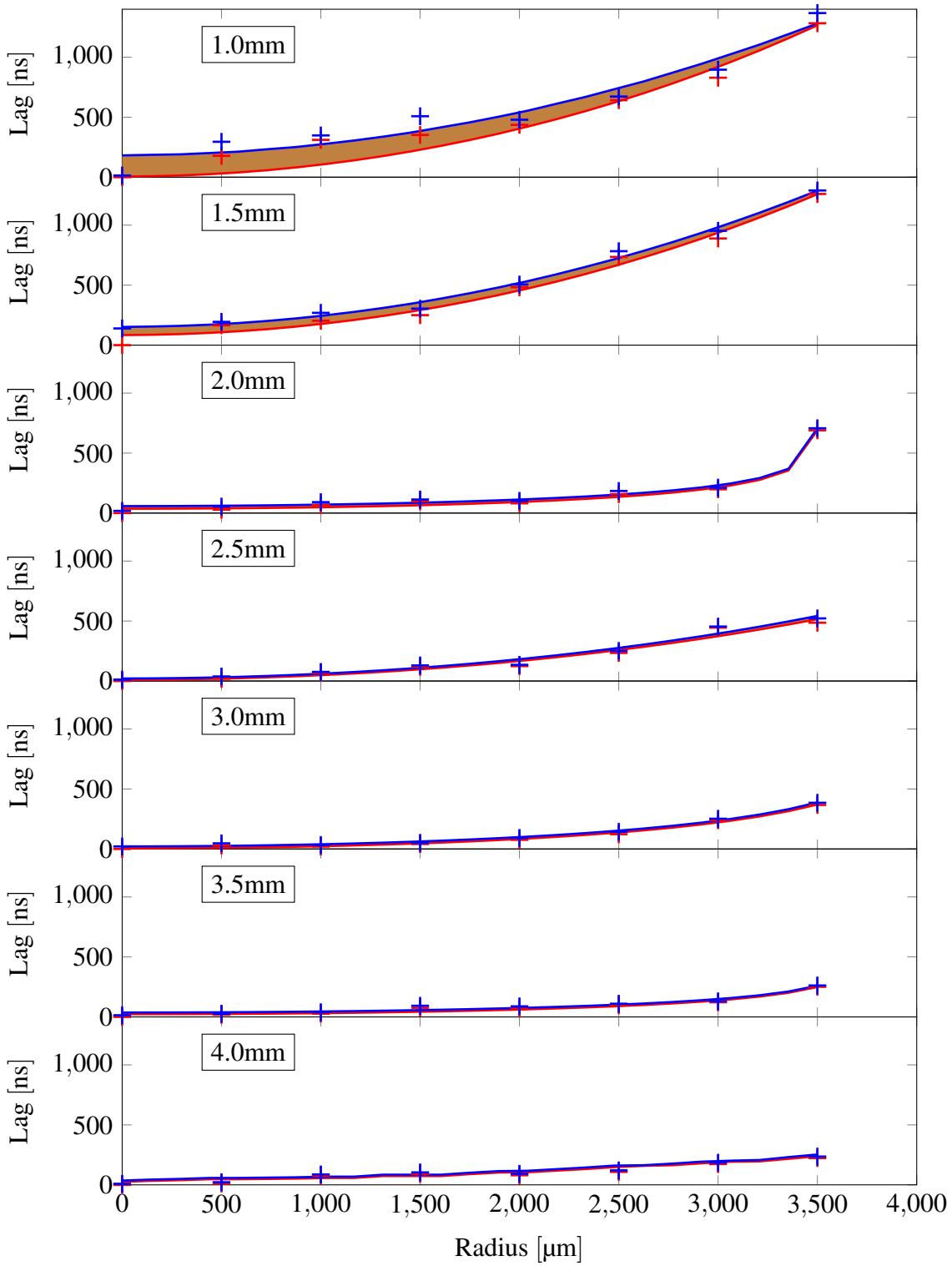

Figure 6.22 Lag curves for 1.20 g cm^{-3} PETN

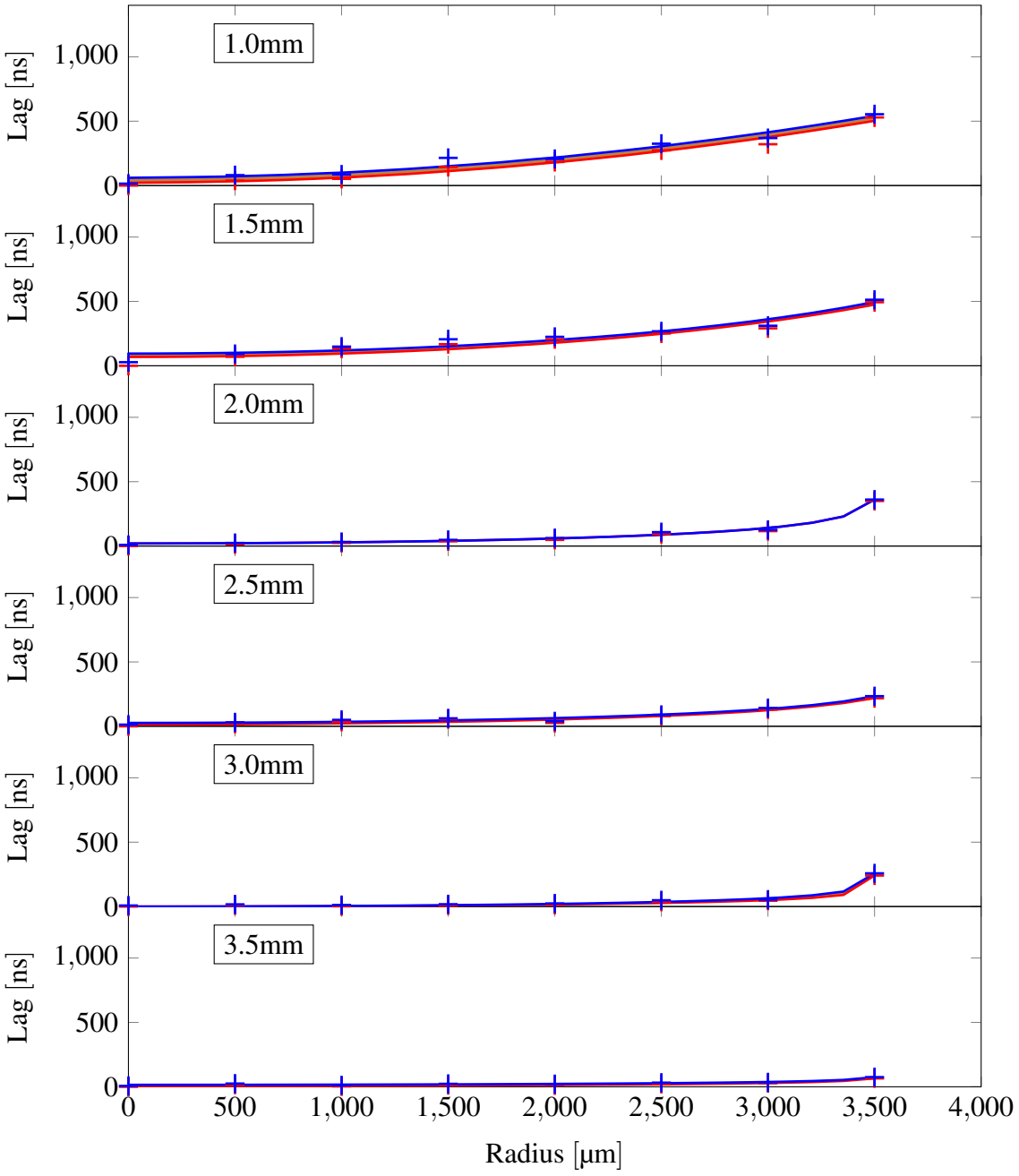

Figure 6.23 Lag curves for 1.35 g cm^{-3} PETN

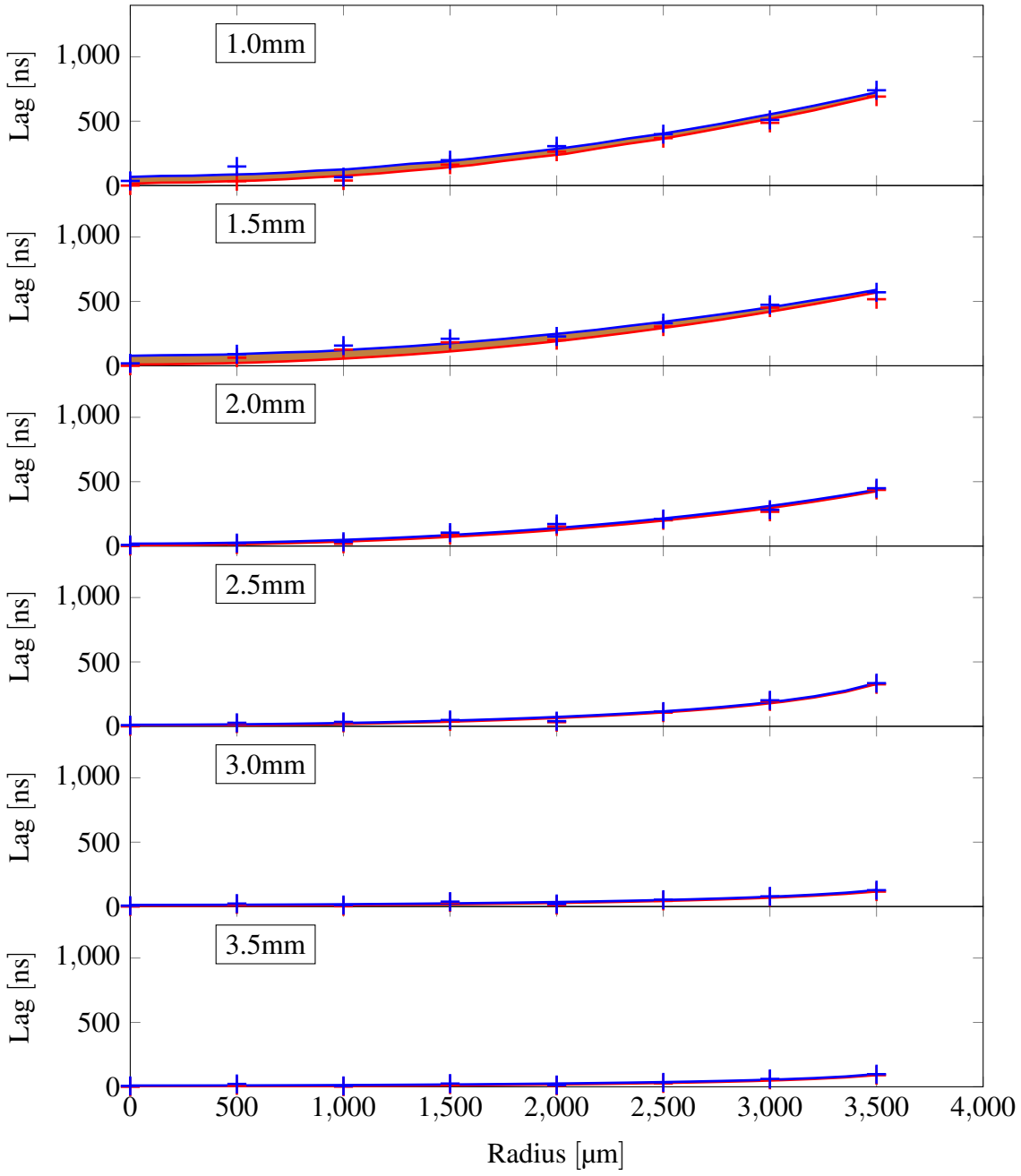

Figure 6.24 Lag curves for 1.50 g cm^{-3} PETN

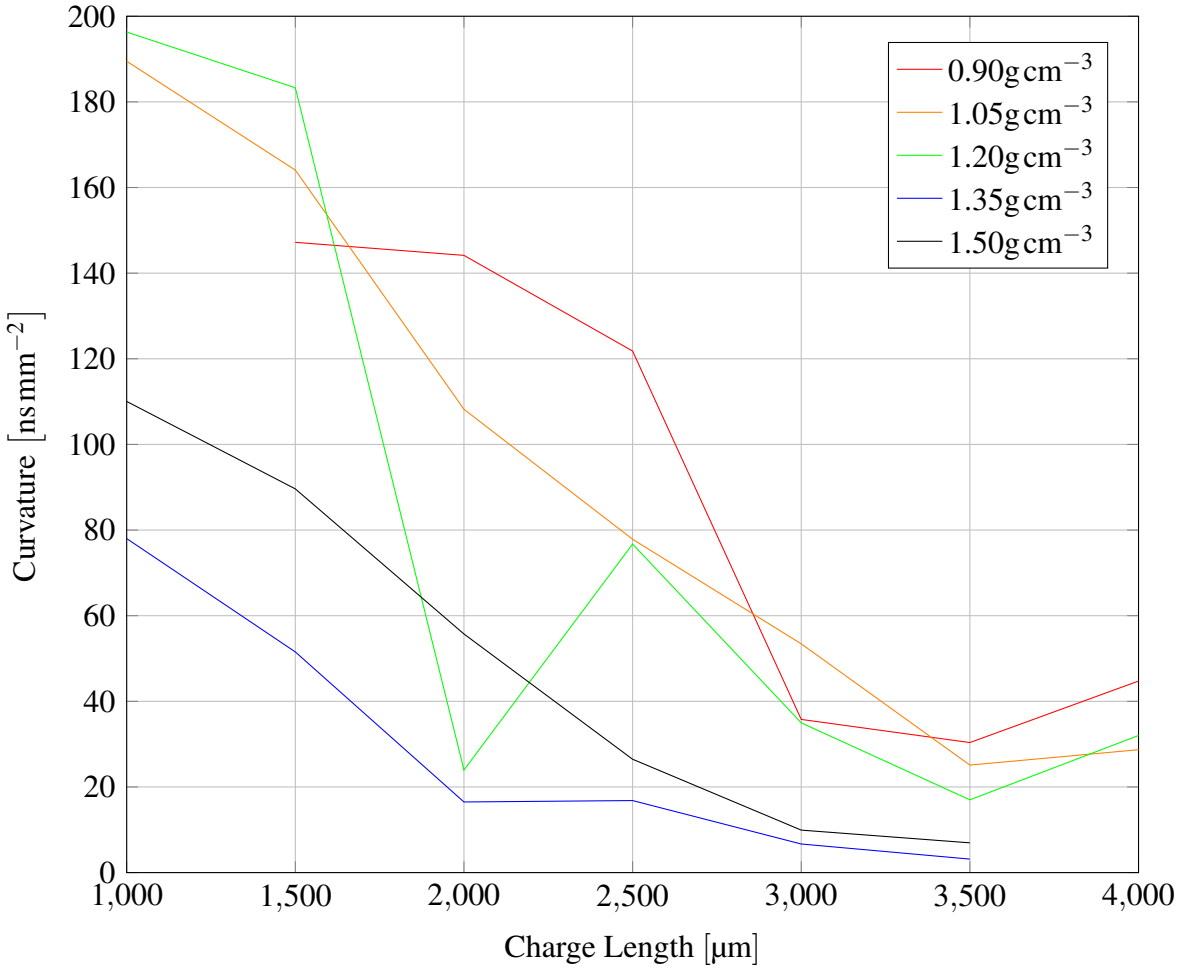

Figure 6.25 The progression of the on-axis curvature of the wave front for a range of densities.

Thus the only contribution to the on-axis curvature is from L_∞. L_∞ has the useful property that the second derivative, and therefore the curvature at $r = 0$ is simply:

$$\kappa = |A| \left(\frac{\pi}{2} \frac{\eta}{R} \right)^2 \tag{6.11}$$

This relationship was used with the fitted values of A and η to evaluate the on-axis curvature for each detonation front lag curve. The evolution of the curvature of the detonation front for each density is shown in Figure 6.25.

The trend is that the curvature of the wave front transitions from an approximately circular shape to a flatter shape, with the flat region increasing in size as the detonation progresses. The reaction zone also gets thinner as the wave travels. At higher densities the curves flattens sooner and by a greater amount.

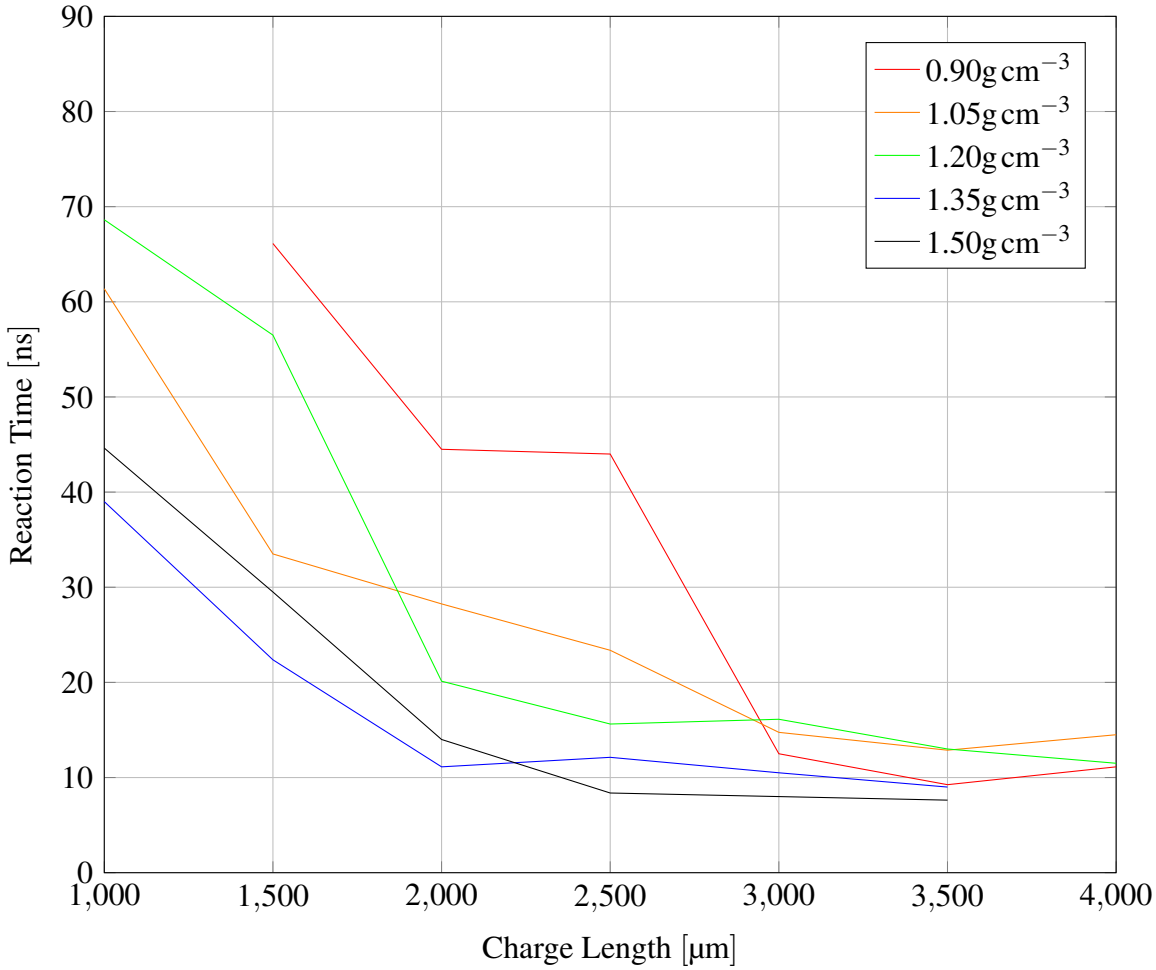

Figure 6.26 The progression of the average reaction time across the wave front for a range of densities. The reaction time decreases with distance, and is generally smaller at higher densities. The variation with respect to distance is much greater than the variation with respect to density.

Reaction Time

The reaction times for each charge length and density were calculated by averaging the interval between the VN point and CJ point across the curve. There did not appear to be any variation in the reaction time across each curve beyond random scatter, so there is no information loss from taking this average. The fact that there is no variation means that the detonation wave propagates isotropically. For a longer charge one might expect to see the reaction time change across the curve as the confinement designates a preferred direction. These results are presented in Figure 6.26.

The trend is broadly the same as that found in the density study shown in Figure 6.14. The reaction time decreases with distance from the initiation site and is slightly lower for

higher densities. The initial reaction time has a lot of scatter, but is generally higher for less dense samples, and higher in the curvature experiments than in the density experiments for comparable densities.

Reassuringly, the values measured at the furthest distance are very similar between the two series of experiments. The lowest density (0.90 $\mathrm{g\,cm^{-3}}$ had a reaction time of 14 ns in the density experiments and 15 ns in the curvature experiments. At 1.35 $\mathrm{g\,cm^{-3}}$ the reaction time was 7 ns in the density experiments and 9 ns in the curvature experiments. The conclusion from this similarity is that the sensors can measure the reaction time regardless of whether the wave is moving parallel or perpendicular to them.

Reaction Zone Length

The reaction zone lengths were calculated using the reaction times and the axial component of the detonation velocity at the centre. This axial component was found by first calculating the velocity at which the breakout travelled radially, and then projecting this velocity onto the detonation axis. These reaction zone lengths are shown in Figure 6.27.

The reaction zone lengths exhibit the same trend as the reaction times of decreasing with distance from the initiation site, albeit with a gentler approach to steady state. The smaller slope is likely due to the end of the ramping up phase of the detonation velocity being counter effective to the decrease in reaction time.

The similarity between the trends in reaction zone length and curvature, as well as theoretical treatments [8] suggests a relationship. The reaction zone length is plotted against curvature in Figure 6.28.

Reaction zone length and curvature are positively correlated in an approximately linear manner. The gradient does not appear to depend on density. At low curvatures (flat wave) the reaction zone length tends to about 40 µm, while it can be 3 to 4× larger for highly curved fronts.

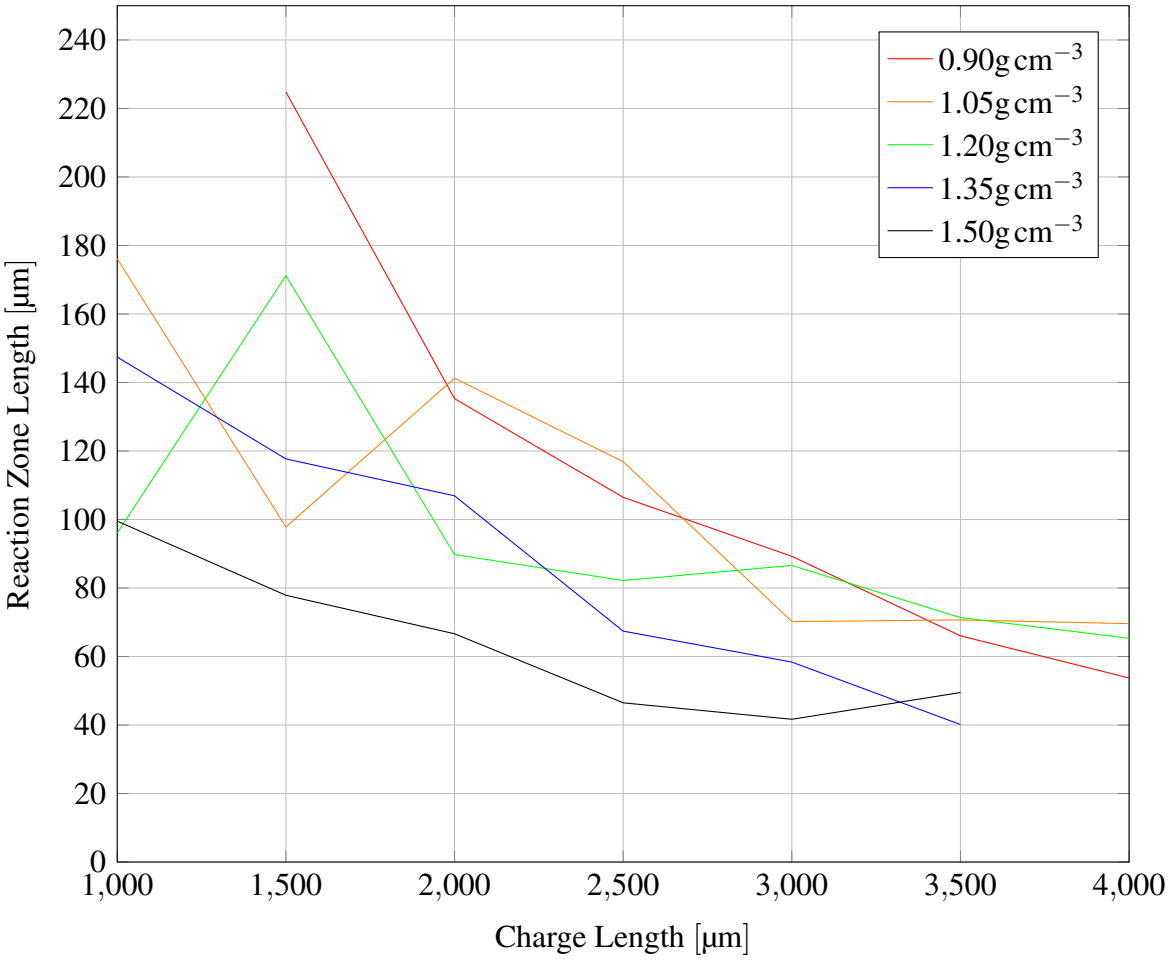

Figure 6.27 The progression of the average reaction zone length across the wave front for a range of densities. There is a trend for reaction zone length to decrease with distance for each density. As with the density experiments, the steady state reaction zone length peaks at an intermediate density ($1.05\,\mathrm{g\,cm^{-3}}$). The initial reaction zone lengths are especially large at lower densities, and exhibit a greater variation.

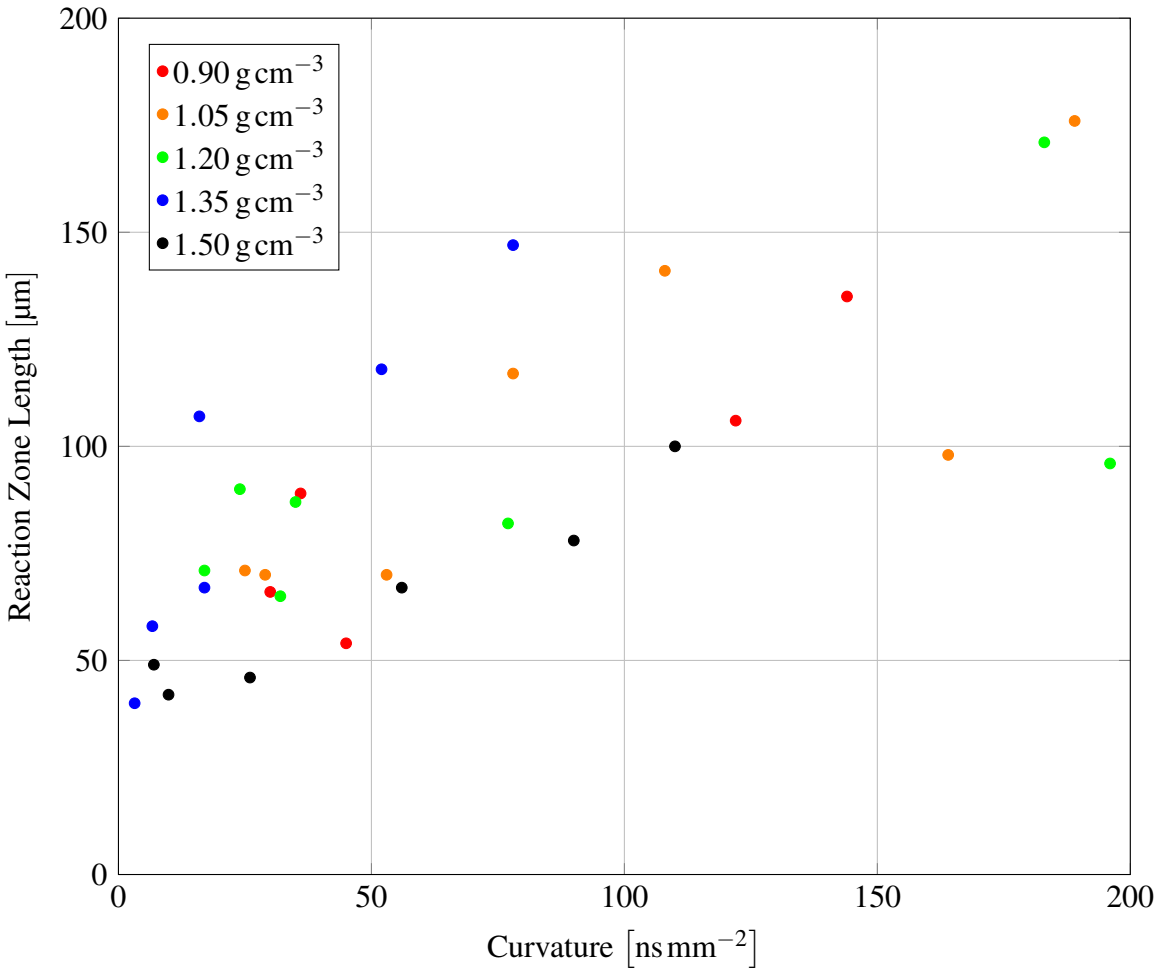

Figure 6.28 Plot of reaction zone length against lag curvature for each density. The different marks in each density series represent different cutback distances. The two variables have an approximately linear positive correlation.

6.3.3 Curvature Study Summary

Table 6.2 Summary table of the curvature study showing the on-axis lag curvature (S), reaction time (τ) and reaction zone length (ξ) for each density tested, and for each cutback distance.

	x/mm	S/ns/mm^2	τ/ns	ξ/μm
0.90 g cm^{-3}	0.5	N/A	N/A	N/A
	1.0	147	66	225
	1.5	144	45	135
	2.0	122	44	106
	2.5	36	13	89
	3.0	30	9	66
	3.5	45	11	54

	x/mm	S/ns/mm^2	τ/ns	ξ/μm
1.05 g cm^{-3}	0.5	189	61	176
	1.0	164	34	98
	1.5	108	28	141
	2.0	78	23	117
	2.5	53	15	70
	3.0	25	13	71
	3.5	29	15	70

	x/mm	S/ns/mm^2	τ/ns	ξ/μm
1.20 g cm^{-3}	0.5	196	69	96
	1.0	183	57	171
	1.5	24	20	90
	2.0	77	16	82
	2.5	35	16	87
	3.0	17	13	71
	3.5	32	12	65

	x/mm	S/ns/mm^2	τ/ns	ξ/µm
1.35 g cm^{-3}	0.5	78	39	147
	1.0	52	22	118
	1.5	16	11	107
	2.0	17	12	67
	2.5	6.7	11	58
	3.0	3.2	9	40
	3.5	N/A	N/A	N/A

	x/mm	S/ns/mm^2	τ/ns	ξ/µm
1.50 g cm^{-3}	0.5	110	45	100
	1.0	90	30	78
	1.5	56	14	67
	2.0	26	8	46
	2.5	9.9	8	42
	3.0	7.0	8	49
	3.5	N/A	N/A	N/A

6.4 Discussion

The experiments performed using the capacitive sensors have given new insights into the evolution of reaction time and curvature, and their dependence on density. The validity of the method is supported by the close agreement with existing detonation velocity measurements across a range of different densities. While previous studies have measured the reaction time and wave shape at steady state, they have not shown the transitory behaviour between initiation and steady state, nor have they examined a wide range of densities as has been done here.

In the density experiments the detonation velocity ramped up from a smaller value to the final steady state value. This behaviour is likely due to the detonation wave overtaking a precursor shock. The precursor desensitises the explosive by collapsing voids and releasing stress, so the reaction is slower until the detonation overtakes the precursor, at which point it accelerates to steady state.

The differing shock impedance of samples results in a higher pressure in the denser samples in response to identical flyers. However, this pressure is large enough such that practically all potential hot spots will be above the critical hot spot size. The limiting factor is therefore hot spot growth.

In both sets of experiments the reaction time exhibits a dependence on density, with a shorter reaction time being seen at higher densities. At higher densities the powder will have smaller and more numerous voids, and more points of contact between particles. There will therefore be more potential sites for hot spot ignition, which will almost all spontaneously grow due to the high pressure. If there are more hot spots, then more particles will start chemical reaction sooner. Grains which do not start reacting will have to wait for jetting, impact or heat conduction from already burning grains before they start burning. Since the reaction time is determined by the time for surface burning to reach the centre of the particles, if a greater fraction of particles start reaction sooner, then less time will elapse before reaction is complete. This process is illustrated in Figure 6.29.

In both the experimental configurations and across all densities, the reaction time was longer closer to the source of initiation before settling down to a shorter steady state value. The most likely explanation for this relationship is that the material compacts as the detonation passes through. The above arguments about density dependence then also apply to the distance dependence, since the material densifies. There may also be heat conduction through the porous material, which could increase the reaction rate, but it is unlikely that this happens fast enough compared to the other mechanisms by which reaction is carried from one particle to another.

It is important to make the distinction between the Lagrangian and Eulerian frames of reference, and which is applicable for each measurement. In the Lagrangian frame, the sensor moves along with the material, so the reaction time can be associated with a particular fluid

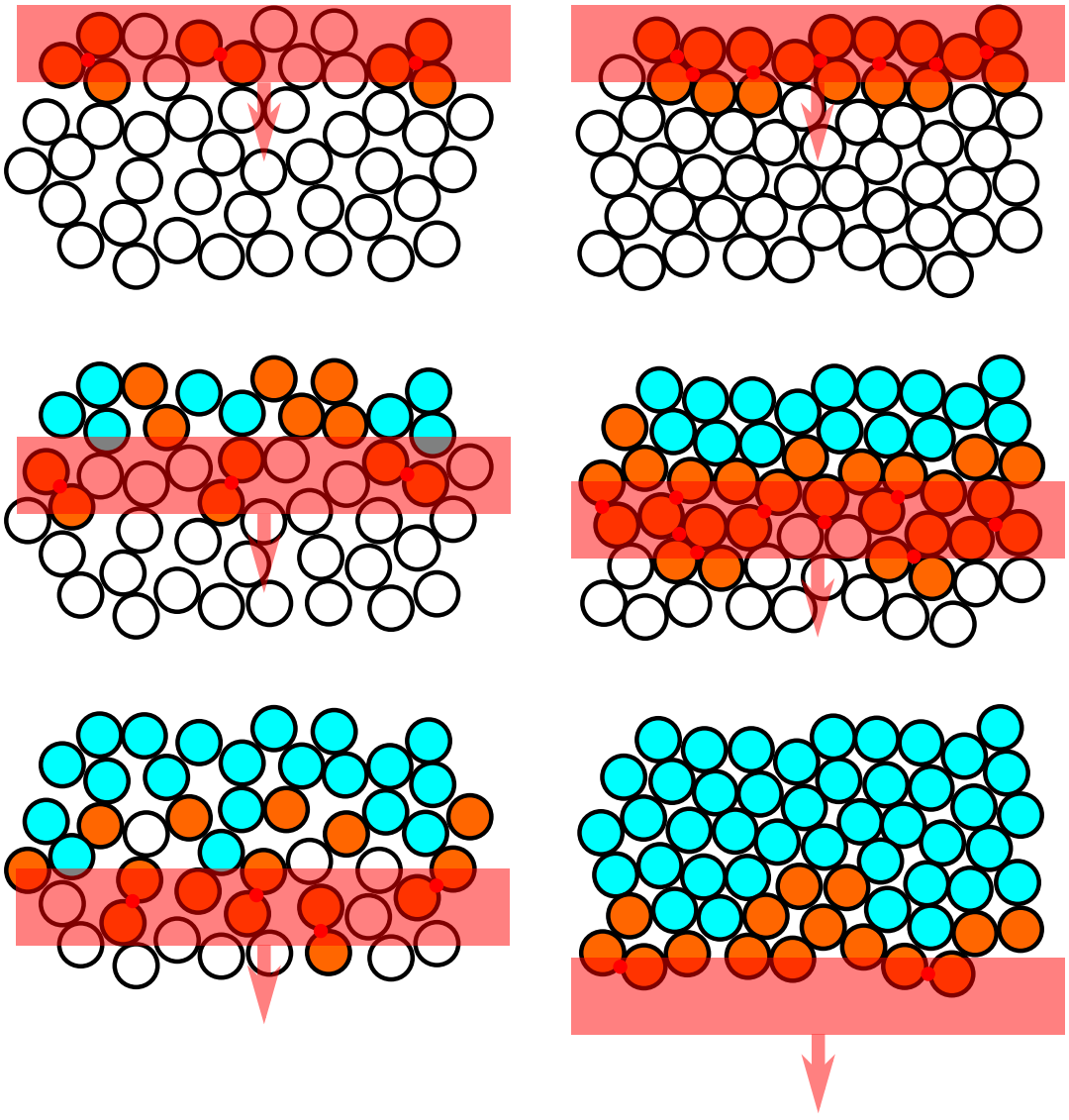

Figure 6.29 Illustration of why denser pressings have shorter reaction times. As the shock (pink) passes through, more critical hot spots (red) are formed in the denser bed (right) since there are more voids and points of contact. Practically all potential hot spots become critical due to the high pressure. Therefore more grains in each layer begin to react (orange). Grains not in proximity to a hot spot can only start to burn later – there are more of these in the lower density bed (left). The former positions of grains that are fully reacted are marked in blue. For low densities, at any given point along the detonation direction, there will be more time before all the grains at that point have completely reacted.

element. In the Eulerian frame, the fluid moves past the sensor as it reacts, therefore the observed reaction time will be shorter since the reacting material is in the sensing zone for less time.

The reference frame argument could also explain why the reaction time was initially larger before shrinking. If the sensor initially moved along with the material, but was then overtaken or arrested, then the frame would shift from Lagrangian to Eulerian. The sensor can move more freely in the curvature configuration than in the density configuration so the breakout likely causes some deformation of the sensor. It is believed that this reference frame argument accounts for the higher initial reaction time in the curvature study compared to the density study, but not the overall decrease with distance, since this trend is the same between experiment series.

The explanations for the dependence of the reaction time on density and distance carry over to the reaction zone length, although the calculation of this quantity also requires the detonation velocity. Detonation velocity increases with density, while reaction time decreases, so there is a trade-off in the reaction zone length. The reaction time trend becomes more important at higher densities, and the detonation velocity trend at lower densities. The steady state reaction zone length was greatest at an intermediate density – $1.10\,\mathrm{g\,cm^{-3}}$ in the density study and $1.05\,\mathrm{g\,cm^{-3}}$ in the curvature study.

In contrast, the reaction time variation with distance is large enough that the ramping up of velocity does not overrule it for any of the experiments performed here. However, the reaction zone length does take longer to reach a steady value than the reaction time, most likely due to this effect.

In general the denser pressings were found to have smaller curvatures, with a lower lag time between the centre and edge. They also reached a flatter shape sooner than the low density pressings, which remained relatively curved for a greater distance. This tendency matches what others have found in other explosives [190]. Flattening occurs because rarefaction waves from the edge of the charge travel inwards and reduce the pressure behind the detonation [191]. Energy flows outwards to support the detonation at the edge [192]. The result is a wave that is accelerating up to the steady state shape and velocity everywhere across the front, but the acceleration is diminished on-axis relative to the edge. At higher densities these rarefaction waves are faster, hence the lead shock decelerates sooner, and the wave front becomes flatter earlier. An illustration of the curvature development is shown in Figure 6.30.

The results of the curvature experiments can further explain the dependence of the lost time on density. Since the wave becomes flatter sooner at higher densities, and the reaction zone is shorter, the velocity deficit will be smaller, and therefore the lost time is shorter. The causal chain of events that explain these relationships is as follows:

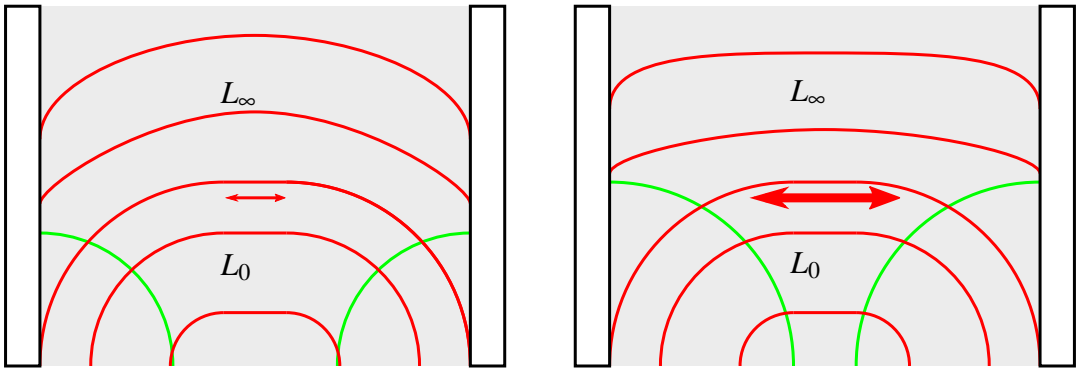

Figure 6.30 Illustration of why denser pressings have lower curvature. Initially both the lower density (left) and higher density (right) have the same shape (L_0) (although the wave will move faster through the higher density). Radial energy flow (represented by the red arrows) and faster release waves (green) cause the edge lag to be reduced in the high density case.

1. The flyer hits the surface of the bed at the same velocity regardless of the material properties. A higher pressure shock is imparted to the higher densities. In all cases the shock is short, and rapidly subsumed by the release wave from the rear of the flyer. Lateral release waves do not significantly affect the size of the shocked region.

2. There is little delay to detonation commencing in all cases. Run to detonation is longer for the denser beds, but due to the strength of the shock it occurs over a much shorter timescale than the other processes at work.

3. Higher density pressings have more (albeit smaller) voids and points of contact in the shocked region, therefore there are more sites for hot spot formation. Due to the high pressure imparted, the hot spots that form are larger than the critical size, and grow spontaneously.

4. A greater proportion of particles start burning promptly, and therefore also finish burning earlier. Therefore the reaction time is shorter, while the reaction zone length depends on both the reaction time and detonation velocity.

5. Densification of the bed causes the reaction time to gently decrease with distance from initiation to a steady state value.

6. For all densities the wave propagates outwards approximately spherically until it reaches the edge. There is a flat region of the wave immediately after initiation, which diminishes in size as energy flows radially outwards in the curved part of the wave.

7. Once the wave reaches the edge of the charge, greater outwards radial energy flux and faster travelling rarefaction waves from the interaction with the confiner mean that the detonation front forms a flatter shape sooner for higher density pressings.

8. Due to a smaller reaction time and lower curvature at higher densities, the detonation velocity deficit is smaller, and so the resulting lost time is smaller.

6.5 Summary

- Capacitive sensors have been used for the first time to measure detonations. They were employed in two different configurations to investigate the detonation of laser flyer initiated PETN. The sensors proved useful in producing a rich dataset without many of the drawbacks associated with alternative methods.
- A novel double-action floating die press was used to minimise density gradients in the explosive pressing.
- A similar relationship to previous literature was found between density and detonation velocity, supporting the use of capacitive sensors for other measurements.
- A velocity deficit in the early stages of detonation caused a density dependent lost time.
- The reaction time also exhibited density dependence, varying from 14 ns at $0.90\,\mathrm{g\,cm^{-3}}$ to 6 ns at $1.40\,\mathrm{g\,cm^{-3}}$. The reaction time was also found to shrink with distance. This work is the first to show the density dependence of the reaction time of PETN over this range, and also to measure it during the early stages of detonation.
- The sensors were capable of directly measuring curvature and reaction time simultaneously, unlike existing diagnostics.
- The curvature was calculated from fitting a semi-phenomenological model to the lag data. It was initially large, but shrank as the wave front grew and flattened out.
- The sensors also measured the reaction time at evenly spaced points across the front. There was good agreement between the reaction time calculated from the curvature experiments and the density experiments.
- The lost time dependence on density was explained by the effects of density on reaction time and curvature.

The experimental work has shed light on the relationship between density, curvature and reaction time in the early stages of PETN detonation However, since there are many more variables that could plausibly affect the detonation, spanning the entire parameter space with experimentation alone would be infeasible. The next chapter describes efforts to create a hydrocode calibrated to these experiments that provides predictive capability beyond the experiments.

Chapter 7

Numerical Modelling

7.1 Introduction

Experimental investigations of detonations have a synergistic relationship with numerical modelling; experiments are used to verify simulations and determine model parameters, while simulations can be used to guide experimental design and predict scenarios outside the scope of experimentation. This chapter describes efforts to simulate the experiments performed in the previous chapter, and use the results of the simulations to predict behaviour in different scenarios.

There are two types of model for simulating detonations: continuum models and mesoscale models [72]. Mesoscale models explicitly include the effect of mesoscale properties of the explosive on hot-spot formation and growth, for example by directly simulating grain burning [193] or pore collapse [194]. If the correct physics is used this approach is potentially highly accurate, but computationally expensive when applied over a large scale. In continuum models the mesoscale effects are aggregated into simpler relationships between reaction rates and thermodynamic properties. While reducing the computational complexity, this approach can require experimentally determined parameters specific to the exact explosive formulation.

A reacting explosive can be described by fluid equations describing the conservation of mass, energy and momentum (Equation (7.3)), and reactive equations describing the rate of conversion from unreacted material to reacted products. The system of equations is closed by a mixture model that describes how the reacted and unreacted phases mix together. A mixture model generates the thermodynamic variables at each point based on the relative proportions of unreacted explosive and detonation products, and their equations of state.

$$\frac{\partial \rho}{\partial t} + \nabla \cdot (\rho u) = 0 \tag{7.1}$$

$$\frac{\partial \rho u}{\partial t} + \nabla \cdot (\rho u u) = -\nabla P \tag{7.2}$$

$$\frac{\partial}{\partial t}\left[\rho\left(e + \frac{1}{2}u^2\right)\right] + \nabla \cdot \left[\rho\left(e + \frac{1}{2}u^2\right)\right] = -\nabla \cdot (Pu) + Q \tag{7.3}$$

By discretising the fluid equations, reactive model and mixture model over space and in time, it is possible to create a computational approximation to the evolution of the detonation. The spatial discretisation involves the construction of a mesh – a finite number of cells each associated with a single value of each field variable. The continuous field can then be reconstructed using interpolation methods. In the finite volume method (FVM) used here, the conservation laws are handled by assigning a flux to the surface of each volume. The temporal discretisation is done by dividing the duration of the simulation into time steps. The governing equations then determine how the field values at each mesh point evolve with each time step. The length of the time step and spacing of the mesh points are interdependent and can be changed on-the-fly in order to maintain numerical stability via adaptive mesh refinement (AMR) and/or time step control.

A finite reaction length means that, unless molecular scale resolution is used, the explosive cannot simply be described as being reacted or unreacted, but may also be partially reacted. Therefore it is necessary to use a continuous reaction progress parameter $0 < \lambda < 1$, describing the fraction of material that has reacted. A burn model is used to calculate the rate of reaction $\dot{\lambda}$ from the thermodynamic variables which is then used to update λ for the next time step. The mixture model then balances the proportions of explosive and product at that particular value of λ.

The modelling geometry used here is similar to the geometry of the experimental configuration presented in the previous chapter – a cylindrical confined charge of explosive initiated from one end by a shock. However, the parameters of the shock, the size of the charge and the initial conditions of the material are varied beyond the experiments. Simulations of EBW and EFI initiation were also performed.

7.2 Reactive Model

A reactive model consists of a burn model which provides a state-dependent reaction rate, an equation of state (EOS) for both the solid explosive and gaseous product, and a mixture model to obtain the relative proportions of explosive and product. The equations of state for both solid explosive and reaction products are often in a broad class of equations called Mie-Grüneisen equations.

The reaction rate equation can take many different forms, and can incorporate multiple sub-reaction processes. Generally the reaction rate depends on the reaction progress, as well as a thermodynamic state variable which is a proxy for the strength of the shock, such as pressure, entropy or temperature (or combinations thereof).

One reactive model is the Lee-Tarver model, which uses a reaction rate dependent on the local pressure [53] and is a popular choice for implementation into hydrocodes due to its simplicity. A serious limitation of pressure dependent models like the Lee-Tarver model is that they do not account for the well-known phenomenon of shock desensitisation, where the reaction rate for a given pressure is lower in preshocked material than in undisturbed material [195] [196]. A simple modification to the Lee-Tarver model was made by Whitworth [72] to include the effects of multiple shocks by capping the reaction rate for shocks after the initial one. This modification was successful in its predictions when the reaction in the first shock was small, but less accurate for instances with more reaction in the first shock.

The burn model used here – the CREST model – has a reaction rate that depends on entropy and can predict shock desensitisation. The reactive model also incorporates a porosity model to account for the heterogeneity of the PETN powder, which modifies both the solid equation of state and the reaction rates.

7.2.1 Products' Equation of State

The equation of state for the products is the Jones-Wilkins-Lee (JWL) equation, a form of the Mie-Grüneisen equation of state. This equation gives the pressure of the detonation products for a volume ratio of $V = \frac{V_g}{V_{s0}}$, where V_g is the current specific volume, and V_{0s} is the initial specific volume of the unreacted explosive.

$$P_g = A\left(1 - \frac{\omega}{R_1 V}\right)\exp\left(-R_1 V\right) + B\left(1 - \frac{\omega}{R_2 V}\right)\exp\left(-R_2 V\right) + \frac{\omega E_g}{V} \tag{7.4}$$

The first term dominates for low values of V (i.e. early expansion), the second term dominates for intermediate values, and the last term for large values. The values of the

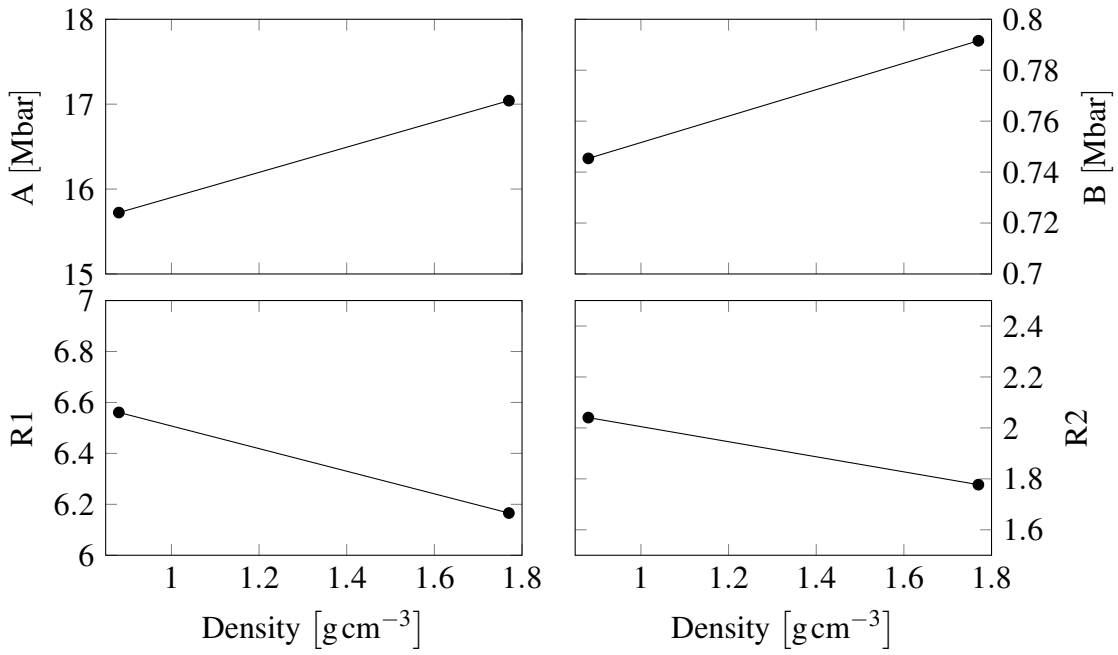

Figure 7.1 Coefficients for Equation (7.4) . Also displayed are the linear interpolation functions used to find their values for arbitrary density

parameters are dependent on the density of the initial pressing [197]. It can be shown that ω is the Grüneisen Γ when the equation is written in Mie-Grüneisen form.

The data of Lee et al. [198] provides JWL parameters for PETN for a range of initial densities. Tarver [199] used a chemical equilibrium code to refine the parameters so they yielded less compressible states at higher pressures. The parameters used here are derived from these sources, adjusted with a small amount of density dependence so they more accurately predict detonation velocities at low initial densities. The value of ω was set to 0.4412 while A, B, R_1 and R_2 were interpolated to the relevant density using the functions shown in Figure 7.1

7.2.2 Reactants' Equation of State

The CREST model also uses a Mie-Grüneisen equation of state for the solid explosive:

$$P_s = P_i(V_s) + \frac{\Gamma(V_s)}{V_s}(E_s - E_i(V_s)) \tag{7.5}$$

P_i and E_i are the pressure and specific internal energy of the reference curve, for which the principal isentrope is used.

There are several choices for defining the reference functions P_i and E_i, although they are related by the following thermodynamic relationship:

$$P_i = -\left(\frac{\partial E_i}{\partial V_s}\right)_S \tag{7.6}$$

The Grüneisen gamma is also a function of specific volume. The reference isentrope functions used here are of the 'Davis' form [200], specifically:

$$P_i = \frac{a^2\rho_0}{4b}\left[\exp(4by) - 1\right] \tag{7.7}$$

$$E_i = \frac{a^2}{16b^2}\left[\exp(4by) - 1\right] + \frac{a^2\rho_0}{4b}(V_s - V_0) + Q \tag{7.8}$$

$$\Gamma = \Gamma_{00} + Zy \tag{7.9}$$

These functions were refined by Stewart et al. [201] by truncating the exponential function, and using the tunable parameter C, so that the Hugoniot is more accurate at high pressures when the material is compressed above the solid density:

$$P_i = \begin{cases} \dfrac{a^2\rho_0}{4b}\left[\exp(4by) - 1\right] & \rho < \rho_0 \\ \dfrac{a^2\rho_0}{4b}\left[\displaystyle\sum_{j=1}^{3}\frac{(4by)^j}{j!} + C\frac{(4by)^4}{4!} + \frac{y^2}{(1-y)^4}\right] & \rho > \rho_0 \end{cases} \tag{7.10}$$

$$E_i = \begin{cases} \dfrac{a^2}{16b^2}\left[\exp(4by) - 1\right] + \dfrac{a^2\rho_0}{4b}(V_s - V_0) + Q & \rho < \rho_0 \\ \dfrac{a^2}{16b^2}\left[\displaystyle\sum_{j=2}^{4}\frac{(4by)^j}{j!} + C\frac{(4by)^5}{5!} + \frac{4y^3}{3(1-y)^3}\right] + Q & \rho > \rho_0 \end{cases} \tag{7.11}$$

$$\Gamma = \Gamma_{00} + Zy \tag{7.12}$$

$$\tag{7.13}$$

The shock Hugoniot can be expressed in terms of its deviation from the principal isentrope:

$$E_s = E_i + \tau Z_s \tag{7.14}$$

The 'function of entropy' $Z_s(V_s)$ is constant along isentropes, and therefore is the difference in specific internal energy between the principal isentrope, and the isentrope which intersects the shock Hugoniot at (V_s, E_s), at $V_s = V_{s0}$. It is therefore constant everywhere, except in the presence of a shock wave, reflecting the thermodynamic irreversibility of shock waves. It is lower for double shocks than single shocks, and hence can be used to incorporate shock

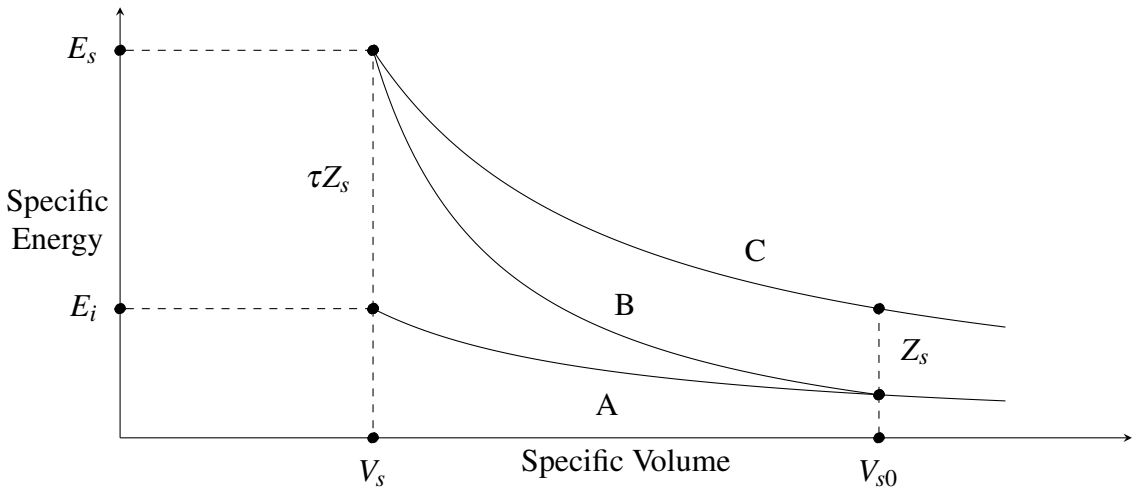

Figure 7.2 The Hugoniot curve (B) is defined by its relation to the principal isentrope (A). The isentrope (C) passing through the Hugoniot at V has energy Z_s at V_0.

desensitisation [202]. τ is a scaling factor such that τZ_s is the difference in specific internal energy at the specific volume of interest. It can be expressed analytically as:

$$\tau\left(V_s\right) = \exp\left[-\int_{V_{s0}}^{V_s} \frac{\Gamma(V)}{V} dV\right] \tag{7.15}$$

The relationship between the reference principal isentrope, the shock Hugoniot, and the intersecting isentrope is shown in Figure 7.2.

7.2.3 ISE Mixture Model

Once the equations of state are defined for both components of the exploding mixture, a set of closure rules that define how the total volume and energy is divided between the two is required. An isentropic solid equation (ISE) model is used to combine the equations of state for the mixture of solid and gaseous phases. The solid fraction of the mixture is in a state on the isentrope passing through the shocked state, and the gaseous fraction of the mixture is in a state such that it occupies the remaining volume and contribution to the internal energy. The relative specific volumes and energies are assumed to be in proportion with the reaction progress variable λ, and the two phases are assumed to reach pressure equilibrium much faster than the characteristic time step [203].

$$V = (1-\lambda)V_s + \lambda V_g \tag{7.16}$$

$$E = (1-\lambda)E_s + \lambda E_g \tag{7.17}$$

$$P_s = P_g \tag{7.18}$$

Root-finding

Each time the ISE model is used, a root-finding method is called to find the equilibrium pressure. This process consists of finding the values of V_s where the absolute value of the pressure difference function $\Delta P = P_s(V_s, E_s) - P_g(V_g, E_g)$ is equal to zero within a certain tolerance $\varepsilon = 10^{-6}$. Each step in the root-finding algorithm involves calculating the solid and gas pressure using the equations of state and the above relationships between V_s and V_g, and E_s and E_g, and then adjusting the value of V_s for the next step in the direction which reduces $|\Delta P|$.

The Newton-Raphson method is a root-finding algorithm in which the next value for V_s is found by updating an initial guess to the root of the linear approximation to the function at the guess, requiring the calculation of the derivative.

$$V_s^{i+1} = V_s^i - \frac{\Delta P}{\frac{d\Delta P}{dV_s}} \tag{7.19}$$

In most circumstances the Newton-Raphson method converges at a second order rate [204], which in practice generally means that around 5 iterations are required to reach the necessary tolerance. Occasionally however, it diverges or gets stuck switching between two values. Divergence can be avoided by restricting the values of V_s to ones that are physically permissible according to the mixture rules:

$$0 \leq V_s \leq \frac{V_0}{1-\lambda} \tag{7.20}$$

When the convergence fails otherwise, another root-finding algorithm must be used.

When the Newton-Raphson method fails the algorithm switches to using a bisection method instead which is guaranteed to converge (for real and continuous functions). In this method, the updated value of V_s is given by:

$$V_s = \frac{1}{2}\left(V_s^L + V_s^R\right) \tag{7.21}$$

where V_s^L and V_s^R are the two bounding values of an interval known to contain the root. Depending on whether V_s is less than or greater than the root then V_s^L or V_s^R is changed to V_s for the next iteration. In this way the bounding interval converges on the root.

Once convergence is achieved, then the resultant pressure $P = P_s = P_g$ and specific volumes V_s and V_g are taken to be the states at that particular time step. For small ($\lambda < \varepsilon$) or large ($\lambda > 1 - \varepsilon$) values of the reaction progress parameter, the root-finding is skipped, and the pressure is calculated from the reactant or product EoS alone, respectively. This step avoids numerical divergence due to floating point arithmetic.

7.2.4 CREST Reaction Rates

The CREST (Computational Reaction Evolution on Entropy (S) and Time) model attempts to avoid the limitations of reaction rates solely dependent on pressure and temperature. Significant motivation for an alternative model came from experiments involving gauges embedded in the material which showed that reaction rates and velocity histories behind the detonation differed from those predicted by existing models [119]. The CREST model has been used extensively to study plastic bonded explosives such as PBX-9502 [205] [72] but also for powdered PETN [206] [207]. A function of entropy is used as a proxy for shock strength and the variable on which the reaction rates depend.

Once V_s and E_s are obtained from the ISE model, the function Z_s can be found, which is then used to calculate the reaction rates:

$$Z_s = \frac{E_s - E_i(V_s)}{\tau(V_s)} \tag{7.22}$$

The stronger the shock, the greater the specific energy of the state at which the isentrope and the shock Hugoniot intersect. Therefore Z_s is greater along that isentrope and can be thought of as a proxy for shock strength.

The rate of reaction is determined by the formation and growth of hot spots – and is calculated as an empirical function of the CREST variable Z_s. Like the Lee-Tarver model, the overall rate of reaction λ is composed of an ignition term and a growth term, with the coefficients m_I and m_G weighting the relative importance:

$$\dot{\lambda} = m_I \dot{\lambda_I} + m_G \dot{\lambda_G} \tag{7.23}$$

Just as λ represents the progress of the whole reaction, λ_I and λ_G represent the progress of the ignition and growth sub-processes respectively. In full:

$$\dot{\lambda_I} = (1-\lambda_I)\left[-2b_1 \ln(1-\lambda_I)\right]^{\frac{1}{2}} \tag{7.24}$$

$$\dot{\lambda_G} = (1-\lambda_G)\,\lambda_I \left[2b_2\left(\frac{b_2\lambda_1}{b_1} - \ln(1-\lambda_G)\right)\right]^{\frac{1}{2}} \tag{7.25}$$

The parameters m_I, m_G, b_1 and b_2 are functions of Z_s:

$$b_1 = c_0\,(Z_s - c_{13})^{c_1} \tag{7.26}$$

$$b_2 = c_2\,(Z_s - c_{13})^{c_3} \tag{7.27}$$

$$m_I = (1-\lambda)\,\frac{c_6\,(Z_s)^{c_{12}}}{\sqrt{b_1}} \tag{7.28}$$

$$m_G = (1-\lambda)\left[\frac{c_8\,(Z_s)^{-c_9} + c_{10}\,(Z_s - c_{13})^{c_{11}}}{\sqrt{b_2}}\right] \tag{7.29}$$

c_{13} is the threshold energy for reaction. The other c_i constants are determined experimentally from gas gun experiments. $\dot{\lambda_I}$ and $\dot{\lambda_G}$ are proportional to $(1-\lambda_I)$ and $(1-\lambda_G)$ respectively – in this way they drop to zero when their part of the overall reaction progress is completed. $\dot{\lambda_G}$ is also proportional to λ_I since a hot spot can only grow once it has been ignited.

If the rate-determining step is hot spot growth, then the model can be reduced to the 'CREST-lite' form [208].

$$\dot{\lambda} = m_2\,(1-\lambda)\,\dot{\lambda_G} \tag{7.30}$$

$$m_2 = \frac{c_{10}}{\sqrt{b_2}}\,(Z_s - c_{13})^{c_{11}} \tag{7.31}$$

$\dot{\lambda_I}$ and $\dot{\lambda_G}$ are plotted against λ_I and λ_G for a range of Z_s in Figure 7.3

A third reaction rate is sometimes included which is slower than λ_G but has the same form, although it is not required for conventional high explosives [209].

Once the reaction rates are known, the reaction progress variables λ, λ_I, and λ_G can be updated

7.2.5 Porosity

The porosity of the explosive has an effect both on the equation of state of the solid explosive and on the reaction rates. One simple way of accounting for porosity is to model the explosive as alternating blocks of air and explosive at TMD [210]. This approach generated reasonably

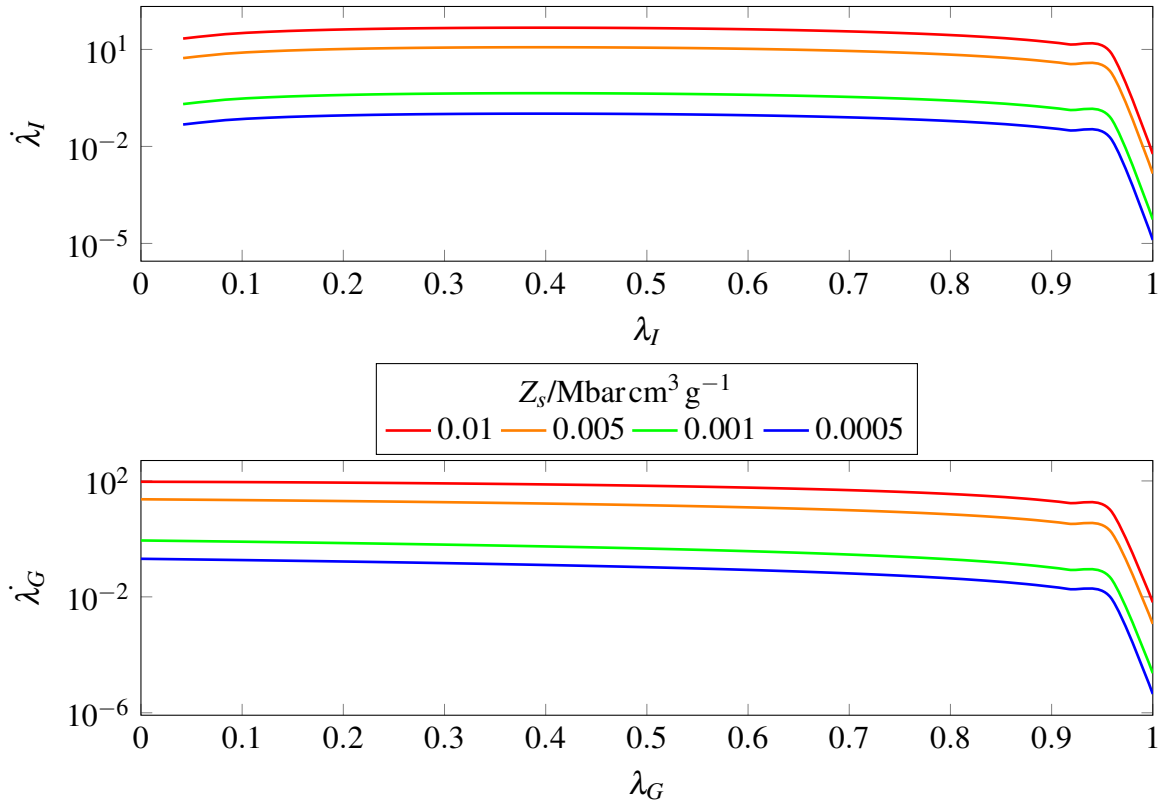

Figure 7.3 The ignition and growth rates vs. their respective progress variables. The rates fall quickly close to 1

accurate detonation velocities and avoids complicated modifications, but also led to large numerical oscillations in the early stages of detonation and so is not suitable for this study. Another very commonly used model is the snowplough model, where the pressure during compaction is 0, and then follows the Hugoniot for the solid material once it is fully compacted. In order to encompass more complex behaviour of porous materials under dynamic loads, the equations of state must be modified in order to smoothly connect the solid Hugoniot with the initial porosity. In the compaction region the porosity, or ratio of specific volumes of the porous solid and compacted solid $\alpha = \frac{V_{porous}}{V_{compact}}$ is a function of another state variable.

In this study the state variable is the pressure; the model is called the $P-\alpha$ model. Alternative porosity models relating α to other state variables such as density ρ or volumetric strain ε also exist [126], although compaction modelling is generally difficult due to the involvement of multiscale phenomena and rate dependent effects. The chosen equation of state and porosity model together match experimental Hugoniot data accurately for pressures up to around 100 GPa [211].

A quadratic $P-\alpha$ model relationship is often used to define the crush curve $\alpha(P)$ [212].

$$\frac{\alpha-1}{\alpha_0-1} = \left(1-\frac{P(\phi)}{P_h}\right)^2 \tag{7.32}$$

$P(\phi)$ is the 'configurational stress' – the pressure above ambient pressure caused by compaction expressed in terms of the volume fraction $\phi = \frac{1}{\alpha}$. The rate of compaction $\dot{\phi}$ is proportional to the difference between the pressure and the configurational stress.

$$\dot{\phi} = k_\phi \left\{ P - P_h \left[1 - \sqrt{\frac{\phi_0(1-\phi)}{\phi(1-\phi_0)}} \right] \right\} \tag{7.33}$$

k_ϕ is an empirically determined parameter that represents the rise time. Here the value of $k_\phi = 31.5 GPa^{-1}\mu s^{-1}$ [213] has been used.

For pressures above the hardening pressure P_h, the material will compress to solid density. Below the hardening pressure the bed will compact, but only up to a maximum value. Another feature of the compaction rate is that a more porous powder compacted to a medium porosity will compact more slowly than a powder that started at that porosity. In this way the model accounts for grain damage and deformation.

Compaction rates for a range of initial volume fractions and pressures above and below the hardening pressure P_h =0.07 GPa [213] are shown in Figure 7.4.

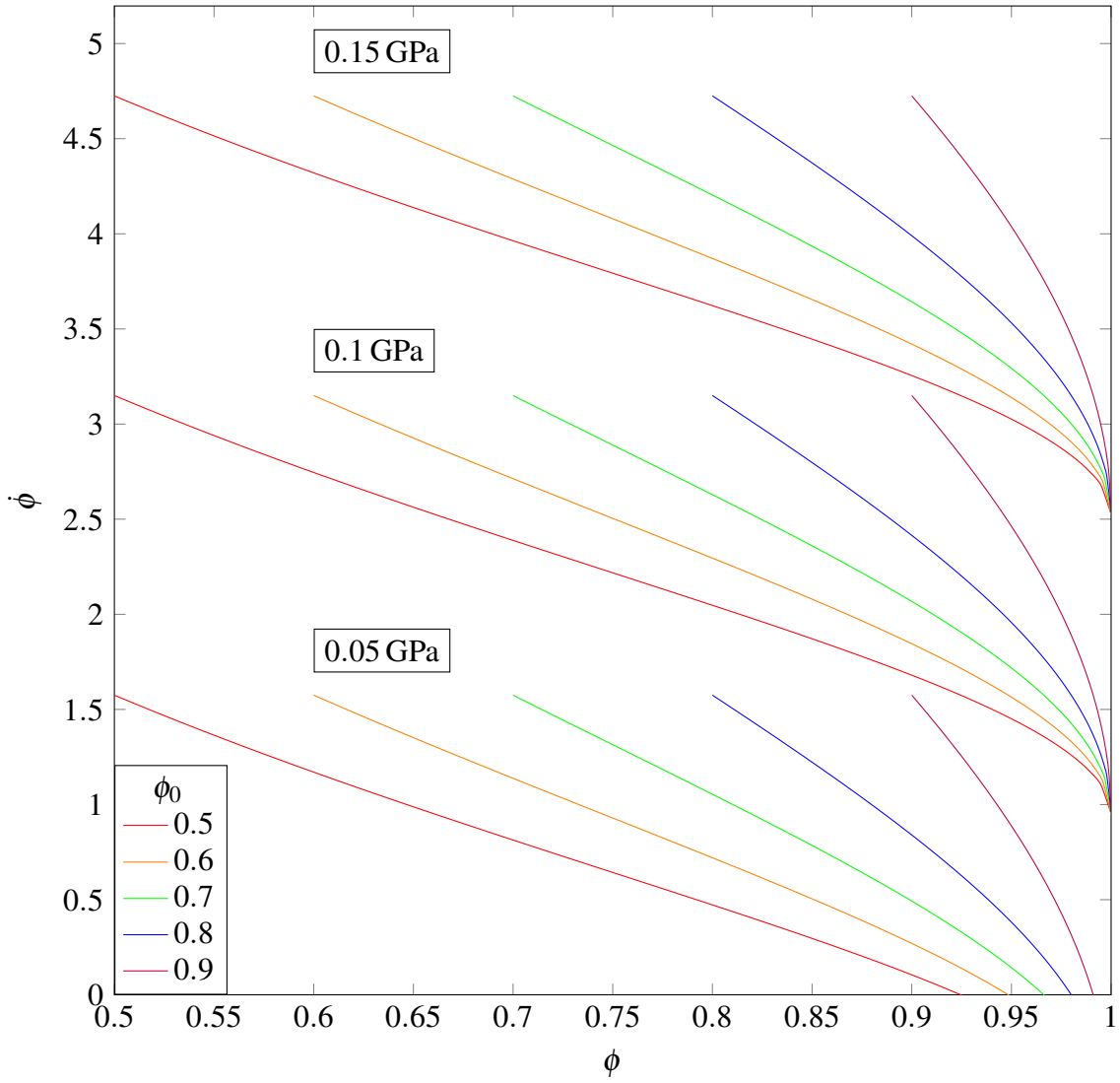

Figure 7.4 The compaction rates for a range of starting porosities and pressures. Above the hardening pressure, the volume fraction always reaches 1, whereas below it the powder stops compacting at an intermediate porosity.

Effect of Porosity on Equation of State

The equation of state for a porous solid explosive differs from the equation of state for the non-porous solid. The $P-\alpha$ model of porosity was introduced [214] to relate the EoS for the solid and porous solid. In the original formulation the porous EoS becomes:

$$P = P\left(\frac{V}{\alpha}, E\right) \tag{7.34}$$

Carroll and Holt [215] developed a modified $P-\alpha$ model which accounts for the volume-averaged stress in the material:

$$P = \frac{1}{\alpha} P\left(\frac{V}{\alpha}, E\right) \tag{7.35}$$

The pressure equilibriation in the ISE model is enacted between the modified porous equation of state for the explosive and the JWL equation of state of the products. The resulting pressure in the occupied fraction of the porous solid is higher than the equilibrium pressure by a factor of $\frac{1}{\phi}$

Effect of Porosity on Reaction Rates

One issue observed by Maheswaran et al. [206] is that a single set of CREST parameters do not work well across a broad range of densities of PETN, and instead caused an overestimation of sensitivity when a set of parameters fitted to a lower porosity was applied to a higher porosity. The function of entropy Z_s is increased by porosity, but the reaction rates do not match this increase. A modification was made to the CREST parameters [216] to deal with this problem. The entropy functions in Equation (7.29) are multiplied by a function $F_c(\phi) < 1$ as follows:

$$b_1 = c_0 \left(F_c \left(Z_s - c_{13}\right)\right)^{c_1} \tag{7.36}$$

$$b_2 = c_2 \left(F_c \left(Z_s - c_{13}\right)\right)^{c_3} \tag{7.37}$$

$$m_I = (1-\lambda)\frac{c_6 \left(Z_s\right)^{c_{12}}}{\sqrt{b_1}} \tag{7.38}$$

$$m_G = (1-\lambda)\left[\frac{c_8 \left(Z_s\right)^{-c_9} + c_{10}\left(F_c \left(Z_s - c_{13}\right)\right)^{c_{11}}}{\sqrt{b_2}}\right] \tag{7.39}$$

The function F_c itself depends on the volume fraction ϕ and parameters A_m and B_m determined by fitting to run-to-detonation distance data [216]. Since $F_c<1$, a given value of Z_s will produce a lower reaction rate when porosity is high. All the other parameters have the same meanings as in Equation (7.29).

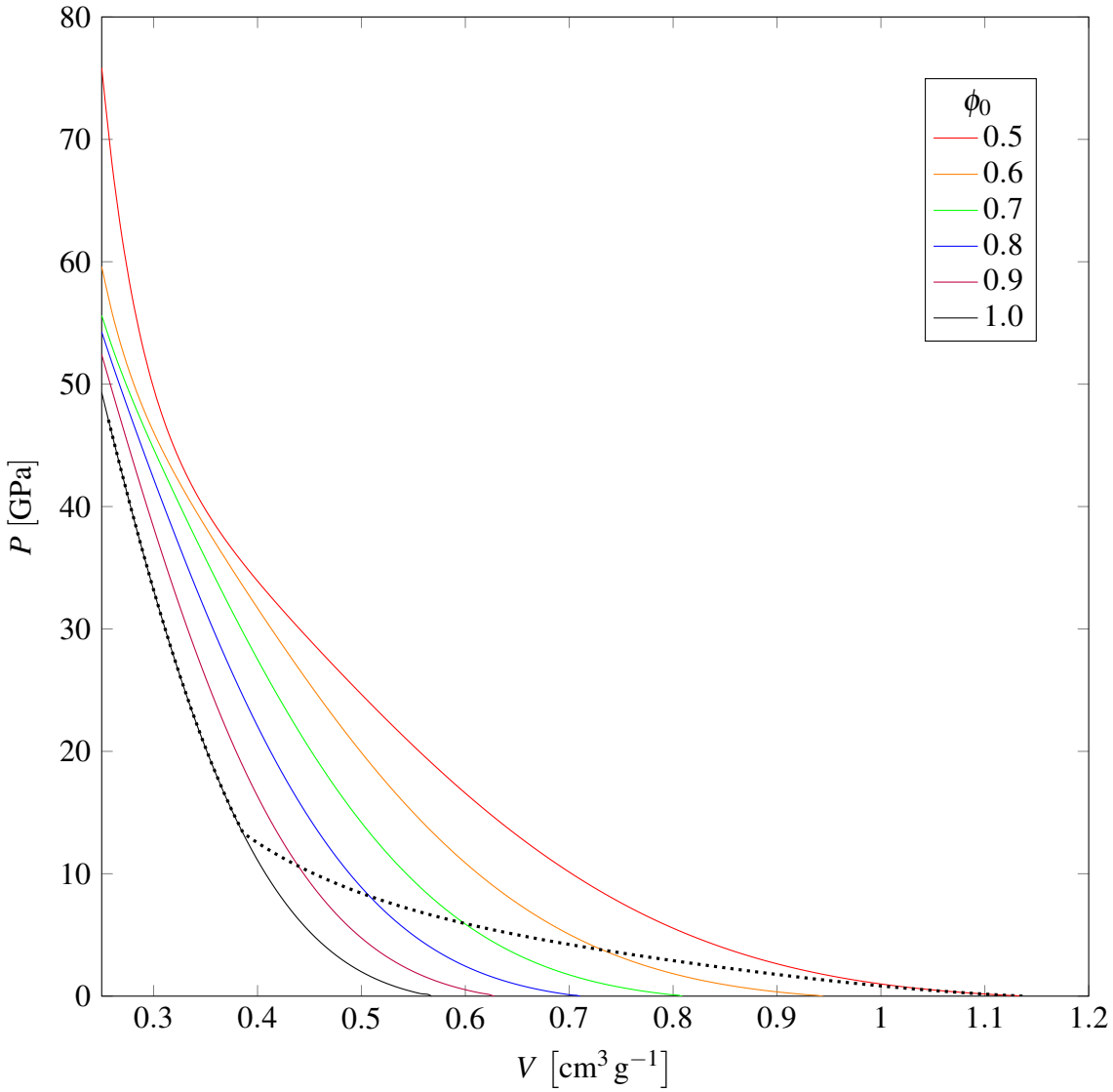

Figure 7.5 The porous Hugoniot curves for the reactants under the $P-\alpha$ model for a range of porosities. The actual compaction path (dotted line) crosses these Hugoniot curves as the volume fraction increases up to 1. Faster compaction results in a steeper compaction curve which meets the Hugoniot at a higher pressure.

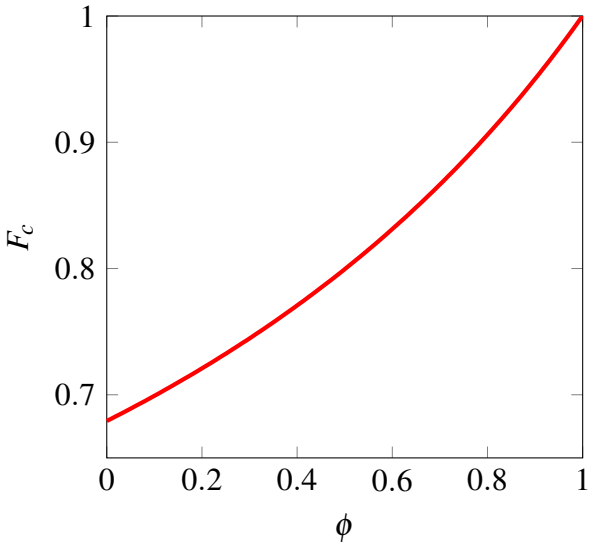

Figure 7.6 The porosity modifier function for the reaction rate coefficients. At a volume fraction of 1, the coefficients are unmodified, and there is a small decrease for smaller volume fractions.

$$F_c(\phi) = \exp\left[-\frac{1-\phi}{A_c + B_c(1-\phi)}\right] \tag{7.40}$$

The data required to calibrate this function is sparse, however, using the reaction zone length data from the previous chapter, a reasonable approximation can be applying the mean value theorem to the reaction rate over the reaction zone:

$$\dot{\lambda} \simeq (D)\frac{\Delta\lambda}{\Delta z} \tag{7.41}$$

Using the above formulation for $\dot{\lambda}$ in terms of A_c and B_c, and the experimentally determined values for the detonation velocities and reaction zone length for the range of initial densities/porosities a function of best fit was produced. Values of A_c =1.88 and B_c =0.704 were obtained.

7.2.6 Sound Speed

The speed of sound in materials described by a Mie-Grüneisen equation of state can be derived as follows:

$$c^2 = \left(\frac{\partial P}{\partial \rho}\right)_S = -V^2 \left(\frac{\partial P}{\partial V}\right)_S \tag{7.42}$$

$$= -V^2 \left[\left(\frac{\partial P}{\partial V}\right)_E + \left(\frac{\partial P}{\partial E}\right)_V \left(\frac{\partial E}{\partial V}\right)_S\right] \tag{7.43}$$

$$= -V^2 \left[\left(\frac{\partial P}{\partial V}\right)_E - \frac{\Gamma}{V} P\right] \tag{7.44}$$

The first term is already calculated for the Newton-Raphson root-finding method.

For a mixture of two materials, the averaged sound speed is found by a volume weighted calculation:

$$\frac{V^2}{c^2} = (1-\lambda)\frac{V_s^2}{c_s^2} + \lambda \frac{V_g^2}{c_g^2} \tag{7.45}$$

The sound speed is used to ensure the size of the time step does not grow too large.

7.3 Numerical Methods

To discretise material properties in space gives requires the use of a mesh, a logical structure of points in space. A Lagrangian hydrocode treats the mesh as being attached to the material, therefore the motion of the material can be inferred from the motion of the mesh. Conversely, an Eulerian hydrocode uses a static mesh through which the material flows from one time step to the next. The hydrocode used here is an Arbitrary Eulerian-Lagrangian (ALE) one, meaning it is a fusion of the two approaches. Within each time step, there is first a Lagrangian step, where the forces on each mesh point are integrated to calculate the material flow. This step is then followed by an Eulerian advection of the material properties back onto the original mesh. By combining the two approaches, the advantages of both are gained: the better accuracy of Lagrangian hydrocodes without the problems caused by large accumulated distortions of the mesh [217]. However, care must be taken to minimise unwanted numerical diffusion in the advection step.

7.3.1 Mesh

The mesh used is a two-dimensional rectilinear array, corresponding to a slice through the centre of the column, with one boundary of the computational domain being the centre of the column, and the other being the outer surface (see Figure 7.7). By assuming azimuthal symmetry the complexity of the modelling is reduced. At the boundaries of the mesh, additional padding cells are included – these are used in the advection calculations for the fluxes and are determined by appropriate boundary conditions. The boundary conditions are reflective – outward fluxes at the boundary are zero.

Within each cell, scalar quantities quantities are attached to cell centres while velocities and fluxes are attached to cell edges. Two additional staggered grids can be constructed with their edges centred at the cell centres of the original mesh. These staggered grids are necessary for advecting momenta. Since the grid spacing is regular, the cell centres of the staggered grids do not necessarily correspond to the cell edges of the original grid. This construction is illustrated in Figure 7.8.

Interpolation is used to map the momenta centred in the staggered grids back to velocities at the edges of the original grid. The extra padding cells ensure that there is sufficient information to calculate quantities at the edge of the mesh.

For all the simulations performed the mesh cell size was $10\,\mu m \times 10\,\mu m$. The results were not significantly different for finer meshes i.e. mesh convergence was achieved at this mesh density. Cell aspect ratio was also investigated – there were no performance advantages for non-square cells.

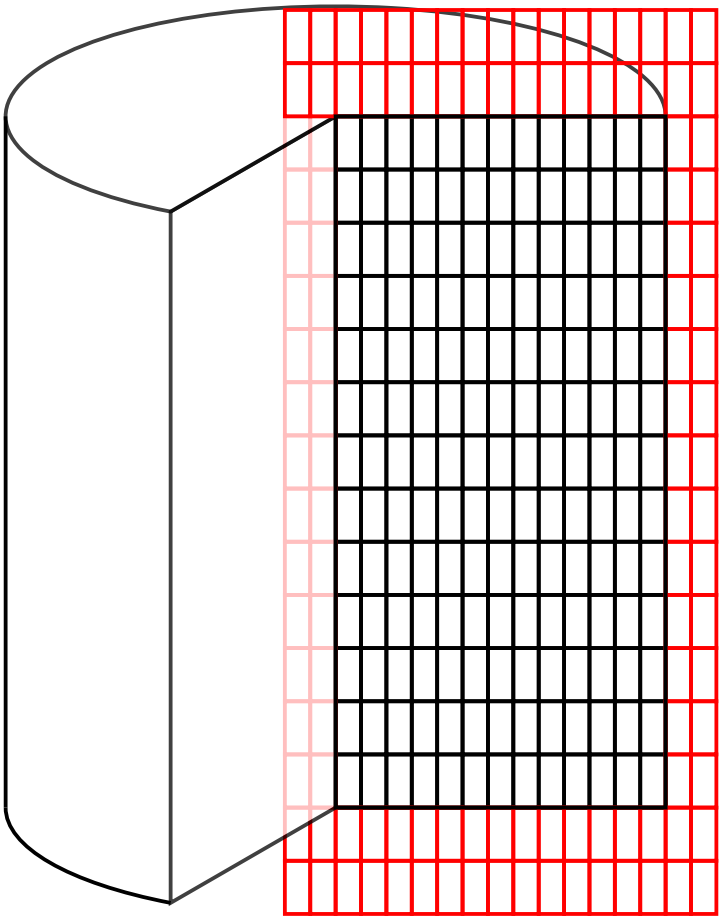

Figure 7.7 The mesh occupies a plane through the radius and axis of a cylinder. The padding cells are shown in red.

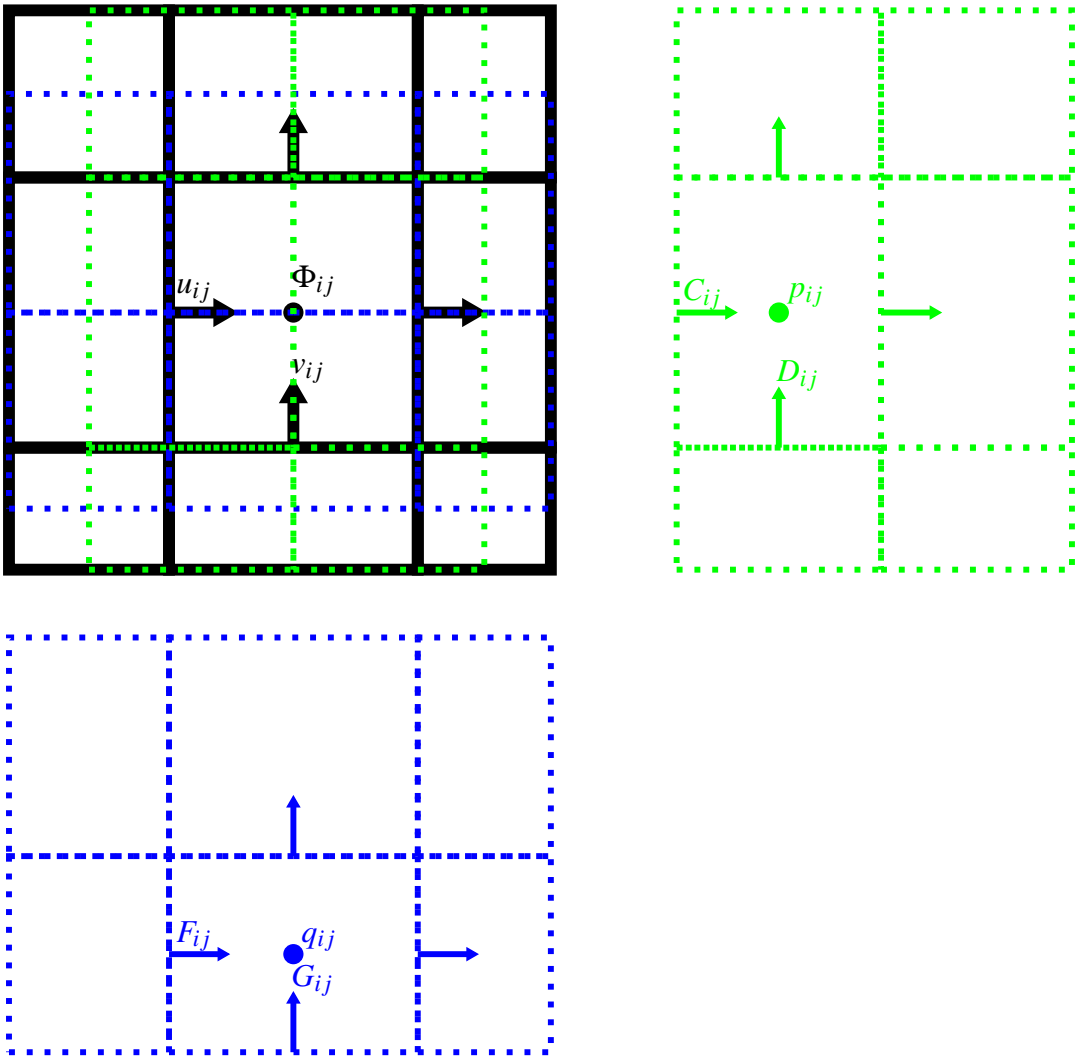

Figure 7.8 Illustration of where the field quantities are defined relative to each other. The two staggered meshes (green and blue) are also displayed outside the main mesh (black) for clarity. Φ is a general scalar quantity such as density or pressure, u and v are the velocities at the edges of the main mesh. p is the radial component of momentum, while C and D are respectively the radial and axial components of radial momentum flux. q is the axial component of momentum, while F and G are respectively the radial and axial components of axial momentum flux. i and j index the radial and axial position within the mesh.

7.3.2 Lagrangian Step

Accuracy of the Lagrangian step is improved by using a predictor-corrector method. An explicit calculation is used to estimate the state variables at an intermediate time step. Gradients calculated at the intermediate time and the original values are then used to produce an improved estimate for the next time step.

Artificial Viscosity

A well-known feature of numerical shock modelling is the presence of unphysical post shock ringing due to the jump discontinuity and discrete mesh. An artificial pressure-like term can be included in the governing equations to damp these oscillations [217]. In order to damp oscillations, the term must be positive when the material is in compression, and zero or negative when the material is in expansion. This term is considered a viscosity because it converts kinetic energy into internal energy – the actual physical viscosity is small enough in shock physics simulations to be ignored.

In this work, the artificial viscosity has two different components in the principal directions. Like the pressure, it is a cell-centred quantity, but requires knowledge of the edge-centred velocities to calculate. The formulation used for the radial (Q) and axial (R) components of the artificial viscosity in terms of the radial (u) and axial (v) velocities is [217]:

$$Q = -C_q \rho \left(\frac{\partial u}{\partial r}\right)_- \left|\frac{\partial}{\partial r}\left(\frac{\partial u}{\partial r}\right)_-\right| \tag{7.46}$$

$$R = -C_q \rho \left(\frac{\partial v}{\partial z}\right)_- \left|\frac{\partial}{\partial z}\left(\frac{\partial v}{\partial z}\right)_-\right| \tag{7.47}$$

where

$$\left(\frac{\partial u}{\partial r}\right)_- = \min\left(0, \frac{\partial u}{\partial r}\right) \tag{7.48}$$

The artificial viscosity is added to the pressure when calculating the changes in momenta and energy. In the latter case it can be identified with the thermodynamic irreversibility of the shock.

Time Step Control

In order to ensure convergence, the Courant-Friedrichs-Lewy (CFL) condition must be met, specifically:

$$v_r \frac{\Delta t}{\Delta r} \leq 1 \tag{7.49}$$

Essentially this condition means that material must not traverse a significant fraction of a cell size in each time step. A further restriction on the time step is made in order to limit the diffusion of momentum by linking the time step to the viscosity.

7.3.3 Advection Step

The advection step involves adjusting the quantities calculated during the Lagrangian step to account for the material's movement through the mesh. This process is necessary so that the same mesh can be used for each time step. The scalar quantities that need to be advected are the density ρ, internal energy E, reaction parameters λ, λ_I, λ_G, and CREST variables V_s, E_s, Z_s. The momenta in the radial and axial directions are also advected, requiring a slight modification to the algorithm. Various algorithms exist for performing the advection step – the one used here is the Van Leer MUSCL scheme [218].

Mass flux at each cell edge is calculated using the pressure gradient and the interpolated edge densities. Interpolated quantities are also found for all of the scalar advection variables, which are transformed into the relevant fluxes.

At the end of the advection step the ISE model is rerun to ensure the reactants and products are at pressure equilibrium, and the reaction rates are recalculated.

Momentum Advection

Since the momenta are defined at the cell centres of the staggered grids the same advection algorithm does not work. By first interpolating the required quantities onto the staggered mesh, this construction allows the same advection algorithm to be used.

One consequence of the advection algorithm is that the kinetic energy is not conserved around shocks – this also affects the entropy and therefore the CREST reaction rates. A correction due to DeBar [219] is applied, where the kinetic energy is advected as a scalar, and then the difference between this quantity and the kinetic energy as calculated from the advected velocities is added back to the internal energy.

Advection in Two Dimensions

A potential issue with advection schemes in 2D is the need for vertex coupling – the transport of material from diagonally adjacent cells. If the naive approach of calculating fluxes only once in each time step is used, then material can only flow to orthogonally adjacent cells, violating the

anisotropy of the system. One method which resolves this problem while maintaining second order accuracy is to perform half an advection in one direction, a full advection in the other, and then the remaining half in the initial direction [217]. An alternative second order method, which is used here is to recalculate the fluxes after performing a half time step of orthogonal advection. The new fluxes are then used to perform the advection over the full time step using the original field values.

Flux Limiting

The fluxes between cells are calculated from interpolated field values at the cell edges. A finite differencing method is used to find the gradients of the field quantities, which are then used to produce a continuous reconstruction of the field, from which the value at any point can be approximated. When there are large differences between adjacent cells, as can be the case with shockwaves, the gradients are very large, which can lead to 'spurious oscillations' – unphysical oscillations of a field quantity between adjacent cells where the calculated flux is unrealistically large. In this situation, the modelling can be improved by artificially limiting the gradients. There is a wide choice of limiting functions that can be applied; a good choice is symmetric, and total variation diminishing (TVD) to at least second order. The limiting function used here is the enhanced monotonised central (MC) limiter [220], which fits all these criteria.

The basic MC limiter has been enhanced with weighting factors to improve its performance on an axisymmetric, irregular mesh. Full details are given in Appendix B.

7.3.4 Validation

In order to verify the numerical methods, the hydrocode was checked against test cases with known analytical solutions. The two tests used were the Sod shock tube test [221] and the cylindrical Sedov blast test [222]. These tests are applied in the axial and radial direction respectively.

Sod Shock Tube

The Sod shock tube problem consists of a tube of ideal gas, divided in two by a diaphragm. The diaphragm separates a high density, high pressure state from a low density, low pressure state. The equation of state for an ideal gas is:

$$P = (\gamma - 1)\, e\rho \tag{7.50}$$

where $\gamma = 1.4$ is the ratio of specific heats.

The initial conditions for the Sod shock tube are:

$$(\rho, e, u) = \begin{cases} (1, 2.5, 0) & 0 \leq z < 0.5 \\ (0.125, 2, 0) & 0.5 \leq z \leq 1 \end{cases} \tag{7.51}$$

At $t = 0$ the diaphragm is removed and the gas is allowed to mix. The solution is the profile of ρ, P, u, e across the length of the tube after a time t. The same profile is obtained for any set of consistent units, therefore units are not given. The features of the solution are a shock wave travelling right, a rarefaction travelling left, and the contact discontinuity between them which travels to the right slower than the shock wave.

Analytical solutions for each of the five regions can be found by solving the Rankine-Hugoniot jump equations [223].

$$P_3 = P_4 \tag{7.52}$$

$$u_3 = u_4 = u_5 + \frac{P_3 - P_5}{\sqrt{\frac{\rho_5}{2}\left[(\gamma+1)P_3 + (\gamma-1)P_5\right]}} \tag{7.53}$$

$$\rho_3 = \rho_1 \left(\frac{P_3}{P_1}\right)^{1/\gamma} \tag{7.54}$$

$$\rho_4 = \rho_5 \frac{P_4 + \Gamma P_5}{P_5 + \Gamma P_4} \tag{7.55}$$

$$\Gamma = \frac{\gamma - 1}{\gamma + 1} \tag{7.56}$$

The analytical and numerical solutions to the Sod shock tube problem are compared in Figure 7.9.

Cylindrical Sedov Blast

Another test of the hydrocode can be performed by calculating the blast wave profile arising after a large amount of energy is deposited in a point or line source. Since the implementation cannot deal with point or line sources, the initial condition for the numerical solution has the energy confined within one cell. The initial conditions (for the numerical solution) are:

$$(\rho, e, u) = \begin{cases} \left(1, \frac{2E}{r_0^2}, 0\right) & 0 \leq r < r_0 \\ (1, 0, 0) & r_0 \leq r \leq 1 \end{cases} \tag{7.57}$$

r_0 is the size of the first cell in the radial direction – the specific energy is scaled so that the total energy $E = 1$. The Sedov test is also self-similar, so units are not required [222].

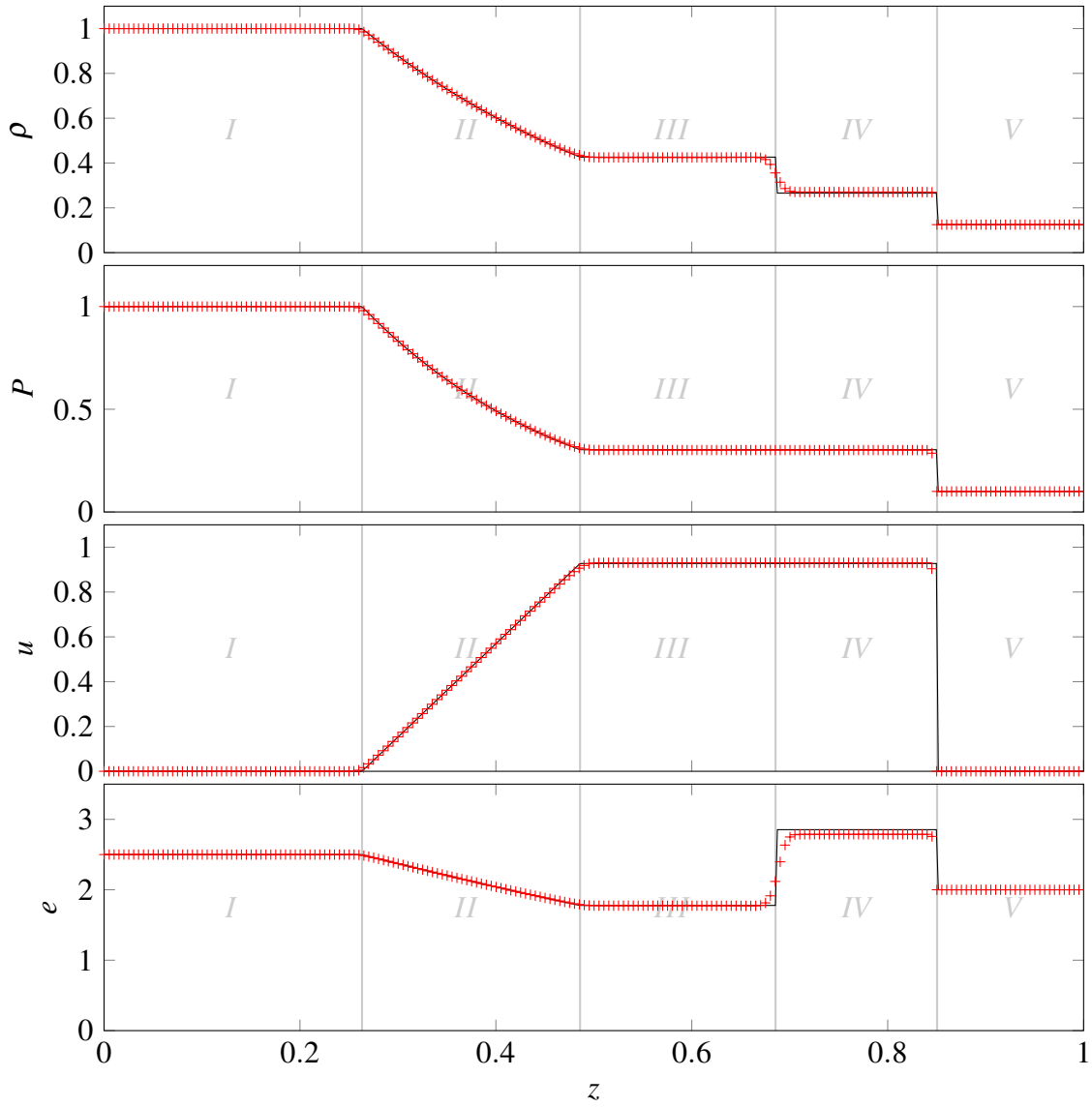

Figure 7.9 The numerical results of the Sod shock tube problem (red) compared with the analytical results (black) at t =0.2. The main discrepancy is at the contact discontinuity (between regions III and IV), which occurs due to numerical dissipation. The greater the zone density, the smaller the error.

Figure 7.10 shows the numerical results for the above initial conditions compared to the analytical results obtained using the methods of Kamm and Timmes [224]

There are some differences between the analytical and numerical solutions arising from discretisation. In the former case the blast originates from a line source, whereas in the latter case the source is a finite cylinder. The position of the shock at later times is fairly sensitive to this difference, while the magnitude is also slightly affected. The finer the mesh spacing, the closer the initial state is to a line source, so the closer the final numerical solution is to the theoretical solution.

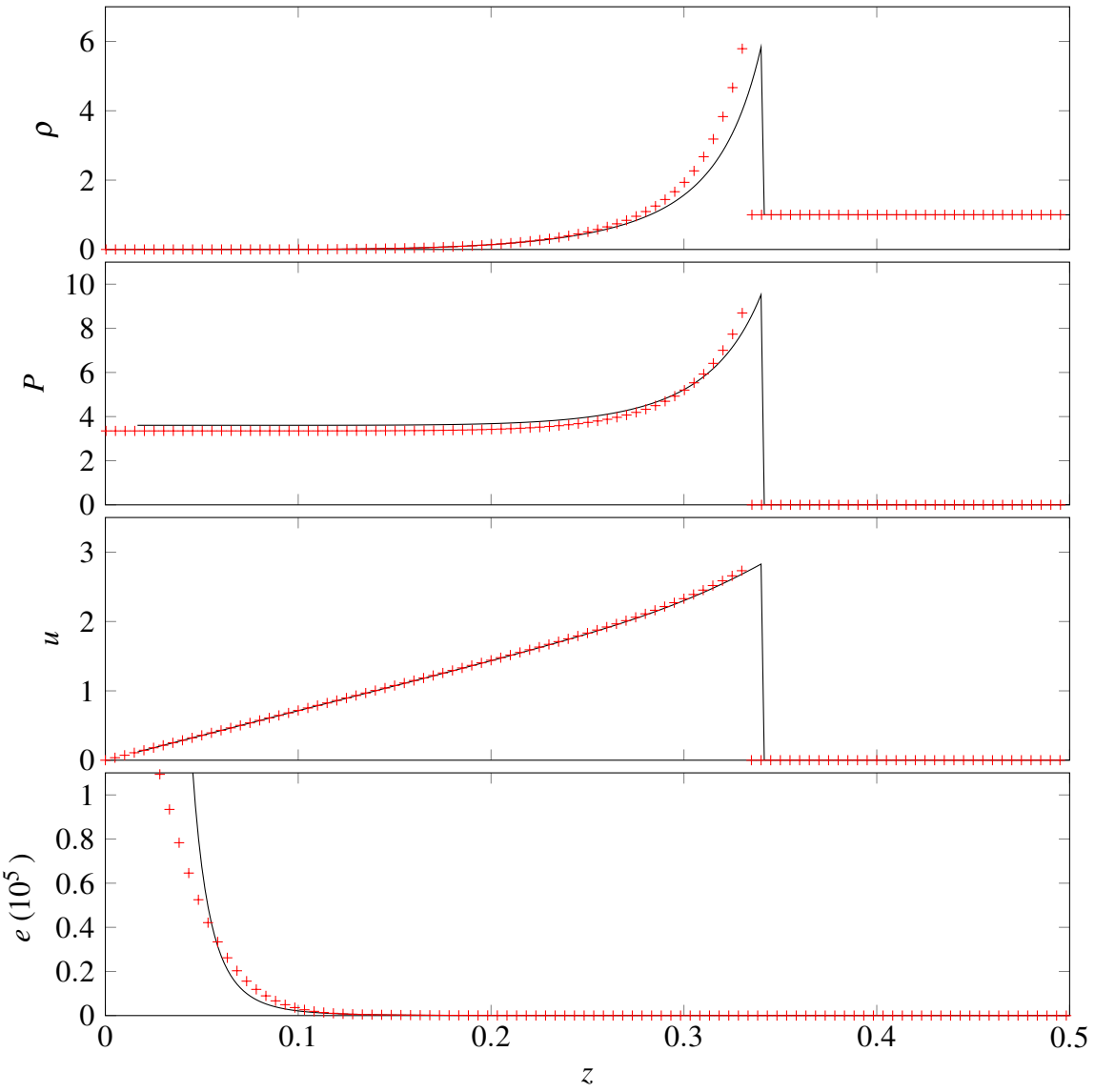

Figure 7.10 The numerical results of the Sedov cylindrical blast problem (red) compared with the analytical results (black) at t =0.05. While the analytical solution treats the blast source as an infinitesimal line, the numerical solution has the blast energy distributed over a single computational cell. For this reason the computed position of the shock is slightly behind the theoretical position

7.4 Laser Flyer Simulation

The hydrocode was first used to simulate initiation by laser flyers and replicate the experimental results of the previous chapter. The programmed input was an initial particle velocity of $5.5\,\mathrm{km\,s^{-1}}$ – equal to the flyer velocity used in the experiments – occupying a thin disk 600 µm in diameter, and 10 µm thick. The geometry was a 5 mm diameter, 5 mm long cylinder with a mesh density of $100\,\mathrm{mm^{-1}}$.

Density plots from the laser flyer simulations are shown in Figure 7.11. As expected, the higher the initial density the faster the detonation wave travels, and the higher pressure.

7.4.1 Comparison with Experiment

The detonation velocity can be extracted from the laser flyer simulations and compared to the values obtained in Chapter 6 to validate the model. Recording the on-axis position of the front over several time steps gives the detonation velocity for each initial density – these results are shown in Figure 7.12. The experimental and literature velocities from Figure 6.11 are reproduced for reference.

The detonation velocities predicted by the simulations match the experiments and the literature data well at the lower densities, however at the higher densities the experimental velocities deviate by up to 10 %. The simulated detonation velocities remain close to the literature data over the full range of densities. As discussed in Chapter 6, the experimental errors were large at higher densities.

While the simulation reproduces the velocity and wave front shape from the experiments, the zone density is not sufficiently high to capture microscale processes like void collapse or fracture. Additional complexities, such as the porosity model and the density modification to the EoS parameters, were included in order to map these microstructural phenomena onto mesoscale variables.

It is possible to use the reaction progress parameter to determine where the explosive was reacting. The reaction zone is taken to be the region where the inequality $\varepsilon_1 < \lambda < 1-\varepsilon_2$ holds for $\varepsilon_1 = 10^{-6}$ and $\varepsilon_2 = 10^{-5}$. The reaction parameter starts as 0 everywhere, so the ε_1 contour can be made small to mark the point where reaction begins. Due to the asymptotic reaction rate the reaction parameter does not reach 1, therefore ε_2 must be relatively large in order to form a contour. Even with this asymmetric definition of ε_1 and ε_2, the rear contour required smoothing to produce a continuous contour.

Just as in the experimental results, the reaction time decreases with density, and the reaction zone length peaks at a density of $1.10\,\mathrm{g\,cm^{-3}}$ as the decreasing reaction time and increasing detonation velocity compete for influence.

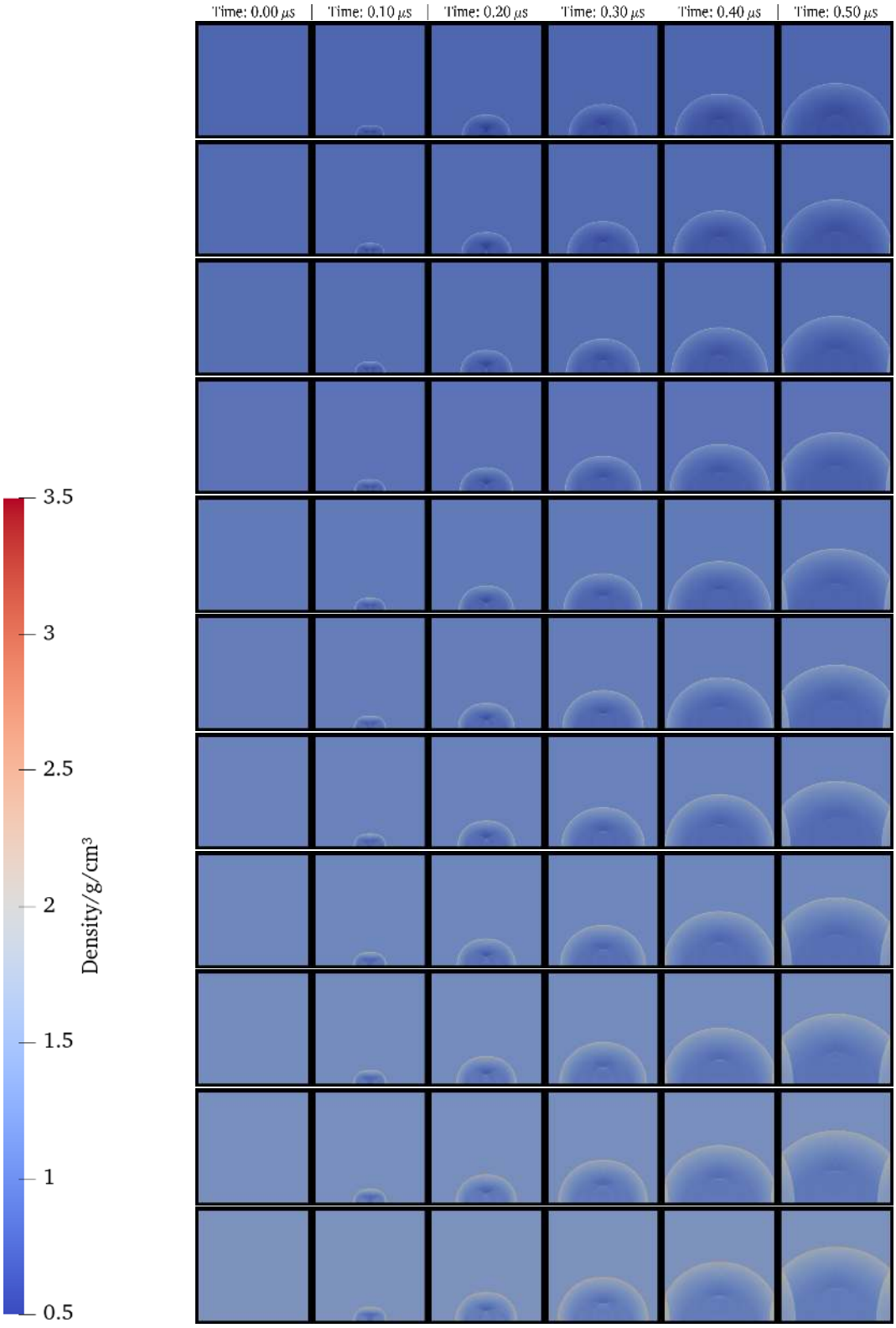

Figure 7.11 Density plots from the laser flyer simulation. From top to bottom, the initial densities are $0.90\,\mathrm{g\,cm^{-3}}$ to $1.40\,\mathrm{g\,cm^{-3}}$ in increments of $0.05\,\mathrm{g\,cm^{-3}}$.

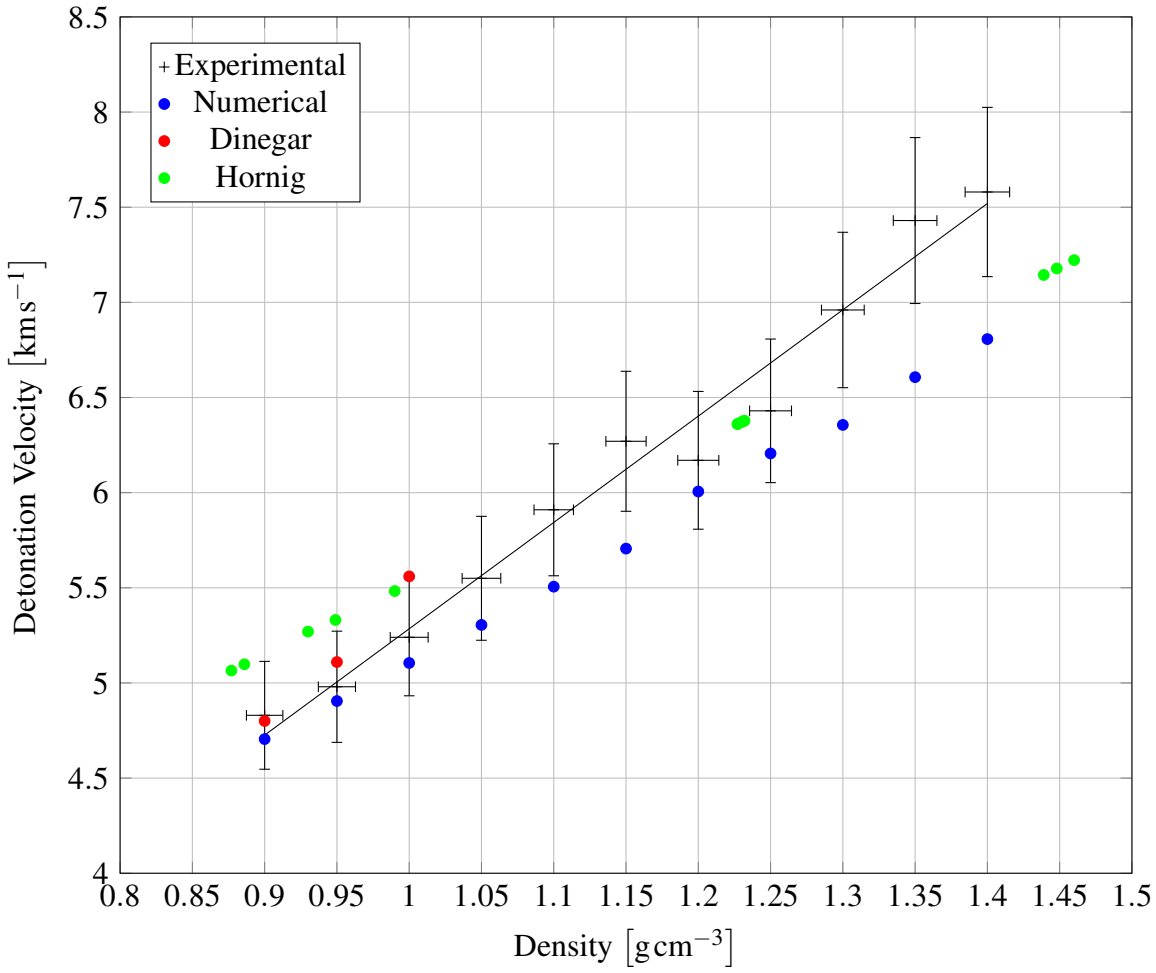

Figure 7.12 Comparison of simulated and experimental detonation velocities. Also shown are values from Dinegar [184] and Hornig [185]. The numerical velocities are similar to both literature and the experimental results at lower densities, however at higher densities the experimental results deviate.

When ε_2 was made larger (10^{-2}) the steady reaction zone lengths did not show much density dependence, ranging from 35 µm to 40 µm. This behaviour corresponds to a front-loaded reaction rate at higher densities, whereas at lower densities the reaction rate peak is wider and has a larger contribution in the tail.

The reaction zone parameters are shown alongside their experimental counterparts in Table 7.1.

	Experimental			Numerical		
ρ/g cm^{-3}	D/km s^{-1}	τ/ns	ξ/um	D/km s^{-1}	τ/ns	ξ/µm
0.90	4.83	14	67	4.7	14	65
0.95	4.98	32	146	4.9	16	77
1.00	5.24	13	64	5.1	15	78
1.05	5.55	34	185	5.3	15	82
1.10	5.91	13	78	5.5	15	83
1.15	6.27	12	76	5.7	13	72
1.20	6.17	12	74	6.0	11	68
1.25	6.43	9	58	6.2	9	58
1.30	6.96	7	49	6.4	8	50
1.35	7.43	7	49	6.6	7	43
1.40	7.58	6	45	6.8	6	40

Table 7.1 Summary table of the laser flyer simulations. Values for the steady detonation velocity (D), reaction time (τ) and reaction zone length (ξ) are given for both the simulations and experiments performed in Chapter 6. The numerical results are in strong agreement with the experimental results, which is not surprising since the model was calibrated using the experiments. The numerical reaction zone lengths could be directly measured, while the experimental results were determined from velocity histories integrated over the reaction time.

7.5 EFI Simulation

The slapper detonator was modelled in the same way as the laser flyer, except with a thicker shock and denser pressing ($1.65\,\mathrm{g\,cm^{-3}}$). The initial conditions were an 800 µm diameter flyer travelling at $4.5\,\mathrm{km\,s^{-1}}$. Frames from the EFI simulation are shown in Figure 7.13.

In the first 0.1 µs the front of the shock is flat, matching the shape of the flyer. However, soon after instabilities from the curved part of the shock grow inwards into the flat part of the shock, causing it to become curved until the whole shock is curved. By approximately 0.3 µs the flat part of the shock has disappeared.

The velocity of the front quickly reaches $8\,\mathrm{km\,s^{-1}}$, in agreement with literature values, while the pressure profile quickly forms the characteristic ZND shape with a von Neumann spike at around 45 GPa followed by the rarefaction tail. There is no stage at which a shock does not exist, so the initiation mechanism is unmistakeably SDT. The curved part of the shock originating from the edge of the impact travels more slowly, and takes longer to reach a steady-state pressure. The pressure variation with angle disappears after the wave has travelled about 3 mm. This angular dependence of transition is illustrated in Figure 7.14.

The reaction zone was again taken to be the region where $\varepsilon_1 < \lambda < 1 - \varepsilon_2$ holds, where $\varepsilon_1 = 10^{-6}$ and $\varepsilon_2 = 10^{-5}$. There is very little change when ε_2 is made larger, indicating that most of the reaction occurs in the front fraction of the reaction zone.

A contour plot of the reaction zone as measured in this way is shown in Figure 7.15 for the same points in time. The thickness of the steady reaction zone reaches 50 µm within 100 ns in the middle of the front; at the same time it is 60 µm at the edges of the front. Within 300 ns it has narrowed to 45 µm on-axis and 50 µm at the edges. The Eulerian reaction time is around 5 ns to 6 ns.

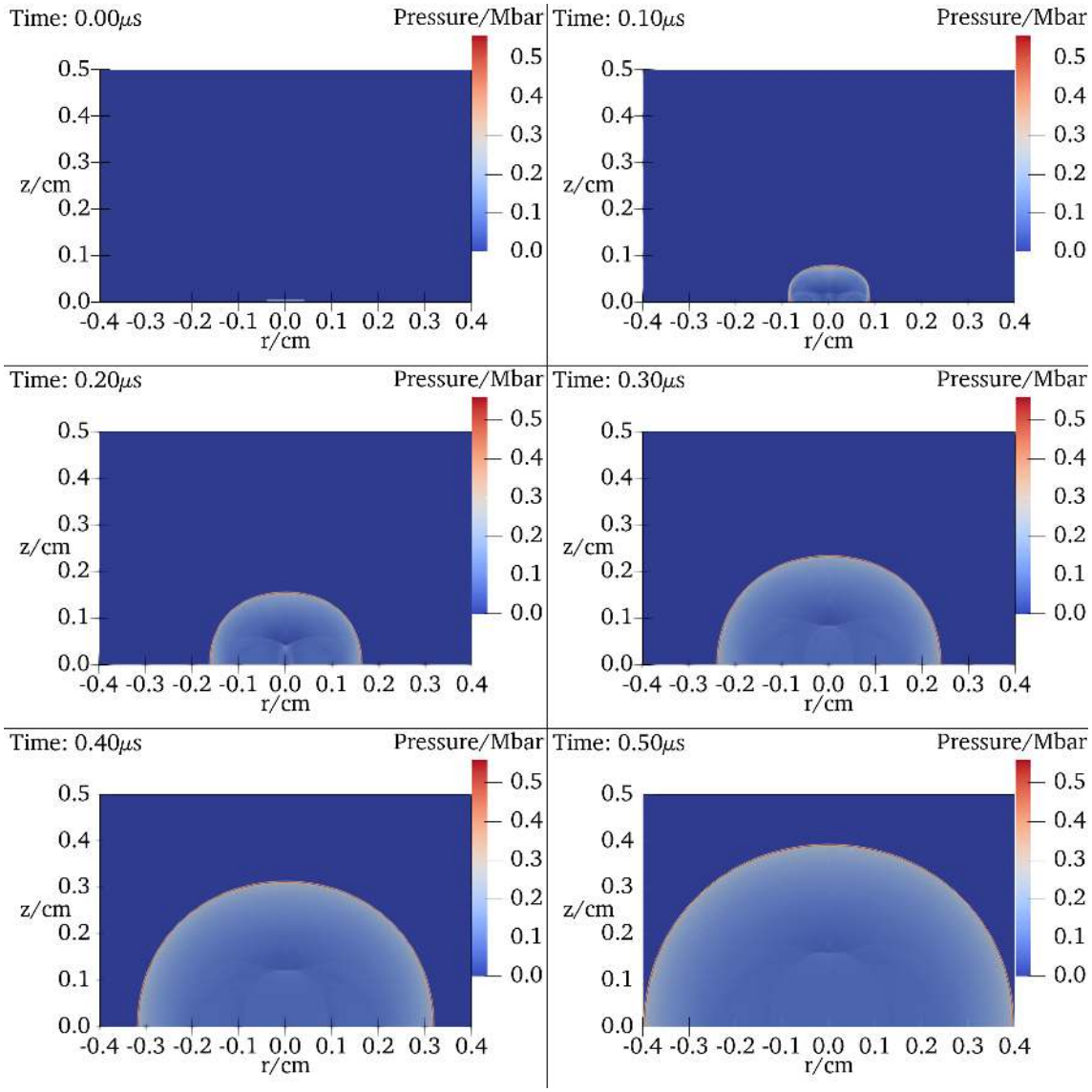

Figure 7.13 Frames from the EFI simulation. The shock initially expands much faster in the axial direction than radially, however the expansion becomes more spherical over time.

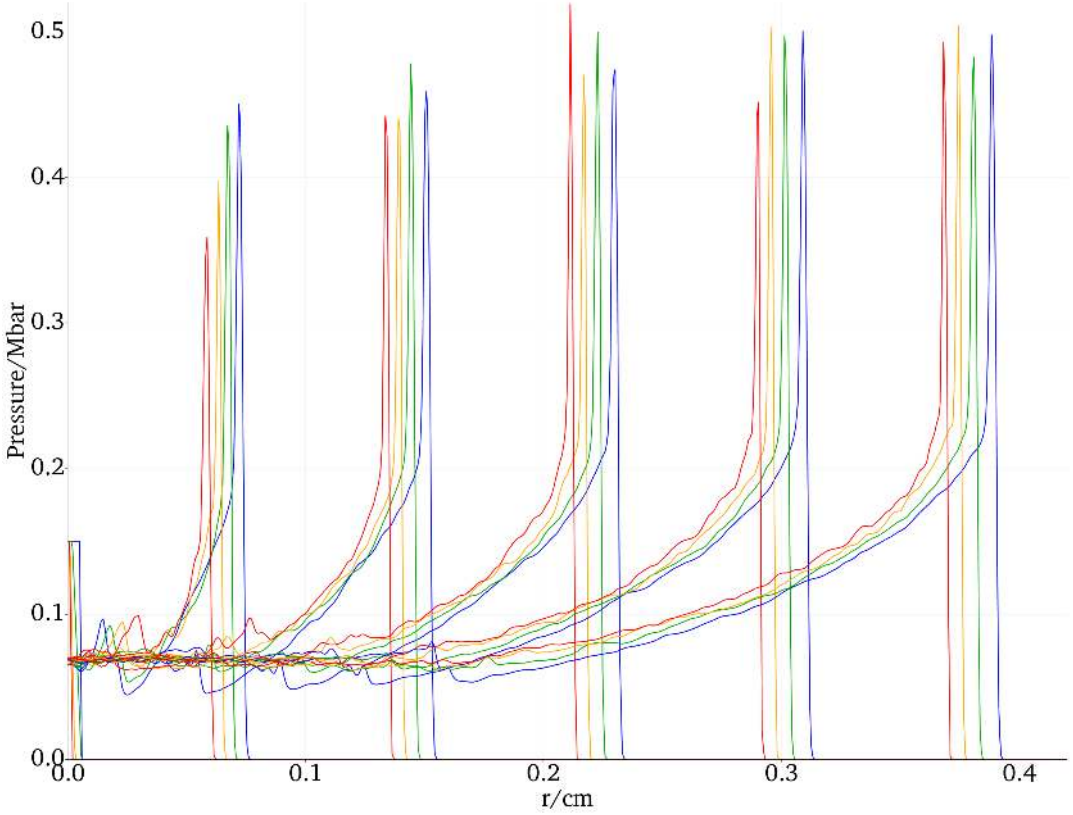

Figure 7.14 Pressure profiles for the EFI simulation every 0.1 µs. The colour represents the angle of the pressure profile relative to the detonation axis: 0°, 15°, 30°, 45°

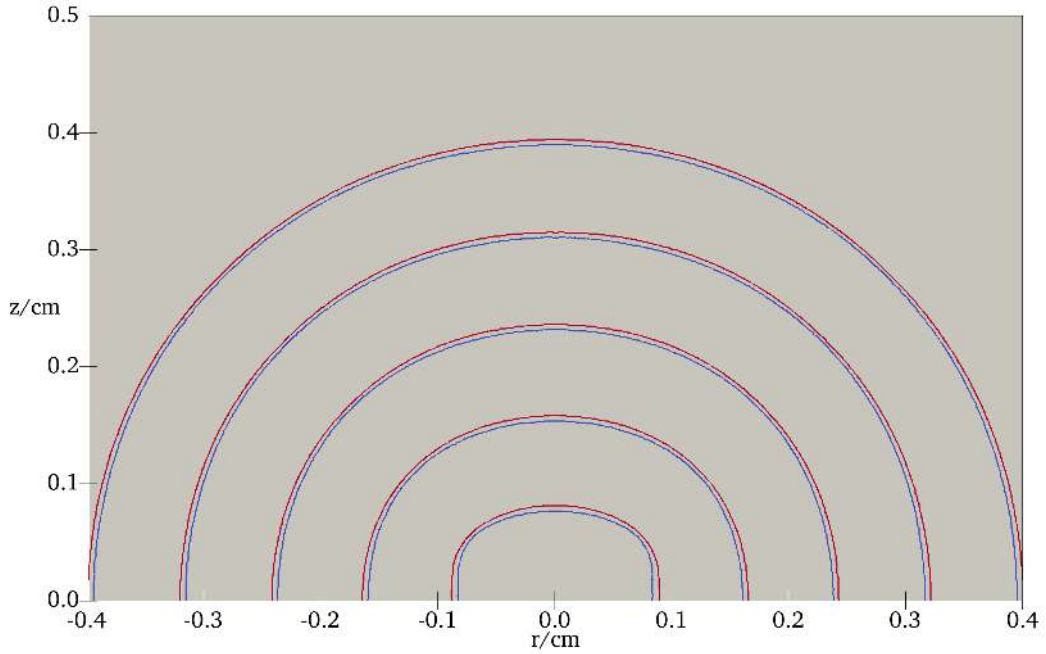

Figure 7.15 The evolution of the region $\varepsilon_1 < \lambda < 1 - \varepsilon_2$ in the EFI simulation. The front is marked in red, and the rear in blue. Snapshots are taken every 0.1 µs.

7.6 EBW Simulation

In order for a bridgewire to initiate the pressing, the input energy up to the burst must exceed that required to vaporise the wire by a threshold amount [82]. If more energy than this threshold is delivered before burst then the time to burst decreases. Increasing the post-burst energy does increases the kinetic energy of the bridgewire products, and also decreases the function time up to a certain point.

There have been several propositions in literature concerning the start of detonation in EBW detonators [4, 87]. To attempt to resolve the mechanism question, Smilowitz et al. [88] made measurements of several observables during detonator function. did not find evidence for a deflagration wave, instead finding a compaction wave followed by a detonation wave. Since these observations are inconsistent with SDT and DDT initiation mechanisms, they proposed a direct thermal initiation (DTI) mechanism. In this process the reaction proceeds within a distance of 1 mm from the bridgewire, but does not propagate for approximately 1 µs.

The bridgewire detonator was modelled in a similar way to the Sedov blast test above, with several differences:

1. The reactive burn model was used instead of the ideal gas EoS.
2. The wire was of finite length and diameter.
3. The energy was deposited over several time steps to represent the effects of post-burst energy.

The dimensions were set to replicate the initial pressing of an RP-80 EBW detonator, a 5 mm long column of PETN pressed to $0.88\,\mathrm{g\,cm^{-3}}$. While a more advanced model would include 3D structures such as the solder posts and full magnetohydrodynamics for the plasma, this simplification is sufficient to capture the most important features of a bridgewire burst.

7.6.1 Energy Input

To represent the time dependence of the post-burst bridgewire energy deposited into the explosive, a source power term was included when calculating the internal energy. The expanding plasma from the bridgewire transfers energy into the solid via both conductive and radiative heating [87]. There is evidence that the initial densification wave from a bridgewire travels at around $3\,\mathrm{km\,s^{-1}}$ [88], so this value was chosen. In this continuous model, the bridgewire output is modelled as a Gaussian function, centred around an expanding front $\sigma_{ebw} = 100\,\mathrm{ns}$ wide travelling at $u_{ebw} = 3\,\mathrm{km\,s^{-1}}$. Additionally the output decays with a characteristic distance of

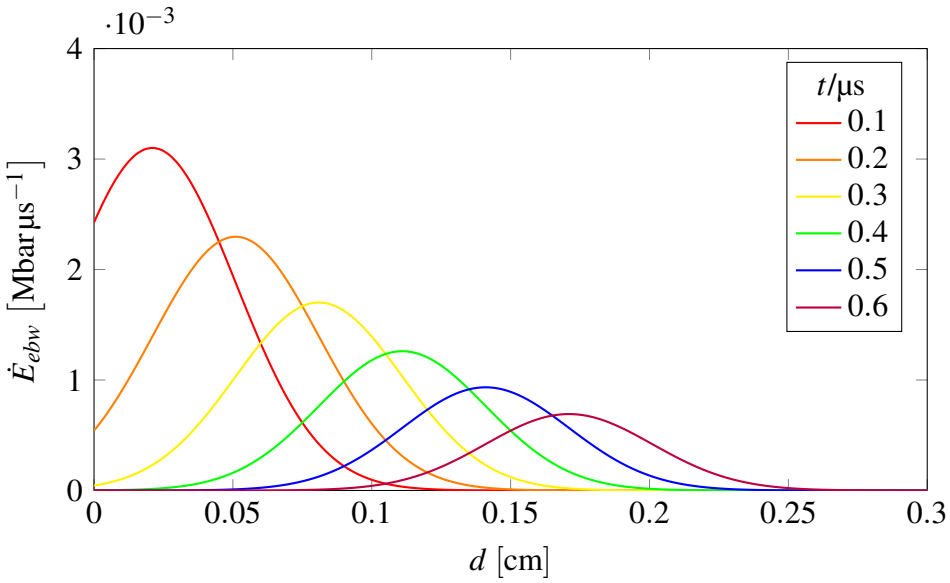

Figure 7.16 In the EBW simulation, the bridgewire is modelled by a time dependent deposition of energy into the mesh zones encompassed by a decaying moving Gaussian function.

δ_{ebw} =1 mm. This energy is then deposited into the mesh at each time step in order to represent the transfer of energy from the bridgewire plasma into the solid which occurs in a real EBW.

The full form of the EBW power density function is:

$$\dot{E}_{ebw} = W_{ebw} \exp\left(-\frac{d}{\delta_{ebw}}\right) \exp\left[-\frac{(d-u_{ebw}t)^2}{2u_{ebw}\sigma_{ebw}}\right] \tag{7.58}$$

W_{ebw} is a scaling constant, d is the distance from the bridgewire, and t the time since burst. This model is plotted for a number of time steps in Figure 7.16.

This simple model avoids the use of magnetohydrodynamics, while reproducing the basic elements of the bridgewire output that are seen in more complex models [225] and experiments [86].

7.6.2 Discussion

Pressure plots from the EBW simulation are shown in Figure 7.17. The behaviour in the first few hundreds of nanoseconds is not visible because the magnitude of the pressure is so small; therefore this time period is not displayed.

There is a weak compression wave travelling at 3 km s^{-1} associated with the bridgewire power function – however the reaction initially proceeds slowly. The compression wave initially only increases the density by around 5 %, although it reaches 0.96 g cm^{-3} by 0.9 µs. Consistent with the experiments of Smilowitz et al. [3], the reaction front does not propagate much until

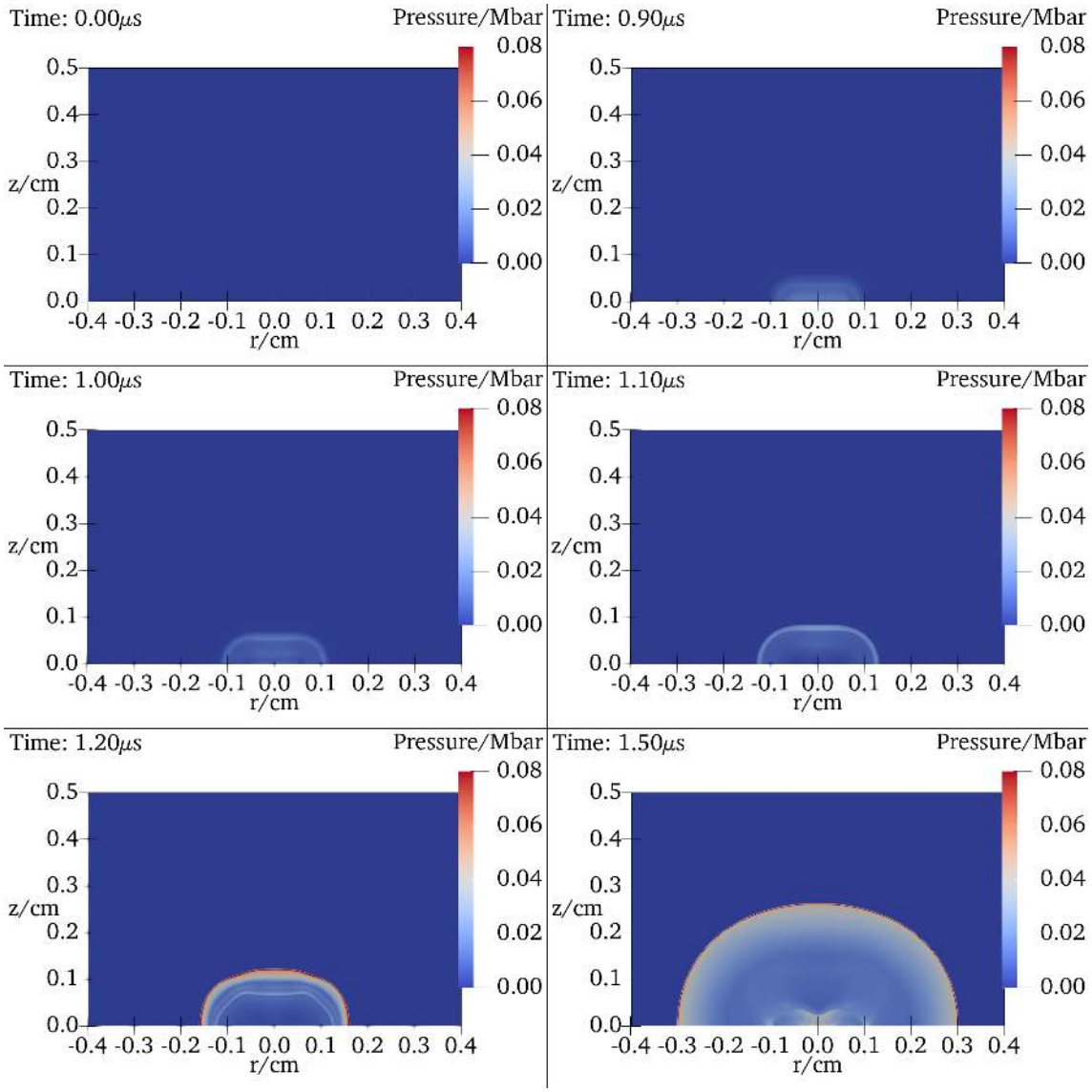

Figure 7.17 Frames from the EBW simulation, viewed perpendicular to the bridgewire. Features of note are the lack of initial propagation and the multiple pressure waves at 1.20 µs.

around 1 µs after the burst. At this point the pressure grows due to slow burning under the compression wave, and a detonation wave starts to form approximately 800 µm into the material. The detonation travels at around $5\,\mathrm{km\,s^{-1}}$ through the pre-compressed material, eventually catching up with the weakening compaction wave after another 400 ns, and around 2 mm into the material, at which point the detonation stabilises at a steady $4.7\,\mathrm{km\,s^{-1}}$ through the uncompressed $0.88\,\mathrm{g\,cm^{-3}}$ PETN.

Unlike the EFI, the EBW simulation demonstrates a slow narrowing of the reaction zone, as illustrated by the reducing gap between the two contours shown in Figure 7.18. Here it can be seen that the delay to propagation of the detonation front at 1 µs after burst is due to the rear of the reaction zone catching up to the front of the compressive wave, which barely moves during this time. The compression wave induces reaction, however until it becomes supported by the much stronger pressure wave, the detonation does not propagate.

The simulations suggest that EBWs behave in a fundamentally different way to laser flyers and EFIs. In the latter case, the planarity and relative integrity of the initiating shock force the initial particle velocity to match the impact velocity. The pressure in the bed is sufficient to bring the reaction to completion, with the compaction and compression being followed almost immediately by reaction. The detonation velocity for each density then depends on curvature and reaction zone width, and becomes steady as these become constant. In EBWs, the initial pressure and energy output is sufficient to cause a compaction wave along with partial reaction, however there is a delay for pressure to build up sufficiently to complete the reaction. The pressure wave accelerates into the pre-compacted and partially reacted material, and a detonation forms a distance into the bed. It does not become steady until it catches up with the compaction wave (by which time the reaction zone and curvature are approximately constant).

This explanation of the lost time is supported by more advanced models [225], which also suggest the existence of multiple shocks emanating from the bridgewire. The modelling performed here also leads to multiple shocks – these can be seen clearly at 1.20 µs in Figure 7.17, just before they coalesce.

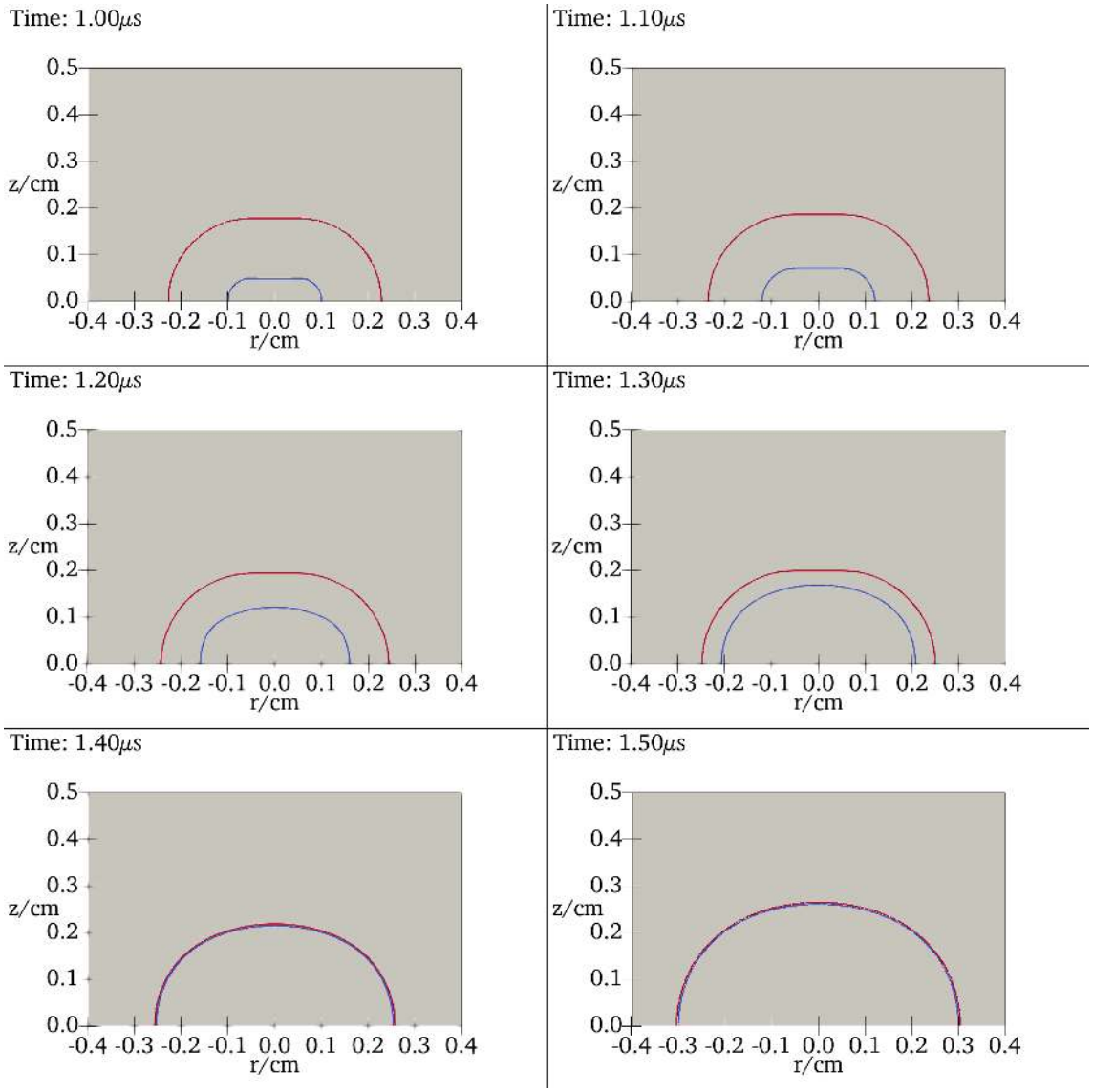

Figure 7.18 The evolution of the region $\varepsilon_1 < \lambda < 1-\varepsilon_2$ following an EBW fire into 0.88 g cm^{-3} PETN, viewed perpendicular to the bridgewire. Here $\varepsilon_1 = 10^{-6}$ and $\varepsilon_2 = 10^{-2}$ – the larger ε_2 produces a smoother contour for illustrative purposes. The $\lambda = \varepsilon_1$ contour is marked in red, and the $\lambda = 1-\varepsilon_2$ contour in blue. Initially the gap between these contours is large, as the compression wave induces a small degree of reaction but it does not go to completion. The detonation catches up around 2 mm into the material, and the gap between the contours narrows.

7.7 Summary

- An ALE hydrocode has been developed to model the experiments using the CREST reaction model.
- A JWL equation of state with density dependent coefficients was used to model the products, while the reactants were modelled using a Mie-Grüneisen equation of state with reference functions that were modified for high pressures.
- A $P-\alpha$ porosity model with a pressure dependent compaction rate was included to adjust the reactant equation of state, and the CREST reaction rates.
- A second order predictor-corrector method and modern advection algorithms make the simulation accurate while parallelisation on a GPU decreases computational time. Two test cases were compared to their analytical solutions with good agreement.
- The experiments performed in Chapter 6 were simulated in order to calibrate the model.
- A slapper detonator and an EBW detonator were simulated. The shock to detonation transition was clear in the EFI simulation, while the EBW simulation exhibited an initially unsteady compaction wave which propagates a distance into the bed before the detonation wave is formed.
- The hydrocode can simulate the experiments in this thesis, as well as observations in literature, using a relatively basic model and representation of detonator output.
- This work provides an explanation for the origin of the observed lost time by using a simple model of a bridgewire burst, without requiring magnetohydrodynamics or 3D simulation.

Chapter 8

Conclusions and Future Work

8.1 Conclusions

This study has approached the problem of determining the reaction zone length in PETN with novel experimental techniques and numerical simulation. The experiments required multiple apparatuses and diagnostic innovation to investigate different facets of the problem.

Finely powdered sugar was tested using a planar shock from a gas gun to investigate the mechanical response of porous materials to shock. The plate impact experiments were primarily concerned with discovering the mechanical properties of an inert powder, so that these effects could be accounted for when the powder was also reactive. In particular, the presence of non-steady behaviour would complicate analysis of the transition to steady state in detonation.

One key finding was that the shock velocity initially ramped up, but then decreased due to lateral release waves. It was discovered that the shock rise time was dependent on the thickness of the bed, which was explained using a force chain argument. Thinner beds have less variability in force chain length so the shock front does not get smeared out as much. It was argued that branching of these force chains could cause a densification effect, which would have consequences for the evolution of the reaction zone and curvature if it was also present in detonating PETN.

Transitory behaviour from shock to steady state was observed a few millimetres into the bed. The shock velocity peaked 2 mm into the bed before plateauing while the shock rise time increased with bed thickness up to about 3 mm. There was a transition from elastic to inelastic release at 1 mm; for thicker beds the lateral release became more important than axial release.

A laser flyer system was built to reliably initiate small columns of pressed PETN powder. The system used an Nd:YAG laser focused into an optical fibre to homogenise the beam; the fibre also carried the pulse to the target. Much of the experimental development was centred on ways to focus the beam into the fibre without causing damage. A series of lenses with a

microlens array achieved a tight beam diameter with few hot spots. A multi-axis stage was used for fine control of the alignment process.

A digital streak camera was used to characterise the flyers as they impacted on a window with a stand off of 100 µm. Thin multi-layer flyers were found to remain intact and largely planar up to the impact site. At energies close to the critical fluence limit for optical damage, the system could launch flyer plates with velocities in excess of $5\,\mathrm{km\,s^{-1}}$ – sufficient for initiating fine grained PETN.

A novel diagnostic based on capacitive sensing was introduced. Single-use sensors consisting of a simple printed circuit were manufactured and used in conjunction with a high frequency wave generator and high bandwidth oscilloscope. The technique exploits the response of the sensor to a conducting object or region in its proximity. The shape of the high frequency signal is modified by the change in capacitance between the sensor and its surroundings. Higher conductivity or closer proximity results in a bigger change to the signal.

Changes to the signal were quantified by applying a continuous wavelet transform to the signal and comparing it with a baseline. The design of the circuit amplified the size of this effect relative to background noise. Active shielding was used to reduce stray capacitance and coaxial lines reduced external noise.

Analysis based on the rise and fall times of the processed signal was developed to convert the data into displacement-time graphs of the front and rear of the reaction zone. From these graphs, the detonation velocity and reaction time could be found. The method was found to be sensitive enough to detect the reaction zone in a detonating explosive, with the high temporal resolution required. Unlike other electromagnetic diagnostics, it does not require high voltages or embedding, since the information is extracted from the explosive via changes in the electric field rather than a current.

Capacitive sensing was applied to small cylindrical PETN charges. The detonation was measured both along its own axis and as it broke out on the back face of the pressing. Detonation velocities closely matched those found by previous work.

The reaction time was found to depend on the density of the pressing: the steady value ranged from 14 ns at $0.90\,\mathrm{g\,cm^{-3}}$ to 6 ns at $1.40\,\mathrm{g\,cm^{-3}}$. It is believed that denser pressings will form a greater number of critical hot spots in any given layer, so more grains in that layer will start burning together (and therefore also finish burning together).

Reaction time also decreased with distance – it is theorised that the same densification mechanism observed in the inert plate impact experiments is responsible for this behaviour. A precursor compaction wave would slightly increase the density as it moved through the bed, and therefore decrease the reaction time. The reaction times found from both sensor orientations

were similar to each other, and to the literature values, although these have more variation (from 'less than 10 ns' [75] to 50 ns [188]).

The geometry of the sensor made it possible to convert the reaction time into the reaction zone length using the measured velocity histories. The reaction zone length's dependence on density inherits the dependence of the detonation velocity and the reaction time. For densities below about $1.10\,\mathrm{g\,cm^{-3}}$ the slower detonation velocity means the reaction zone length shrinks with decreasing density, despite the reaction time increasing. Above this density the reaction zone length follows the same decreasing trend as the reaction time, albeit tempered by the increasing detonation velocity.

The steady reaction zone lengths measured ranged from 67 µm at $0.90\,\mathrm{g\,cm^{-3}}$ to 45 µm at $1.40\,\mathrm{g\,cm^{-3}}$, with a peak of 78 µm at $1.10\,\mathrm{g\,cm^{-3}}$. Similar values were found when the sensor was oriented perpendicular to the axis.

Using this perpendicular orientation, and samples with a range of cutback lengths it was possible to obtain off-axis break-out lags and calculate curvatures. The evolution of the curvature showed the detonation front flattening as it approached the steady state shape. The flattening occurred earlier and to a greater degree at higher powder densities. An argument was given using radial energy flow and rarefaction waves from the edge to explain this trend.

A velocity deficit was observed in the build up to detonation, leading to a lost time. The higher the density, the smaller the velocity deficit and resulting lost time were. Run to detonation was ruled out as an explanation, leaving the finite reaction time and curvature as the causes. A longer reaction time (as seen in less dense pressings) means that the energy is released more slowly by chemical reactions. Therefore there is a smaller build up of pressure in the reaction zone.

While the centre part of the wave was initially flat due to the planar shock, its curvature increased due to radial energy flow. Interaction with the confiner also influences the curvature once the wave reaches the edge. When there is curvature, less pressure builds up behind the wave front as the energy flux is not parallel to the detonation axis.

The greater curvature and longer reaction time at lower densities meant that the detonation was less supported in its direction of travel, so took longer to reach the steady detonation velocity. It is likely that the variation in the lost time with density stems mostly from the variation in reaction time and curvature in the first few millimetres, since that is where these differences are greatest. The curvature variation takes longer to develop than the reaction time variation, since in the former case the curvature must first travel from the edge of the impact to the centre axis. The large factor by which the reaction time shrinks (5–10×) suggests that it plays a greater role.

The experiments were used to guide the development and calibration of an ALE hydrocode, which produces accurate simulations of detonating PETN for a range of densities and inputs. The hydrocode made use of modern numerical methods, the CREST reaction rates and porosity-dependent equations of state and rate adjustments. With sufficient resolution the numerical reaction zone length matches the experimental conductive zone reasonably well. Simulations were also performed of EBW and EFI detonators which demonstrated the different initiation mechanisms.

The simulations of the laser flyers and slapper detonators behaved similarly, exhibiting a shock to detonation transition promptly after initiation. Both featured an initially flat front in front of the impact site, which became curved as energy flowed outwards. The reaction zone reached a steady value within a few hundred nanoseconds – this occurred marginally faster on-axis than off-axis.

The output of the EBW detonator was modelled using a travelling wave that deposited diminishing amounts of energy into the bed – this simplification recreated the lost time. A compaction wave induced some reaction but the build up of pressure and detonation were delayed by approximately 1 µs. The reaction zone was initially large, and shrank as the detonation wave caught up with the compaction wave – effectively finishing off the reaction.

8.2 Future Work

Based on the experiments carried out, several suggestions are given here for work that would expand upon the research presented in this thesis. These are divided into improvements to the experimental apparatus and ideas for additional experiments that would build upon this work.

8.2.1 Plate Impact Improvements

The techniques used in the plate impact study are well established so there is less room for improvement. Lateral release of the initial shock was found to be an important feature for thicker beds, whereas the same did not hold true in the PETN experiments, where axial release dominated. Using a thinner projectile would have provided a better benchmark.

Some of the results from the plate impact study call into question how well the copper mirror matched the velocity of the rear surface. A better solution might be to forego gluing the copper to the PMMA cell, and instead have it behind a window. In this way the copper is only acting as a mirror on the surface, and not as part of the material confinement. This modification would improve the accuracy of the final particle velocity, although information about the release behaviour would be lost.

8.2.2 Laser Flyer System Improvements

The laser flyer system worked as intended, so there is not huge scope for improvement. The limiting factor in the throughput of experiments was the need to replace the ferrule and repolish the fibre end after each shot due to damage caused by the detonation – since this was performed by hand it was a fairly slow process. The nature of the experiment means that the damage is inevitable, but a fibre polishing machine would increase the speed of experimental work. Furthermore it would improve consistency in the fibre output face and therefore also the flyer planarity.

8.2.3 Capacitive Sensor Improvements

While the capacitive sensors worked successfully, there are several improvements that could be made to improve the quality of the data they produce.

1. Increasing the sensing zone density. The sensors used in this work were limited by the number of oscilloscope channels and manufacturing process. However there is no reason why a greater number of smaller sensing zones cannot be used if more channels are available. To compensate for the loss in signal strength from smaller sensing zones, a wave generator capable of producing a higher voltage input signal might be required.

2. Removing the sensing zone tracks from the detonation path. Since the detonation passes over the tracks of previous sensing zones there is some degree of signal merging which reduces the sharpness of the processed signal, and by extension the accuracy of the timing points. By taking the tracks out of the way of the detonation the signals from each zone should be more distinct.

3. Changing the shape of the shielding electrode. Examination of the raw signals revealed that there was some cross-channel signal leaking, which is undesirable. Using individual shielding electrodes for each sensing zone rather than a single one would hopefully reduce this phenomenon.

4. Using different sensors for axial and radial measurements. In this work, a single design was used for both configurations (axially along the length of the charge and radially on the back face). This design has the disadvantage that the sensor must be geometrically suitable for both. Customising the design for each case with greater geometrical specificity would improve the measurement technique.

With these improvements in mind, upgraded sensors are shown below.

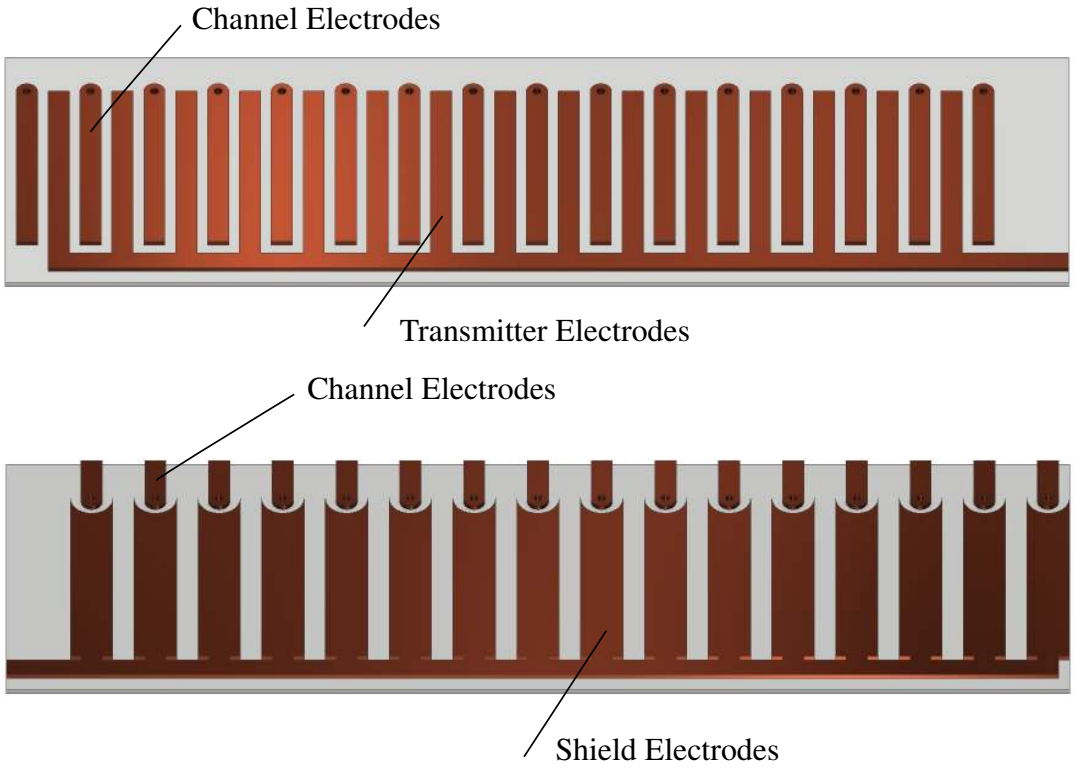

Figure 8.1 The two sides of the head of an improved axial sensor. There are 16 channels, which are interdigitated with the transmitter electrodes. Through-holes have been used to move the tracks out of the path of the detonation, the shielding electrode has been made larger and split across the channels

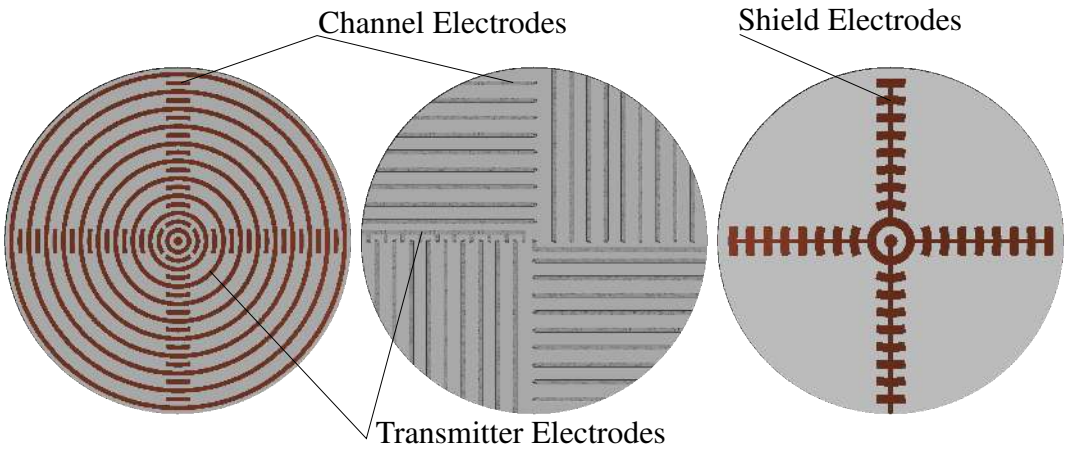

Figure 8.2 The improved radial sensor is a three layer printed PCB, since flexibility is not as important in this configuration. The channel electrodes have both radial and angular dimensions

The improved axial sensor (Figure 8.1 has a higher sensing zone density, which would give improved spatial resolution and a more accurate velocity history.

The improved radial sensor (Figure 8.2) has more sensing zones that span the full angular range, thereby producing a 3D picture of the wavefront. With this data it would be possible to investigate a wider range of phenomena such as tilt, 2D curvature and oscillations.

If the number of oscilloscope channels is restricted, it may be possible to feed multiple sensing zone signals into one channel, provided that they are spatially separated enough that the useful regions of each signal can be clearly disambiguated. Multiplexing of multiple spatially separated channels in this way has previously been performed with PDV [226].

The temporal resolution of the method could be improved by using a higher frequency wave generator and a higher bandwidth oscilloscope – there exist instruments with better specifications than the ones used in this work.

8.2.4 Further Experiments

There are a large number of parameters that could be varied in the experimental work. While not possible here due to a limited supply of material, there is an opportunity for future research to further investigate these parameters and expand the dimensionality of the data. Repeating the experiments that were performed would also be beneficial given more material.

Input Variation

Almost all the experiments in this study were performed with the same flyer launch parameters (thickness, diameter and velocity). Gathering data for a range of flyer velocities (and therefore

input pressures) and showing that the lost time was not affected would confirm that the run to detonation distance does not significantly affect the lost time. The effect on the reaction time could also be determined. A stronger shock ought to create more critical hot spots, making the reaction time shorter, or at least allow it to reach a steady value sooner.

Experimenting with different flyer thicknesses would allow one to vary the duration of the shock into the bed. A longer shock would encompass more grains, so burning would commence over a greater distance. The expected outcome is that the reaction time would initially be longer, but the long term behaviour of the detonation would remain unchanged.

Using flyers of varying diameters would also be an interesting set of experiments to do. The degree to which the size of the flyer affected the curvature on and near the axis was not particularly evident in this research, but using the capacitive sensors with very short charge lengths and a range of flyer diameters might provide some more insight.

Detonator Type

EBW detonators would produce a less planar, lower strength shock than EFI or laser flyers. Repeating the experiments of this study with an EBW detonator head would be worthwhile. The expanding plasma could potentially be detected by the capacitive sensors since it is conducting, although care would need to be taken to ensure the bridgewire does not discharge directly into the sensor and overload the system, as happened on one occasion with an EFI detonator. Including circuitry to direct any stray power surges away from the sensitive electronic equipment would circumvent this problem and allow electrical detonators to be used without risk.

Since a bridgewire is essentially a line source of shock rather than a plane, it is expected that the transition from the initial front shape to the steady shape would happen differently. The front would have to evolve from having azimuthal symmetry around the bridgewire to having azimuthal symmetry around the charge axis. There would be complex 2D modes in the front shape during the intermediate period, which would require the upgraded sensors described above to detect.

Explosive Specification

Due to availability and initiation limitations, only one type of PETN powder – 1 µm to 2 µm ultrafine – was studied. The particle size is an obvious choice of parameter to vary to extend this research; in particular it would be useful to test larger particles and particles of different shapes. One would expect larger particles to exhibit a longer reaction time, but the detonation velocity would not change. It is not clear how the evolution of curvature would depend on

particle size. Repeating the curvature series of experiments using a range of different particle sizes would be a useful investigation.

It would also be worthwhile to gather data on other explosives besides PETN. Besides being short, the reaction zone of PETN has a relatively low conductivity compared to other secondary explosives due to the lack of solid carbon formation. It is therefore expected that the capacitive sensors would perform just as well with other explosives, if not better.

Less conventional structures, such as single crystal or deposited film, may also be of interest for a full understanding of PETN, although they are not of much relevance to studying detonators.

Charge Size

While this study incorporated some variation of the charge size, it was not the principal independent variable. Of particular interest would be smaller diameter charges, where the size of the laser flyer would be more significant. Unusual behaviour might be observed close to the critical diameter.

It proved difficult to press compacts thinner than 1 mm without them falling apart, particularly at lower densities. If a way could be found to produce these pressings, perhaps *in situ* then it would be a worthwhile endeavour in order to extend the data gathered here.

Finally more unorthodox charge shapes could be examined. A charge that changes diameter as the distance from the input increases, either conically or with a step change would be another way of studying the development of curvature.

References

[1] R. Varosh. Electric detonators: EBW and EFI. *Propell. Explos. Pyrotech.*, 21:150–154, 1996.

[2] E.A. Lee, R.C. Drake, and J. Richardson. A view on the functioning mechanism of EBW detonators. 3: Explosive initiation characterisation. *J. Phys.: Conf. Ser.*, 500:182023, 2014.

[3] L. Smilowitz, B. Henson, D. Remelius, N. Suvorova, D. Oschwald, and K.A. Thomas. Measurements of observables during detonator function. In *AIP Conference Proceedings*, volume 1979, page 150035. AIP Publishing, 2018.

[4] P.J. Rae and P.M. Dickson. A review of the mechanism by which exploding bridge-wire detonators function. *Proceedings of the Royal Society A*, 475(2227):20190120, 2019.

[5] C.M. Tarver, R.D. Breithaupt, and J.W. Kury. Detonation waves in pentaerythritol tetranitrate. *J. Appl. Phys.*, 81:7193–7202, 1997.

[6] S.N. Lubyatinsky and B.G. Loboiko. Density effect on detonation reaction zone length in solid explosives. In S.C. Schmidt, D.P. Dandekar, and J.W. Forbes, editors, *Shock Compression of Condensed Matter - 1997*, pages 743–746. American Institute of Physics, Woodbury, New York, 1998.

[7] B.G. Loboiko and S.N. Lubyatinsky. Reaction zones of detonating solid explosives. *Combust. Explos. Shock Waves*, 36:716–733, 2000.

[8] W.W. Wood and J.G. Kirkwood. Diameter effect in condensed explosives: The relation between velocity and radius of curvature of the detonation wave. In W.W. Wood, editor, *Shock and Detonation Waves*, pages 101–109. Gordon and Breach, New York, 1967.

[9] D.M. Chambers. Perspectives on pentaerythritol tetranitrate (PETN) decomposition. *UCRLID-148956, July*, 1, 2002.

[10] C.M. Tarver, A.S. Lefrancois, R.S. Lee, and K.S. Vandersall. Shock initiation of the PETN-based explosive LX-16. In *Thirteenth International Detonation Symposium*, pages 881–889, 2006.

[11] P.W. Cooper. *Explosives engineering*. John Wiley & Sons, 2018.

[12] F. Ullmann, W. Gerhartz, Y.S. Yamamoto, F.T. Campbell, R. Pfefferkorn, and J.F Rounsaville. *Ullmann's encyclopedia of industrial chemistry*. VCH publishers, 1985.

[13] B.D. Roos and T.B. Brill. Thermal decomposition of energetic materials 82. correlations of gaseous products with the composition of aliphatic nitrate esters. *Combustion and Flame*, 128(1-2):181–190, 2002.

[14] Y. Zhang, Q. Li, and Y. He. Analysis of chemical reaction process after pentaerythritol tetranitrate hot spot ignition. *ACS omega*, 5(45):28984–28991, 2020.

[15] J. Kimura. Chemiluminescence study on thermal decomposition of nitrate esters (PETN and NC). *Propellants, explosives, pyrotechnics*, 14(3):89–92, 1989.

[16] M.L. Hobbs, W.B. Wente, and M.J. Kaneshige. PETN ignition experiments and models. *The Journal of Physical Chemistry A*, 114(16):5306–5319, 2010.

[17] J-S. Lee, C-K. Hsu, and C-L. Chang. A study on the thermal decomposition behaviors of PETN, RDX, HNS and HMX. *Thermochimica Acta*, 392:173–176, 2002.

[18] G.R. Miller and A.N. Garroway. A review of the crystal structures of common explosives. part I: RDX, HMX, TNT, PETN, and tetryl. Technical report, DTIC Document, 2001.

[19] R.N. Rogers and R.H. Dinegar. Thermal analysis of some crystal habits of PETN. *Thermochim. Acta*, 3:367–378, 1972.

[20] D.C. Monroe, K.E. Laintz, J.F. Kramer, and P. Peterson. PETN: Variation in physical and chemical characteristics related to aging. In *Proc. 37th Int. Ann. Conf. of Institut für Chemische Technologie*, page paper 33. Karlsruhe, Germany, 2006.

[21] X. Song, Y. Wang, and C. An. Thermochemical properties of nanometer CL-20 and PETN fabricated using a mechanical milling method. *AIP Advances*, 8(6):065009, 2018.

[22] E. Edmonds, A. Hazelwood, T. Lilly, and J. Mansell. Development of in-situ surface area analysis for detonators. *Powder technology*, 174(1-2):42–45, 2007.

[23] S. Young. *Method Development and Validation for Measuring the Particle Size Distribution of Pentaerythritol Tetranitrate (PETN) Powders*. New Mexico Institute of Mining and Technology, 2005.

[24] M.F. Foltz. Aging of pentaerythritol tetranitrate (PETN). *LLNLTR-415057, Lawrence Livermore National Laboratory, Livermore, CA, USA*, 2009.

[25] W.G. Proud, E.J.W. Crossland, and J.E. Field. High-speed photography and spectroscopy in determining the nature, number, and evolution of hot spots in energetic materials. In *25th international Congress on High-Speed photography and Photonics*, pages 510–518. International Society for Optics and Photonics, 2003.

[26] J.K.A. Amuzu, B.J. Briscoe, and M.M. Chaudhri. Frictional properties of explosives. *Journal of Physics D: Applied Physics*, 9(1):133, 1976.

[27] J.T. Hagan and M.M. Chaudhri. Fracture surface energies of high explosives PETN and RDX. *J. Mater. Sci.*, 12:1055–1058, 1977.

[28] M. Zhai and G.B. McKenna. Mechanical properties of pentaerythritol tetranitrate (PETN) single crystals from nano-indentation: Depth dependent response at the nano meter scale. *Crystal Research and Technology*, 51(7):414–427, 2016.

[29] J.J. Dick. Plane shock initiation of detonation in γ-irradiated pentaerythritol tetranitrate. *Journal of Applied Physics*, 53(9):6161–6167, 1982.

[30] A.B. Kunz. An Ab Initio investigation of crystalline PETN. *MRS Online Proceedings Library Archive*, 418, 1995.

[31] R.H. Dinegar, R.H. Rochester, and M.S. Millican. Effect of specific surface on the shock sensitivity of pressed granular PETN. *Explosivstoffe*, 11:188–189, 1963.

[32] J.J. Lannutti. Characterization and control of compact microstructure. *MRS Bulletin*, 22 (12):38–44, 1997.

[33] M.D. Vannet and G.L. Ball. Pourability enhancement of PETN explosive powders. *Journal of energetic materials*, 5(1):35–55, 1987.

[34] M.W.G. Burt and C.A. Fewtrell. The preparation of powder beds by a centrifugal compaction technique. *Particle Size Analysis; Groves, MJ, Wyatt-Sargent, JL, Eds*, pages 321–338, 1970.

[35] C.B. Skidmore, D.S. Phillips, P.M. Howe, J.T. Mang, and J.A. Romero. The evolution of microstructural changes in pressed HMX explosives. Technical report, Los Alamos National Lab., NM (United States), 1998.

[36] G.E. Seay and L.B. Seely Jr. Initiation of low-density PETN pressing by a plane shock wave. *J. Appl. Phys.*, 32:1092–1097, 1961.

[37] J.F. Baytos. *LASL explosive property data*, volume 4. Univ of California Press, 1980.

[38] D. Stirpe, J.O. Johnson, and J. Wackerle. Shock initiation of XTX-8003 and pressed PETN. *J. Appl. Phys.*, 41:3884–3893, 1970.

[39] K.S. Vandersall, C.M. Tarver, F. Garcia, P.A. Urtiew, and S.K. Chidester. Shock initiation experiments on the HMX based explosive LX-10 with associated ignition and growth modeling. In *AIP Conference Proceedings*, volume 955, pages 1010–1013. AIP, 2007.

[40] P.A. Urtiew, K.S. Vandersall, C.M. Tarver, F. Garcia, and J.W. Forbes. Shock initiation experiments and modeling of composition B and C-4. Technical report, Lawrence Livermore National Laboratory (LLNL), Livermore, CA, 2006.

[41] M.J. Gifford, W.G. Proud, and J.E. Field. Observations on type II deflagration-to-detonation transitions. In *AIP Conference Proceedings*, volume 620, pages 878–881. AIP, 2002.

[42] J.E. Field. Hot spot ignition mechanisms for explosives. *Accounts Chem. Res.*, 25: 489–496, 1992.

[43] F.P. Bowden and A. Yoffe. Hot spots and the initiation of explosion. In *Proc. Third Symp. on Combustion and Flame and Explosion Phenomena*, pages 551–560. Williams and Wilkins, Baltimore, Maryland, 1949.

[44] N.E. Taylor. *Hot spots in ammonium nitrate*. Phd, Cambridge, 2011.

[45] F.P. Bowden and O.A. Gurton. Initiation of solid explosives by impact and friction: The influence of grit. *Proceedings of the Royal Society of London. Series A. Mathematical and Physical Sciences*, 198(1054):337–349, 1949.

[46] J.L. Maienschein, P.A. Urtiew, F. Garcia, and J.B. Chandler. Effect of microvoids on the shock initiation of PETN. In S.C. Schmidt, D.P. Dandekar, and J.W. Forbes, editors, *Shock Compression of Condensed Matter - 1997*, pages 711–714. American Institute of Physics, Woodbury, New York, 1998.

[47] V.K Mohan, J.E. Field, and G.M. Swallowe. Effects of physical inhomogeneities on the impact sensitivity of solid explosives: A high-speed photographic study. *Combust. Sci. Technol.*, 40:269–278, 1984.

[48] M.C. Chick. The effect of interstitial gas on the shock sensitivity of low density explosive compacts. In *Proc. Fourth Symp. (Int.) on Detonation*, pages 349–358. Office of Naval Research, Washington DC, 1965.

[49] A.Y. Apin and L.N. Stesik. Explosion physics. 1955.

[50] B.A. Khasainov, B.S. Ermolaev, H.N. Presles, and P. Vidal. On the effect of grain size on shock sensitivity of heterogeneous high explosives. *Shock Waves*, 7:89–105, 1997.

[51] B.C. Taylor and L.W. Ervin. Separation of ignition and buildup to detonation in pressed TNT. In D.J. Edwards, editor, *Proc. Sixth Symp. (Int.) on Detonation*, pages 3–10. Office of Naval Research, Arlington, Virginia, 1976.

[52] P. Howe, R. Frey, B. Taylor, and V. Boyle. Shock initiation and the critical energy concept. In D.J. Edwards, editor, *Proc. Sixth Symp. (Int.) on Detonation*, pages 11–19. Office of Naval Research, Arlington, Virginia, 1976.

[53] E.L. Lee and C.M. Tarver. Phenomenological model of shock initiation in heterogeneous explosives. *Phys. Fluids*, 23:2362–2372, 1980.

[54] A.I. Korotkov, A.A. Sulimov, A.V. Obmenin, V.F. Dubovitskii, and A.I. Kurkin. Transition from combustion to detonation in porous explosives. *Combustion, Explosion, and Shock Waves*, 5(3):216–222, 1969.

[55] J.B. Bdzil. Steady-state two-dimensional detonation. *J. Fluid Mech.*, 108:195–226, 1981.

[56] D.L. Chapman. On the rate of explosion in gases. *Philos. Mag. (Ser. 5)*, 47:90–104, 1899.

[57] E. Jouguet. Sur la propagation des réactions chimiques dans les gaz: Les ondes de choc. *J. Math. Pures Appliquées (6ème Sér.)*, 2:5–86, 1906.

[58] W.G. Proud. Ignition and detonation in energetic materials: An introduction. 2014.

[59] J.B. Bdzil and A.K. Kapila. Shock-to-detonation transition: A model problem. *Physics of Fluids A: Fluid Dynamics*, 4(2):409–418, 1992.

[60] Y.B. Zeldovich. To the question of energy use of detonation combustion. *Zh. Tekh. Fiz*, 10:1453–1461, 1940.

[61] J. von Neumann. Theory of detonation waves. In A.H. Taub, editor, *John von Neumann Collected Works. Volume 6: Theory of Games, Astrophysics, Hydrodynamics and Meteorology*, pages 203–218. Pergamon, Oxford, 1963.

[62] W. Döring. Über den detonationsvorgang in gasen. *Ann. Phys.*, 43:421–436, 1943.

[63] R. Menikoff. Detonation wave profile. Technical report, Los Alamos National Lab.(LANL), Los Alamos, NM (United States), 2015.

[64] H. Jones. A theory of the dependence of the rate of detonation of solid explosives on the diameter of the charge. *Proc. R. Soc. Lond. A*, 189:415–426, 1947.

[65] H. Eyring, R.E. Powell, G.H. Duffey, and R.P. Parlin. The stability of detonation. *Chem. Rev.*, 45:69–181, 1949.

[66] R.C. Drake. Assessing the effect of the role of detonation wave curvature on the firing times of high voltage detonators. In *AIP Conference Proceedings*, volume 1979, page 100010. AIP Publishing, 2018.

[67] A.W. Campbell, M.E. Malin, T.J. Boyd, and J.A. Hull. Technique for the measurement of detonation velocity. In *Proc. Second ONR Symp. on Detonation (republ. 1987)*, pages 136–150. Office of Naval Research, Washington DC, 1955.

[68] W.C. Davis, R.G. Craig, and J.B. Ramsay. Failure of the Chapman-Jouguet theory for liquid and solid explosives. *Phys. Fluids*, 8:2169–2182, 1965.

[69] A.W. Campbell and R. Engelke. The diameter effect in high-density heterogeneous explosives. In D.J. Edwards, editor, *Proc. Sixth Symposium (Int.) on Detonation*, pages 642–652. Office of Naval Research, Arlington, Virginia, 1976.

[70] W. Fickett and W.W. Wood. Flow calculations for pulsating one-dimensional detonations. *The Physics of Fluids*, 9(5):903–916, 1966.

[71] L.M. Faria, A.R. Kasimov, and R.R. Rosales. Study of a model equation in detonation theory. *SIAM Journal on Applied Mathematics*, 74(2):547–570, 2014.

[72] N.J. Whitworth. Mathematical and numerical modelling of shock initiation in heterogeneous solid explosives. 2008.

[73] C.A. Handley. The CREST reactive burn model. In *AIP Conference Proceedings*, volume 955, pages 373–376. AIP, 2007.

[74] J.E. Reaugh. HERMES model modifications and applications 2012. Technical report, Lawrence Livermore National Laboratory (LLNL), Livermore, CA, 2013.

[75] C.M. Tarver. Detonation reaction zones in condensed explosives. In M.D. Furnish, M. Elert, T.P. Russell, and C.T. White, editors, *Shock Compression of Condensed Matter - 2005*, pages 1026–1029. American Institute of Physics, Melville, NY, 2006.

[76] D.G. Tasker, R.J. Lee, and P.K. Gustavson. The measurement of electrical conductivity in detonating condensed explosives. Technical report, NAVAL SURFACE WARFARE CENTER DAHLGREN DIV VA, 1993.

[77] A.P. Ershov, N.P. Satonkina, and G.M. Ivanov. Reaction zones and conductive zones in dense explosives. In *Thirteenth International Detonation Symposium*, pages 79–88, 2006.

[78] R.R. IJsselstein. Reaction zone measurements in high explosive detonation waves by means of shock-induced polarization. *Combustion & Flame*, 66:27–35, 1986.

[79] A. Frank, H. Chau, R. Lee, P. Vitello, and P.C. Souers. Reaction zones in ultrafine TATB. *Propell. Explos. Pyrotech.*, 28:259–264, 2003.

[80] T.J. Tucker. Explosive initiators. Technical report, Sandia Labs., Albuquerque, N. Mex., 1972.

[81] E.A. Lee, R.C. Drake, and J. Richardson. A view on the functioning mechanism of EBW detonators. 1: Electrical characterisation. *J. Phys.: Conf. Ser.*, 500:192008, 2014.

[82] E.A. Lee and M.D. Bowden. The effect of post-burst energy on exploding bridgewire output. In *AIP Conference Proceedings*, volume 1793, page 040030. AIP Publishing, 2017.

[83] P.W. Cooper, R.N. Owenby, and J.H. Stofleth. Excess transit time as a function of burst current in an exploding bridgewire detonator. Technical report, Sandia National Labs., Albuquerque, NM (USA), 1990.

[84] D.S. Stewart, K.A. Thomas, S.A. Clarke, H. Mallett, E.S. Martin, M.E. Martinez, A. Munger, and J. Saenz. On the initiation mechanism in exploding bridgewire and laser detonators. In *AIP Conference Proceedings*, volume 845, pages 471–474. AIP, 2006.

[85] E.S. Martin, K.A. Thomas, S.A. Clarke, J.E. Kennedy, and D.S. Stewart. Measurements of the DDT process in exploding bridgewire detonators. In *AIP Conference Proceedings*, volume 845, pages 1093–1096. AIP, 2006.

[86] E.A. Lee, R.C. Drake, and J. Richardson. A view on the functioning mechanism of EBW detonators. 2: Bridgewire output. *J. Phys.: Conf. Ser.*, 500:052024, 2014.

[87] W.D. Neal. PETN exploding bridgewire (EBW) detonators: A review. 2020.

[88] L. Smilowitz, D. Remelius, N. Suvorova, P. Bowlan, D. Oschwald, and B.F. Henson. Finding the "lost-time" in detonator function. *Applied Physics Letters*, 114(10):104102, 2019.

[89] J.E. Kennedy, J.W. Early, K.A. Thomas, and C.S. Lester. Direct laser initiation of PETN. In N. Burman, editor, *Proc. 28th Int. Pyrotechnics Seminar*, pages 407–415. International Pyrotechnics Society, Chicago, 2001.

[90] E.A. Lee and R.C. Drake. Relationship between exploding bridgewire and spark initiation of low density PETN. In *AIP Conference Proceedings*, volume 1793, page 040012. AIP Publishing, 2017.

[91] F. Roeski, J. Benterou, R. Lee, and R. Roos. Transition to detonation in exploding bridgewire detonators. Technical report, Lawrence Livermore National Lab., CA (US), 2003.

[92] A.M. Frank. Mechanisms of EBW HE initiation. In S.C. Schmidt, R.D. Dick, J.W. Forbes, and D.G. Tasker, editors, *Shock Compression of Condensed Matter - 1991*, pages 683–686. Elsevier, Amsterdam, 1992.

[93] J.R. Stroud. A new kind of detonator: The slapper. In *Proc. Ninth Symp. on Explosives and Pyrotechnics*, page paper 22. Franklin Institute Research Laboratories, Philadelphia, PA, 1976.

[94] H.R. Brierley. *The performance of exploding foil initiators and laser driven flyers*. Phd, Cambridge, 2011.

[95] H.R. Davies, D.J. Chapman, T.A. Vine, and W.G. Proud. Characterisation of an exploding foil initiator (EFI) system. In M.L. Elert, W.T. Buttler, M.D. Furnish, W.W. Anderson, and W.G. Proud, editors, *Shock Compression of Condensed Matter - 2009*, pages 283–286. American Institute of Physics, Melville, NY, 2009.

[96] R. Mendes, J. Campos, I. Plaksin, and J. Ribeiro. Shock initiation of explosives by micro slapper. In *12th International Detonation Symposium*, page 330, 2002.

[97] L.M. Barker and R.E. Hollenbach. Laser interferometer for measuring high velocities of any reflecting surface. *J. Appl. Phys.*, 43:4669–4675, 1972.

[98] L.M. Barker and R.E. Hollenbach. Interferometer technique for measuring the dynamic mechanical properties of materials. *Rev. Sci. Instrum.*, 36:1617–1620, 1965.

[99] W.F. Hemsing. Velocity sensing interferometer (VISAR) modification. *Review of scientific instruments*, 50(1):73–78, 1979.

[100] D.H. Dolan. Foundations of VISAR analysis. Technical Report SAND2006-1950, Sandia National Laobratories, 2006.

[101] D.D. Bloomquist and S.A. Sheffield. Optically recording velocity interferometer system (ORVIS) for subnanosecond particle velocity measurements in shock waves. In *15th Intl Congress on High Speed Photography and Photonics*, volume 348, pages 523–528. International Society for Optics and Photonics, 1983.

[102] W.F. Hemsing, A.R. Mathews, R.H. Warnes, M.J. George, and G.R. Whittemore. VISAR: Line-imaging interferometer. In *Shock Compression of Condensed Matter–1991*, pages 767–770. Elsevier, 1992.

[103] R.L. Gustavsen, S.A. Sheffield, and R.R. Alcon. Progress in measuring detonation wave profiles in PBX 9501. In J.M. Short and J.E. Kennedy, editors, *Proc. 11th Int. Detonation Symposium*, pages 821–827. Office of Naval Research, Arlington, Virginia, 2000.

[104] O.T. Strand, L.V. Berzins, D.R. Goosman, W.W. Kuhlow, P.D. Sargis, and T.L. Whitworth. Velocimetry using heterodyne techniques. *Proc. SPIE*, 5580:593–599, 2005.

[105] D.H. Dolan. Accuracy and precision in photonic Doppler velocimetry. *Review of Scientific Instruments*, 81(5):053905, 2010.

[106] R.L. Gustavsen, B.D. Bartram, and N.J. Sanchez. Detonation wave profiles measured in plastic bonded explosives using 1550nm photon Doppler velocimetry. In M.L. Elert, W.T. Buttler, M.D. Furnish, W.W. Anderson, and W.G. Proud, editors, *Shock Compression of Condensed Matter - 2009*, pages 253–256. American Institute of Physics, Melville, NY, 2009.

[107] V. Bouyer, M. Doucet, and L. Decaris. Experimental measurements of the detonation wave profile in a TATB-based explosive. *EPJ Web Conferences*, 10:00030, 2010.

[108] A. Guinier, G. Fournet, and K.L. Yudowitch. Small-angle scattering of X-rays. 1955.

[109] K.A. Ten, V.M. Titov, E.R. Pruuel, L.A. Lukyanchikov, B.P. Tolochko, I.L. Zhogin, Y.A. Aminov, V.P. Filin, B.G. Loboyko, and A.K. Muzyrya. Measurements of SAXS signal during TATB detonation using synchrotron radiation. In *Proceedings of the 14th International Detonation Symposium*, pages 387–391, 2010.

[110] R.L. Gustavsen, D.M. Dattelbaum, E.B. Watkins, M.A. Firestone, D.W. Podlesak, B.J. Jensen, B.S. Ringstrand, R.C. Huber, J.T. Mang, and C.E. Johnson. Time resolved small angle X-ray scattering experiments performed on detonating explosives at the advanced photon source: Calculation of the time and distance between the detonation front and the x-ray beam. *Journal of Applied Physics*, 121(10):105902, 2017.

[111] T.J. Davis, D. Gao, T.E. Gureyev, A.W. Stevenson, and S.W. Wilkins. Phase-contrast imaging of weakly absorbing materials using hard X-rays. *Nature*, 373(6515):595, 1995.

[112] B.J. Jensen, K.J. Ramos, A.J. Iverson, J. Bernier, C.A. Carlson, J.D. Yeager, K. Fezzaa, and D.E. Hooks. Dynamic experiment using impulse at the advanced photon source. In *Journal of Physics: Conference Series*, volume 500, page 042001. IOP Publishing, 2014.

[113] N.J. Sanchez, B.J. Jensen, K.J. Ramos, A.J. Iverson, M.E. Martinez, G.H. Liechty, J.R. Gibson, C.T. Owens, S.A. Clarke, and F. Kamel. Dynamic initiator experiments using IMPULSE (impact system for ultrafast synchrotron experiments) at the Advanced Photon Source. Technical report, Los Alamos National Lab.(LANL), Los Alamos, NM (United States), 2016.

[114] N.J. Sanchez, B.J. Jensen, W.D. Neal, A.J. Iverson, and C.A. Carlson. Dynamic exploding foil initiator imaging at the advanced photon source. In *AIP Conference Proceedings*, volume 1979, page 160023. AIP Publishing, 2018.

[115] W.L. Shaw, C. Grant, C. Fox, H.E. Reinstein, T.M. Willey, M. Bagge-Hansen, M.H. Nielsen, J.A. Hammons, L.M. Lauderbach, and R.L. Hodgin. Evaluating the ignitibility of PETN by aged exploding foil initiators. Technical report, Lawrence Livermore National Lab.(LLNL), Livermore, CA (United States), 2018.

[116] A.P. Ershov, P.I. Zubkov, and L.A. Luk'yanchikov. Measurements of the electrical conductivity profile in the detonation front of solid explosives. *Combustion, Explosion and Shock Waves*, 10(6):776–782, 1974.

[117] B. Hayes. Particle–velocity gauge system for nanosecond sampling rate of shock and detonation waves. *Review of Scientific Instruments*, 52(4):594–603, 1981.

[118] S.A. Sheffield, D.D. Bloomquist, and C.M. Tarver. Subnanosecond measurements of detonation fronts in solid high explosives. *The Journal of Chemical Physics*, 80(8): 3831–3844, 1984.

[119] R.L. Gustavsen, S.A. Sheffield, R.R. Alcon, J.W. Forbes, C.M. Tarver, and F. Garcia. Embedded electromagnetic gauge measurements and modeling of shock initiation in the TATB based explosives LX-17 and PBX 9502. In *AIP Conference Proceedings*, volume 620, pages 1019–1022. AIP, 2002.

[120] C. Stennett, G.A. Cooper, P.J. Hazell, and G. Appleby-Thomas. Initiation of secondary explosives measured using embedded electromagnetic gauges. In *AIP Conference Proceedings*, volume 1195, pages 267–270. AIP, 2009.

[121] M. Goff, M. Burns, R.L. Gustavsen, C. Stennett, P.J. Hazell, and G.J. Appleby-Thomas. Effects observed when using metallic flyers and barriers with the embedded particle velocity gauge technique. In *Journal of Physics: Conference Series*, volume 500, page 142017. IOP Publishing, 2014.

[122] S.A. Sheffield, R.L. Gustavsen, and R.R. Alcon. In-situ magnetic gauging technique used at LANL-method and shock information obtained. In *AIP Conference Proceedings*, volume 505, pages 1043–1048. American Institute of Physics, 2000.

[123] J.C.F. Millett and N.K. Bourne. Development of magnetic gauges for the measurement of particle velocities during one-dimensional shock loading. *Meas. Sci. Technol.*, 14: 601–606, 2003.

[124] J.I. Perry. *The dynamic response of sand: Effects of moisture and morphology*. Phd, Cambridge, 2017.

[125] W.D. Neal, D.J. Chapman, and W.G. Proud. Shock-wave stability in quasi-mono-disperse granular materials. *The European Physical Journal-Applied Physics*, 57(3), 2012.

[126] D.J. Chapman. *Shock-compression of porous materials and diagnostic development*. Phd, Cambridge, 2009.

[127] W.M. Trott, L.C. Chhabildas, M.R. Baer, and J.N. Castañeda. Investigation of dispersive waves in low-density sugar and HMX using line-imaging velocity interferometry. In *AIP Conference Proceedings*, volume 620, pages 845–848. AIP, 2002.

[128] K.J. Ramos, B.J. Jensen, A.J. Iverson, J.D. Yeager, C.A. Carlson, D.S. Montgomery, D.G. Thompson, K. Fezzaa, and D.E. Hooks. In situ investigation of the dynamic response of energetic materials using IMPULSE at the Advanced Photon Source. In *Journal of Physics: Conference Series*, volume 500, page 142028. IOP Publishing, 2014.

[129] M. Kamoda, F. Onda, H. Ito, T. Shirasaki, T. Miki, and T. Ando. On the formation of needle-shaped sugar crystals. *Int Soc Sugar Cane Technol Proc Congr*, 1969.

[130] N.K. Bourne, Z Rosenberg, D.J. Johnson, J.E. Field, A.E. Timbs, and R.P. Flaxman. Design and construction of the UK plate impact facility. *Measurement Science and Technology*, 6(10):1462, 1995.

[131] C.H. Braithwaite, J.I. Perry, N.E. Taylor, and A.P. Jardine. Behaviour of sand during release from a shocked state. *Applied Physics Letters*, 103(15):154103, 2013.

[132] M.E. Möbius, B.E. Lauderdale, S.R. Nagel, and H.M. Jaeger. Size separation of granular particles. *Nature*, 414(6861):270–270, 2001.

[133] L.M. Barker and R.E. Hollenbach. Shock-wave studies of PMMA, fused silica, and sapphire. *Journal of Applied Physics*, 41(10):4208–4226, 1970.

[134] D.R. Christman. Dynamic properties of poly(methylmethacrylate) (PMMA) (Plexiglas). Technical report, GENERAL MOTORS TECHNICAL CENTER WARREN MI MATERIALS AND STRUCTURES LAB, 1972.

[135] S.P. Marsh. *LASL shock Hugoniot data*, volume 5. Univ of California Press, 1980.

[136] G.I. Kerley. Calculation of release adiabats and shock impedance matching. *arXiv preprint arXiv:1306.6913*, 2013.

[137] P.M. Celliers, G.W. Collins, D.G. Hicks, and J.H. Eggert. Systematic uncertainties in shock-wave impedance-match analysis and the high-pressure equation of state of al. *Journal of applied physics*, 98(11):113529, 2005.

[138] E.T. Owens and K.E. Daniels. Sound propagation and force chains in granular materials. *EPL (Europhysics Letters)*, 94(5):54005, 2011.

[139] R.E. Setchell. Effects of precursor waves in shock initiation of granular explosives. *Combustion and flame*, 54(1-3):171–182, 1983.

[140] M. Grujicic, B. Pandurangan, W.C. Bell, and S. Bagheri. Shock-wave attenuation and energy-dissipation potential of granular materials. *Journal of Materials Engineering and Performance*, 21(2):167–179, 2012.

[141] W.M. Trott, M.R. Baer, J.N. Castaneda, L.C. Chhabildas, and J.R. Asay. Investigation of the mesoscopic scale response of low-density pressings of granular sugar under impact. *Journal of Applied Physics*, 101(2):024917, 2007.

[142] L.C. Yang and V.J. Menichelli. Detonation of insensitive high explosives by a Q-switched ruby laser. *Applied Physics Letters*, 19(11):473–475, 1971.

[143] L.C. Yang. Performance characteristics of a laser initiated microdetonator. *Propellants, Explosives, Pyrotechnics*, 6(6):151–157, 1981.

[144] A.A. Volkova, A.D. Zinchenko, I.V. Sanin, V.I. Tarzhanov, and B.B. Tokarev. Time characteristics of laser initiation of PETN. *Combustion, Explosion and Shock Waves*, 13 (5):645–650, 1977.

[145] A.M. Renlund, P.L. Stanton, and W.M. Trott. Laser initiation of secondary explosives. In *Presented at the 9th International Symposium on Detonation, Portland, OR, Sep. 1989*, 1989.

[146] V.I. Tarzhanov, A.D. Zinchenko, V.I. Sdobnov, B.B. Tokarev, A.I. Pogrebov, and A.A. Volkova. Laser initiation of PETN. *Combustion, Explosion and Shock Waves*, 32(4): 454–459, 1996.

[147] V.I. Tarzhanov, A.D. Zinchenko, B.N. Smirnov, A.I. Pogrebov, V.I. Sdobnov, and B.B. Tokarev. PETN initiation by a light-induced explosion of a metal film. *Combustion, Explosion and Shock Waves*, 32(2):214–218, 1996.

[148] D.L. Paisley. *Laser-driven miniature flyer plates for shock initiation of secondary explosives*. Conference: American Physical Society topical conference on shock compression of condensed matter, Albuquerque, NM, USA, 14-17 Aug 1989; Other Information: Portions of this document are illegible in microfiche products. ; Los Alamos National Lab., NM (USA), 1989.

[149] W.M. Trott and K.D. Meeks. High-power Nd:glass laser transmission through optical fibers and its use in acceleration of thin foil targets. *Journal of Applied Physics*, 67(7): 3297–3301, 1990.

[150] A.M. Frank and W.M. Trott. Investigation of thin laser-driven flyer plates using streak imaging and stop motion microphotography. *AIP Conference Proceedings*, 370(1): 1209–1212, 1996.

[151] D.J. Hatt and J.A. Waschl. A study of laser-driven flyer plates. *AIP Conference Proceedings*, 370(1):1221–1224, 1996.

[152] M.D. Bowden. The development of a laser detonator system. 2015.

[153] A.M. Frank and W.M. Trott. Stop-motion microphotography of laser-driven plates. In *Ultrahigh-and High-Speed Photography, Videography, and Photonics' 94*, volume 2273, pages 196–206. International Society for Optics and Photonics, 1994.

[154] K.E. Brown, W.L. Shaw, X. Zheng, and D.D. Dlott. Simplified laser-driven flyer plates for shock compression science. *Rev. Sci. Instrum.*, 83:103901, 2012.

[155] W.L. Shaw, A.D. Curtis, A.A. Banishev, and D.D. Dlott. Laser-driven flyer plates for shock compression spectroscopy. *J. Phys.: Conf. Ser.*, 500:142011, 2014.

[156] D.C. Swift, J.G. Niemczura, D.L. Paisley, R.P. Johnson, S-N. Luo, and T.E. Tierney IV. Laser-launched flyer plates for shock physics experiments. *Review of scientific instruments*, 76(9):093907, 2005.

[157] S. Watson, M.J. Gifford, and J.E. Field. The initiation of fine grain PETN by laser-driven flyer plates. *J. Appl. Phys.*, 88:65–69, 2000.

[158] M.D. Bowden and M.P. Maisey. The development of a heterodyne velocimeter system for use in sub-microsecond time regimes. *Proc. SPIE*, 6662:66620B, 2007.

[159] R.J. Lawrence and W.M. Trott. Theoretical analysis of a pulsed-laser-driven hypervelocity flyer launcher. *International Journal of Impact Engineering*, 14(1-4):439–449, 1993.

[160] R.W. Gurney. The initial velocities of fragments from bombs, shell and grenades. Technical report, Army Ballistic Research Lab Aberdeen Proving Ground Md, 1943.

[161] S. Watson and J.E. Field. Integrity of thin, laser-driven flyer plates. *Journal of Applied Physics*, 88(7):3859–3864, 2000.

[162] ISO 11146-1:. Lasers and laser-related equipment–test methods for laser beam widths, divergence angles and beam propagation ratios–part 1: Stigmatic and simple astigmatic beams. 2005.

[163] X. Zhao, X. Zhao, G. Shan, and Y. Gao. Fiber-coupled laser-driven flyer plates system. *Review of Scientific Instruments*, 82(4):043904, 2011.

[164] D. Véron, H. Ayral, C. Gouedard, D. Husson, J. Lauriou, O. Martin, B. Meyer, M. Rostaing, and C. Sauteret. Optical spatial smoothing of Nd-glass laser beam. *Optics communications*, 65(1):42–46, 1988.

[165] S.W. Allison, G.T. Gillies, D.W. Magnuson, and T.S. Pagano. Pulsed laser damage to optical fibers. *Applied optics*, 24(19):3140–3145, 1985.

[166] M.D. Bowden and S.L. Knowles. Optimisation of laser-driven flyer velocity using photonic Doppler velocimetry. volume 7434, pages 743403–743403–11, 2009.

[167] Y. Huang, Z. Zhan, and N. Bowler. Optimization of the coplanar interdigital capacitive sensor. In *AIP conference proceedings*, volume 1806, page 110017. AIP Publishing LLC, 2017.

[168] A. Romani, N. Manaresi, L. Marzocchi, G. Medoro, A. Leonardi, L. Altomare, M. Tartagni, and R. Guerrieri. Capacitive sensor array for localization of bioparticles in CMOS lab-on-a-chip. In *2004 IEEE International Solid-State Circuits Conference (IEEE Cat. No. 04CH37519)*, pages 224–225. IEEE, 2004.

[169] E. Ghafar-Zadeh, M. Sawan, and D. Therriault. A $0.18 - \mu m$ CMOS capacitive sensor lab-on-chip. *Sensors and Actuators A: Physical*, 141(2):454–462, 2008.

[170] S. Guha, K. Schmalz, C. Wenger, and F. Herzel. Self-calibrating highly sensitive dynamic capacitance sensor: towards rapid sensing and counting of particles in laminar flow systems. *Analyst*, 140(9):3262–3272, 2015.

[171] D-Y. Shin, H. Lee, and S. Kim. A delta–sigma interface circuit for capacitive sensors with an automatically calibrated zero point. *IEEE Transactions on Circuits and Systems II: Express Briefs*, 58(2):90–94, 2011.

[172] B.L. Mackey. Sensor patterns for a capacitive sensing apparatus, 2006.

[173] D.A. Speck, G.J. McCaughan, and B.L. Mackey. Capacitive sensing pattern, 2007.

[174] K. Hamamoto. Capacitive humidity sensor, 2006.

[175] D. Wang. Capacitive sensing: Ins and outs of active shielding. *Texas Instruments, Application report SNOA926A–February*, 2015.

[176] Tektronix Application Notes. XYZs of oscilloscope, 2001.

[177] M. Kristeková, J. Kristek, and P. Moczo. Time-frequency misfit and goodness-of-fit criteria for quantitative comparison of time signals. *Geophysical Journal International*, 178(2):813–825, 2009.

[178] G.F. Brent, A.H. Noble, and D.P. Sutton. Signal transmission tubing with low incendivity for use in methane/air environments. *Journal of energetic materials*, 11(4-5):245–260, 1993.

[179] M.J. Gifford, P.E. Luebcke, and J.E. Field. A new mechanism for deflagration-to-detonation in porous granular explosives. *Journal of applied physics*, 86(3):1749–1753, 1999.

[180] D. Price, A.R. Clairmont Jr, and I. Jaffe. Explosive behaviour of ammonium perchlorate. *Combustion and Flame*, 11(5):415–425, 1967.

[181] B.J. Briscoe and S.L. Rough. The effects of wall friction in powder compaction. *Colloids and Surfaces A: Physicochemical and Engineering Aspects*, 137(1-3):103–116, 1998.

[182] L. Lauderbach, K.T. Lorenz, E.L. Lee, and P.C. Souers. Getting detonation rates from front curvature. Technical report, Lawrence Livermore National Lab.(LLNL), Livermore, CA (United States), 2015.

[183] A.S. Kumar, S.S. Samudre, and J.S. Gharia. New pressing technique for preparation of small-calibre shaped charge. *Defence Science Journal*, 45(1):51, 1995.

[184] R.H. Dinegar. Detonation velocity of PETN in small confined cylindrical charges. *Propell. Explos.*, 1:97–100, 1976.

[185] H.C. Hornig. Equation of state of detonation products. In *5th Symposium (International) on Detonation, 1970*, pages 503–511, 1970.

[186] M.D. Bowden and R.C. Drake. The initiation of high surface area pentaerythritol tetranitrate using fiber-coupled laser-driven flyer plates. In *Photonic Devices+ Applications*, page 66620D. International Society for Optics and Photonics, 2007.

[187] A.P. Ershov, N.P. Satonkina, A.V. Plastinin, and A.S. Yunoshev. Diagnostics of the chemical reaction zone in detonation of solid explosives. *Combustion, Explosion, and Shock Waves*, 56(6):705–715, 2020.

[188] A.V. Utkin, V.M. Mochalova, A.I. Rogacheva, and V.V. Yakushev. Structure of detonation waves in PETN. *Combustion, Explosion, and Shock Waves*, 53(2):199–204, 2017.

[189] R.A. Catanach and L.G. Hill. Diameter effect curve and detonation front curvature measurements for ANFO. In M.D. Furnish, N.N. Thadhani, and Y. Horie, editors, *Shock Compression of Condensed Matter - 2001*, pages 906–909. American Institute of Physics, Melville, NY, 2002.

[190] L.W. Guo, B. Wang, X.X. Zheng, G.S. Zhang, L.J. Yang, and Q. Li. Effect of initial density on the curvature effect of detonation front for JBO-9021 explosive. *Huozhayao Xuebao/Chinese Journal of Explosives and Propellants*, 40:51–55, 2017.

[191] J. Li, X. Mi, and A.J. Higgins. Propagation distance required to reach steady-state detonation velocity in finite-sized charges. *arXiv preprint arXiv:1407.1940*, 2014.

[192] P.C. Souers. Kinetic information from detonation front curvature. Technical report, Lawrence Livermore National Lab., CA (United States), 1998.

[193] G.D. Kosiba, H.K. Springer, W.L. Shaw, and R.H. Gee. Determining shock reponse of PETN-based explosives with grain-scale simulations. In *AIP Conference Proceedings*, volume 2272, page 070022. AIP Publishing LLC, 2020.

[194] M.A. Wood, D.E. Kittell, C.D. Yarrington, and A.P. Thompson. Multiscale modeling of shock wave localization in porous energetic material. *Physical Review B*, 97(1):014109, 2018.

[195] N.J. Whitworth and J.R. Maw. Modeling shock desensitisation of heterogeneous explosives. In *AIP Conference Proceedings*, volume 370, pages 425–428. American Institute of Physics, 1996.

[196] C.A. Handley, B.D. Lambourn, N.J. Whitworth, H.R. James, and W.J. Belfield. Understanding the shock and detonation response of high explosives at the continuum and meso scales. *Applied Physics Reviews*, 5(1):011303, 2018.

[197] P.A. Urtiew and B. Hayes. Parametric study of the dynamic JWL-EOS for detonation products. *Combustion, Explosion and Shock Waves*, 27(4):505–514, 1991.

[198] E. Lee, M. Finger, and W. Collins. JWL equation of state coefficients for high explosives. Technical report, Lawrence Livermore National Lab.(LLNL), Livermore, CA (United States), 1973.

[199] C.M. Tarver. Jones-Wilkins-Lee (JWL) reaction product equations of state for overdriven PETN detonation waves. In *AIP Conference Proceedings*, volume 2272, page 030031. AIP Publishing LLC, 2020.

[200] W.C. Davis. Complete equation of state for unreacted solid explosive. *Combustion and Flame*, 120(3):399–403, 2000.

[201] D.S. Stewart, S. Yoo, and W.C. Davis. Equation of state for modeling the detonation reaction zone. In *12th Symp.(Intl) on Detonation*, pages 1–11. Citeseer, 2002.

[202] D.E. Kittell and C.D. Yarrington. A physically-based Mie–Grüneisen equation of state to determine hot spot temperature distributions. *Combustion Theory and Modelling*, 20 (5):941–957, 2016.

[203] A.K. Kapila, R. Menikoff, J.B. Bdzil, S.F. Son, and D.S. Stewart. Two-phase modeling of deflagration-to-detonation transition in granular materials: Reduced equations. *Physics of fluids*, 13(10):3002–3024, 2001.

[204] S.D. Wilkinson, M. Braithwaite, N. Nikiforakis, and L. Michael. A complete equation of state for non-ideal condensed phase explosives. *Journal of Applied Physics*, 122(22): 225112, 2017.

[205] C.A. Handley, N.J. Whitworth, H.R. James, B.D. Lambourn, and M.A. Maheswaran. The CREST reactive-burn model for explosives. In *EPJ web of conferences*, volume 10, page 00004. EDP Sciences, 2010.

[206] M.A. Maheswaran, J. Curtis, and J. Reaugh. Modelling shock to detonation transition in PETN using HERMES and CREST. In *APS Shock Compression of Condensed Matter Meeting Abstracts*, page K6. 002, 2013.

[207] J.E. Reaugh, J.P. Curtis, and M.A. Maheswaran. Modelling of deflagration to detonation transition in porous PETN of density 1.4 g/cc with HERMES. In *AIP Conference Proceedings*, volume 1979, page 100032. AIP Publishing LLC, 2018.

[208] J.E. Reaugh. HERMES model developments and status to support simulations and analyses of XDT and DDT. Technical report, Lawrence Livermore National Lab.(LLNL), Livermore, CA (United States), 2014.

[209] C.A. Handley and M.A. Christie. Calibrating reaction rates for the CREST model. In *AIP Conference Proceedings*, volume 1793, page 030027. AIP Publishing LLC, 2017.

[210] S. Kubota, T. Saburi, Y. Ogata, and K. Nagayama. Numerical simulation of detonation propagation in PETN at arbitrary intitial density by simple model. In *AIP Conference Proceedings*, volume 1426, pages 231–234. American Institute of Physics, 2012.

[211] B.L. Wescott, D.S. Stewart, and W.C. Davis. Equation of state and reaction rate for condensed-phase explosives. *Journal of applied physics*, 98(5):053514, 2005.

[212] M. Jutzi, W. Benz, and P. Michel. Numerical simulations of impacts involving porous bodies: I. implementing sub-resolution porosity in a 3D SPH hydrocode. *Icarus*, 198(1): 242–255, 2008.

[213] J.A. Sáenz and D.S. Stewart. Modeling deflagration-to-detonation transition in granular explosive pentaerythritol tetranitrate. *Journal of Applied Physics*, 104(4):043519, 2008.

[214] W. Herrmann. Constitutive equation for the dynamic compaction of ductile porous materials. *Journal of applied physics*, 40(6):2490–2499, 1969.

[215] M. Carroll and A.C. Holt. Suggested modification of the $p - \alpha$ model for porous materials. *Journal of Applied Physics*, 43(2):759–761, 1972.

[216] J.E. Reaugh, B.W. White, J.P. Curtis, and H.K. Springer. A computer model to study the response of energetic materials to a range of dynamic loads. *Propellants, Explosives, Pyrotechnics*, 43(7):703–720, 2018.

[217] D.J. Benson. Computational methods in Lagrangian and Eulerian hydrocodes. *Computer methods in Applied mechanics and Engineering*, 99(2-3):235–394, 1992.

[218] B. Van Leer. Towards the ultimate conservative difference scheme. IV. a new approach to numerical convection. *Journal of computational physics*, 23(3):276–299, 1977.

[219] R.B. DeBar. Fundamentals of the KRAKEN code. [Eulerian hydrodynamics code for compressible nonviscous flow of several fluids in two-dimensional (axially symmetric) region]. Technical report, California Univ., Livermore (USA). Lawrence Livermore Lab., 1974.

[220] X. Zeng. A general approach to enhance slope limiters on non-uniform rectilinear grids. *arXiv preprint arXiv:1301.0967*, 2013.

[221] G.A. Sod. A survey of several finite difference methods for systems of nonlinear hyperbolic conservation laws. *Journal of computational physics*, 27(1):1–31, 1978.

[222] L.I. Sedov, M. Friedman, M. Holt, and J.D. Cole. Similarity and dimensional methods in mechanics. 1961.

[223] S. Roy. An introduction to fluid dynamics and numerical solution of shock tube problem by using Roe solver. *arXiv preprint arXiv:2103.02794*, 2021.

[224] J.R. Kamm and F.X. Timmes. On efficient generation of numerically robust Sedov solutions. Technical report, Technical Report LA-UR-07-2849, Los Alamos National Laboratory, 2007.

[225] C.A. Hrousis and J.S. Christensen. Advances in modeling exploding bridgewire initiation. Technical report, Lawrence Livermore National Lab.(LLNL), Livermore, CA (United States), 2010.

[226] E. Daykin, M. Burk, D.B. Holtkamp, E.K. Miller, A. Rutkowski, O.T. Strand, M. Pena, C. Perez, and C. Gallegos. Multiplexed photonic Doppler velocimetry for large channel count experiments. In *AIP Conference Proceedings*, volume 1793, page 160004. AIP Publishing LLC, 2017.

[227] G. Römer and A.J. Huis in 't Veld. Matlab laser toolbox. In *International Congress on Applications of Lasers & Electro-Optics*, volume 2010, pages 523–529. LIA, 2010.

[228] A. Mignone. High-order conservative reconstruction schemes for finite volume methods in cylindrical and spherical coordinates. *Journal of Computational Physics*, 270:784–814, 2014.

Appendix A

M^2 Calculation

The following describes the process used to measure and calculate the beam quality factor M^2 in more detail. The procedure is defined in ISO11146 - Lasers and laser-related equipment — Test methods for laser beam widths, divergence angles and beam propagation ratios [162]. It is first necessary to define the divergence of a laser beam. This quantity is the angle in radians at which the beam's diameter $d_\sigma(z)$ increases or decreases with distance along the z axis.

The divergence of a pure Gaussian TEM_{00} beam is diffraction limited, and given by

$$\Theta_{\sigma 0} = \frac{4\lambda}{\pi d_0} \tag{A.1}$$

M^2 is the ratio of the beam divergence to a pure Gaussian beam's divergence.

$$M^2 = \frac{\Theta_\sigma}{\Theta_{\sigma 0}} = \frac{\pi}{\lambda}\frac{d_{\sigma 0}\Theta_\sigma}{4} \tag{A.2}$$

A.1 Beam Profile

The first and second moments of the intensity distribution $I(x,y,z)$ are used to characterise the beam profile. The first order moments $\bar{x}$ and $\bar{y}$ give the centroid position, and the second order moments σ_{xx}^2, σ_{xy}^2 and σ_{yy}^2 describe the variance.

$$\bar{x}(z) = \frac{\int_{-\infty}^{\infty}\int_{-\infty}^{\infty} I(x,y,z)\, x dx dy}{\int_{-\infty}^{\infty}\int_{-\infty}^{\infty} I(x,y,z)\, dx dy} \tag{A.3}$$

$$\bar{y}(z) = \frac{\int_{-\infty}^{\infty}\int_{-\infty}^{\infty} I(x,y,z)\, y dx dy}{\int_{-\infty}^{\infty}\int_{-\infty}^{\infty} I(x,y,z)\, dx dy} \tag{A.4}$$

$$\sigma_{xx}^2(z) = \frac{\int_{-\infty}^{\infty}\int_{-\infty}^{\infty} I(x,y,z)\,(x-\bar{x})^2\,dxdy}{\int_{-\infty}^{\infty}\int_{-\infty}^{\infty} I(x,y,z)\,dxdy} \tag{A.5}$$

$$\sigma_{yy}^2(z) = \frac{\int_{-\infty}^{\infty}\int_{-\infty}^{\infty} I(x,y,z)\,(y-\bar{y})^2\,dxdy}{\int_{-\infty}^{\infty}\int_{-\infty}^{\infty} I(x,y,z)\,dxdy} \tag{A.6}$$

$$\sigma_{xy}^2(z) = \frac{\int_{-\infty}^{\infty}\int_{-\infty}^{\infty} I(x,y,z)\,(x-\bar{x})\,(y-\bar{y})\,dxdy}{\int_{-\infty}^{\infty}\int_{-\infty}^{\infty} I(x,y,z)\,dxdy} \tag{A.7}$$

The azimuthal angle - the angle formed between the x axis and the closest principal axis is given by:

$$\phi(z) = \frac{1}{2}\arctan\left(\frac{2\sigma_{xy}^2}{\sigma_{xx}^2-\sigma_{yy}^2}\right) \tag{A.8}$$

The $D4\sigma$ beam widths are defined as four standard deviation widths along the principal axes. In terms of the second order moments along the x and y axes these are:

$$d_{\sigma x}(z) = 2\sqrt{2}\left\{\left(\sigma_{xx}^2+\sigma_{yy}^2\right) + \frac{\sigma_{xx}^2-\sigma_{yy}^2}{\left|\sigma_{xx}^2-\sigma_{yy}^2\right|}\left[\left(\sigma_{xx}^2-\sigma_{yy}^2\right)^2+4\left(\sigma_{xy}^2\right)^2\right]^{\frac{1}{2}}\right\}^{\frac{1}{2}} \tag{A.9}$$

$$d_{\sigma y}(z) = 2\sqrt{2}\left\{\left(\sigma_{xx}^2+\sigma_{yy}^2\right) - \frac{\sigma_{xx}^2-\sigma_{yy}^2}{\left|\sigma_{xx}^2-\sigma_{yy}^2\right|}\left[\left(\sigma_{xx}^2-\sigma_{yy}^2\right)^2+4\left(\sigma_{xy}^2\right)^2\right]^{\frac{1}{2}}\right\}^{\frac{1}{2}} \tag{A.10}$$

A.2 Curve Fitting

To calculate M^2 a number of beam profiles need to be measured at several points along the beam. Typically around 10 measurements are needed, of which roughly half should be within one Rayleigh length z_R of the beam waist (i.e. where the beam width increases by $\sqrt{2}$). The diameters are fitted to a hyperbolic function of the form:

$$d_\sigma(z) = \sqrt{a+bz+cz^2} \tag{A.11}$$

Minimising d_σ leads to:

$$d_{\sigma 0} = \frac{1}{2\sqrt{c}}\sqrt{4ac-b^2} \tag{A.12}$$

$$z_R = \frac{1}{2c}\sqrt{4ac - b^2} \tag{A.13}$$

$$M^2 = \frac{\pi}{8\lambda}\sqrt{4ac - b^2} \tag{A.14}$$

The calculations required were performed in Matlab using a specialised laser toolbox [227]

Appendix B

Details of Hydrocode

A detailed description of the hydrocode is given in this appendix. All quantities are in the centimetre-gram-microsecond system of units. The derived units in this system are in Table B.1.

Quantity	Unit	SI equivalent
Length	cm	10^{-2} m
Mass	g	10^{-3} kg
Time	µs	10^{-9} s
Pressure	Mbar	10^{11} Pa
Energy	Mbar cm^3	10^5 J
Temperature	K	K

Table B.1 The centimetre-gram-microsecond system of units

The code was written in CUDA C/C++ (with several helper functions in Python) and executed on an NVIDIA GeForce GTX 1070. Visualisations were performed in ParaView.

B.1 Overall Structure

The overall code structure is given in Algorithm 1. The main body of the code is the arbitrary Lagrangian Eulerian time step, the details of which are given in later sections.

Algorithm 1: `main`

input : Mesh parameters, Initial conditions, Reactive model parameters, Number of iterations t_{max}

`/* Start of Code */`

Construct the mesh from the mesh parameters;

Allocate memory for the data;

Set the timestep;

Calculate total mass;

`/* Main time loop */`

for $n = 0 \rightarrow t_{max}$ **do**

- *Perform Lagrangian Step using Algorithm 2*;
- $P'^n, p'^n, q'^n, \Xi'^n, \dot{\lambda}'^n, \dot{\lambda_I}'^n, \dot{\lambda_G}'^n, \dot{\varphi}'^n$ = `lagrangian(`$P^n, p^n, q^n, \Xi^n, \dot{\lambda}^n, \dot{\lambda_I}^n, \dot{\lambda_G}^n, \dot{\varphi}^n, \Delta t$`)`;
- *Perform Advection Step using Algorithm 15*;
- $u^{n+1}, v^{n+1}, \Xi^{n+1}, p^{n+1}, q^{n+1}, \dot{\lambda}^{n+1}, \dot{\lambda_I}^{n+1}, \dot{\lambda_G}^{n+1}, P^{n+1}$ = `advect(`$u'^n, v'^n, \Xi'^n, p'^n, q'^n$`)`;
- *Write data to .vtk file*

`/* End of main time loop */`

Recalculate total mass;

`/* End of Code */`

output : Dataset in .vtk file format

B.2 Lagrangian Step

The Lagrangian step involves calculating the velocities that result from pressure and viscous forces, and then calculating the work done in each element of the mesh. The Lagrangian step also contains the reactive model – itself consisting of the ISE mixture model and the reaction rate burn model. A predictor-corrector method is used to give second order accuracy.

In all cases the superscript refers to the time index and the subscripts to the spatial directions. Primed ($'$) variables refer to fields on a distorted Lagrangian mesh, while unprimed quantities refer to fields on the undistorted mesh. Primed quantities are mapped back to unprimed quantities during the advection step.

Algorithm 2: `lagrangian`

input : P^n, p^n, q^n, Ξ^n, $\dot{\lambda}^n$, $\dot{\lambda_I}^n$, $\dot{\lambda_G}^n$, $\dot{\varphi}^n$, Δt

`/* Start of Code */`

Perform Predictor step using Algorithm 3;

$P'^{n+\frac{1}{2}}, p'^{n+\frac{1}{2}}, q'^{n+\frac{1}{2}}, \Xi'^{n+\frac{1}{2}}, \dot{\lambda}'^{n+\frac{1}{2}}, \dot{\lambda_I}'^{n+\frac{1}{2}}, \dot{\lambda_G}'^{n+\frac{1}{2}}, \dot{\varphi}'^{n+\frac{1}{2}} =$ `predictor(`P^n, p^n, q^n, Ξ^n, $\dot{\lambda}^n$, $\dot{\lambda_I}^n$, $\dot{\lambda_G}^n$, $\dot{\varphi}^n$, Δt`)`;

Perform Corrector step using Algorithm 4;

$P'^{n+1}, p'^{n+1}, q'^{n+1}, \Xi'^{n+1}, \dot{\lambda}'^{n+1}, \dot{\lambda_I}'^{n+1}, \dot{\lambda_G}'^{n+1}, \dot{\varphi}'^{n+1} =$ `corrector(`$P'^{n+\frac{1}{2}}$, $p'^{n+\frac{1}{2}}$, $q'^{n+\frac{1}{2}}$, $\Xi'^{n+\frac{1}{2}}$, $\dot{\lambda}'^{n+\frac{1}{2}}$, $\dot{\lambda_I}'^{n+\frac{1}{2}}$, $\dot{\lambda_G}'^{n+\frac{1}{2}}$, $\dot{\varphi}'^{n+\frac{1}{2}}$, Δt`)`;

Perform adaptive time step control using Algorithm 14;

$\Delta t^n, \Delta t^{n+\frac{1}{2}} =$ `settimestep(`Δt^{n-1}, $\Delta t^{n-\frac{1}{2}}$, c, Q, R, ρ`)`;

`/* End of Code */`

output : $P'^{n+1}, p'^{n+1}, q'^{n+1}, \Xi'^{n+1}, \dot{\lambda}'^{n+1}, \dot{\lambda_I}'^{n+1}, \dot{\lambda_G}'^{n+1}, \dot{\varphi}'^{n+1}$

B.2.1 Predictor Step

The predictor step in Algorithm 3 is used to provide a first order estimate for the next time step.

Algorithm 3: `predictor`

input : P^n, p^n, q^n, Ξ^n, $\dot{\lambda}^n$, $\dot{\lambda_I}^n$, $\dot{\lambda_G}^n$, $\dot{\varphi}^n$, Δt

`/* Start of Code */`

Calculate velocities due to pressure using Algorithm 5;

for $i = 0 \rightarrow N_r + 1,\ j = 0 \rightarrow N_z + 1$ **do**

$\tilde{u}'^{n+\frac{1}{2}}, \tilde{v}'^{n+\frac{1}{2}}, \tilde{p}'^{n+\frac{1}{2}}, \tilde{q}'^{n+\frac{1}{2}}$ = `pressureacceleration(`$i, j, P^n, p^n, q^n, \rho^n, \Delta t$`);`

Calculate artificial viscosity using Algorithm 7;

for $i = 0 \rightarrow N_r + 1,\ j = 0 \rightarrow N_z + 1$ **do**

$Q'^{n+\frac{1}{2}}, R'^{n+\frac{1}{2}}$ = `artificialviscosity(`$i, j, u'^{n+\frac{1}{2}}, v'^{n+\frac{1}{2}}, C_q, \rho^n$`);`

Update velocities due to artificial viscosity using Algorithm 8;

for $i = 0 \rightarrow N_r + 1,\ j = 0 \rightarrow N_z + 1$ **do**

$u'^{n+\frac{1}{2}}, v'^{n+\frac{1}{2}}, p'^{n+\frac{1}{2}}, q'^{n+\frac{1}{2}}$ = `viscousvelocity(`$i, j, \tilde{p}'^{n+\frac{1}{2}}, \tilde{q}'^{n+\frac{1}{2}}, Q'^{n+\frac{1}{2}}, R'^{n+\frac{1}{2}}, \tilde{u}'^{n+\frac{1}{2}}, \tilde{v}'^{n+\frac{1}{2}}, \rho^n, \Delta t$`);`

Predict energy using Algorithm 6;

for $i = 0 \rightarrow N_r + 1,\ j = 0 \rightarrow N_z + 1$ **do**

$E'^{n+\frac{1}{2}}, ke'^{n+\frac{1}{2}}$ = `energies(`$i, j, P^n, Q'^{n+\frac{1}{2}}, R'^{n+\frac{1}{2}}, u'^{n+\frac{1}{2}}, v'^{n+\frac{1}{2}}, \rho^n, E^n, \Delta t$`);`

Calculate pressures due to hydrodynamics Algorithm 9;

for $i = 0 \rightarrow N_r + 1,\ j = 0 \rightarrow N_z + 1$ **do**

$\tilde{P}'^{n+\frac{1}{2}}, \tilde{Z}_s'^{n+\frac{1}{2}}$ = `isemodel(`$\rho^n, \rho_s^n, E^n, \lambda^n, P^n, \varphi^n$`);`

Update burn variable Algorithm 11;

for $i = 0 \rightarrow N_r + 1,\ j = 0 \rightarrow N_z + 1$ **do**

$\lambda'^{n+\frac{1}{2}}, \lambda_I'^{n+\frac{1}{2}}, \lambda_G'^{n+\frac{1}{2}}, \varphi'^{n+\frac{1}{2}}$ = `updatelambda(`$\lambda^n, \lambda_I^n, \lambda_G^n, \varphi^n, \dot{\lambda}^n, \dot{\lambda_I}^n, \dot{\lambda_G}^n, \dot{\varphi}^n, \Delta t$`);`

Calculate pressures due to reaction Algorithm 9;

for $i = 0 \rightarrow N_r + 1,\ j = 0 \rightarrow N_z + 1$ **do**

$P'^{n+\frac{1}{2}}, Z_s'^{n+\frac{1}{2}}$ = `isemodel(`$\rho^n, \rho_s^n, E'^{n+\frac{1}{2}}, \lambda'^{n+\frac{1}{2}}, P'^{n+\frac{1}{2}}, \varphi'^{n+\frac{1}{2}}$`);`

Calculate reaction rates Algorithm 10;

for $i = 0 \rightarrow N_r + 1,\ j = 0 \rightarrow N_z + 1$ **do**

$\dot{\lambda}'^{n+\frac{1}{2}}, \dot{\lambda_I}'^{n+\frac{1}{2}}, \dot{\lambda_G}'^{n+\frac{1}{2}}, \dot{\varphi}'^{n+\frac{1}{2}}$ = `reactionrates(`$\lambda'^{n+\frac{1}{2}}, \lambda_I'^{n+\frac{1}{2}}, \lambda_G'^{n+\frac{1}{2}}, Z_s'^{n+\frac{1}{2}}, \varphi'^{n+\frac{1}{2}}, P'^{n+\frac{1}{2}}$`);`

`/* End of Code */`

output : $P'^{n+\frac{1}{2}}, p'^{n+\frac{1}{2}}, q'^{n+\frac{1}{2}}, \Xi'^{n+\frac{1}{2}}, \dot{\lambda}'^{n+\frac{1}{2}}, \dot{\lambda_I}'^{n+\frac{1}{2}}, \dot{\lambda_G}'^{n+\frac{1}{2}}, \dot{\varphi}'^{n+\frac{1}{2}}$

B.2.2 Corrector Step

The corrector step in Algorithm 4 is used to refine the estimates made in the predictor step.

Algorithm 4: `corrector`

input : $P'^{n+\frac{1}{2}}$, $p'^{n+\frac{1}{2}}$, $q'^{n+\frac{1}{2}}$, $\Xi'^{n+\frac{1}{2}}$, $\dot{\lambda}'^{n+\frac{1}{2}}$, $\dot{\lambda_I}'^{n+\frac{1}{2}}$, $\dot{\lambda_G}'^{n+\frac{1}{2}}$, $\dot{\varphi}'^{n+\frac{1}{2}}$, Δt

`/* Start of Code */`

Calculate velocities due to pressure using Algorithm 5;

for $i = 0 \rightarrow N_r + 1,\ j = 0 \rightarrow N_z + 1$ **do**

  $\tilde{u}'^{n+1}, \tilde{v}'^{n+1}, \tilde{p}'^{n+1}, \tilde{q}'^{n+1}$ = `pressureacceleration(`$i,\ j,\ P'^{n+\frac{1}{2}},\ p^n,\ q^n,\ \rho'^{n+\frac{1}{2}},\ \Delta t$`);`

Calculate artificial viscosity using Algorithm 7;

for $i = 0 \rightarrow N_r,\ j = 0 \rightarrow N_z$ **do**

  Q'^{n+1}, R'^{n+1} = `artificialviscosity(`$i,\ j,\ \tilde{u}'^{n+1},\ \tilde{u}'^{n+1},\ C_q,\ \rho'^{n+\frac{1}{2}}$`);`

Update velocities due to artificial viscosity using Algorithm 8;

for $i = 0 \rightarrow N_r + 1,\ j = 0 \rightarrow N_z + 1$ **do**

  $u'^{n+1}, v'^{n+1}, p'^{n+1}, q'^{n+1}$ = `viscousvelocity(`$i,\ j,\ \tilde{p}'^{n+1},\ \tilde{q}'^{n+1},\ Q'^{n+1},\ R'^{n+1},\ \tilde{u}'^{n+1},\ \tilde{u}'^{n+1},\ \rho'^{n+\frac{1}{2}},\ \Delta t$`);`

Correct energy using Algorithm 6;

for $i = 0 \rightarrow N_r + 1,\ j = 0 \rightarrow N_z + 1$ **do**

  E'^{n+1}, ke'^{n+1} = `energies(`$i,\ j,\ P'^{n+\frac{1}{2}},\ Q'^{n+1},\ R'^{n+1},\ u'^{n+1},\ v'^{n+1},\ \rho^n,\ E^n,\ \Delta t$`);`

Calculate pressures due to hydrodynamics Algorithm 9;

for $i = 0 \rightarrow N_r + 1,\ j = 0 \rightarrow N_z + 1$ **do**

  $\tilde{P}'^{n+1}, \tilde{Z_s}'^{n+1}$ = `isemodel(`$\rho'^{n+\frac{1}{2}},\ \rho_s'^{n+\frac{1}{2}},\ E'^{n+\frac{1}{2}},\ \lambda'^{n+\frac{1}{2}},\ P'^{n+\frac{1}{2}},\ \varphi'^{n+\frac{1}{2}}$`);`

Update burn variable Algorithm 11;

for $i = 0 \rightarrow N_r + 1,\ j = 0 \rightarrow N_z + 1$ **do**

  $\lambda'^{n+1}, \lambda_I'^{n+1}, \lambda_G'^{n+1}, \varphi'^{n+1}$ = `updatelambda(`$\lambda^n,\ \lambda_I^n,\ \lambda_G^n,\ \varphi^n,\ \dot{\lambda}'^{n+\frac{1}{2}},\ \dot{\lambda_I}'^{n+\frac{1}{2}},\ \dot{\lambda_G}'^{n+\frac{1}{2}},\ \dot{\varphi}'^{n+\frac{1}{2}},\ \Delta t$`);`

Calculate pressures due to reaction Algorithm 9;

for $i = 0 \rightarrow N_r + 1,\ j = 0 \rightarrow N_z + 1$ **do**

  $P'^{n+1}, Z_s'^{n+1}$ = `isemodel(`$\rho'^{n+\frac{1}{2}},\ \rho_s'^{n+\frac{1}{2}},\ E'^{n+1},\ \lambda'^{n+1},\ \tilde{P}'^{n+1},\ \varphi'^{n+1}$`);`

Calculate reaction rates Algorithm 10;

for $i = 0 \rightarrow N_r + 1,\ j = 0 \rightarrow N_z + 1$ **do**

  $\dot{\lambda}'^{n+1}, \dot{\lambda_I}'^{n+1}, \dot{\lambda_G}'^{n+1}, \dot{\varphi}'^{n+1}$ = `reactionrates(`$\lambda'^{n+1},\ \lambda_I'^{n+1},\ \lambda_G'^{n+1},\ Z_s'^{n+1},\ \varphi'^{n+1},\ P'^{n+1}$`);`

`/* End of Code */`

output : P'^{n+1}, p'^{n+1}, q'^{n+1}, Ξ'^{n+1}, $\dot{\lambda}'^{n+1}$, $\dot{\lambda_I}'^{n+1}$, $\dot{\lambda_G}'^{n+1}$, $\dot{\varphi}'^{n+1}$

B.2.3 Lagrangian algorithms

The first calculation in the Lagrangian substep is to use the pressure gradient to find the change in the velocity field using Algorithm 5.

Algorithm 5: `pressureacceleration`

input : i, j, P, p, q, ρ, Δt

`/* Start of Code */`

Increment the momenta using the pressure gradient;

$$p'_{(i,j+\frac{1}{2})} = p_{(i,j+\frac{1}{2})} - 2\Delta t \frac{P_{(i+\frac{1}{2},j+\frac{1}{2})} - P_{(i-\frac{1}{2},j+\frac{1}{2})}}{\Delta r_{i-\frac{1}{2}} + \Delta r_{i+\frac{1}{2}}};$$

$$q'_{(i+\frac{1}{2},j)} = q_{(i+\frac{1}{2},j)} - 2\Delta t \frac{P_{(i+\frac{1}{2},j+\frac{1}{2})} - P_{(i+\frac{1}{2},j-\frac{1}{2})}}{\Delta z_{j-\frac{1}{2}} + \Delta z_{j+\frac{1}{2}}};$$

Calculate edge densities;

$$\rho_{(i,j+\frac{1}{2})} = \frac{\rho_{(i+\frac{1}{2},j+\frac{1}{2})}\Delta r_{i-\frac{1}{2}} + \rho_{(i-\frac{1}{2},j+\frac{1}{2})}\Delta r_{i+\frac{1}{2}}}{\Delta r_{i-\frac{1}{2}} + \Delta r_{i+\frac{1}{2}}};$$

$$\rho_{(i+\frac{1}{2},j)} = \frac{\rho_{(i+\frac{1}{2},j+\frac{1}{2})}\Delta z_{j-\frac{1}{2}} + \rho_{(i+\frac{1}{2},j-\frac{1}{2})}\Delta z_{j+\frac{1}{2}}}{\Delta z_{j-\frac{1}{2}} + \Delta z_{j+\frac{1}{2}}};$$

Calculate new velocities;

$$u' = \frac{p'}{\rho_{(i,j+\frac{1}{2})}};$$

$$v' = \frac{q'}{\rho_{(i+\frac{1}{2},j)}};$$

`/* End of Code */`

output : u', v', p', q'

The specific internal energy and kinetic energy are derived from the pressure and velocities as shown in Algorithm 6.

Algorithm 6: `energies`

input : i, j, P, Q, R, u, v, ρ, E, Δt

`/* Start of Code */`

Calculate specific kinetic energy;

$$ke'_{\left(i+\frac{1}{2},j+\frac{1}{2}\right)} = \frac{1}{8}\left(u^2_{\left(i,j+\frac{1}{2}\right)} + u^2_{\left(i+1,j+\frac{1}{2}\right)} + v^2_{\left(i+\frac{1}{2},j\right)} + v^2_{\left(i+\frac{1}{2},j+1\right)}\right);$$

Calculate specific internal energy;

$$E'_{\left(i+\frac{1}{2},j+\frac{1}{2}\right)} = E_{\left(i+\frac{1}{2},j+\frac{1}{2}\right)} - \Delta t P_{\left(i+\frac{1}{2},j+\frac{1}{2}\right)}\left((\nabla_r u)_{\left(i+\frac{1}{2},j+\frac{1}{2}\right)} + (\nabla_z v)_{\left(i+\frac{1}{2},j+\frac{1}{2}\right)}\right) - \Delta t Q_{\left(i+\frac{1}{2},j+\frac{1}{2}\right)}(\nabla_r u)_{\left(i+\frac{1}{2},j+\frac{1}{2}\right)} - \Delta t R_{\left(i+\frac{1}{2},j+\frac{1}{2}\right)}(\nabla_z v)_{\left(i+\frac{1}{2},j+\frac{1}{2}\right)};$$

`/* End of Code */`

output : E, ke

Artificial Viscosity

The artificial viscosity is calculated using the Schulz formulation with Algorithm 7. The viscous terms are then used to update the velocity using Algorithm 8. The min functions means that the viscosity is zero when the fluid is expanding.

Algorithm 7: `artificialviscosity`

input : i, j, u, v, C_q, ρ

`/* Start of Code */`

$$du_{\left(i+\frac{1}{2},j+\frac{1}{2}\right)} = \min\left(0, u_{(i+1,j)} - u_{(i,j)}\right);$$

$$dv_{\left(i+\frac{1}{2},j+\frac{1}{2}\right)} = \min\left(0, v_{(i,j+1)} - v_{(i,j)}\right);$$

$$Du_{\left(i+\frac{1}{2},j+\frac{1}{2}\right)} = \frac{1}{2}\left[\left|du_{\left(i+\frac{3}{2},j+\frac{1}{2}\right)} - du_{\left(i+\frac{1}{2},j+\frac{1}{2}\right)}\right| + \left|du_{\left(i+\frac{1}{2},j+\frac{1}{2}\right)} - du_{\left(i-\frac{1}{2},j+\frac{1}{2}\right)}\right|\right];$$

$$Dv_{\left(i+\frac{1}{2},j+\frac{1}{2}\right)} = \frac{1}{2}\left[\left|dv_{\left(i+\frac{1}{2},j+\frac{3}{2}\right)} - dv_{\left(i+\frac{1}{2},j+\frac{1}{2}\right)}\right| + \left|dv_{\left(i+\frac{1}{2},j+\frac{1}{2}\right)} - dv_{\left(i+\frac{1}{2},j-\frac{1}{2}\right)}\right|\right];$$

$$Q_{\left(i+\frac{1}{2},j+\frac{1}{2}\right)} = -C_q \rho_{\left(i+\frac{1}{2},j+\frac{1}{2}\right)} \cdot du_{\left(i+\frac{1}{2},j+\frac{1}{2}\right)} \cdot Du_{\left(i+\frac{1}{2},j+\frac{1}{2}\right)};$$

$$R_{\left(i+\frac{1}{2},j+\frac{1}{2}\right)} = -C_q \rho_{\left(i+\frac{1}{2},j+\frac{1}{2}\right)} \cdot dv_{\left(i+\frac{1}{2},j+\frac{1}{2}\right)} \cdot Dv_{\left(i+\frac{1}{2},j+\frac{1}{2}\right)};$$

`/* End of Code */`

output : Q, R

Algorithm 8: `viscousvelocity`

input : i, j, p, q, Q, R, ρ, Δt

`/* Start of Code */`

Increment the momenta using the viscous pressure gradients;

$$p'_{(i,j+\frac{1}{2})} = p_{(i,j+\frac{1}{2})} - 2\Delta t \frac{Q_{(i+\frac{1}{2},j+\frac{1}{2})} - Q_{(i-\frac{1}{2},j+\frac{1}{2})}}{\Delta r_{i-\frac{1}{2}} + \Delta r_{i+\frac{1}{2}}};$$

$$q'_{(i+\frac{1}{2},j)} = q_{(i+\frac{1}{2},j)} - 2\Delta t \frac{R_{(i+\frac{1}{2},j+\frac{1}{2})} - R_{(i+\frac{1}{2},j-\frac{1}{2})}}{\Delta z_{j-\frac{1}{2}} + \Delta z_{j+\frac{1}{2}}};$$

Calculate edge densities;

$$\rho_{(i,j+\frac{1}{2})} = \frac{\rho_{(i+\frac{1}{2},j+\frac{1}{2})}\Delta r_{i-\frac{1}{2}} + \rho_{(i-\frac{1}{2},j+\frac{1}{2})}\Delta r_{i+\frac{1}{2}}}{\Delta r_{i-\frac{1}{2}} + \Delta r_{i+\frac{1}{2}}};$$

$$\rho_{(i+\frac{1}{2},j)} = \frac{\rho_{(i+\frac{1}{2},j+\frac{1}{2})}\Delta z_{j-\frac{1}{2}} + \rho_{(i+\frac{1}{2},j-\frac{1}{2})}\Delta z_{j+\frac{1}{2}}}{\Delta z_{j-\frac{1}{2}} + \Delta z_{j+\frac{1}{2}}};$$

Calculate new velocities;

$$u' = \frac{p'}{\rho_{(i,j+\frac{1}{2})}};$$

$$v' = \frac{q'}{\rho_{(i+\frac{1}{2},j)}};$$

`/* End of Code */`

output : u', v', p', q'

ISE model

The calculation of pressure requires finding the equilibrium between reactant and product by iteratively using the equations of state for each phase and adjusting the specific volume fractions until the pressures are equal. The method for this iteration is shown in Algorithm 9.

Algorithm 9: `isemodel`

input : ρ, ρ_s, E, λ, P, φ

`/* Start of Code */`

$V = \frac{1}{\rho}$; $V_{s0} = \frac{1}{\rho_s}$; $flag =$ **true**;

while $\left|P_s - P_g\right| > \varepsilon$ **do**

$s = b - \frac{P_s - P_g}{\frac{dP_s}{dV} - \frac{dP_g}{dV}}$;

if $(s - \frac{1}{4}(3a+b))(b-s) < 0$ **or**

$(flag$ **and** $|s-b| \geq \frac{1}{2}|b-c|)$ **or**

$(!flag$ **and** $|s-b| \geq \frac{1}{2}|c-d|)$ **or**

$(flag$ **and** $|b-c| < 10^{-18})$ **or**

$(!flag$ **and** $|c-d| < 10^{-18})$

then

$s = \frac{1}{2}(a+b)$;

$flag =$ **true**;

else

$flag =$ **false**;

$E_s = \texttt{max}(E_{s0} - P(s - V_{s0}),\ E_i + \tau Z_s)$;

$P_s = \varphi \cdot \texttt{reactanteos}(\varphi V_s,\ E_s)$;

$V_g = \frac{V - (1-\lambda)V_s}{\lambda}$;

$E_g = \frac{E - (1-\lambda)E_s}{\lambda}$;

$P_g = \texttt{producteos}(V_g,\ E_g)$;

$f_s = P_s - P_g$;

$d = c$; $c = b$;

if $f_a \cdot f_s < 0$ **then**

$b = s$; $f_b = f_s$;

else

$a = s$; $f_a = f_s$;

if $f_a < f_b$ **then**

`swap(`a, b`)`

$P = P_s$;

$Z_s = \frac{E_s - E_i}{\tau}$;

`/* End of Code */`

output : P, Z_s

Reaction Rates

Algorithm 10 calculates the CREST reaction rates and volume fraction rate of change for the porosity model, while Algorithm 11 updates the reaction progress variables and volume fraction to the next time step.

Algorithm 10: `reactionrates`

input : λ, λ_I, λ_G, Z_s, φ, P

`/* Start of Code */`

$$b_1 = c_0 (Z_s - c_{13})^{c_1};$$

$$b_2 = c_2 (Z_s - c_{13})^{c_3};$$

$$m_I = (1-\lambda) \frac{c_6 (Z_s)^{c_{12}}}{\sqrt{b_1}};$$

$$m_G = (1-\lambda) \left[\frac{c_8 (Z_s)^{-c_9} + c_{10} (Z_s - c_{13})^{c_{11}}}{\sqrt{b_2}} \right];$$

$$m_2 = \frac{c_{10}}{\sqrt{b_2}} (Z_s - c_{13})^{c_{11}};$$

$$\dot{\lambda}_I = (1-\lambda_I) \left[-2 b_1 \ln (1-\lambda_I) \right]^{\frac{1}{2}};$$

$$\dot{\lambda}_G = (1-\lambda_G) \lambda_I \left[2 b_2 \left(\frac{b_2 \lambda_1}{b_1} - \ln (1-\lambda_G) \right) \right]^{\frac{1}{2}};$$

$$\dot{\lambda} = m_2 (1-\lambda) \dot{\lambda}_G;$$

$$\dot{\varphi} = k_\varphi \left[P - P_h \left(1 - \sqrt{\frac{\varphi_0 (1-\varphi)}{(\varphi (1-\varphi_0)}} \right) \right];$$

`/* End of Code */`

output : $\dot{\lambda}'$, $\dot{\lambda_I}'$, $\dot{\lambda_G'}$, $\dot{\varphi}'$

Algorithm 11: `updatelambda`

input : λ, λ_I, λ_G, φ, $\dot{\lambda}$, $\dot{\lambda_I}$, $\dot{\lambda_G}$, $\dot{\varphi}$, Δt

`/* Start of Code */`

$$\lambda' = \lambda + \Delta t \dot{\lambda};$$

$$\lambda_I' = \lambda_I + \Delta t \dot{\lambda_I};$$

$$\lambda_G' = \lambda_G + \Delta t \dot{\lambda_G};$$

$$\varphi' = \varphi + \Delta t \dot{varphi};$$

`/* End of Code */`

output : λ', λ_I', λ_G', φ'

Reactant EoS

Algorithm 12 shows the calculation of the solid pressure P_s using the Mie-Grüneisen equation of state.

Algorithm 12: `reactanteos`

input : V_s, E_s

`/* Start of Code */`

$\Gamma = \Gamma_{00} + Zy;$

if $\rho < \rho_0$ **then**

$$E_i(V_s) = \frac{a^2}{16b^2}\left[\exp(4by) - 1\right] + \frac{a^2\rho_0}{4b}(V_s - V_0) + Q;$$

$$P_i(V_s) = \frac{a^2\rho_0}{4b}\left[\exp(4by) - 1\right];$$

else

$$E_i(V_s) = \frac{a^2}{16b^2}\left[\sum_{j=2}^{4}\frac{(4by)^j}{j!} + C\frac{(4by)^5}{5!} + \frac{4y^3}{3(1-y)^3}\right] + Q;$$

$$P_i(V_s) = \frac{a^2\rho_0}{4b}\left[\sum_{j=1}^{3}\frac{(4by)^j}{j!} + C\frac{(4by)^4}{4!} + \frac{y^2}{(1-y)^4}\right];$$

$$P_s = P_i(V_s) + \frac{\Gamma(V_s)}{V_s}(E_s - E_i(V_s));$$

`/* End of Code */`

output : P_s

Product EoS

Algorithm 13 shows the calculation of the gas pressure P_g using the JWL equation of state.

Algorithm 13: `producteos`

input : V_g, E_g

`/* Start of Code */`

$$A = A_0 + A_1\rho;$$

$$B = B_0 + B_1\rho;$$

$$R1 = R1_0 + R1_1\rho;$$

$$R2 = R2_0 + R2_1\rho;$$

$$P_g = A\left(1 - \frac{\omega}{R1V_g}\right)\exp(-R1V_g) + B\left(1 - \frac{\omega}{R2V_g}\right)\exp(-R2V_g) + \frac{\omega E_g}{V_g};$$

`/* End of Code */`

output : P_g

B.2.4 Time step control

The size of the time step is adjusted with each iteration to ensure the CFL condition is met. The maximum CFL number c_t is set to < 0.3 for safety. The time step is interpolated for when a time centred time step is needed. Algorithm 14 contains the time step setting function.

Algorithm 14: `settimestep`

input : Δt^{n-1}, $\Delta t^{n-\frac{1}{2}}$, c, Q, R, ρ

`/* Start of Code */`

Find the minimum time step over all cells;

for $i = 0 \rightarrow N_r,\ j = 0 \rightarrow N_z$ **do**

$\Delta t^n_{\left(i+\frac{1}{2},j+\frac{1}{2}\right)} = \texttt{min}\left(\frac{\Delta r}{\sqrt{c^2+\frac{Q}{\rho}}}, \frac{\Delta z}{\sqrt{c^2+\frac{R}{\rho}}}\right)$;

$\tilde{\Delta t} = \texttt{min}(\Delta t^n_{i,j})$;

Limit the amount by which the time step can change with each step;

$\Delta t^{n+\frac{1}{2}} = c_t\ \texttt{min}(c_m \Delta t^{n-\frac{1}{2}}, \tilde{\Delta t})$;

Calculate the mid step time steps;

$\Delta t^n = \frac{1}{2}\left(\Delta t^{n-\frac{1}{2}} + \Delta t^{n+\frac{1}{2}}\right)$;

`/* End of Code */`

output : Δt^n, $\Delta t^{n+\frac{1}{2}}$,

B.3 Advection Step

If performed in a single step, two dimensional advection only accounts for material transport between edge coupled (orthogonally adjacent) cells, and not between vertex coupled (diagonally adjacent) cells. Since the mesh is rectilinear, a single step scheme would result in non-physical anisotropy. The advection is therefore performed in two tranches to achieve transport between diagonally adjacent cells. The first step advects the fields forward by half the time step, where the flux is recalculated and used for the second half time step. Therefore a vertex coupled cell receives information from the original cell via the two mutually edge coupled cells within one time step. This two step procedure is shown in Algorithm 15.

The following shorthand is used for the scalar quantities and their fluxes in the radial and axial directions respectively.

$$\Xi = (\rho, E, \lambda, \lambda_I, \lambda_G, \rho_s, E_s, Z_s, \varphi) \tag{B.1}$$

$$\Phi = (f(\rho), f(E), f(\lambda), f(\lambda_I), f(\lambda_G), f(\rho_s), f(E_s), f(Z_s), f(\varphi)) \tag{B.2}$$

$$\Psi = (g(\rho), g(E), g(\lambda), g(\lambda_I), g(\lambda_G), g(\rho_s), g(E_s), g(Z_s), g(\varphi)) \tag{B.3}$$

Algorithm 15: `advect`

input : u^n, v^n, Ξ^n, p^n, q^n

`/* Start of Code */`

Perform half advection using Algorithm 16;

$\Xi^{n+\frac{1}{2}}$, $u^{n+\frac{1}{2}}$, $v^{n+\frac{1}{2}}$, $p^{n+\frac{1}{2}}$, $q^{n+\frac{1}{2}}$ = `halfadvect(`u^n, v^n, Ξ^n, p^n, q^n, $0.5\Delta t$`);`

Perform full advection using Algorithm 17;

Ξ^{n+1}, u^{n+1}, v^{n+1} = `fulladvect(`Ξ^n, p^n, q^n, $u^{n+\frac{1}{2}}$, $v^{n+\frac{1}{2}}$, $\Xi^{n+\frac{1}{2}}$, Δt`);`

Equilibrium correction using Algorithm 28;

$\dot{\lambda}^{n+1}$, $\dot{\lambda_I}^{n+1}$, $\dot{\lambda_G}^{n+1}$, P^{n+1}, Z_s^{n+1} = `correcttoeqm(`ρ^{n+1}, ρ_s^{n+1}, E^{n+1}, E_s^{n+1}, P^{n+1}, φ^{n+1}, λ^{n+1}, λ_I^{n+1}, λ_G^{n+1}, Z_s^{n+1}`);`

`/* End of Code */`

output : u^{n+1}, v^{n+1}, Ξ^{n+1}, p^{n+1}, q^{n+1}, $\dot{\lambda}^{n+1}$, $\dot{\lambda_I}^{n+1}$, $\dot{\lambda_G}^{n+1}$, P^{n+1}

The steps within the half advection and full advection are similar, and are shown in Algorithms 16 and 17 respectively.

Algorithm 16: `halfadvect`

input : u^n, v^n, Ξ^n, p^n, q^n, Δt

`/* Start of Code */`

Calculate the radial scalar fluxes using Algorithm 18;

for $i = 0 \to N_r + 1,\ j = 0 \to N_z$ **do**

  Φ^n = `radialscalarflux(`$i,\ j,\ \Xi^n,\ u^n,\ \Delta t$`)`;

Calculate the axial scalar fluxes using Algorithm 19;

for $i = 0 \to N_r,\ j = 0 \to N_z + 1$ **do**

  Ψ^n = `axialscalarflux(`$i,\ j,\ \Xi^n,\ v^n,\ \Delta t$`)`;

Update the densities and other field values using Algorithm 20;

for $i = 0 \to N_r, j = 0 \to N_z$ **do**

  $\Xi^{n+\frac{1}{2}}$ = `scaladvect(`$i,\ j,\ \Xi^n,\ \Phi^n,\ \Psi^n,\ \Delta t$`)`;

Calculate the radial fluxes of radial momentum using Algorithm 21;

for $i = 0 \to N_r,\ j = 0 \to N_z$ **do**

  $C^n_{\left(i-\frac{1}{2},j+\frac{1}{2}\right)}$ = `radialradialmomentumflux(`$i,\ j,\ u^n,\ f(\rho^n),\ \Delta t$`)`;

Calculate the axial fluxes of radial momentum using Algorithm 22;

for $i = 0 \to N_r + 1,\ j = 0 \to N_z + 1$ **do**

  $D^n_{(i,j)}$ = `axialradialmomentumflux(`$i,\ j,\ u^n,\ v^n,\ g(\rho^n),\ \Delta t$`)`;

Calculate the radial fluxes of axial momentum using Algorithm 23;

for $i = 0 \to N_r + 1,\ j = 0 \to N_z + 1$ **do**

  $F^n_{(i,j)}$ = `radialaxialmomentumflux(`$i,\ j,\ u^n,\ v^n,\ f(\rho^n),\ \Delta t$`)`;

Calculate the axial fluxes of axial momentum using Algorithm 24;

for $i = 0 \to N_r,\ j = 0 \to N_z$ **do**

  $G^n_{\left(i+\frac{1}{2},j-\frac{1}{2}\right)}$ = `axialaxialmomentumflux(`$i,\ j,\ v^n,\ g(\rho^n),\ \Delta t$`)`;

Update the radial momenta and velocities using Algorithm 25;

for $i = 0 \to N_r + 1, j = 0 \to N_z$ **do**

  $p^{n+\frac{1}{2}}_{\left(i,j-\frac{1}{2}\right)}, u^{n+\frac{1}{2}}_{\left(i,j-\frac{1}{2}\right)}$ = `radialmomentumadvect(`$i,\ j,\ p^n,\ C^n,\ D^n,\ \Delta t,\ \rho^{n+\frac{1}{2}}$`)`;

Update the axial momenta and velocity using Algorithm 26;

for $i = 0 \to N_r, j = 0 \to N_z + 1$ **do**

  $q^{n+\frac{1}{2}}_{\left(i-\frac{1}{2},j\right)}, v^{n+\frac{1}{2}}_{\left(i,j-\frac{1}{2}\right)}$ = `axialmomentumadvect(`$i,\ j,\ q^n,\ F^n,\ G^n,\ \Delta t,\ \rho^{n+\frac{1}{2}}$`)`;

Correct the energy using Algorithm 27;

for $i = 0 \to N_r, j = 0 \to N_z$ **do**

  $e^{n+\frac{1}{2}}$ = `debarcorrect(`$i,\ j,\ e^{n+\frac{1}{2}},\ ke^{n+\frac{1}{2}},\ u^{n+\frac{1}{2}},\ v^{n+\frac{1}{2}}$`)`;

`/* End of Code */`

output : $\Xi^{n+\frac{1}{2}}$, $u^{n+\frac{1}{2}}$, $v^{n+\frac{1}{2}}$, $p^{n+\frac{1}{2}}$, $q^{n+\frac{1}{2}}$

Algorithm 17: `fulladvect`

input : Ξ^n, p^n, q^n, $u^{n+\frac{1}{2}}$, $v^{n+\frac{1}{2}}$, $\Xi^{n+\frac{1}{2}}$, Δt

`/* Start of Code */`

Calculate the radial scalar fluxes using Algorithm 18;

for $i = 0 \rightarrow N_r + 1,\ j = 0 \rightarrow N_z$ **do**

$\Phi^{n+\frac{1}{2}} =$ `radialscalarflux(`$i,\ j,\ \Xi^{n+\frac{1}{2}},\ u^{n+\frac{1}{2}},\ \Delta t$`);`

Calculate the axial scalar fluxes using Algorithm 19;

for $i = 0 \rightarrow N_r,\ j = 0 \rightarrow N_z + 1$ **do**

$\Psi^{n+\frac{1}{2}} =$ `axialscalarflux(`$i,\ j,\ \Xi^{n+\frac{1}{2}},\ v^{n+\frac{1}{2}},\ \Delta t$`);`

Update the densities and other field values using Algorithm 20;

for $i = 0 \rightarrow N_r, j = 0 \rightarrow N_z$ **do**

$\Xi^{n+1} =$ `scalaradvect(`$i,\ j,\ \Xi^n,\ \Phi^{n+\frac{1}{2}},\ \Psi^{n+\frac{1}{2}},\ \Delta t$`);`

Calculate the radial fluxes of radial momentum using Algorithm 21;

for $i = 0 \rightarrow N_r,\ j = 0 \rightarrow N_z$ **do**

$C^{n+\frac{1}{2}}_{\left(i-\frac{1}{2},j+\frac{1}{2}\right)} =$ `radialradialmomentumflux(`$i,\ j,\ u^n,\ f\left(\rho^{n+\frac{1}{2}}\right),\ \Delta t$`);`

Calculate the axial fluxes of radial momentum using Algorithm 22;

for $i = 0 \rightarrow N_r + 1,\ j = 0 \rightarrow N_z + 1$ **do**

$D^{n+\frac{1}{2}}_{(i,j)} =$ `axialradialmomentumflux(`$i,\ j,\ u^n,\ v^n,\ g\left(\rho^{n+\frac{1}{2}}\right),\ \Delta t$`);`

Calculate the radial fluxes of axial momentum using Algorithm 23;

for $i = 0 \rightarrow N_r + 1,\ j = 0 \rightarrow N_z + 1$ **do**

$F^{n+\frac{1}{2}}_{(i,j)} =$ `radialaxialmomentumflux(`$i,\ j,\ u^n,\ v^n,\ f\left(\rho^{n+\frac{1}{2}}\right),\ \Delta t$`);`

Calculate the axial fluxes of axial momentum using Algorithm 24;

for $i = 0 \rightarrow N_r,\ j = 0 \rightarrow N_z$ **do**

$G^{n+\frac{1}{2}}_{\left(i+\frac{1}{2},j-\frac{1}{2}\right)} =$ `axialaxialmomentumflux(`$i,\ j,\ v^n,\ g\left(\rho^{n+\frac{1}{2}}\right),\ \Delta t$`);`

Update the radial momenta and velocities using Algorithm 25;

for $i = 0 \rightarrow N_r + 1, j = 0 \rightarrow N_z$ **do**

$p^{n+1}_{\left(i,j-\frac{1}{2}\right)}, u^{n+1}_{\left(i,j-\frac{1}{2}\right)} =$ `radialmomentumadvect(`$i,\ j,\ p^n,\ C^{n+\frac{1}{2}},\ D^{n+\frac{1}{2}},\ \Delta t,\ \rho^{n+1}$`);`

Update the axial momenta and velocity using Algorithm 26;

for $i = 0 \rightarrow N_r, j = 0 \rightarrow N_z + 1$ **do**

$q^{n+1}_{\left(i-\frac{1}{2},j\right)}, v^{n+1}_{\left(i,j-\frac{1}{2}\right)} =$ `axialmomentumadvect(`$i,\ j,\ q^n,\ F^{n+\frac{1}{2}},\ G^{n+\frac{1}{2}},\ \Delta t,\ \rho^{n+1}$`);`

Correct the energy using Algorithm 27;

for $i = 0 \rightarrow N_r, j = 0 \rightarrow N_z$ **do**

$e^{n+1} =$ `debarcorrect(`$i,\ j,\ e^{n+1},\ ke^{n+1},\ u^{n+1},\ v^{n+1}$`);`

`/* End of Code */`

output : Ξ^{n+1}, u^{n+1}, v^{n+1}

B.3.1 Scalar Flux Calculation

Fluxes of cell centred scalar quantities are calculated using Algorithms 18 and 19. Volume centred quantities are interpolated to interface values using the piecewise linear method (PLM) of [228]. A slope limiter is applied in order to avoid unphysical oscillations prevalent to shock simulations - here the monotonised central symmetric Van Leer limiter [218] is used.

$$\sigma_r(\chi_i) = \phi(\theta)\frac{\chi_{i+1}-\chi_i}{\Delta r_i} \tag{B.4}$$

$$\phi(\theta) = \texttt{max}\left[0, \texttt{min}\left(2\theta, \frac{B}{A+1}(\theta+1), 2\right)\right] \tag{B.5}$$

with:

$$A = \frac{\Delta r_{i-1}+\Delta r_i}{\Delta r_i+\Delta r_{i+1}} \qquad B = \frac{2\Delta r_i}{\Delta r_i+\Delta r_{i+1}} \qquad \theta = \frac{\chi_i-\chi_{i-1}}{\chi_{i+1}-\chi_i} \tag{B.6}$$

Algorithm 18: `radialscalarflux`

input : i, j, Ξ, u, Δt

`/* Start of Code */`

Approximate the time centred radial velocity;

$\tilde{u}_{(i,j+\frac{1}{2})} = u_{(i,j+\frac{1}{2})} - \frac{1}{2}u_{(i,j+\frac{1}{2})}\sigma_r\left(u_{(i,j+\frac{1}{2})}\right)\Delta t$;

Interpolate scalar quantities to the edge centres using MUSCL scheme;

if $\tilde{u}_{(i,j+\frac{1}{2})} > 0$ **then**

  $\rho_{(i,j+\frac{1}{2})} = \rho_{(i-\frac{1}{2},j+\frac{1}{2})} + \sigma_r\left(\rho_{(i-\frac{1}{2},j+\frac{1}{2})}\right)\left[r_i - \bar{r}_{i-\frac{1}{2}} - \frac{1}{2}\tilde{u}_{(i,j+\frac{1}{2})}\Delta t\right]$;

else

  $\rho_{(i,j+\frac{1}{2})} = \rho_{(i+\frac{1}{2},j+\frac{1}{2})} + \sigma_r\left(\rho_{(i+\frac{1}{2},j+\frac{1}{2})}\right)\left[r_i - \bar{r}_{i+\frac{1}{2}} - \frac{1}{2}\tilde{u}_{(i,j+\frac{1}{2})}\Delta t\right]$;

Calculate the radial scalar fluxes;

$f(\rho)_{(i,j+\frac{1}{2})} = \rho_{(i,j+\frac{1}{2})}\tilde{u}_{(i,j+\frac{1}{2})}$;

$f(e\rho)_{(i,j+\frac{1}{2})} = e_{(i,j+\frac{1}{2})}f(\rho)_{(i,j+\frac{1}{2})}$;

`/* End of Code */`

output : Φ

B.3.2 Scalar Advection

The scalar quantities are advected according to Algorithm 20. The specific energy is multiplied by the density before advection in order to make a conserved quantity.

Algorithm 19: `axialscalarflux`

input : i, j, Ξ, v, Δt

`/* Start of Code */`

Approximate the time centred axial velocity;

$$\tilde{v}_{\left(i+\frac{1}{2},j\right)} = v_{\left(i+\frac{1}{2},j\right)} - \frac{1}{2} v_{\left(i+\frac{1}{2},j\right)} \sigma_z \left(v_{\left(i+\frac{1}{2},j\right)} \right) \Delta t;$$

Interpolate scalar quantities to the edge centres using MUSCL scheme;

if $\tilde{v}_{\left(i+\frac{1}{2},j\right)} > 0$ **then**

$$\rho_{\left(i+\frac{1}{2},j\right)} = \rho_{\left(i+\frac{1}{2},j-\frac{1}{2}\right)} + \sigma_z \left(\rho_{\left(i+\frac{1}{2},j-\frac{1}{2}\right)} \right) \left[z_j - \bar{z}_{j-\frac{1}{2}} - \frac{1}{2} \tilde{v}_{\left(i+\frac{1}{2},j\right)} \Delta t \right]$$

else

$$\rho_{\left(i+\frac{1}{2},j\right)} = \rho_{\left(i+\frac{1}{2},j+\frac{1}{2}\right)} + \sigma_z \left(\rho_{\left(i+\frac{1}{2},j+\frac{1}{2}\right)} \right) \left[z_j - \bar{z}_{j+\frac{1}{2}} - \frac{1}{2} \tilde{v}_{\left(i+\frac{1}{2},j\right)} \Delta t \right]$$

Calculate the axial scalar fluxes;

$$g(\rho)_{\left(i+\frac{1}{2},j\right)} = \rho_{\left(i+\frac{1}{2},j\right)} \tilde{v}_{\left(i+\frac{1}{2},j\right)};$$

$$g(e\rho)_{\left(i+\frac{1}{2},j\right)} = e_{\left(i+\frac{1}{2},j\right)} g(\rho)_{\left(i+\frac{1}{2},j\right)};$$

`/* End of Code */`

output : Ψ

Algorithm 20: `scalaradvect`

input : i, j, Ξ, Φ, Ψ, Δt

`/* Start of Code */`

$$\Xi'_{\left(i+\frac{1}{2},j+\frac{1}{2}\right)} = \Xi_{\left(i+\frac{1}{2},j+\frac{1}{2}\right)} - \Delta t \left[\frac{\Phi_{\left(i+1,j+\frac{1}{2}\right)} r_{i+1} - \Phi_{\left(i,j+\frac{1}{2}\right)} r_i}{r_{i+1}^2 - r_i^2} + \frac{\Psi_{\left(i+\frac{1}{2},j+1\right)} - \Psi_{\left(i+\frac{1}{2},j\right)}}{z_{j+1} - z_j} \right];$$

`/* End of Code */`

output : Ξ'

B.3.3 Momentum Flux Calculation

The momenta fluxes are calculated using interpolation onto a staggered grid. The interpolated mass fluxes are multiplied by the interpolated velocities to obtain momenta fluxes Algorithms 21 to 24 are used to calculate the fluxes. The radial radial momentum flux and axial axial momentum flux are cell centred quantities, while the axial radial momentum flux and radial axial momentum flux are defined at cell corners.

Algorithm 21: `radialradialmomentumflux`

input : i, j, u, $f(\rho)$, Δt

`/* Start of Code */`

Make a preliminary guess for the cell centred radial velocity;

$$\tilde{u}_{\left(i+\frac{1}{2},j+\frac{1}{2}\right)} = \frac{1}{2}\left[u_{\left(i,j+\frac{1}{2}\right)} + u_{\left(i+1,j+\frac{1}{2}\right)}\right];$$

Refine the guess using MUSCL scheme;

if $\tilde{u}_{\left(i+\frac{1}{2},j+\frac{1}{2}\right)} > 0$ **then**

$$u_{\left(i+\frac{1}{2},j+\frac{1}{2}\right)} = u_{\left(i,j+\frac{1}{2}\right)} + \sigma_r\left(u_{\left(i,j+\frac{1}{2}\right)}\right)\left[\xi_{i+\frac{1}{2}} - \bar{\xi}_i - \frac{1}{2}\Delta t\tilde{u}_{\left(i+\frac{1}{2},j+\frac{1}{2}\right)}\right];$$

else

$$u_{\left(i+\frac{1}{2},j+\frac{1}{2}\right)} = u_{\left(i+1,j+\frac{1}{2}\right)} + \sigma_r\left(u_{\left(i+1,j+\frac{1}{2}\right)}\right)\left[\xi_{i+\frac{1}{2}} - \bar{\xi}_{i+1} - \frac{1}{2}\Delta t\tilde{u}_{\left(i+\frac{1}{2},j+\frac{1}{2}\right)}\right];$$

Interpolate radial mass flux to cell centre;

$$f(\rho)_{\left(i+\frac{1}{2},j+\frac{1}{2}\right)} = \frac{1}{2}\left[f(\rho)_{\left(i,j+\frac{1}{2}\right)} + f(\rho)_{\left(i+1,j+\frac{1}{2}\right)}\right];$$

Finally, calculate radial flux of radial momentum;

$$C_{\left(i+\frac{1}{2},j+\frac{1}{2}\right)} = u_{\left(i+\frac{1}{2},j+\frac{1}{2}\right)} f(\rho)_{\left(i+\frac{1}{2},j+\frac{1}{2}\right)};$$

`/* End of Code */`

output : C

Algorithm 22: `axialradialmomentumflux`

input : i, j, u, v, $g(\rho)$, Δt

`/* Start of Code */`

Make a preliminary guess for the corner centred axial velocity;

$$\tilde{v}_{(i,j)} = \frac{v_{\left(i-\frac{1}{2},j\right)}\Delta r_{i+\frac{1}{2}} + v(\rho)_{\left(i+\frac{1}{2},j\right)}\Delta r_{i-\frac{1}{2}}}{\Delta r_{i+\frac{1}{2}} + \Delta r_{i-\frac{1}{2}}};$$

Find the corner centred radial velocity using MUSCL scheme;

if $\tilde{v}_{(i,j)} > 0$ **then**

$$u_{(i,j)} = u_{\left(i,j-\frac{1}{2}\right)} + \sigma_z\left(u_{\left(i,j-\frac{1}{2}\right)}\right)\left[z_j - \bar{z}_{j-\frac{1}{2}} - \frac{1}{2}\Delta t\tilde{v}_{(i,j)}\right];$$

else

$$u_{(i,j)} = u_{\left(i,j+\frac{1}{2}\right)} + \sigma_z\left(u_{\left(i,j+\frac{1}{2}\right)}\right)\left[z_j - \bar{z}_{j+\frac{1}{2}} - \frac{1}{2}\Delta t\tilde{v}_{(i,j)}\right];$$

Interpolate axial mass flux to cell corner;

$$g(\rho)_{(i,j)} = \frac{g(\rho)_{\left(i-\frac{1}{2},j\right)}\Delta r_{i+\frac{1}{2}} + g(\rho)_{\left(i+\frac{1}{2},j\right)}\Delta r_{i-\frac{1}{2}}}{\Delta r_{i+\frac{1}{2}} + \Delta r_{i-\frac{1}{2}}};$$

Finally, calculate axial flux of radial momentum;

$$D_{(i,j)} = u_{(i,j)} g(\rho)_{(i,j)};$$

`/* End of Code */`

output : D

Algorithm 23: `radialaxialmomentumflux`

input : i, j, u, v, $f(\rho)$, Δt

`/* Start of Code */`

Make a preliminary guess for the corner centred radial velocity;

$$\tilde{u}_{(i,j)} = \frac{u_{\left(i,j-\frac{1}{2}\right)}\Delta z_{j+\frac{1}{2}} + u(\rho)_{\left(i,j+\frac{1}{2}\right)}\Delta z_{j-\frac{1}{2}}}{\Delta z_{j+\frac{1}{2}} + \Delta z_{j-\frac{1}{2}}};$$

Find the corner centred axial velocity using MUSCL scheme;

if $\tilde{u}_{(i,j)} > 0$ **then**

$$v_{(i,j)} = v_{\left(i-\frac{1}{2},j\right)} + \sigma_r\left(v_{\left(i-\frac{1}{2},j\right)}\right)\left[r_i - \bar{r}_{i-\frac{1}{2}} - \tfrac{1}{2}\Delta t\tilde{u}_{(i,j)}\right];$$

else

$$v_{(i,j)} = v_{\left(i+\frac{1}{2},j\right)} + \sigma_r\left(v_{\left(i+\frac{1}{2},j\right)}\right)\left[r_i - \bar{r}_{i+\frac{1}{2}} - \tfrac{1}{2}\Delta t\tilde{u}_{(i,j)}\right];$$

Interpolate radial mass flux to cell corner;

$$f(\rho)_{(i,j)} = \frac{f(\rho)_{\left(i,j-\frac{1}{2}\right)}\Delta z_{j+\frac{1}{2}} + f(\rho)_{\left(i,j+\frac{1}{2}\right)}\Delta z_{j-\frac{1}{2}}}{\Delta z_{j+\frac{1}{2}} + \Delta z_{j-\frac{1}{2}}};$$

Finally, calculate radial flux of axial momentum;

$$F_{(i,j)} = v_{(i,j)}f(\rho)_{(i,j)};$$

`/* End of Code */`

output : F

Algorithm 24: `axialaxialmomentumflux`

input : i, j, v, $g(\rho)$, Δt

`/* Start of Code */`

Make a preliminary guess for the cell centred axial velocity;

$$\tilde{v}_{\left(i+\frac{1}{2},j+\frac{1}{2}\right)} = \tfrac{1}{2}\left[v_{\left(i+\frac{1}{2},j\right)} + v_{\left(i+\frac{1}{2},j+1\right)}\right];$$

Refine the guess using MUSCL scheme;

if $\tilde{v}_{\left(i+\frac{1}{2},j+\frac{1}{2}\right)} > 0$ **then**

$$v_{\left(i+\frac{1}{2},j+\frac{1}{2}\right)} = v_{\left(i+\frac{1}{2},j\right)} + \sigma_z\left(v_{\left(i+\frac{1}{2},j\right)}\right)\left[\zeta_{j+\frac{1}{2}} - \bar{\zeta}_j - \tfrac{1}{2}\Delta t\tilde{v}_{\left(i+\frac{1}{2},j+\frac{1}{2}\right)}\right];$$

else

$$v_{\left(i+\frac{1}{2},j+\frac{1}{2}\right)} = v_{\left(i+\frac{1}{2},j+1\right)} + \sigma_z\left(v_{\left(i+\frac{1}{2},j+1\right)}\right)\left[\zeta_{j+\frac{1}{2}} - \bar{\zeta}_{j+1} - \tfrac{1}{2}\Delta t\tilde{v}_{\left(i+\frac{1}{2},j+\frac{1}{2}\right)}\right];$$

Interpolate axial mass flux to cell centre;

$$g(\rho)_{\left(i+\frac{1}{2},j+\frac{1}{2}\right)} = \tfrac{1}{2}\left[g(\rho)_{\left(i+\frac{1}{2},j\right)} + g(\rho)_{\left(i+\frac{1}{2},j+1\right)}\right];$$

Finally, calculate axial flux of axial momentum;

$$G_{\left(i+\frac{1}{2},j+\frac{1}{2}\right)} = v_{\left(i+\frac{1}{2},j+\frac{1}{2}\right)}g(\rho)_{\left(i+\frac{1}{2},j+\frac{1}{2}\right)};$$

`/* End of Code */`

output : G

B.3.4 Momentum Advection

The momenta are advected by the same method as the scalar quantities, except on the staggered grids. Algorithms 25 and 26 show this process.

Algorithm 25: `radialmomentumadvect`

input : i, j, p, C, D, Δt, ρ

`/* Start of Code */`

$$p'_{(i,j+\frac{1}{2})} = p_{(i,j+\frac{1}{2})} - \Delta t \left[\frac{C_{(i+\frac{1}{2},j+\frac{1}{2})}\bar{r}_{i+\frac{1}{2}} - C_{(i-\frac{1}{2},j+\frac{1}{2})}\bar{r}_{i-\frac{1}{2}}}{\bar{r}^2_{i+\frac{1}{2}} - \bar{r}^2_{i-\frac{1}{2}}} + \frac{D_{(i,j+1)} - D_{(i,j)}}{z_{j+1} - z_j} \right];$$

$$\rho_{(i,j+\frac{1}{2})} = \frac{\rho_{(i+\frac{1}{2},j+\frac{1}{2})}\Delta r_{i-\frac{1}{2}} + \rho_{(i-\frac{1}{2},j+\frac{1}{2})}\Delta r_{i+\frac{1}{2}}}{\Delta r_{i-\frac{1}{2}} + \Delta r_{i+\frac{1}{2}}};$$

$$u'_{(i,j+\frac{1}{2})} = \frac{p'_{(i,j+\frac{1}{2})}}{\rho_{(i,j+\frac{1}{2})}};$$

`/* End of Code */`

output : p', u'

Algorithm 26: `axialmomentumadvect`

input : i, j, q, F, G, Δt, ρ

`/* Start of Code */`

$$q'_{(i+\frac{1}{2},j)} = q_{(i+\frac{1}{2},j)} - \Delta t \left[\frac{F_{(i+1,j)}r_{i+1} - F_{(i,j)}r_i}{r^2_{i+1} - r^2_i} + \frac{G_{(i+\frac{1}{2},j+\frac{1}{2})} - G_{(i+\frac{1}{2},j-\frac{1}{2})}}{\bar{z}_{j+\frac{1}{2}} - \bar{z}_{j-\frac{1}{2}}} \right];$$

$$\rho_{(i+\frac{1}{2},j)} = \frac{\rho_{(i+\frac{1}{2},j+\frac{1}{2})}\Delta z_{j-\frac{1}{2}} + \rho_{(i+\frac{1}{2},j-\frac{1}{2})}\Delta z_{j+\frac{1}{2}}}{\Delta z_{j-\frac{1}{2}} + \Delta z_{j+\frac{1}{2}}};$$

$$v'_{(i+\frac{1}{2},j)} = \frac{q'_{(i+\frac{1}{2},j)}}{\rho_{(i+\frac{1}{2},j)}};$$

`/* End of Code */`

output : q', v'

The Debar correction algorithm (Algorithm 27) ensures conservation of total energy as well as internal energy. The difference between the advected kinetic energy and the kinetic energy as calculated from the advected velocities is added to the internal energy.

Algorithm 27: `debarcorrect`

input : i, j, E, ke, u, v

`/* Start of Code */`

$$E'_{\left(i+\frac{1}{2},j+\frac{1}{2}\right)} = E_{\left(i+\frac{1}{2},j+\frac{1}{2}\right)} + \left\{ ke_{\left(i+\frac{1}{2},j+\frac{1}{2}\right)} - \frac{1}{8}\left(u^2_{\left(i,j+\frac{1}{2}\right)} + u^2_{\left(i+1,j+\frac{1}{2}\right)} + v^2_{\left(i+\frac{1}{2},j\right)} + v^2_{\left(i+\frac{1}{2},j+1\right)} \right) \right\};$$

`/* End of Code */`

output : E'

B.3.5 Equilibrium Correction

Following the advection it is necessary to ensure that the gas and solid phases are still in equilibrium and to re-equilibrate if not. The reaction rates are also recalculated for the beginning of the next time step. This equilibrium correction is shown in Algorithm 28.

Algorithm 28: `correcttoeqm`

input : ρ, ρ_s, E, E_s, P, φ, λ, λ_I, λ_G, Z_s

`/* Start of Code */`

Reevaluate the reaction rates using Algorithm 10;

$\dot{\lambda}'$, $\dot{\lambda_I}'$, $\dot{\lambda_G}'$, $\dot{\varphi}$= `reactionrates(`λ, λ_I, λ_G, Z_s, φ, P`);`

Calculate the new equilibrium pressure using Algorithm 9;

P', Z'_s = `isemodel(`ρ, ρ_s, E, E_s, λ, P, φ`);`

`/* End of Code */`

output : $\dot{\lambda}'$, $\dot{\lambda_I}'$, $\dot{\lambda_G}'$, $\dot{\varphi}$, P', Z'_s

B.4 Table of Parameters

Hydrocode					
c_t	0.3		c_m	5	
c_q	3				

Reactant EoS					
ρ_0	1.778	$\mathrm{g\,cm^{-3}}$	a	0.23	$\mathrm{cm\,\mu s^{-1}}$
Q	0.061259	$\mathrm{Mbar\,cm^3\,g^{-1}}$	b	2.5	
Γ_{00}	1.22		C	0.7	
Z	−0.8066				

Porosity Model					
k_φ	3150	$\mathrm{Mbar^{-1}\,\mu s^{-1}}$	P_h	0.0007	Mbar
A_c	1.88		B_c	0.7044	

Product EoS					
A_0	14.419	Mbar	$R1_0$	6.9514	
A_1	1.4815	$\mathrm{Mbar\,cm^3\,g^{-1}}$	$R1_1$	−0.4439	$\mathrm{g^{-1}\,cm^{-3}}$
B_0	0.6997	Mbar	$R2_0$	2.3009	
B_1	0.0519	$\mathrm{Mbar\,cm^3\,g^{-1}}$	$R2_1$	−0.2959	$\mathrm{g^{-1}\,cm^{-3}}$
ω	0.4421				

CREST					
c_0	6.1×10^{11}	$\mathrm{\mu s^{-2}(Mbar\,cm^3\,g^{-1})^{-c_1}}$	c_1	4	
c_2	8.88×10^{13}	$\mathrm{\mu s^{-2}(Mbar\,cm^3\,g^{-1})^{-c_3}}$	c_3	5	
c_{10}	2.68×10^{8}	$\mathrm{\mu s^{-2}(Mbar\,cm^3\,g^{-1})^{-c_{11}}}$	c_{11}	1.5	
c_{13}	3.3×10^{-5}	$\mathrm{Mbar\,cm^3\,g^{-1}}$			

Table B.2 Table of hydrocode and reactive model parameters